Spring 2023

IRON CHELATOR AND FLUOROPHORE PEPTIDE BIOCONJUGATES FOR THE STUDY OF CELLULAR IRON METABOLISM

Leonid I. Povolotskiy
University of New Hampshire, Durham

IRON CHELATOR AND FLUOROPHORE PEPTIDE BIOCONJUGATES FOR THE STUDY OF CELLULAR IRON METABOLISM

By

Leonid I. Povolotskiy

B.S. Biochemistry, University of Vermont, 2018

DISSERTATION

Submitted to the University of New Hampshire

in partial fulfillment of

the requirements for the degree of

Doctor of Philosophy

In

Chemistry

May 2023

This thesis/dissertation was examined and approved in partial fulfillment of the requirements for the degree of

Doctor of Philosophy in Chemistry by:

Dissertation Director, Roy P. Planalp,

Associate Professor of Chemistry

Glen Miller,

Professor of Chemistry

Richard Johnson,

Professor of Chemistry and Material Science

Nate Oldenhuis,

Assistant Professor of Chemistry

Alan Packard,

Associate Professor of Radiology and Senior Research Associate

Harvard Medical School

Boston Children’s Hospital

DEDICATION

I dedicate this dissertation to my partner, Haley Marie Roy. Without her, I would not be the man, scholar, and scientist I am today or for that matter, made it halfway through graduate school. She may not have contributed directly to the work discussed here, but she has, and in no small part, made it happen.

ACKNOWLEDGEMENTS

I would like to acknowledge my advisor, Roy Planalp. His high expectations have molded me into the chemist and person I am today. Forever pushing me to reach higher and put myself outside of my comfort zone.

I would also like to acknowledge my undergraduate advisor, Rob Hondal. It is he who prepared me for graduate school. I was treated as a legitimate researcher in that laboratory with expectations to match. It is there that I first began to solve complicated problems and found my passion for research.

I would be remiss to not mention Dr. Suzy Torti and Lia Tesfay, the talented cell biologists who performed all our cellular studies and who are responsible for every micrograph in this dissertation.

Finally, I want to acknowledge all of the group members and friends past and present, that have gotten me here. Listed here in no particular order, Dr. Ryan Fitzgerald, Evan Jaworski, Nick Pollack, Emily Andrews, Michael Moheban, Taylir Bullick, Son Vihn Nguyen, Jackson Kaspari, Erinn Kaspari, Dylan Stolba, Francis Gomez and Nathan Bartlett. Thank you all for the part you played in my journey.

Table of Contents

List of Figures and Schemes

Scheme

Figures

STRUCTURE KEY

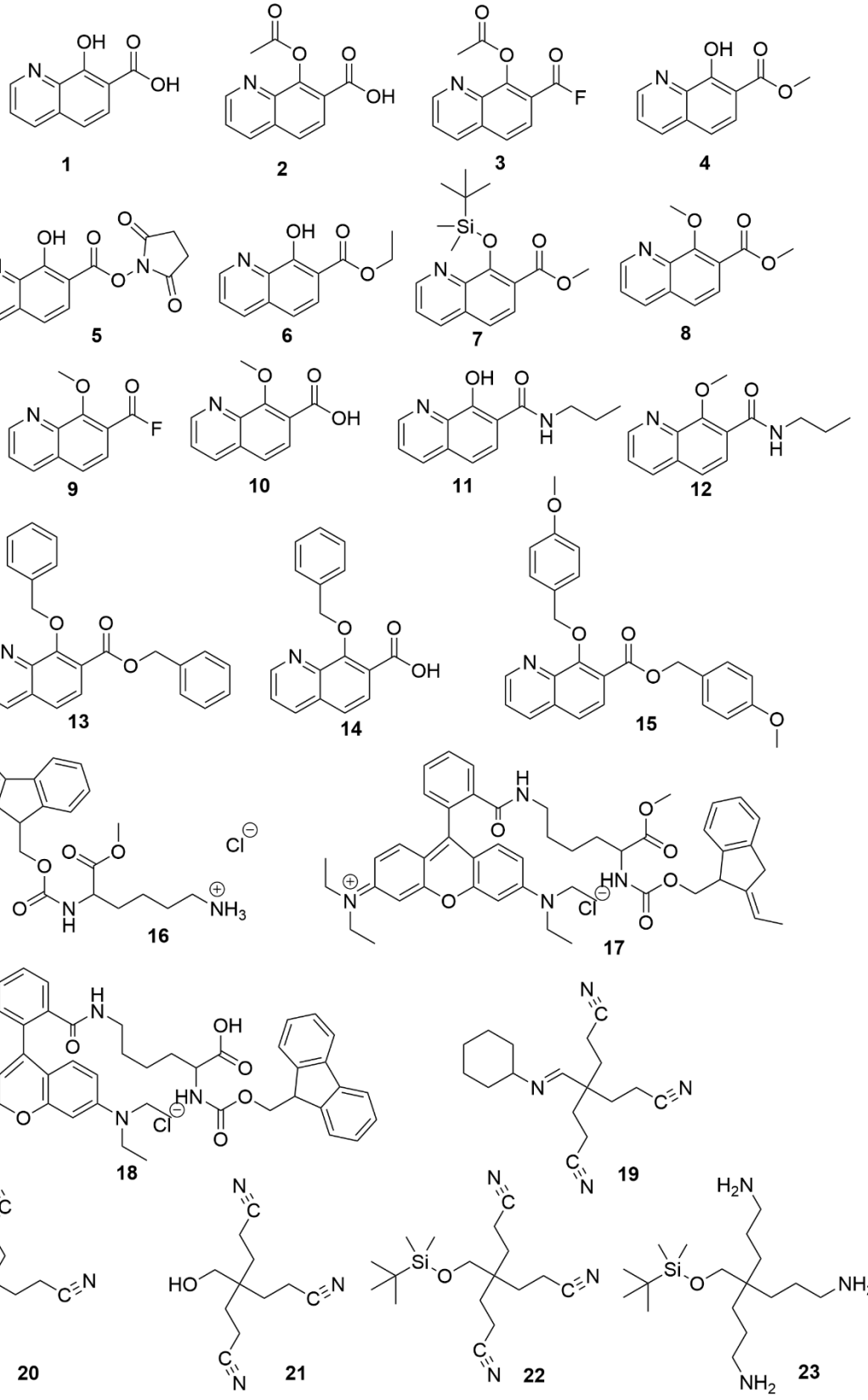

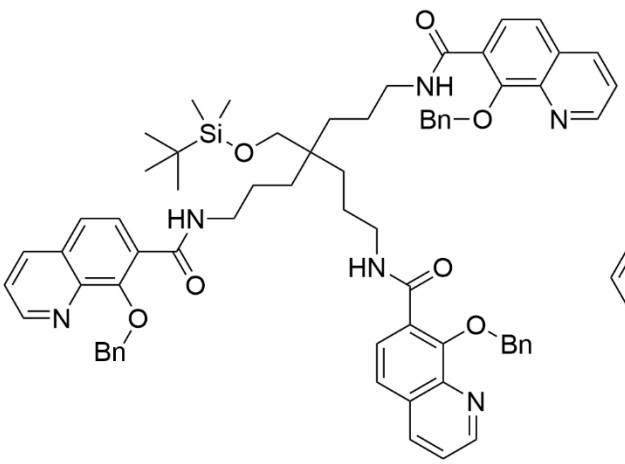

24

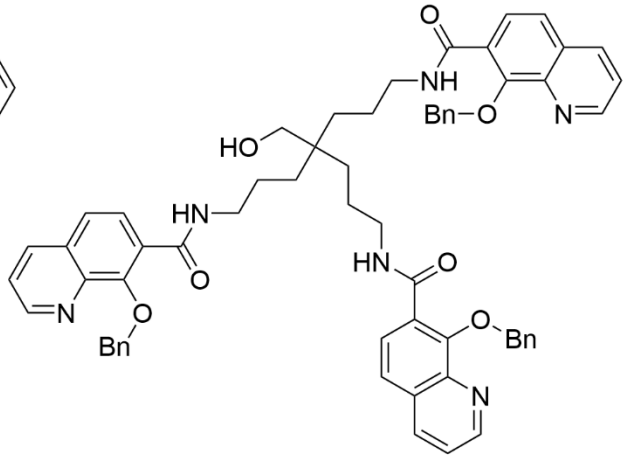

25

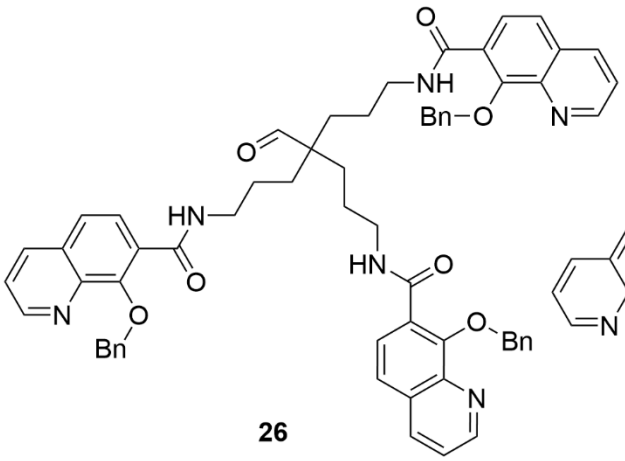

26

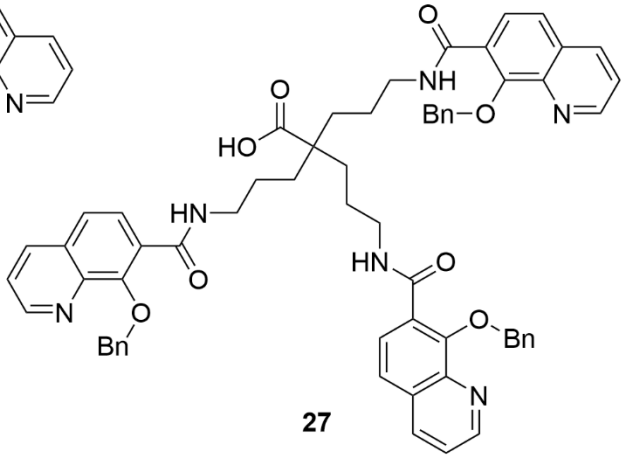

27

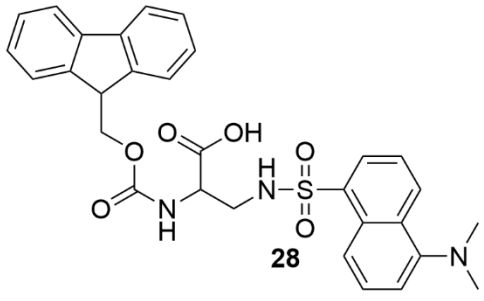

28

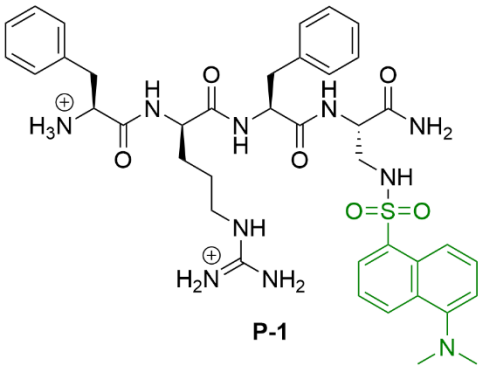

P-1

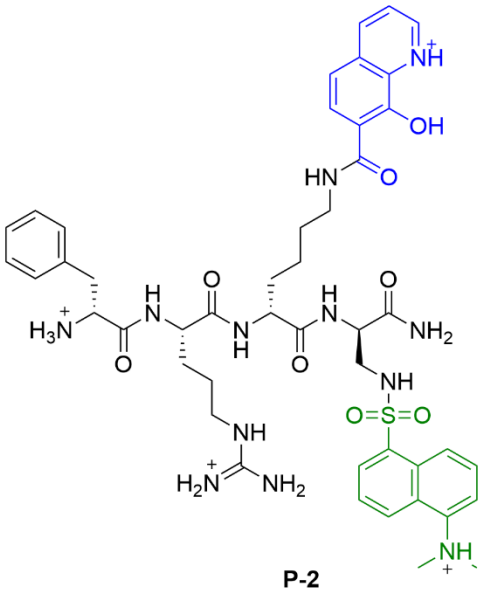

P-2

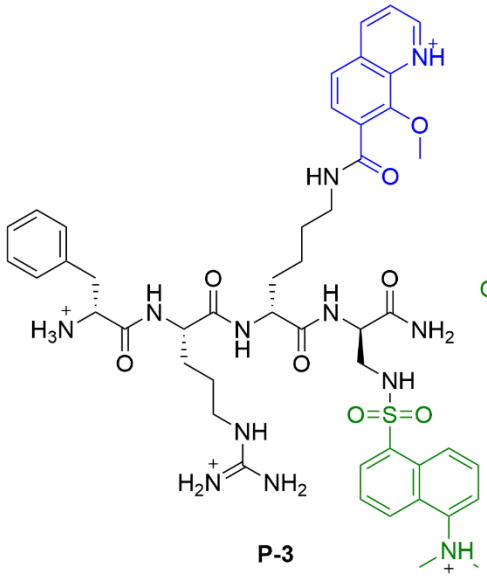

P-3

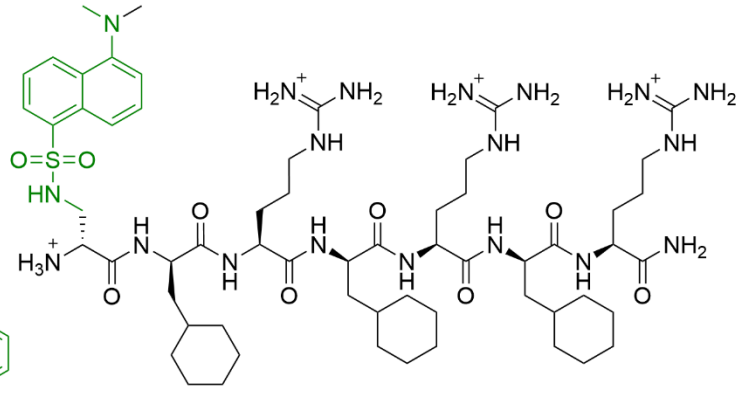

P-4

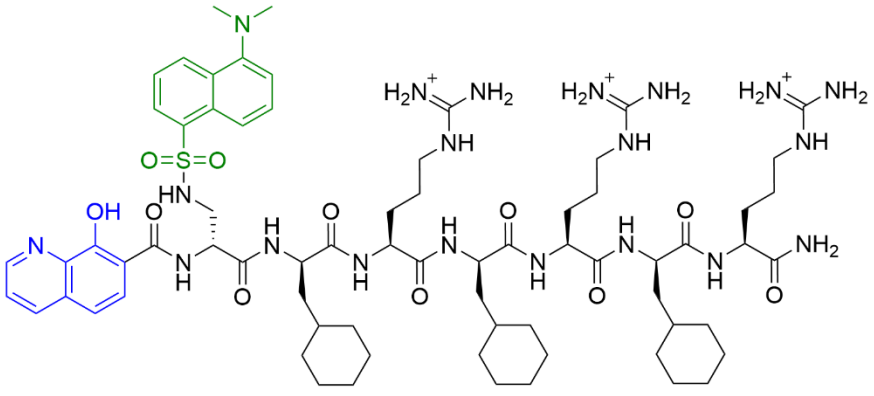

P-5

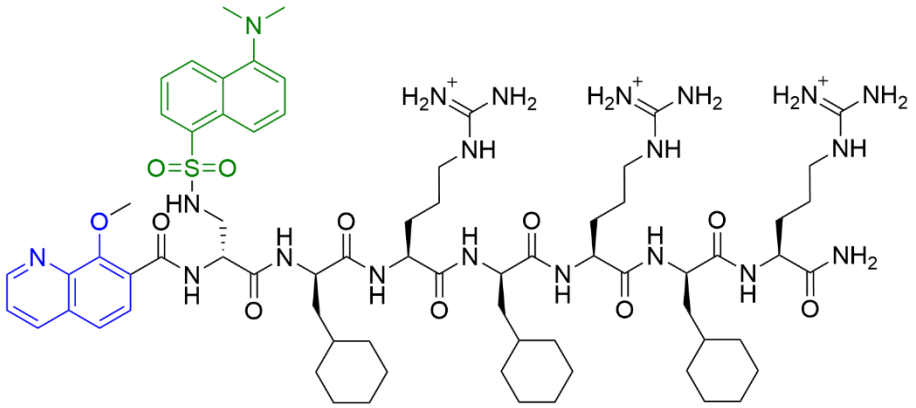

P-6

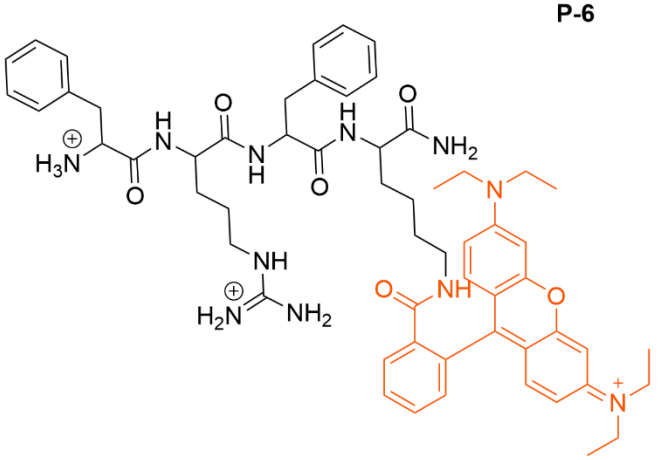

P-7

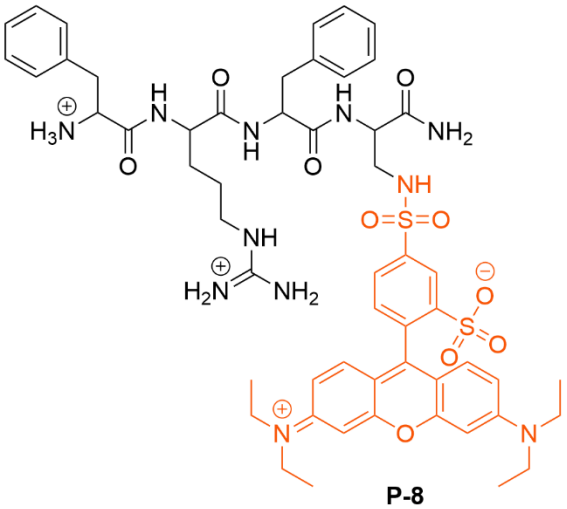

P-8

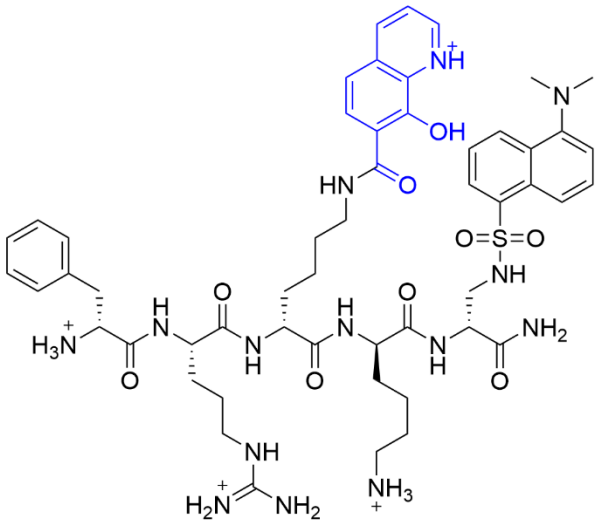

P-9

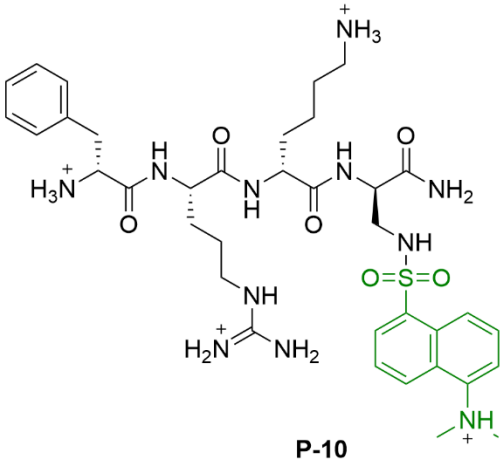

P-10

ABSTRACT

Bifunctional Szeto-Schiller (SS) peptides provide new tools for the study of cellular processes and drug delivery at the organelle level. SS-peptides have been shown to localize to the inner mitochondrial membrane (IMM), which holds a large fraction of intracellular labile iron. Dysregulation of iron has been linked to a variety of disorders ranging from neurodegeneration to cancer. Previous studies have employed the hydroxypyridinone and catechol chelating families which fail to inhibit Fenton-style redox cycling of iron. It has been shown independently, that tripodal 8-hydroxyquinoline (8HQ) structures can prevent Fenton chemistry. SS-peptide variants containing 8HQ as the iron-chelating group along with a fluorescent reporter were prepared. It was determined that the peptide backbone does not interfere with iron binding and there is a fluorescent response to increasing iron concentrations. Additionally, the iron-peptide complexes were shown to prevent the generation of hydroxyl radicals when compared to an EDTA-iron complex. These conjugates were successfully targeting to mitochondria in an ovarian cancer cell model and cellular experiments are ongoing. The synthesis of a linkable 8HQ tripodal structure has been completed but final deprotection conditions remain elusive. The effect of the fluorophore was also examined through substitution of the dansyl group to a rhodamine B analogue. The new conjugates were subjected to the same cellular localization studies but failed to colocalize with commercially available mitochondrial stains.

Chapter I

Synthesis of 8-Hydroxyquioline Based Iron Chelators, their Conjugation to Peptide Substrates and Iron Binding Activity

Introduction

Metals undoubtably play a pivotal role in facilitating the countless chemical reactions critical to all life on this planet. The various activities and trafficking of metals has been explored extensively for many years and continues to be an active field of study. Many metals have been shown to be necessary for life at least in some capacity. These include the "macro-nutrients" like magnesium, calcium and sodium as well as "micro-nutrients" like iron, copper, zinc and manganese.[1-4] Excessive amounts of either the macro or micro-nutrients results in environments that are toxic for biological systems.[1, 5, 6] Owing to the inherit toxicity that metals can have, coupled with the inherit compartmentalization of cellular biology, increasingly complex regulatory pathways have evolved that are dedicated to the control of metal ions.[7, 8] Of particular interest are the so called redox-active metals, which belong to the transition metal block of the periodic table. While many of the first row transition metals are important to life in some capacity, iron and copper are by far the most abundant and consequently contribute to a much larger array of disorders and diseases.[9] It has been known for some time that excess amounts, commonly referred to as overload contribute to oxidative stress in the body that can lead to neurological, cardiovascular and even oncological consequences. As a result, numerous undertakings have revealed many of the intricacies of overload disorders and contributed to the development of biologically available ligands to treat the condition.[10-12] While there is little doubt that there are still avenues to probe, much of the attention has shifted to the dysregulation

of redox active metals. For example, it's currently thought that iron and copper accumulate in the amyloid plaques associated with Alzheimer's disease, generate reactive oxygen species (ROS) and help accelerate the onset of the disease.[1, 13, 14] Additionally, the discovery of labile sources of redox-active metals has opened to door for new drug targets and a chance to further the understanding of cellular metabolism.[15, 16]

Iron is by far the most abundant transition metal in biological systems with expansive roles in oxygen transport, DNA replication and redox homeostasis.[5] Much of the biological iron is relatively stable, due to high formation constants with bioligands like heme and encapsulation in enzymes. However, a significant portion of iron does exist as labile iron and is often associated with relatively weak intracellular chelators like citrate.[17, 18] The labile iron pool (LIP) predominantly exists as Fe^{2+}, as the intracellular environment is generally reducing and its concentration is tightly controlled by cells to limit oxidative damage through Fenton-like reactions.[19] The complete role of LIP remains elusive however it has been well documented that the LIP plays a critical role in the cell death pathway known as ferroptosis.[20-22] Ferroptosis is an

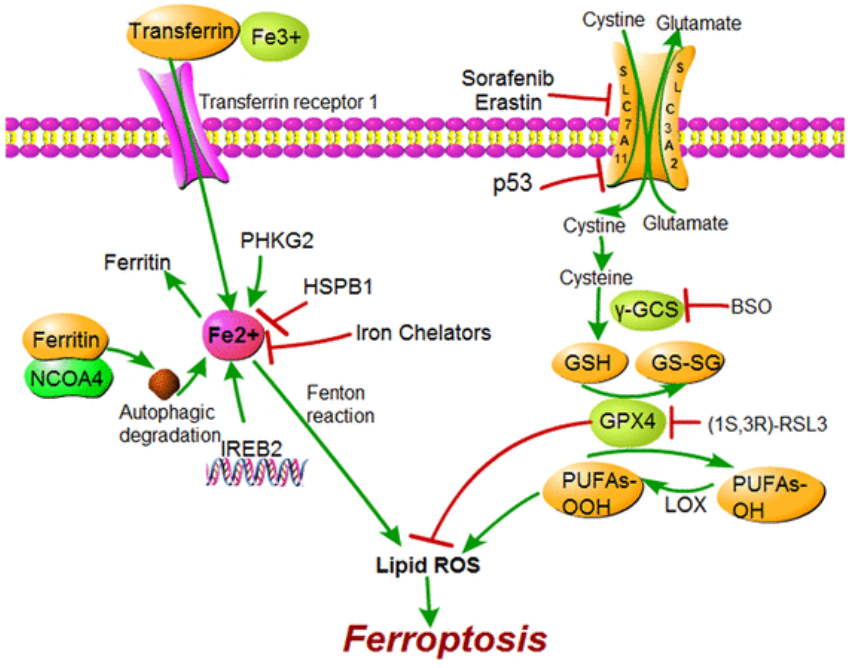

Figure 1: Cartoon representation of factors leading to ferroptosis. Reproduced from reference 14.

iron dependent programmed cell death pathway that is distinctly independent of other cell death processes. It has been shown to proceed via lipid peroxidation though Fenton-style reactions and to initiate in and around the mitochondrion.[22-24] (**Figure 1**). The expansive role and careful control of intracellular iron has led to the development of many fluorescent probes tailored to the visualization of labile iron at the organelle level.[25-27]

Recognition-based turn-on probes for iron have been particularly challenging as recognition-based approaches, because Fe^{3+} and high-spin Fe^{2+} are paramagnetic and therefore their complexes induce significant fluorescence quenching.[28] One strategy to overcome this phenomenon has been the recent advent of activity based sensors (ABS) that use the redox activity of iron to promote chemical reactions that induce fluorescence.[25] Several unique approaches have been reported, in which iron is detected through reduction of fluorophore N-oxides, oxidative cleavage of endoperoxides and C-O bond cleavage to liberate fluorescent molecules.[25, 29-31] Probes that rely on the redox activity of Fe^{2+} sometimes struggle with selectivity against other reductants like glutathione and even ascorbate.[32] Other redox-active bio-metals like copper or cobalt may also interfere depending on probe localization.[1, 29] Unlike recognition based probes, these reactions are irreversible, greatly limiting the ability to monitor dynamic iron fluctuations. Additionally, ABS probes are indirect measures of iron, and more accurately a measurement of the activity of iron toward a certain intracellular transformation under the assumption that only iron can cause the reaction. It is for reasons such as these we have chosen to pursue recognition-based iron probes.

Recognition based probes for Fe^{2+}/Fe^{3+} are typically iron ligands that behave as turn-off style probes due to the paramagnetic nature of all Fe^{3+} complexes and high spin Fe^{2+} complexes. Unlike ABS probes, recognition-based probes are typically not used for Fe^{2+} due to selectivity

concerns that arise from iron's average ligand affinity in the Irving-Williams series. Consequently, most recognition-based probes are tailored for Fe^{3+}, which has hard Lewis acid characteristics that distinguish it from other bioavailable metal ions allowing for selective chelation. There have been many turn-on probes reported for Fe^{3+} based on the spirolactam equilibrium of rhodamine but many of these examples do not account for the aqueous speciation of Fe^{3+}.[33-36] Measurements should be conducted in buffers at physiological pH with an additional chelator to keep the iron soluble. The predominate form of iron at this pH is $Fe(OH)_3$, which is essentially insoluble ($K_{sp} = 10^{-36}$).[36] Without any soluble iron present, the ring opening of the spirolactam may be caused by a host of different reasons and we therefore avoid this strategy.[37]

Although the visualization of intracellular iron has been accomplished with SS peptide-iron chelator conjugates, monitoring, and modulating its redox activity remains elusive. Previous work has focused on hydroxypyridinone and catechol ligand families which have high iron binding constants, but show no evidence of modulating the redox activity of iron.[18] Unrelated work using tripodal 8-hydroxyquinoline (8HQ) chelators has demonstrated that a kinetic barrier

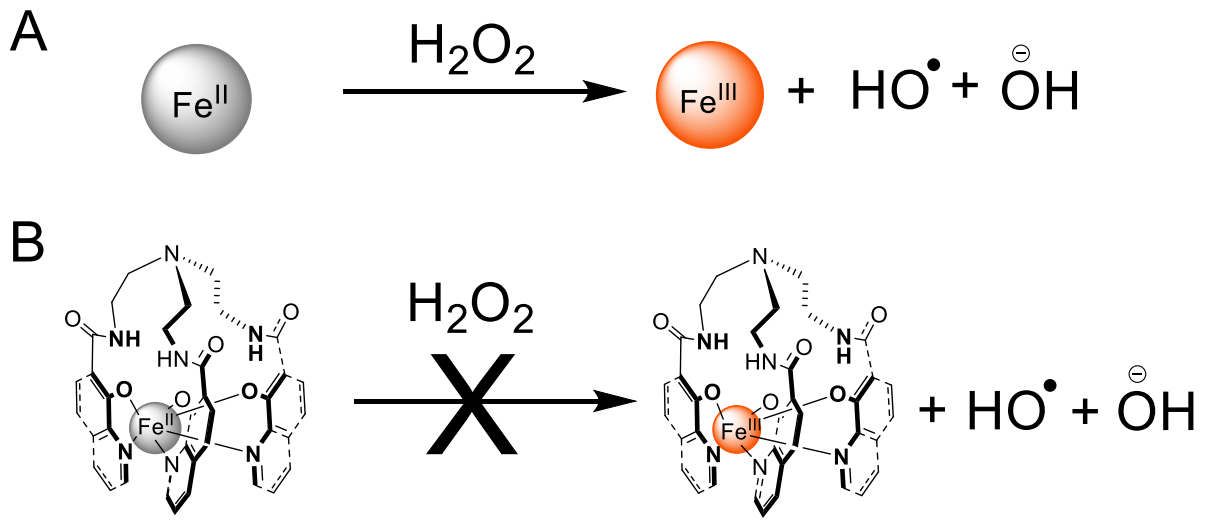

Scheme 1: **A**: Generic Fenton reaction scheme. One electron oxidation of iron (II) resulting in the formation of hydroxyl radical. **B:** Trensox ligand results in no detection of hydroxyl radical.

to the Fenton reaction **(Scheme 1B)** can be achieved while maintaining binding constants comparable to natural siderophores.[38, 39] Despite the promising properties of this class of chelator, its use on biological systems remains limited. Our aim is to incorporate tripodal 8HQ based chelators into an organelle targeting peptide probe to monitor and modulate cellular responses to iron while decoupling iron concentration and reactive oxygen species (ROS). Outlined here is the synthesis and characterization of a bifunctional tripodal 8HQ iron chelator **(Figure 2)** as well as the peptide conjugation and iron binding activity of 8HQ based iron chelating probes.

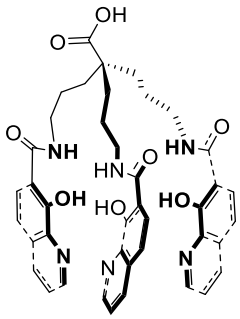

Figure 2: Structure of bifunctional tripodal 8HQ based iron chelator.

Results and Discussion

Synthesis

The ε-amine of a pendant lysine residue was first functionalized using 7-carboxy 8HQ(**1**), HATU and DIPEA. We hypothesized that the amide formation would be the predominant product as the nucleophilicity of the ε-N is greater than the phenolic oxygen and that amides are thermodynamically favored over esters. Unfortunately, MALDI-TOF MS analysis showed formation of 8HQ esters in addition to the desired couplings **(Figure 3).** We attempted to minimize this effect with stochiometric amounts of **1,** HATU and DIPEA (relative to resin loading) but this resulted in incomplete couplings even after 48 hours (Kaiser test). The succinyl ester (**5)** was also prepared but also resulted in incomplete coupling even with large excess of **5**.

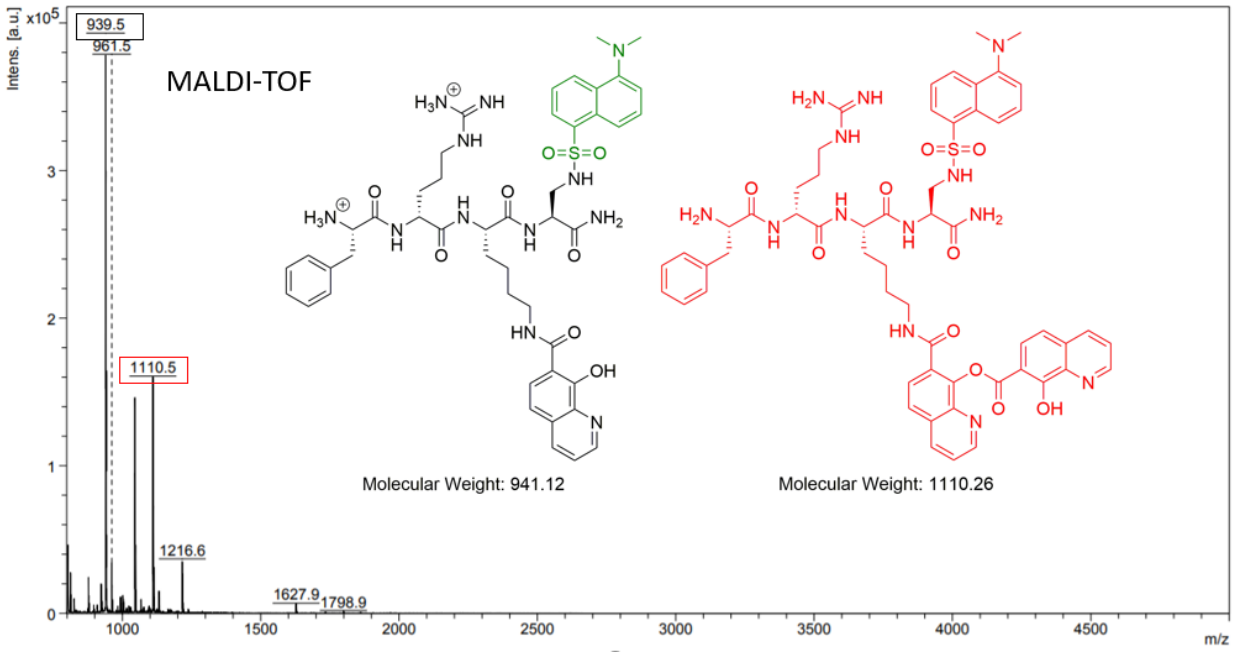

Figure 3: MALDI-TOF MS of **P-2** prepared with unprotected 8HQ. Desired product (Black) and 8HQ ester product (Red). The low intensity peak at 1216 m/z represents an ester chain of 3 8HQ molecules (not shown). Dansyl fluorophore is indicated in green on the desired product structure.

We therefore sought to protect the phenol with an easily removable protecting group that would be orthogonal with solid phase peptide synthesis (SPPS). An acetal group was introduced in one step with acetic anhydride and sulfuric acid (**2)**, and the resulting ester was subsequently reacted with the free ε-N of lysine in the same way as described for **1**. Quantitative coupling was achieved within 24 hr but the resulting peptide still contained 8HQ esters as evidenced by MS and shoulders found in the aromatic region of the NMR **(Figure 4)**. Premature removal of the acetyl group may occur through nucleophilic attack by the 1-hydroxy-7-azabenzotriazole (HOAt) unit which is encapsulated in the HATU reagent. While additional experiments are required to confirm this hypothesis, it is supported by the observation that a DIC mediated coupling (without HOAt) and reaction with the acyl fluoride (**3)** accompanied by excess DIPEA both did not result in premature deprotection.

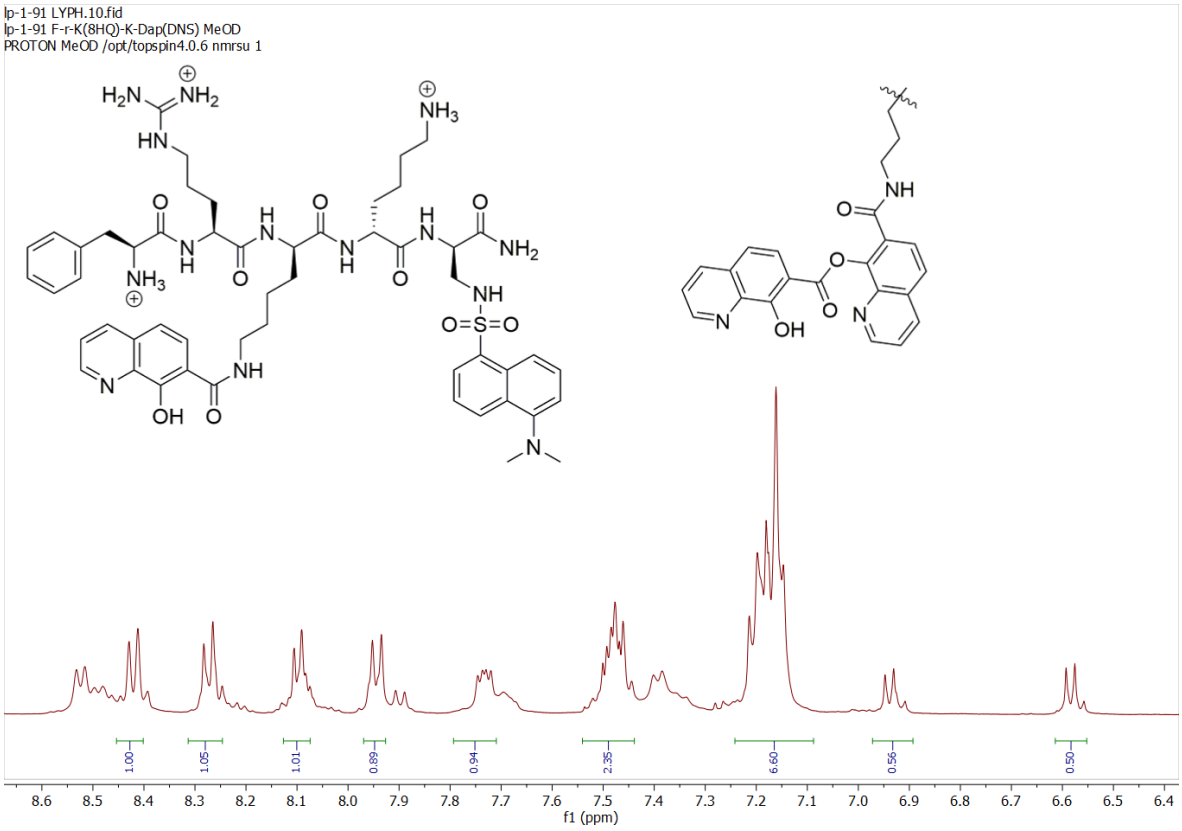

Figure 4: Aromatic region of ^{1}H NMR of **P-9**. Shoulders indicate the presence of 8HQ esters. Full spectrum can be found in appendix.

Further functionalization required the protection of the carboxylic acid group of **1** and so the ethyl ester (**6)** was prepared. Initially the methyl ester (**4**) was prepared via Fisher esterification, but stoichiometric amounts of sulfuric acid were required as only the pyridyl N was protonated under catalytic conditions. Any attempts to esterify **1** with catalytic Bronsted acid resulted in no reaction. Consequently, a small excess of sulfuric acid was required and **4** was isolated as the sulfate salt. Further modifications **4** failed even with excess additions of non-nucleophilic bases like DIPEA. This prompted the change to a Lewis acid catalyzed esterification and **6** was prepared from BF_3•(OEt_2)/EtOH. **6** was then reacted directly with propylamine to form model compound **11**.

For peptide coupling a silyl ether was initially chosen as the phenol protecting group as the deprotection conditions (F^-) were mild and can be easily achieved with a resin bound peptide. A tert-butyl dimethyl silyl group was introduced to the **6** via TBS-Cl and imidazole to form **7**. Unfortunately, the TBDMS group proved to be too labile for our conditions. Attempts to hydrolyze the **7** to the carboxylic acid resulted in loss of the silyl ether before any hydrolysis of the ester bond could be observed. Both acid and base mediated hydrolysis were attempted but, in each case, only **1** and **6** could be recovered.

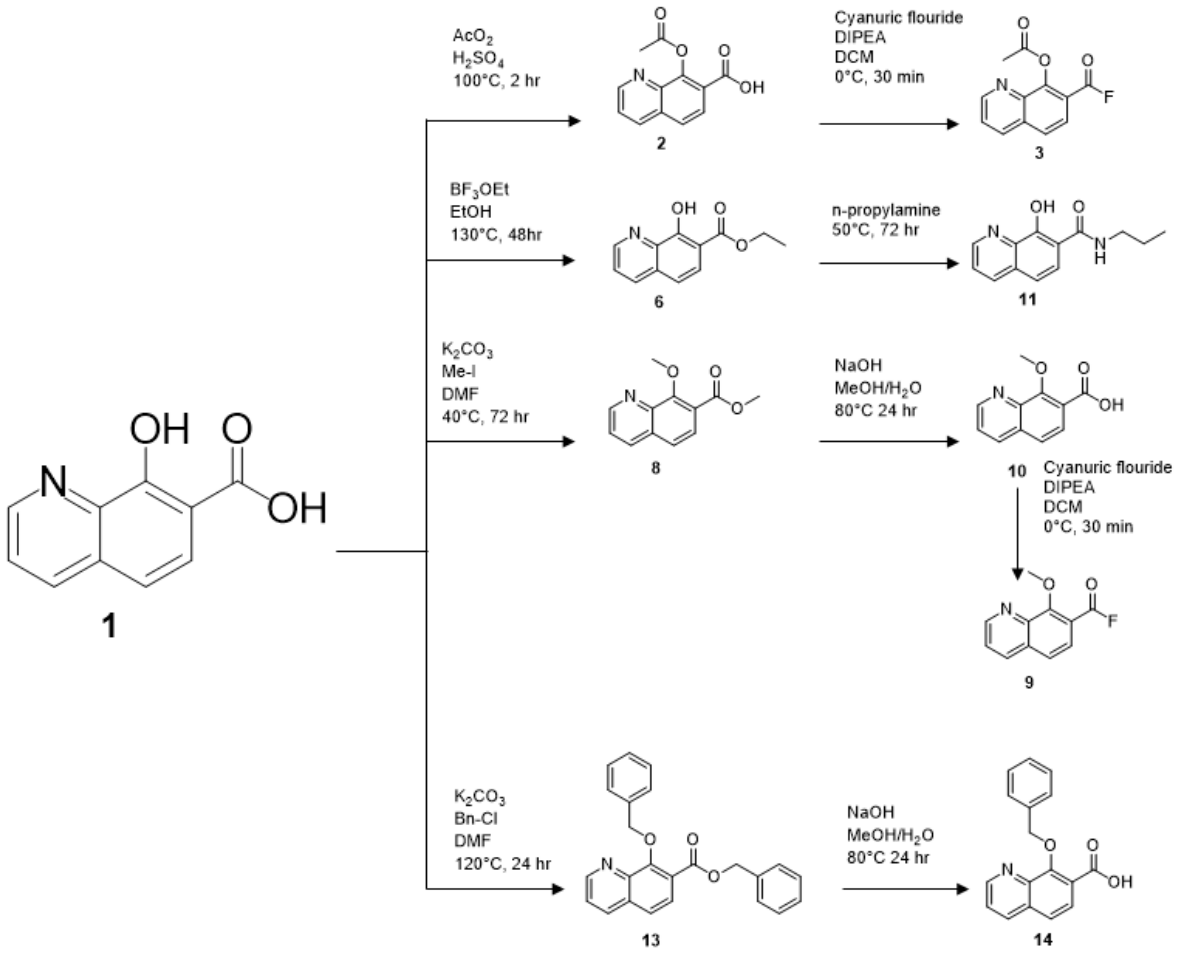

Scheme 2: Schematic representation of derivations of **1** to achieve model compound **11** and protected compounds for peptide coupling.

Inspired by methodology found in literature for catechol derivatives, the methyl ether (**10**) was prepared[23, 40, 41]. This was accomplished through a reaction with excess Me-I and the subsequent demethylated product (**8**) was hydrolyzed to the desired monomethyl ether **10**. DIC, PyBOP and HATU coupling agents were attempted but in each case, coupling of **10** to the ε-N of resin-bound lysine was incomplete after 24 hours. The electron donating group positioned ortho the carboxylic acid results in a destabilized carboxylate anion and as such the acid was sluggish to react with any coupling agent. To achieve quantitative on resin coupling, the acid fluoride (**9)** was prepared, and complete reaction was achieved with moderate excess (3-4 x) and short reaction times of 45 min-1 hour. This SS-20 peptide (**P-3**) would serve as a non-metal binding control. To generate the metal binding peptide, **P-3** was cleaved from the resin, isolated and a BBr_3 mediated deprotection of the methyl ether was attempted. The reaction was carried out as reported for similar substrates but and only peptide fragments were detected and no desired product was observed in the mass spec.[23] This approach was abandoned in lieu of protecting groups that could be removed with less harsh conditions.

To achieve the free phenol as the final product, the acetyl protected variant was revisited and the acid fluoride (**3**) prepared. **3** was subsequently coupled to the free ε-N in the same method as described for **10** and resulted in the free phenol after TFA mediated peptide-resin cleavage as evidenced by MS. Both the SS and Kelley peptide variants were prepared in this way.

For coupling to the tripodal linker a benzyl ether was used to protect the phenol (**14**). This was chosen in place of the methyl ether due to both its ease of preparation and its milder deprotection conditions. The previously successful acid fluoride coupling method was incompatible with the tripodal linker due to the TBS ether group present in **23**. Any fluoride

liberated from acid fluoride coupling would deprotect the alcohol and introduce additional nucleophiles. Attempts to use the **2**, the acetyl protected variant resulted in either premature deprotection, leading to numerous side products and/or very low yields. To ensure a facile deprotection, the monomethyl benzyl ether (**15**) was also attempted but unfortunately any attempted hydrolysis resulted in loss of both monomethyl benzyl groups.

The tripodal linker was synthesized as reported in the thesis of Dr. Ryan Fitzgerald and coupling of **14** was accomplished with CDI to form **24**. PyBOP was also attempted but resulted in similar yields and a slightly more complicated purification. Following coupling, **24** was deprotected with TBAF and then oxidized consecutively with a Swern, then Pinnick oxidation. The benzyl protected tripodal ligand (**27**) was synthesized in 11% overall yield. Deprotection conditions for the final peptide-ligand conjugate still need to be elucidated. Serratrice and coworkers reported substantial over reduction of the quinoline backbone when using catalytic hydrogenation to deprotect the phenol.[39] An initial model reaction using transfer hydrogenation with cyclohexadiene and Pd/C was attempted but the resulting NMR showed no evidence of the desired product. Other methods of removing benzyl ethers involve the use of strong Lewis acids like BCl_3 or BBr_3. As outlined previously, BBr_3 deprotection conditions are incompatible with the peptide scaffold, however, there are some promising reports of milder BCl_3 mediated cleavage using pentamethylbenzene as a carbocation scavenger.[42]

Iron Binding and Redox Activity

Electronic spectra (**Figure 5**) of both model compound Fe(**11**)$_3$ and Fe(**P-2**)$_3$ agree well with similar reported Fe^{3+} complexes.[43] In both Fe(**11**)$_3$ and Fe(**P-2**)$_3$, two main absorption bands are detected at 450 and 595-600 nm respectively. Molar absorptivity constants were calculated for Fe(**11**)$_3$ (ε_{450} = 3450 $M^{-1}cm^{-1}$ and ε_{595} = 3550 $M^{-1}cm^{-1}$) and were found to be within 25%

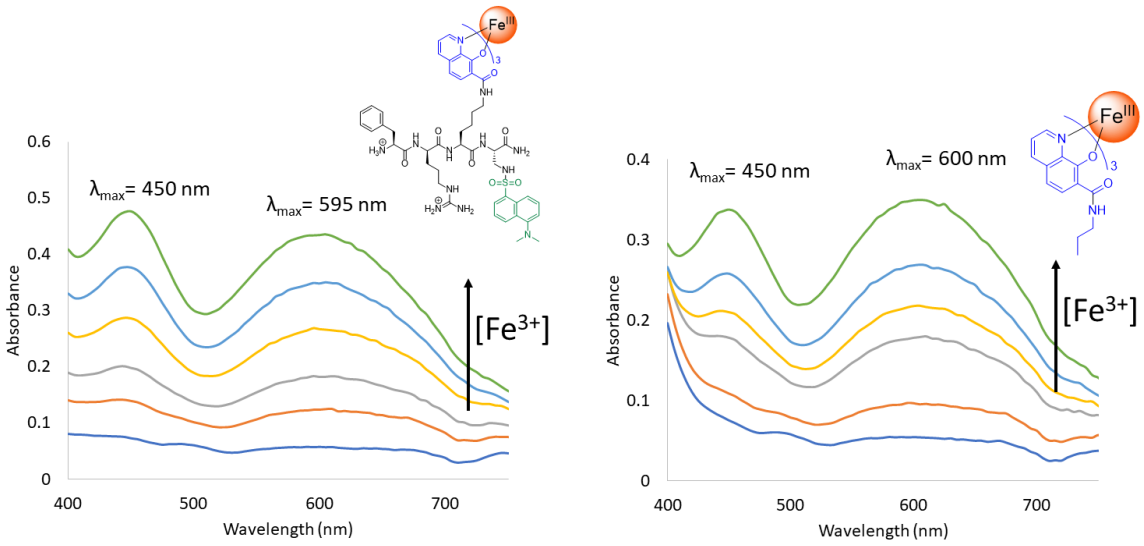

Figure 5: UV-Vis spectra of Fe(**P-2**)$_3$ (left) and Fe(**11**)$_3$ (right) with increasing concentrations of Fe^{3+}.

difference of the values reported by Serratrice and coworkers for similar complexes.[44] Spectrophotometric titrations conducted by Serratrice et al. allow us to assign the higher energy band to LMCT of the phenol, and the lower energy band as the LMCT of the pyridinyl N. Binding stoichiometry was confirmed as 3:1 ligand to Fe with Jobs' plots for both **11** and **P-2** (**Figure 6)**. Taken together with the excellent alignment of the Fe(**11**)$_3$ and Fe(**P-2**)$_3$ UV-Vis

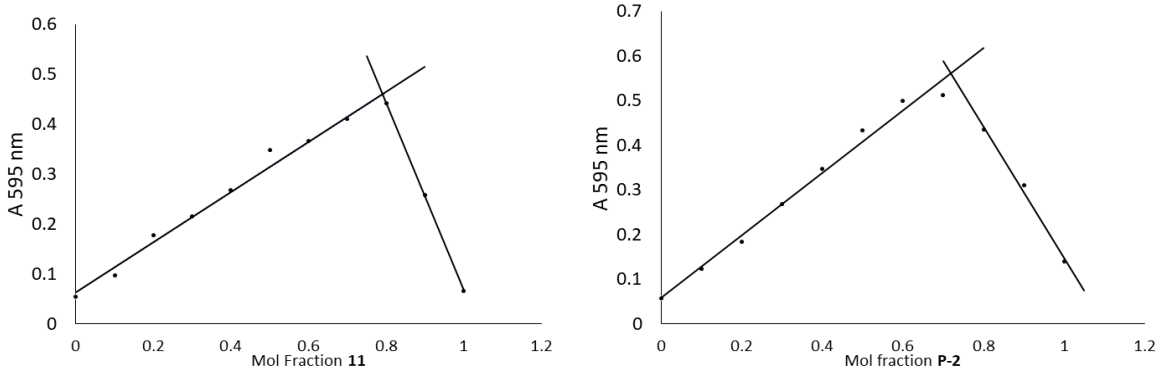

Figure 6: Job's Plots of Fe(**11**)$_3$ (**Left**) and Fe(P-2)$_3$ (**Right**).

spectra, it can be concluded that the peptide scaffold does not participate significantly in iron binding.

Selectivity for iron of **P-2** was tested with the addition of 1/3 eq of various metals and fluorescence quenching was monitored upon addition of Fe^{2+} and Fe^{3+} (**Figure 7**). We observed fluorescence quenching in all cases except for Co^{2+} and Cu^{2+} indicating at least qualitative selectivity against common bio-metals. The selectivity against Co^{2+} and Cu^{2+} is difficult to determine as the resulting complex is paramagnetic and so fluorescence is quenched significantly before the introduction of Fe. Selectivity for iron against cobalt or copper is challenging due to iron's position in the Irving-Williams series. Any complex with cobalt or copper will be inherently more stable than the iron complex. Interestingly however, we observed an increase in fluorescence intensity after Fe^{2+} addition suggests that some reaction must be occurring, and possibly some Fe(**P-2**)$_3$ is forming. Normalizing the fluorescence intensity to **P-2** without any

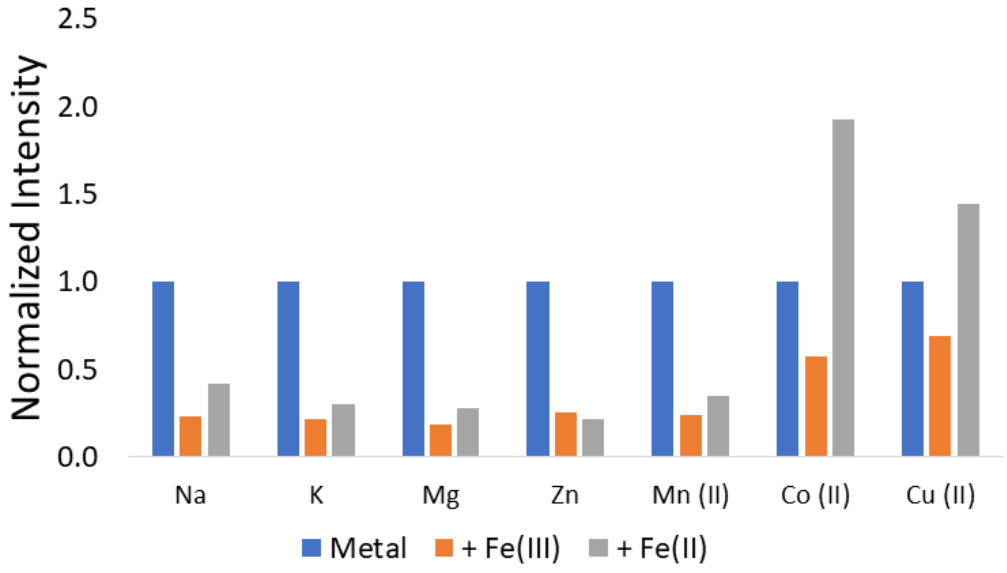

Figure 7: Normalized fluorescence intensity of various metals complexed with **P-2** (Blue). Addition of Fe^{2+} (Grey) and Fe^{3+} (Orange) indicates selectivity against all metals tested. Metals to **P-2** stoichiometry was fixed at 3:1.

metal shows that the intensity of **P-2**/Cu^{2+}, Co^{2+} after Fe^{2+} addition is comparable to that of the other metals, indicating that there may indeed be some selectivity against Cu^{2+} and Co^{2+} (Appendix).

The $logK_f$ for Fe(**11**)$_3$ was found to be 7.50 ± 0.36 over six different concentrations**.** This does represent a significantly lower formation constant than that of Fe(8HQ)$_3$ and of other similar reported complexes which come in on the lower end $logK_f$ of at least 10.[43-46] We postulate that this may be due to steric interactions between the alkyl chains of **11** during complexation and/or the electron withdrawing nature of the amide group, but further experimentation is needed. Additionally, the values calculated here were achieved using a spectroscopic method where additional absorbances may complicate the generation of a reliable calibration curve. The thermodynamics of binding are better determined using isothermal titration calorimetry and plans are in place to measure the binding constant this way.[47]

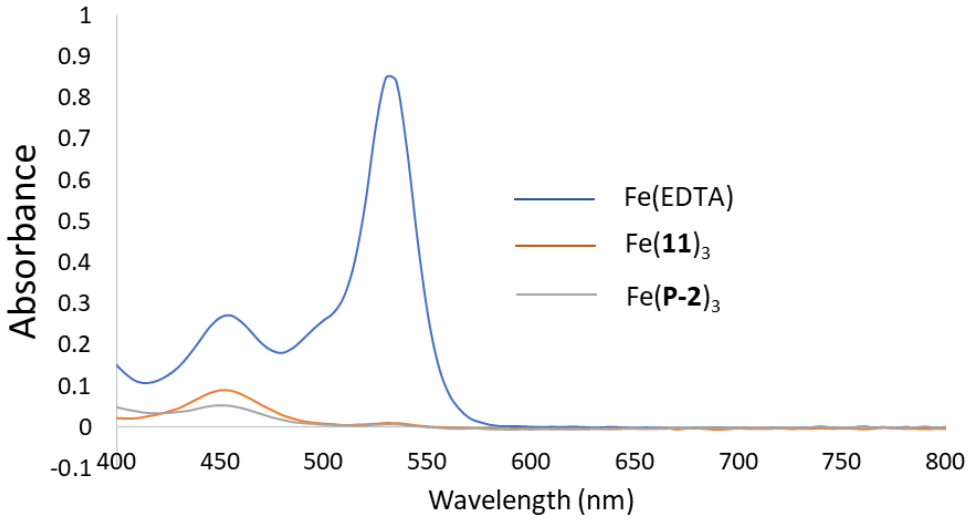

Figure 8: Overlayed UV-Vis spectra of 2-deoxyribose degradation assay mixture.

Nevertheless, the concentration of iron in the labile pool is well agreed upon as micromolar and so a $\log K_f$ over 6 represents significant iron binding at those concentrations.[15] Any attempts to complex Fe^{2+} resulted in rapid oxidation to Fe^{3+}. However from **Figure 7** it can be seen that the ligand is still selective for Fe^{2+} against most bio-metals, and most notably Zn^{2+} which is found in similar labile concentrations to Fe.[48] Additional experiments and anaerobic conditions are required to determine the binding constant of Fe^{2+}.

The redox activity of the tris-peptide iron complex was examined using a TBA-deoxyribose degradation assay and was compared to Fe(EDTA), Fe(**11**)$_3$ and Fe(**P-2**)$_3$ (**Figure 8**). This assay was used to measure hydroxyl radical formation through the degradation of 2-deoxyribose to malondialdehyde which subsequently forms a colored adduct with TBA.[49]

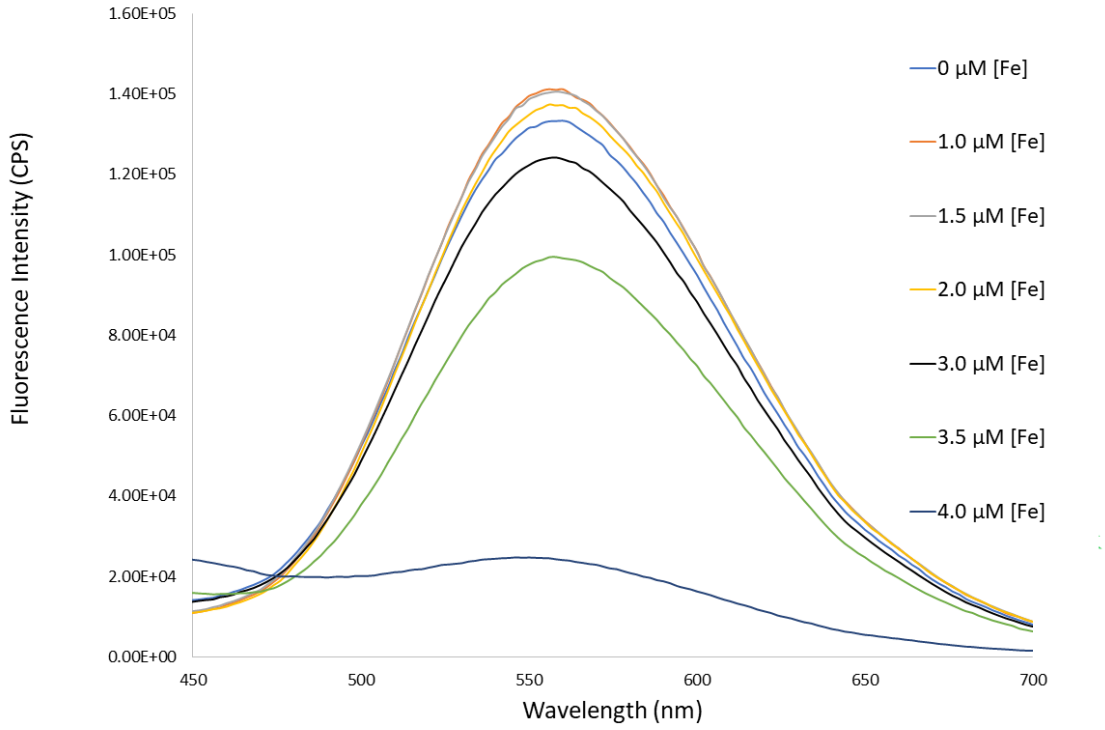

Figure 9: Fluorescence response of **P-2** with increasing iron concentrations. [**P-2**] = 12µM in 50mM Mops, pH=7.4.

Fe(**11**)$_3$ and Fe(**P-2**)$_3$ complexes both prevented hydroxyl radical generation as evidenced by the absence of the strong absorbance peak at 530 nm while Fe(EDTA) clearly shows substantial generation of the colored adduct. This result indicates that **11** and **P-2** have some antioxidant properties, but it is still unclear if Fenton chemistry is inhibited, or if the hydroxyl radical is rapidly scavenged by the ligand. Electrochemical studies are required to completely elucidate the redox properties of **11**, **P-2** and ultimately **27.**

Titration of Fe^{3+} into a solution of the **P-2** (**Figure 9**) showed that fluorescence quenching reaches a maximum at the coordination stoichiometry of 3:1 peptide:iron which is consistent with the Jobs' plots. Plotting the relationship between fluorescence intensity versus iron concentration (Stern-Volmer) results in a non-linear fit, indicating that the quenching cannot be attributed to random collisions between the fluorophore and quencher.[50] Unfortunately, our results here do not give reliable iron concentrations and more experiments are required to "calibrate" the sensor. At present the probe functions in an on-off style and a reference signal is required to use this sensor quantitatively. A ratiometric response is desired and is in consideration for future probes.

General Conclusions

A peptide-fluorophore-chelator conjugate and a linkable tripodal 8HQ based ligand were successfully prepared. The on-resin conjugation of the 8HQ unit proved challenging, but efficient coupling conditions via the acyl fluoride were elucidated. The iron binding activity of the peptide conjugate was indistinguishable from model compound **11** and a fluorescence response was observed with **P-2** with varying iron concentrations. A lack of hydroxyl radical generation during Fenton reaction conditions gives promise for decoupling intracellular iron

concentrations and ROS generation. The tripodal linker is ready for coupling to a peptide but deprotection conditions must be approached carefully to ensure substrate compatibility.

Chapter II

Synthesis and Cellular Targeting of Szeto-Schiller Peptide Conjugates

Introduction

Mitochondria are organelles that are nearly ubiquitous to life and through oxidative phosphorylation, synthesize arguably life's most important molecule, ATP.[51] Colloquially known as "the powerhouse of the cell", current understanding depicts mitochondrial function as two-fold.[52] Undoubtedly, the mitochondrion hosts the machinery responsible for ATP synthesis and generates the majority of ATP used by an organism.[53] Over the past several decades, mitochondria have also gained recognition as signaling organelles in complex cellular signaling cascades like the caspase-mediated apoptosis pathway and the iron-mediated ferroptosis pathway.[22, 24, 52] Mitochondria are membrane-rich organelles consisting of a porous outer membrane (OMM) and a highly folded inner membrane (IMM). Owing to the ATP synthesis machinery, the inside of the IMM displays a significantly negative electric potential as protons

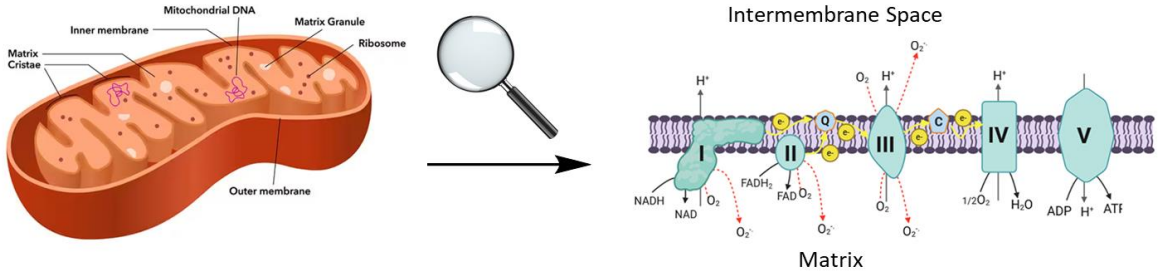

Figure 10: Cartoon representation of the IMM and the biochemical processes occurring there. Reproduced in part from reference 55.

are actively pumped out of mitochondrial matrix (**Figure 10**).[54, 55] This negative potential is often exploited as a target for molecules destined to localize to the organelle.[56] Another consequence of oxidative phosphorylation is the generation of reactive oxygen species (ROS) which must be carefully controlled.[57] Without careful control, a buildup of reactive oxygen species (ROS) can occur leading to mitochondrial DNA damage or an undesired signaling cascade.[58, 59]

Consequently, oxidative processes of the mitochondrion have become an active field of study with many small molecule and peptide probes developed in recent years.[60] The negative potential, coupled with large hydrophobic regions allows some lipophilic cations to localize to mitochondria. The most common small molecule used to traffic payloads to mitochondria are alkylated triphenyl phosphoniums (TPP).[56, 61] While TPPs have undoubtedly demonstrated their

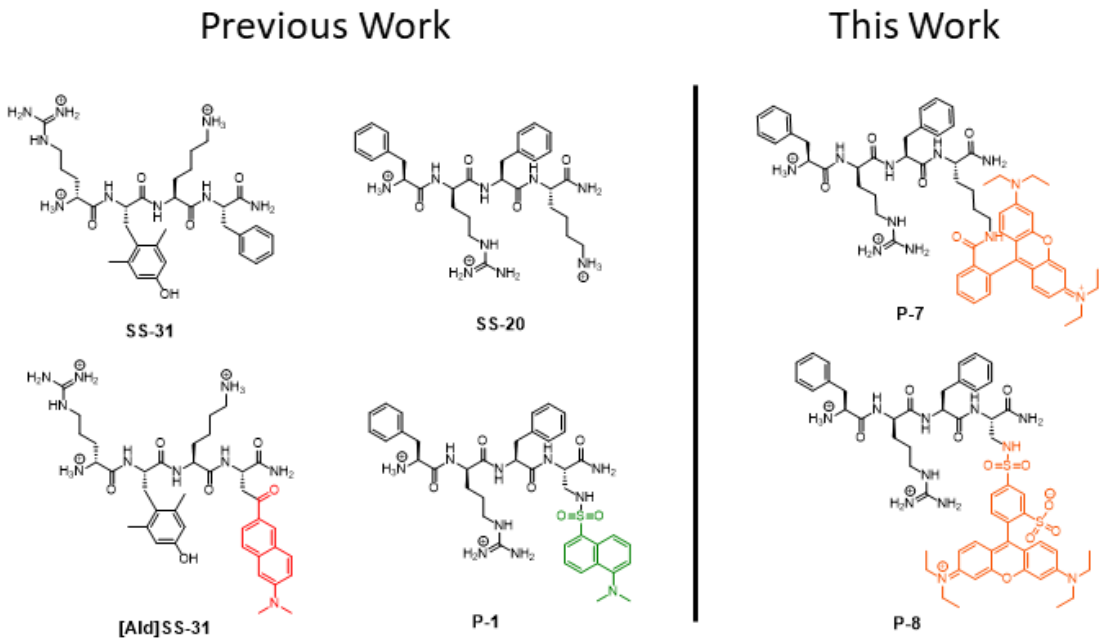

Figure 11: Structures of commonly used SS peptides and their respective fluorescent aladan (Red) and dansyl (Green) counterparts (Right). Structures of peptides **P-7** and **P-8** (Left).

utility, they are also known to depolarize the mitochondrial membrane which disqualifies their use for monitoring dynamic processes.[62] Other small molecules have also seen success, chief among them being the rhodamine 123 scaffold, which several of the commercially available Mito-Tracker dye series are based off. However, many of these approaches suffer from poor payload capacities and cellular toxicity.[56, 63] Some issues have been addressed via a class of mitochondrial targeting cell penetrating peptides known as the Szeto-Schiller (SS) peptide family.[23, 64-66] SS-peptides contain a characteristic motif of repeating hydrophobic and cationic residues which are believed to be critical for mitochondrial localization.[67] The most popular of these variants, SS-31 and SS-20 are known to localize to the inner mitochondrial membrane (IMM) and have received attention as therapeutics of mitochondrial oxidative stress, attributed to electrostatic interactions between the cationic peptides, the anionic mitochondrial membrane and complex interactions between the hydrophobic residues and the lipid tails of the IMM exclusive lipid, cardiolipin.[66-68]

Molecule	Log P
MitoTracker Orange	3.49
MitoTracker Red	4.23
SS-31	-2.74
SS-20	-1.79
P-1	-1.99
P-7	-0.51
P-8	-2.90

Table 1: Calculated logP values of relevant molecules. All logP values were calculated using Molinspiration Cheminformatics free web services (https://www.molinspiration.com) and calculated with the appropriate charges on ionizable groups at physiological pH.

Localization and uptake of these peptides is traditionally monitored via radioactive labeling or by attachment of a fluorescent group to the peptide, as the examples shown in **Figure 11**, [Ald]SS-31 and [Dns]SS-20 (**P-1**).[66, 69, 70] The fluorescent

reporters in these examples have a high energy excitation wavelength, requiring the use of complex two-photon excitation techniques to avoid interference from biomolecules like NADH and undesired photolysis of cell contents.[71] To confirm mitochondrial localization, commercially available mitochondrial stains such as the MitoTracker series are often used in tandem with fluorescently labeled peptides (**Figure 12B**).[18, 23, 66] The primary mechanism of localization is still an active field of study but is thought to be partially due to electrostatic interactions between the IMM and cationic peptides as well as complex interactions with the unique lipid structure of the IMM.[56, 66, 73]

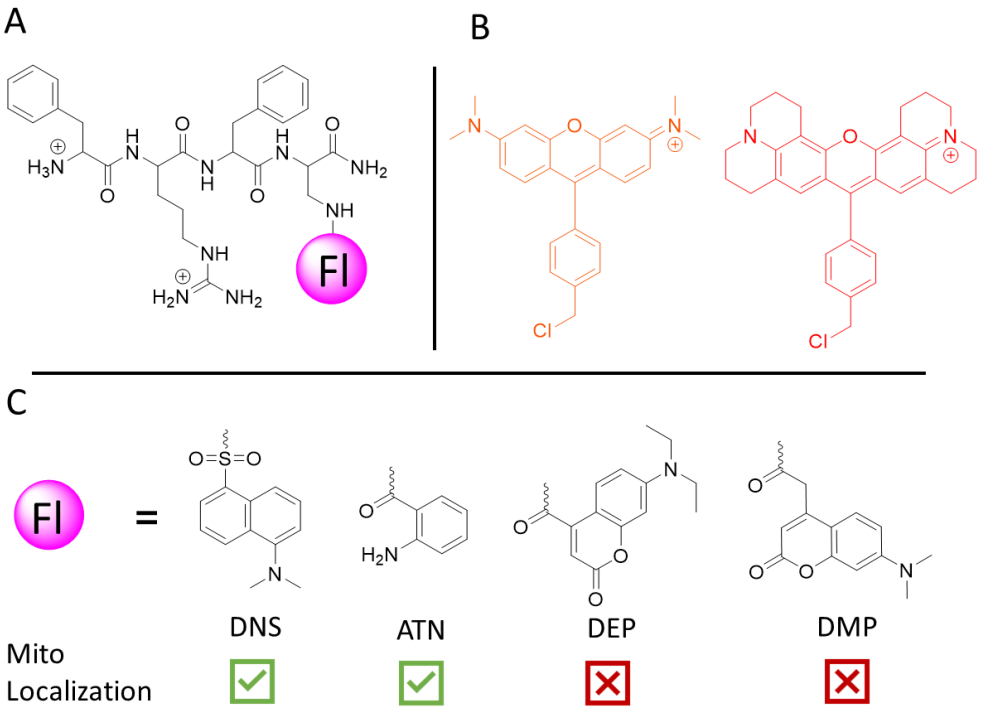

Figure 12: General structure of SS-20 fluorescent derivatives (**A**), Structure of commercial MitoTracker Orange and Red dyes (**B-left and right respectively**) and structure of fluorophore along with mitochondrial localization results as reported in ref. 23 (**C**).

Unlike the SS-peptides, the MitoTracker series relies strictly on membrane-potential to achieve targeting and therefore employs lipophilic and cationic fluorescent scaffolds such as rhodamine 123 **(Figure 12B)**.[74] However, the mechanism of targeting concerning the SS-peptides appears to be more complicated. For one, the log P values of the SS-peptides (**Table 1**) suggest that they should fail to cross membranes reliably, but SS-20 and SS-31 have been shown to cross membranes in an energy independent process.[69, 75, 76] In addition to this, Abbate and coworkers prepared a series of 4 peptides all based on SS-20 while varying the attached fluorophore and observed different localization behaviors for some seemingly similar scaffolds (**Figure 12**).[23] As we and others have observed, the complex localization parameters of SS-peptides can limit their utility for practical use. To avoid such complications, we prepared a small series of rhodamine-based SS-20 analogs for improved photophysics and hydrophobicity. Unfortunately, these probes failed to colocalize with their rhodamine 1,2,3 counterparts which prompted the recent switch to a different family of mitochondrial targeting peptides composed of alternating D-arginine and cyclohexyl alanine residues.[77] Reported in this chapter is the synthesis and localization behavior of a library of peptides.

Results and Discussion

Synthesis

Peptides were successfully synthesized either manually in fritted glass tubes or using a aapptec Vantage automated peptide synthesizer. In both cases, orthogonal Fmoc-SPPS method was used. The peptides were all amidated on the C-terminus and prepared with D-arginine to prevent premature degradation by peptidases once inside the cell.[78, 79] Primary characterization was accomplished with mass spectrometry and purity accessed with reverse phase analytical

HPLC which can be found in the appendix. All peptides were collected as TFA salts and used without further purification.

Careful consideration to the side chain protecting groups was required to achieve selective deprotection of the ε-N of the lysine residue while on resin. All peptides were prepared using a rink amide resin linker with either a phenoxy or ChemMatrix® resin core. During the preperation of **P-7** and **P-8,** hydrophobic interactions between the phenoxy resin core and rhodamine scaffold resulted in ineffective washing steps and impure peptides. ChemMatrix® resin, which is composed of a more hydrophilic core was used instead in the preparation of rhodamine containing peptides to avoid unwanted substrate-resin interactions.[80] Mono methoxy trityl (Mmt) was used as the ε-N protecting group as it can be deprotected with 1% TFA, which is orthogonal with other acid labile protecting groups like O-TBu and Boc. On-resin modification of the peptide was first attempted whenever possible as it eliminates the need for several isolation and purification steps. Unfortunately, efforts to conjugate the dansyl fluorophore on resin as reported were unsuccessful so dansyl chloride was instead condensed with Fmoc-Dap-OH to prepare the fluorescent amino acid **28** which for use directly in peptide synthesis.[23, 81]

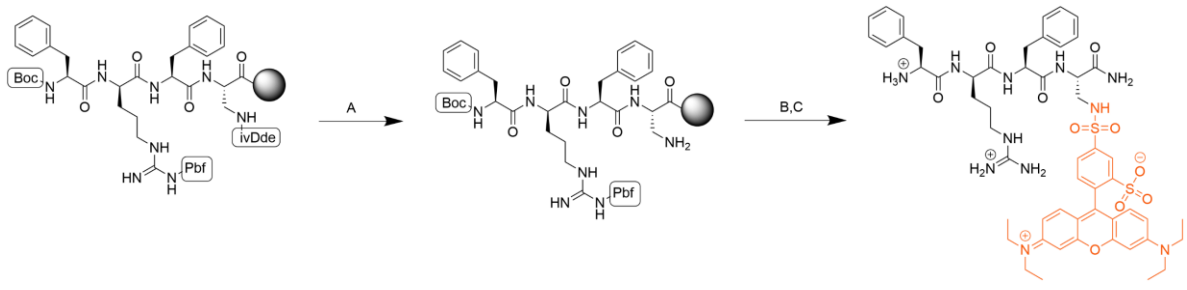

Scheme 3: Synthetic scheme for the preparation of [Lis]SS-20 (**P-8**). Conditions: A: 2% Hydrazine Hydrate/DMF B: Lissamine Rhodamine B sulfonyl chloride, DIPEA C: 98:2:2 TFA, H_2O TIPS.

In addition to the **P-1**, [Rho]SS-20 (**P-7**) and [Lis]SS-20 (**P-8**) were prepared to achieve detection without using two-photon microscopy. The rhodamine fluorescent scaffold was chosen because of favorable photophysics for conventional fluorescence microscopy and the structural similarity to commercially available MitoTracker dyes.[82] Rhodamine B was directly coupled to the methyl ester of Fmoc-Lys (**17)** and following ester hydrolysis **18** was used directly in peptide synthesis. Lissamine Rhodamine B was introduced via an on-resin modification of a diamino propionic acid residue which was installed with an IvDDE protecting group. IvDDE was removed using a dilute hydrazine solution and in this case, the N-terminal amine was BOC protected as FMOC will be removed by these conditions **(Scheme 3).**[83]

Peptide Localization

Colocalization of **P-1** and **P-2** with commercially available MitoTracker dye was observed with fixed OVCAR-4 cells (**Figure 12**). Colocalization was not observed for **P-10** which breaks the pattern of alternating hydrophobic and cationic residues. This is consistent with the parameters outlined by Szeto and coworkers.[84] The IMM is enriched in the phospholipid cardiolipin (CL) which has a unique conical structure and is found exclusively within the mitochondria.[73] Through a combination of experimental techniques and molecular dynamics simulations, Mitchell et al. have recently shown that peptide association to CL is vital to the antioxidant activity of SS-31. It is thought that the association occurs via specific interactions where the anionic head groups are partially neutralized by the cationic residues, leading to a loss of hydration and leading to the hydrophobic residues embedding within the lipid tails.[66] Loss of the alternating pattern will greatly affect how the peptide interacts with the IMM and therefore its membrane permeability.

Interestingly colocalization was not observed when viewing live cells, unlike what has been reported previously.[18, 41, 85] Instead, distinct puncta were observed throughout the cells. The punctate distribution suggests that association with another subcellular component is possible. Abbate and coworkers reported minor colocalization with lysosomes using the **P-1** probe which would appear as distinct puncta like observed.[18] Additionally, it has been reported that the counterions present in a peptide samples can significantly perturb a cellular system.[86, 87]The

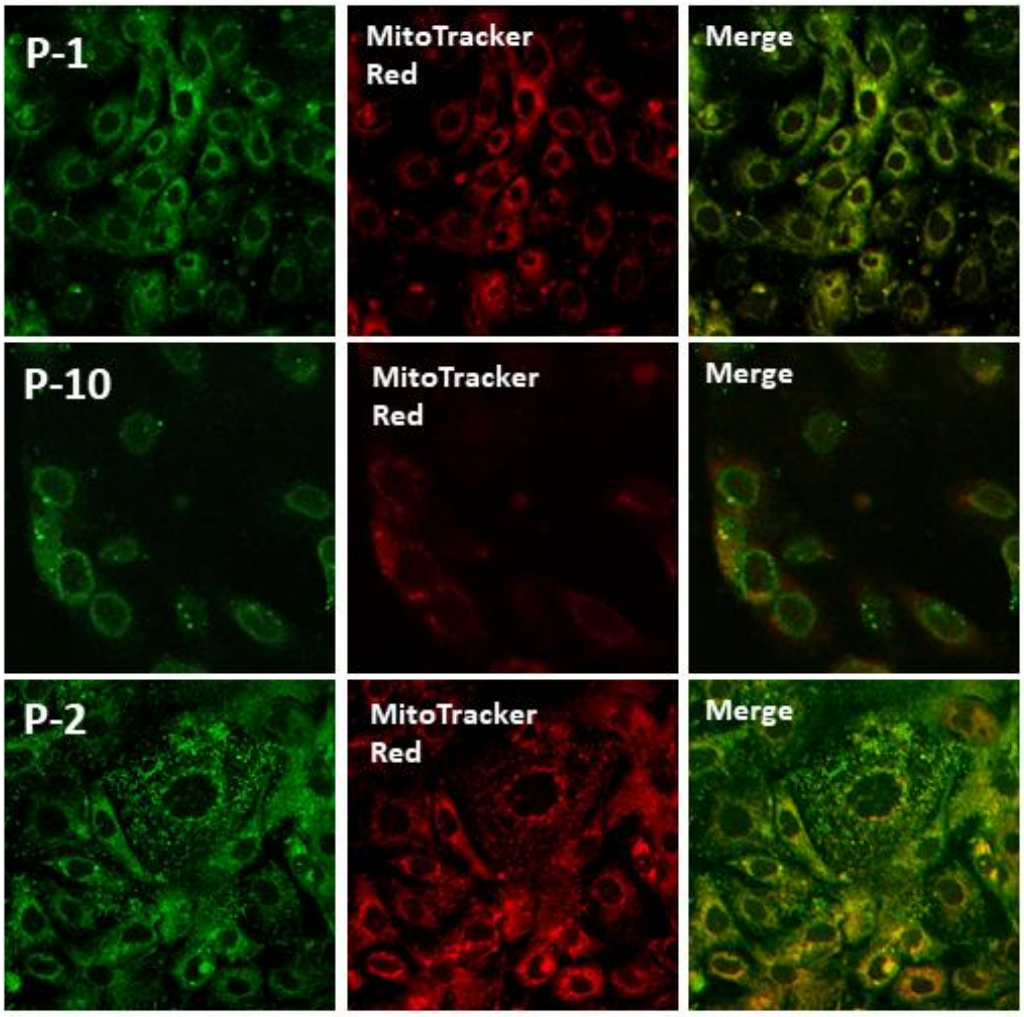

Figure 13: Confocal fluorescent micrographs of SS-20 variants. OVCAR4 cells were treated with 100 µM **P-1**, **P-2** and **P-10** for 24 hrs, then washed and treated with 200 nM MitoTracker Red for 45 minutes.

peptides used herein each contain multiple positive charges and would carry a molar excess of trifluoroacetate anions relative to peptide which may have led to unforeseen cellular processes. However, without radiolabeling or costaining with additional organelle specific dyes, it is impossible to determine the ultimate location of the probes.

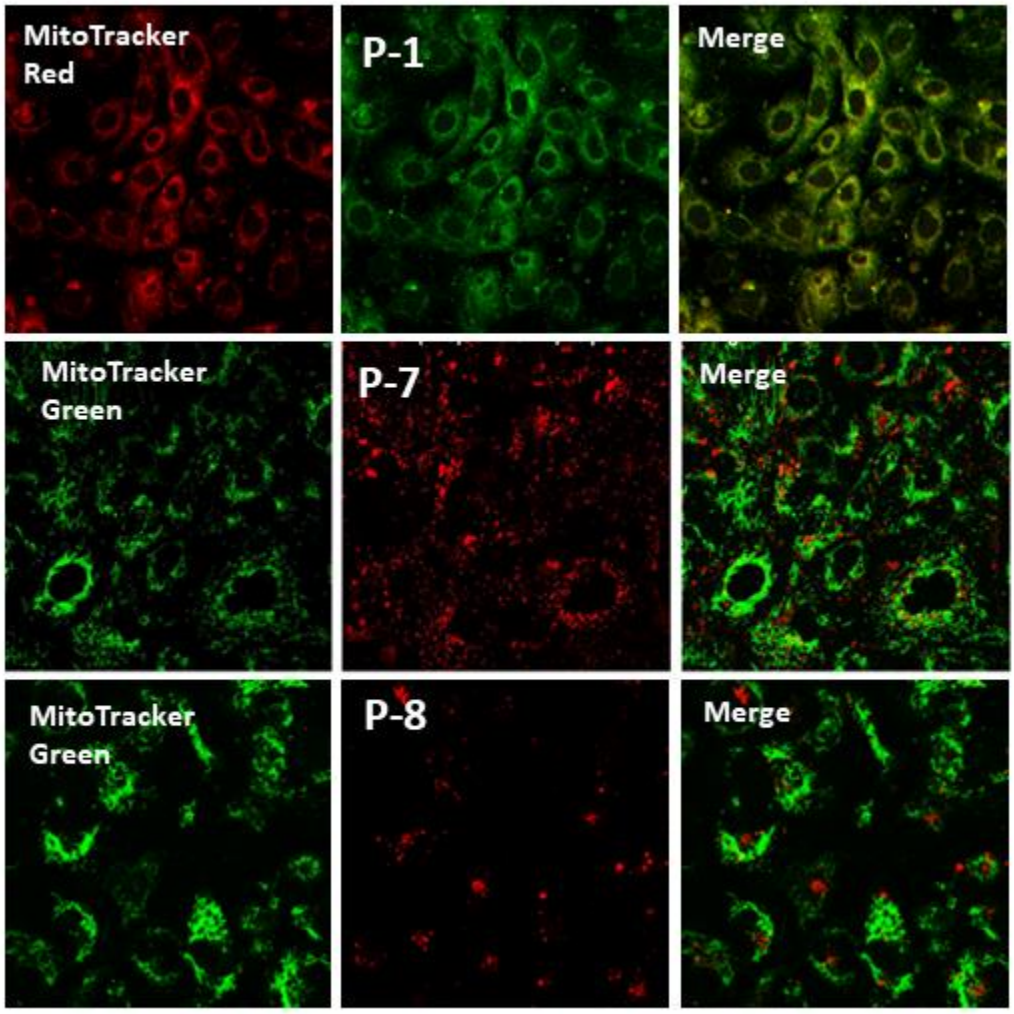

Figure 14: Confocal fluorescent micrographs of SS-20 variants. OVCAR4 cells were treated with 100 µM **P-1**, 10 µM **P-8** or 20 µM **P-7** probe for 24 hrs, then washed and treated with 200 nM MitoTracker Green or MitoTracker Red for 45 minutes.

Unfortunately, localization to the mitochondria was not observed by either of the rhodamine containing peptides. **P-7** and **P-8** did appear to show membrane permeability and much like **P-1** and **P-2** in the live cell case, presented distinct puncta within the cells (**Figure 14**) and was confirmed with Z-stacks in the case of **P-7**. This is further supported by calculated log P values, which are similar to **P-1** and in the case of **P-7**, actually more favorable for membrane penetration as more hydrophobic substances tend to diffuse through membranes better **(Table 1)**.[75, 88] This distribution again suggests that association with another subcellular component may be occurring but additional experiments are required to elucidate the localization behavior of these probes.

Reasons that **P-7** and **P-8** did not embed in the IMM may lie with size and hydrophobicity of the attached fluorophores.[65, 66, 69] As outlined for **P-10**, the specificity of the interactions between CL and the peptide are critical. The increased size of the rhodamine scaffold may have prevented the more hydrophilic regions of the membrane from moving into a favorable orientation for binding. The importance of these interactions is also supported by the findings of Abbate et al., where the identity of seemingly similar fluorescent scaffolds impeded some peptides from localizing in mitochondria (**Figure 12**).[23] We postulate that the bulky nature of the rhodamine scaffolds prevented the necessary interactions required to alter the packing of the CL head groups and therefore our peptides were unable to associate with the CL in the IMM. The peptides may have then been shuttled to the lysosomes for degradation. We are therefore pursuing other fluorescent tag derivatives of SS peptides, which will be reported in due course. Molecular simulations are currently ongoing to aid in future rational design of SS-20 peptide derivatives.

Many reports describe the targeting of SS peptides as a consequence of only electrostatics and lipophilicity but taken with the results outlined here, there is clear evidence that more complex processes are at play.[64, 66, 89] Nevertheless, **P-1** and **P-2** colocalized with commercially available Rhodamine based MitoTracker dyes and their cellular activity is currently being investigated.

General Conclusion

An efficient on-resin synthesis of a Lissamine rhodamine B SS-20 analogue was completed as well as the prepration of multiple SS-20 analogues. The cellular targeting of the probes was examined, and we uncovered the hidden complexities of cellular targeting. At present we do not have a substantial understanding of targeting intricacies to say for certain the elements necessary for mitochondrial localization. We believe that mitochondrial targeting, at least for the SS-peptides relies on more than electrostatics and further investigation is required to determine criteria for rational design. We are also currently investigating the effects of the counterion of the peptide probes and those results will be reported in due course.

Chapter III

Experimental

Materials and Instrumentation

Phenoxy Rink amide resin (Substitution 0.74 mmol/g) was purchased from Chem-impex International (Illinois, USA). Fmoc-dap-OH and Fmoc-dap(ivDDE)-OH was purchased from Bachem (Bubendorf, Switzerland). Peptide synthesis grade DMF, HPLC grade water, HPLC grade acetonitrile and Lissamine rhodamine B sulfonyl chloride were purchased from Fisher Chemical (Massachusetts, USA). Piperidine was purchased from Beantown Chemical Corporation (New Hampshire, USA). Dansyl chloride, rhodamine B and all other peptide synthesis reagents were purchased from Tokyo Chemical Industry (Tokyo, Japan). All reagents were used as received except for the DMF which was degassed via nitrogen sparging before use. NMR spectra were taken on either a 400 MHz and 500 MHz Oxford Instruments spectrometer or 700 MHz Bruker spectrometer. UV-Vis spectra were taken on a Cary 50 spectophotometer and spectrofluorimetric measurements were taken on an Edinburgh instruments Spectrofluorometer FS5. HRMS was conducted by Dr. Furong Sun through the University of Illinois mass spectrometry lab. Microscopy and cellular studies were conducted by Dr. Suzy Torti at the University of Connecticut Health Center.

Synthesis

8-Hydroxyquinoline-7-carboxylic acid (1): In a 250 mL Schlenk flask fitted with a magnetic stir bar, sodium metal (1 g, 43.5 mmol) was dissolved in 50 mL of dry methanol. To this was added 8-hydroxyquinoline (5 g, 34.4 mmol) and the mixture was stirred under N_2 at room temperature until complete dissolution. The mixture was evaporated under reduced pressure and

the residue was placed into an autoclave, charged with CO_2 to 40 bar and heated to 170ºC for 72 hours. The residue was then dissolved in water and the pH adjusted with HCl until pH=4. The resulting yellow precipitate was collected via vacuum filtration and recrystallized from water to yield yellow needle crystals (3.9 g, 60%). **^{1}H NMR** (500 MHz, DMSO) δ 8.92 (dd, *J* = 4.6, 1.6 Hz, 1H), 8.61 (dd, *J* = 8.4, 1.6 Hz, 1H), 7.92 (d, *J* = 8.6 Hz, 1H), 7.81 (dd, *J* = 8.3, 4.6 Hz, 1H), 7.32 (d, *J* = 8.7 Hz, 1H). **^{13}C NMR** (125 MHz DMSO) δ 171.7, 162.24, 147.28, 138.94, 138.64, 132.32, 128.14, 123.74, 114.01, 113.20.

8-acetylquinoline-7-carboxylic acid (2): In a 50 mL round-bottom flask equipped with a magnetic stir bar and reflux condenser, **1** (500 mg, 2.64 mmol) was suspended in 15 mL of acetic anhydride. Concentrated H_2SO_4 (14.2 µL, 0.26 mmol) was added and the reaction mixture was heated to 100°C. The reaction mixture was stirred at 100°C for 1 hour. The mixture was then allowed to cool to room temperature before 25 mL of ice-cold water was added to the flask. The precipice was collected and recrystallized from absolute ethanol to obtain 427.3 mg of pale-yellow powder (70.0%). **^{1}H NMR** (400 MHz, DMSO-d_6) δ 2.40 (s, 3H), 7.70 (dd, *J* = 4.0, 8.5 Hz, 1H), 8.00 (m, 2H), 8.50 (dd, *J* = 1.5, 8.5 Hz, 1H), 9.01 (dd, *J* = 2.5, 3.5 Hz, 1H), 13.44 (s, 1H, broad). **^{13}C NMR** (100 MHz, DMSO-d_6) δ 169.24, 166.23, 152.09, 147.95, 141.43, 136.63, 131.36, 127.10, 126.15, 124.12, 124.09, 21.22.

8-acetylquinoline-7-carboxyl fluoride (3): In a 100 mL Schleck flask equipped with a magnetic stir bar, **2** (501.4 mg, 1.8 mmol) was suspended in 10 mL of dry DCM. The mixture was cooled to 0ºC and cyanuric fluoride (148 µL, 1.8 mmol) was added. Then DIPEA (622 µL, 3.5 mmol) was added slowly. The mixture quickly became homogenous and was stirred at 0ºC for an additional 1.5 hr. Ice water (20 mL) was then added and the organic layer washed with water (3 x 20 mL), brine (3x 20 mL), dried with anhydrous Na_2SO_4 and evaporated under reduced pressure

to afford a yellow powder (363 mg, 87%). **1H NMR** (500 MHz, CDCl3) δ 9.01 (dd, *J* = 4.2, 1.7 Hz, 1H), 8.19 (dd, *J* = 8.4, 1.7 Hz, 1H), 7.98 (d, *J* = 8.7 Hz, 1H), 7.77 (d, *J* = 8.7 Hz, 1H), 7.55 (dd, *J* = 8.4, 4.1 Hz, 1H), 2.57 (s, 3H). **^{13}C NMR** (126 MHz, $CDCl_3$) δ 168.02, 154.70, 150.94, 150.58, 140.43, 134.91, 131.89, 125.59, 125.05, 123.40, 116.73, 116.25, 19.83. ^{19}F NMR (470 MHz, $CDCl_3$) δ 32.10.

8-Hydroxyquinoline-7-methyl ester (4): In a 500 mL two-neck flask equipped with a magnetic stir bar, nitrogen inlet and reflux condenser, **1** (10 g, 52.9 mmol) was suspended in 200 mL of dry methanol. To this was added BF_3•MeOH (45.72 mL, 420 mmol) dropwise over 30 minutes. The mixture was then heated to reflux for 16 hr. The volatiles were then evaporated under reduced pressure and the residue suspended in DCM (200 mL). The pH was adjusted slowly with 4M NaOH until pH = 4. The mixture was filtered, and the filtrate washed with water (3x 100 mL), brine (3x 100 mL) and dried with anhydrous $NaSO_4$. The solvent was removed under reduced pressure to afford a white powder. (7.4g, 69%). **^{1}H NMR** (500 MHz, $CDCl_3$) δ 11.87 (s, 1H), 8.97 (dd, *J* = 4.1, 1.6 Hz, 1H), 8.10 (dd, *J* = 8.2, 1.7 Hz, 1H), 7.87 (d, *J* = 8.7 Hz, 1H), 7.51 (dd, *J* = 8.3, 4.1 Hz, 1H), 7.25 (d, *J* = 8.8 Hz, 1H), 4.02 (s, 3H). **^{13}C NMR** (126 MHz, $CDCl_3$) δ 170.77, 160.01, 149.75, 139.73, 135.71, 132.30, 125.39, 123.85, 117.68, 109.20, 52.57.

8-hydroxyquinoline-7-N-Hydroxysuccinyl ester (5): In a 50 mL round-bottom flask equipped with a magnetic stir bar, **1** (1.00g, 5.29 mmol) and N-hydroxysuccinimid (603 mg, 5.29 mmol) were suspended in 20 mL of THF. Then N,N'-Dicyclohexylcarbodiimide (1.094g, 5.29 mmol) was added and the mixture was stirred at room temp. under nitrogen for 3 hours. The resulting red suspension was filtered, and the filtrate concentrated in vacuo to obtain brown oily solid. The residue was then recrystallized from DCM to yield 1.24 g of a brown solid (81.9%). **^{1}H NMR**

(500MHz, $CDCl_3$) δ 2.95 (s, 4H), 7.37 (d, *J* = 9.0 Hz, 1H), 7.61 (dd, *J* = 8.0, 8.5 Hz, 1H), 8.03 (d, *J* Hz, 1H), 8.19 (dd, *J* = 1.5, 8.5 Hz, 1H), 8.96 (dd, *J* = 1.5, 4.5 Hz, 1H).

8-Hydroxyquinoline-7-ethyl ester (6): In a 250 mL Schlenk flask equipped with a magnetic stir bar and reflux condenser, **1** (7 g, 37 mmol) was suspended in 150 mL of absolute ethanol. To this was added BF_3•OEt_2 (38.5 mL, 278 mmol) dropwise over 30 minutes. The mixture was then heated to reflux for 16 hours. The volatiles were then evaporated under reduced pressure and the residue suspended in 100 mL of DCM. The pH was adjusted to pH=4 with 4M NaOH and the mixture filtered. The filtrate was then washed with water (3x 100 mL), brine (3 x 100 mL) and dried with Na_2SO_4. The solvent was removed under reduced pressure to afford a yellow granular solid (7.5 g, 93%). **^{1}H NMR** (500 MHz, $CDCl_3$) δ 12.01 (s, 1H), 8.98 (dd, *J* = 4.2, 1.7 Hz, 1H), 8.10 (dd, *J* = 8.3, 1.7 Hz, 1H), 7.89 (d, *J* = 8.8 Hz, 1H), 7.51 (dd, *J* = 8.3, 4.2 Hz, 1H), 7.25 (d, *J* = 8.7 Hz, 1H), 4.49 (q, *J* = 7.2 Hz, 2H), 1.47 (t, *J* = 7.2 Hz, 3H). **^{13}C NMR** (126 MHz, $CDCl_3$) δ 170.47, 160.14, 149.72, 139.75, 135.75, 132.29, 125.43, 123.80, 117.57, 109.43, 61.80, 14.23.

8-tertbutyl dimethylsioloxyquinoline-7-methyl ester (7): In a 250 mL two-neck flask equipped with a magnetic stirbar, nitrogen inlet and reflux condenser was added **4** (2 g, 9.8 mmol) and imidazole (1.4 g, 20.5 mmol) were dissolved in 50 mL of dry THF. To this, TBDMS-Cl (1.6 g, 10.8 mmol) was added all at once. The mixture was heated to reflux under N_2 for 48 hr and then the volatiles removed under reduced pressure. The resulting residue was dissolved in DCM (50 mL) and washed with water (3x 75 mL), brine (3x 75 mL) and dried with anhydrous Na_2SO_4. The solvent was evaporated under reduced pressure and the grey solid recrystallized from hexanes to yield off white crystals (2.7 g, 87%). **^{1}H NMR** (500 MHz, $CDCl_3$) δ 8.82 (dd, *J* = 4.1, 1.7 Hz, 1H), 8.09 (dd, *J* = 8.3, 1.7 Hz, 1H), 7.83 (d, *J* = 8.6 Hz, 1H), 7.43 (dd, *J* = 8.3, 4.1 Hz, 1H), 7.34 (d, *J* = 8.6 Hz, 1H), 3.95 (s, 3H), 1.05 (s, 9H), 0.34 (s, 6H). **^{13}C NMR** (126 MHz,

$CDCl_3$) δ 167.87, 153.74, 147.50, 141.38, 135.52, 131.19, 127.89, 122.66, 119.27, 118.65, 52.11, 25.81, 19.39, -2.51.

8-methoxyquinoline-7-methyl ester (8): In a 250 mL round-bottom flask equipped with a magnetic stir bar and reflux condenser, **1** (5 g, 26 mmol) was dissolved in 50 mL of DMF. To this was added K_2CO_3 (18.3 g, 130 mmol) and iodomethane (8.2 mL, 130 mmol). The flask was heated to 50ºC under N_2 for 72 hours. The now dark red mixture was filtered, and the volatiles removed under reduced pressure. The residue was redissolved in DCM (50 mL) and washed with water (5x 75 mL), brine (3x 75 mL) and dried with anhydrous Na_2SO_4. The solvent was evaporated under reduced pressure. The resulting red liquid was purified with flash chromatography (SiO_2 9:1 DCM:MeOH) to afford an amber oil. (2.5 g, 44 %). **^{1}H NMR** (400 MHz, $cdcl_3$) δ 8.61 (dd, *J* = 4.1, 1.9 Hz, 1H), 7.73 (dd, *J* = 8.4, 1.9 Hz, 1H), 7.44 (d, *J* = 8.6 Hz, 1H), 7.13 (s, 1H), 7.06 (dd, *J* = 8.3, 4.1 Hz, 1H), 3.92 (s, 3H), 3.62 (s, 3H). **^{13}C NMR** (101 MHz, $cdcl_3$) δ 166.33, 156.83, 149.90, 142.76, 135.77, 131.23, 126.58, 123.30, 122.66, 122.45, 63.18, 52.04.

8-methoxyquinoline-7-carboxyl fluoride (9): In a 50 mL Schlenk flask equipped with a magnetic stir bar, **10** (500 mg, 2.5 mmol) was suspended in 25 mL of dry DCM. The mixture was cooled to 0ºC and cyanuric fluoride (212 µL, 2.5 mmol) was added followed by DIPEA (440 µL, 2.6 mmol). The mixture was stirred at 0ºC for 30 minutes. The mixture was then diluted with DCM (50 mL) and washed with ice water (3 x 50 mL), brine (3x 50 mL) and dried with anhydrous Na_2SO_4. The solvent was evaporated under reduced pressure to afford a white solid (404 mg, 80%).**^{1}H NMR** (500 MHz, $CDCl_3$) δ 8.92 (dd, *J* = 4.2, 1.7 Hz, 1H), 8.10 (dd, *J* = 8.4, 1.7 Hz, 1H), 7.89 (d, *J* = 8.8 Hz, 1H), 7.68 (d, *J* = 8.7 Hz, 1H), 7.46 (dd, *J* = 8.4, 4.1 Hz, 1H),

2.48 (s, 3H). **^{13}C NMR** (126 MHz, $CDCl_3$) δ 168.02, 150.94, 134.91, 131.89, 125.59, 125.58, 125.05, 123.40, 52.47, 19.83. **^{19}F NMR** (470 MHz, $CDCl_3$) δ 34.27.

8-methoxyquinoline-7-carboxylic acid (10): In a 100 mL round-bottom flask equipped with a magnetic stir bar and reflux condenser, **8** (3.3 g, 15.2 mmol) was dissolved in 25 mL of methanol. To this was added NaOH (10.9 g, 272 mmol) that was dissolved in 25 mL of water. The mixture was heated to reflux for 24 hours and then the pH was adjusted to pH=4 with 3M HCl. The volatiles were then evaporated, and the product was extracted from the residue using $CHCl_3$ with a Soxhlet extractor. The $CHCl_3$ was removed under reduced pressure to afford a white powder (2.5 g, 80%). **^{1}H NMR** (700 MHz, $CDCl_3$) δ 9.02 (dd, *J* = 4.2, 1.7 Hz, 1H), 8.25 – 8.20 (m, 2H), 7.68 (d, *J* = 8.6 Hz, 1H), 7.56 (dd, *J* = 8.3, 4.1 Hz, 1H), 4.51 (s, 3H). **^{13}C NMR** (176 MHz, $CDCl_3$) δ 165.30, 165.28, 156.40, 150.28, 141.56, 136.42, 132.77, 127.72, 124.19, 123.46, 120.32, 64.74.

8-hydroxyquinoline-7-propylcarboxamide (11): In a 50 mL round-bottom flask equipped with magnetic stir bar and reflux condenser was suspended **4** (1g, 4.6 mmol) in 5 mL of n-propylamine. The flask was fitted with a reflux condenser and mixture heated to reflux for 72 hr. The volatiles were then evaporated under reduced pressure and the residue redissolved in DCM (50 mL). The organic layer was then washed with 10% NH_4Cl solution (3x 50 mL) and brine (3x 75mL). Organic layer dried with Na_2SO_4, and solvent evaporated under reduced pressure to yield an orange solid (919 mg 91%). **^{1}H NMR(500 MHz, $CDCl_3$)** δ 1.03 (t, *J* = 6.9 Hz, 3H), 1.71 (sextet J= 7.4 *Hz*, 2H), 3.5 (q, *J*= 6.0 *Hz*,2H), 7.36 (d, *J*= 8.8 *Hz*, 1H), 7.51 (dd, *J*= 8.3, 4.3 *Hz*, 1H), 7.85 (s, broad 1H) 8.12 (m, 2H), 8.84 (dd J = *4.18, 1.5 Hz*,1H) **^{13}C NMR** (101 MHz, $CDCl_3$): δ 11.55, 22.88, 113.98, 117.55, 123.22, 127.21, 130.02, 136.09, 138.67, 148.49, 152.27, 165.94

8-methoxyquinoline-7-propylcarboxamide (12): In a 50 mL round-bottom flask equipped with a magnetic stir bar and reflux condenser, **8** (275 mg, 1.3 mmol was dissolved in 5 mL of methanol. To this was added n-propyl amine (5 mL, 61 mmol) and the mixture heated to reflux for 18 hours. The volatiles were evaporated, and the residue redissolved in 50 mL of DCM. The organic layer was washed with water (3x 75 mL) brine (3x 75 mL) and dried with Na_2SO_4. The solvent was evaporated under reduced pressure to afford an amber oil (295 mg, 95 %). **H NMR** (500 MHz, $CDCl_3$) δ 8.86 (dd, *J* = 4.1, 1.7 Hz, 1H), 8.20 (t, *J* = 5.4 Hz, 1H, N-H), 8.13 (d, *J* = 8.7 Hz, 1H), 8.04 (dd, *J* = 8.3, 1.8 Hz, 1H), 7.51 (d, *J* = 8.7 Hz, 1H), 7.35 (dd, *J* = 8.3, 4.2 Hz, 1fH), 4.14 (s, 3H) 3.41 (td, *J* = 7.1, 5.7 Hz, 2H), 1.60 (h, *J* = 7.3 Hz, 2H), 0.94 (t, *J* = 7.4 Hz, 2H). **^{13}C NMR** (126 MHz, $CDCl_3$) δ 163.98, 153.76, 148.95, 141.40, 135.14, 130.34, 126.59, 124.05, 122.43, 121.42, 62.22, 40.51, 21.81, 10.52.

8-benzyloxyquinoline-7-benzyl ester (13): In a 500 mL Schlenk flask equipped with a magnetic stir bar, **1** (6g, 31.7 mmol) and benzyl chloride (9.2 mL, 79.3 mmol) were dissolved in 200 mL of dry DMF. To this was added K_2CO_3 (13.2g, 158.5 mmol) and the mixture heated to 120ºC under N_2 for 16 hours. The volatiles were then evaporated, and the residue dissolved in DCM and passed through a plug of SiO_2 (100% DCM). Evaporation of solvent afforded a viscous amber oil (9.283 g, 79%). **^{1}H NMR** (700 MHz, $CDCl_3$) δ 8.90 – 8.71 (s, 1H), 7.85 (dt, *J* = 8.6, 2.0 Hz, 1H), 7.75 (d, *J* = 8.7 Hz, 1H), 7.54 (dd, *J* = 8.4, 1.8 Hz, 2H), 7.35 – 7.31 (m, 4H), 7.28 (dd, *J* = 8.6, 6.6 Hz, 2H), 7.25 – 7.10 (m, 5H), 5.46 (s, 2H), 5.28 (s, 2H). **^{13}C NMR** (176 MHz, $CDCl_3$) δ 165.25, 154.64, 149.03, 142.15, 136.67, 134.99, 134.83, 134.83, 130.51, 127.51, 127.46, 127.31, 127.28, 127.21, 127.17, 126.84, 126.03, 125.82, 125.73, 123.29, 122.12, 121.66, 76.28, 66.01.

8-benzyloxyquinoline-7-carboxylic acid (14): In a 100 mL round-bottom flask equipped with a magnetic stirbar and reflux condenser, **13** (1.7g, 4.6 mmol) was dissolved in 20 mL of methanol. To this was added NaOH (3.3g, 82.5mmol) that was dissolved in 20 mL of water. The mixture was heated to reflux for 16 hours. DCM (100 mL) was added and aqueous layer extracted with DCM (3x 50 mL). The pH of the aqueous layer was then adjusted to pH=4 with 3M HCl and extracted with DCM (3x 100 mL). Only the second organic layer was then washed with brine (3x 100 mL) and dried with anhydrous Na_2SO_4. The solvent was evaporated under reduced pressure to afford an orange solid (1.1 g, 86%). **^{1}H NMR** (500 MHz, $CDCl_3$) δ 9.07 (dd, *J* = 4.1, 1.7 Hz, 1H), 8.23 (dd, *J* = 8.4, 1.7 Hz, 1H), 8.19 (d, *J* = 8.6 Hz, 1H), 7.67 (d, *J* = 8.7 Hz, 1H), 7.59 (dd, *J* = 8.3, 4.1 Hz, 1H), 7.49 (qd, *J* = 3.8, 1.6 Hz, 2H), 7.44 – 7.35 (m, 3H), 5.89 (s, 2H). **^{13}C NMR** (126 MHz, $CDCl_3$) δ 165.20, 154.95, 150.16, 141.80, 136.45, 134.81, 132.72, 129.47, 129.46, 128.96, 127.82, 124.07, 123.46, 120.94, 79.64.

8-paramethylbenzoxyquinoline-7-paramethylbenzoxy ester (15): In a 200 mL Schlenk flask equipped with a magnetic stir bar, **1** (1g, 5.2 mmol) was dissolved in 75 mL of DMF. To this was added para methoxybenzyl chloride (1.8 mL, 13mmol) and K_2CO_3 (2.2g, 26 mmol) and the mixture was heated to 80ºC under an N_2 atmosphere for 18 hours. The volatiles were then evaporated and the residue purified by flash chromatography (SiO_2, 9:1 DCM:EtOAc). The solvents evaporated to afford a viscous amber oil (1.6 g, 72**%). ^{1}H NMR** (500 MHz, $CDCl_3$) δ 8.97 (dd, *J* = 4.1, 1.8 Hz, 1H), 8.09 (dd, *J* = 8.3, 1.7 Hz, 1H), 7.80 (d, *J* = 8.5 Hz, 1H), 7.50 (d, *J* = 8.6 Hz, 1H), 7.46 – 7.38 (m, 3H), 7.37 – 7.33 (m, 2H), 6.90 – 6.80 (m, 5H), 5.41 (s, 2H), 5.28 (s, 2H), 3.77 (s, 6H). **^{13}C NMR** (126 MHz, $CDCl_3$) δ 166.53, 159.68, 159.46, 155.74, 150.09, 143.47, 136.07, 131.60, 130.35, 130.25, 129.82, 128.59, 128.04, 127.06, 124.65, 122.97, 122.67, 113.98, 113.89, 113.63, 66.97, 55.29, 55.27.

Fmoc-Lys-OMe (16): In a 250 mL round-bottom flask equipped with magnetic stir bar and reflux condenser, Fmoc-Lys-OH (5.1 g, 13.6 mmol) was dissolved in 75 mL of dry methanol and cooled to 0°C before $SOCl_2$ (2 mL, 27.7 mmol) was added dropwise via syringe. The mixture was then heated to reflux for two hours. The reaction mixture was allowed to cool to room temperature and the solvent evaporated under reduced pressure. The resulting residue was redissolved in 10 mL of methanol and added dropwise to cold diethyl ether (100 mL). The resulting white precipitate was collected via vacuum filtration to yield Fmoc-Lys-OMe • HCl. (5.3 g, 91%) **^{1}H NMR (**500 MHz, DMSO**)**: δ = 1.25-1.43 (m, 2 H), 1.46-1.61 (m, 2 H), 1.61-1.73 (m, 2 H), 2.74 (t, *J= 7.2 Hz*, 2 H), 3.63 (s, 3 H), 3.97-4.04 (m, 1 H), 4.23 (m, 1 H), 4.27-4.35 (m, 2 H), 7.34 (t, *J= 7.5* Hz, 2 H), 7.43 (t, *J =7.5 Hz*, 2 H), 7.73 (t, *J =6.5 Hz*, 2 H), 7.82 (d, *J= 7.7 Hz*, 1 H), 7.90 (d, *J =7.8 Hz*, 2 H), 8.11 (s, 3 H). **^{13}C NMR** (DMSO-d6, TMS): δ = 172.84, 156.14, 143.79, 143.76, 140.74, 127.65, 127.07, 125.25, 125.23, 120.14, 65.61, 53.72, 51.89, 46.65, 38.32, 30.04, 26.40, 22.44.

Fmoc-Lys(Rho)-OMe (17): In a 100 mL round-bottom flask equipped with a magnetic stir bar, Rhodamine B (1.0g, 2.1 mmol), PyBOP (1.3g, 2.5 mmol) and DIPEA (800 μL, 4.6 mmol) was dissolved in 50 mL of dry DCM and stirred at room temperature for 10 minutes. Then, Fmoc-Lys-OMe • HCl (1.1 g, 2.5 mmol) was added all at once and the reaction mixture stirred at room temperature overnight. The reaction mixture was diluted with DCM and washed with 1M HCl (3 x 50 mL), saturated $NaHCO_3$ (3 x 50 mL) and brine (3 x 50 mL). The organic layer was then dried with anhydrous Na_2SO_4 and the solvent evaporated under reduced pressure. The resulting residue was purified via flash chromatography (SiO_2 DCM:MeOH 9:1) to yield a purple foam. (1.47g, 87%) ESI MS calculated m/z = 807.4121, found m/z = 807.4111. **^{1}H NMR** ($CDCl_3$) δ= 1.07 (m, 2H), 1.17 (m, 2H), 1.25 (t, 12H), 1.58 (m, 2H), 3.16 (m, 3H), 3.53 (s, broad 8H), 3.71

(s, 3H), 4.19 (m, 2H), 4.31 (m, 1H), 4.37 (m, 1H), 5.54 (s, 3H), 5.69 (d, *J = 8.6 Hz* 1H), 6.78 (m, 2H), 7.03 (m, 1H), 7.29 (m 2H), 7.38 (t, *J = 7.7 Hz* 2H), 7.54 (m, 2H), 7.61 (t, *J = 8.8 Hz*, 2H), 7.75 (d, *J = 7.65 Hz*, 2H), 7.97 (m, 1H). **^{13}C NMR** ($CDCl_3$) δ = 173.04, 168.46, 156.12, 153.64, 153.36, 153.29, 148.80, 144.07, 143.88, 141.29, 132.34, 131.30, 128.93, 128.88, 128.05, 127.68, 127.65, 127.11, 125.24, 123.77, 122.78, 119.92, 108.09, 108.04, 105.80, 105.76, 97.74, 66.92, 64.98, 54.00, 53.47, 52.25, 47.25, 44.38, 44.35, 39.29, 31.27, 30.95, 27.73, 22.53, 12.61.

Fmoc-Lys(Rho)-OH (18): In a 50 mL round-bottom flask equipped with a magnetic stir bar, Fmoc-Lys(Rho)-OMe (503 mg, 0.623 mmol) was dissolved in 7 mL of THF. This was cooled to 0°C at which point aqueous LiOH was added (44.8 mg, 1.87 mmol dissolved in 5 mL of H_2O). The mixture was stirred at 0°C for two hours at which point the reaction was quenched with 1 M HCl (10 mL). The resulting mixture was extracted into EtOAc (5 x 20 mL). the extracts were pooled and washed with brine and dried with Na_2SO_4. The solvent was removed under reduced pressure to afford a purple powder. (347 mg, 70 %). **^{1}H NMR** (500 MHz, DMSO) δ = 0.85 (m, 2H), 0.98 (m, 2H), 1.06 (m,12H), 1.22 (m, 2H), 3.00 (m, 2H), 3.32 (s broad, 8H), 3.76 (m, 1H), 3.16 (m, 3H), 6.37 (m, 4H), 7.04 (m, 1H), 7.27 (m, 2H), 7.38 (m, 3H), 7.51 (m, 2H), 7.69 (t, *J = 7.7 Hz* 2H), 7.79 (m, 1H), 7.84 (m, 3H).

4-(2-Cyanoethyl)-4-cyclohexyliminomethylheptane-1,7-dinitrile (19): In a 250 mL Schlenk flask equipped with an additional funnel and magnetic stir bar, cyclohexyl amine (40 mL, 350 mmol) was dissolved in 15 mL of toluene and cooled to 0ºC. To this was added acetaldehyde (20 mL, 358 mmol) dropwise over 20 minutes. Then K_2CO_3 (3g, 22 mmol) was added and the mixture stirred at 0ºC for an additional 10 minutes before being allowed to warm to room temperature. The organic layer (top) was then transferred via cannula into a 250 mL glass pressure reactor containing acrylonitrile (70 mL, 1055 mmol). The reaction vessel was then

sealed and heated to 170ºC for 4 hours. The black reaction mixture was cooled to -20ºC and 500 mL of ice-cold diethyl ether was added. The resulting yellow solid was collected via vacuum filtration and washed with more cold diethyl ether to afford an off-white solid (60.3g, 61%). **^{1}H NMR** (500 MHz, $CDCl_3$) δ 7.43 (s, 1H), 3.08 (m, 1 H), 2.34 (t, *J*=7.94Hz, 6H), 1.93 (t, *J*=7.94Hz, 6H), 1.78-1.30 (m, 10H). **^{13}C NMR** (125 MHz, $CDCl_3$) δ 160.30, 119.09, 68.36, 45.78, 36.05, 30.77, 25.44, 24.33, 11.88.

4-(2-Cyanoethyl)-4-formylheptane-1,7-dinitrile (20): In a 500 mL round-bottom flask equipped with a magnetic stir bar and reflux condenser was added **19** (20 g, 70.4 mmol) and 200 mL of 0.5M HCl. The mixture was heated to reflux for 30 min, filtered hot and cooled to 0ºC. The resulting yellow crystals were collected via vacuum filtration (12.2 g, 85%). **^{1}H NMR** (500 MHz, DMSO) δ 9.44 (s, 1H), 2.46 – 2.37 (t, *J*=8.09 Hz, 6H), 1.90 – 1.83 (t, *J*= 8.9 Hz, 6H). **^{13}C NMR** (126 MHz, DMSO) δ 204.90, 120.81, 50.86, 26.30, 11.67.

4-(2-Cyanoethyl)-4-hydroxymethylheptane-1,7-dinitrile (21): Compound **20** (12.8 g, 63 mmol) was dissolved in 200 mL of methanol and the mixture cooled to 0ºC. To this was added $NaBH_4$ (3 g, 79 mmol) and the mixture stirred at 0ºC under N_2 for 2.5 hours. The reaction was allowed to warm slowly to room temperature at which point it was quenched with 100 mL of H_2O. The pH was adjusted to pH = 1 with HCl and the methanol removed under reduced pressure. The product was then extracted into DCM (3x 100 mL) and the organic extracts washed with brine (3x 75 mL) and dried with Na_2SO_4. The solvents evaporated under reduced pressure to afford an orange solid (11.6 g, 90%). **^{1}H NMR** (500 MHz, DMSO) δ 4.78 (t, *J* = 5.2 Hz, 1H), 3.13 (d, *J* = 5.2 Hz, 2H), 2.43 – 2.36 (t, *J*=7.94 Hz, 6H), 1.56 – 1.47 (t, *J*=7.94 Hz, 6H). **^{13}C NMR** (126 MHz, DMSO) δ 121.03, 63.09, 39.29, 28.24, 11.01.

4-(*tert*-Butyldimethylsilanyloxymethyl)-4-(2-cyanoethyl)-heptane-1,7-dinitrile (22): In a 250 mL round-bottom flask equipped with a magnetic stir bar and reflux condenser, **21** (7.7 g, 37.3 mmol), tert-butyldimethylsilyl chloride (6.2 g, 41 mmol) and imidazole (5.9 g, 86 mmol) were dissolved in 100 mL of anhydrous DCM. The mixture was heated to reflux under N_2 for 48 hours. The mixture was cooled to room temperature, diluted with 150 mL of DCM and washed with water (3x 150 mL) and brine (3x 150 mL). The organic layer was dried with Na_2SO_4 and evaporated under reduced pressure to afford a white solid (9.8 g, 82%). **^{1}H NMR** (500 MHz, $CDCl_3$) δ 3.37 (s, 2H), 2.38 – 2.30 (t, *J*=8.24Hz, 6H), 1.74 – 1.68 (t, *J*=8.24Hz, 6H), 0.89 (s, 9H), 0.07 (s, 6H). **^{13}C NMR** (126 MHz, $CDCl_3$) δ 118.32, 64.78, 38.81, 28.39, 24.75, 17.02, 10.81, -6.71.

4-(3-Aminopropyl)-4-(*tert*-butyldimethylsilanyloxymethyl)heptane-1,7-diamine (23): In a 2L three-neck flask fitted with nitrogen inlet, reflux condenser and magnetic stir bar, **22** (11.3g, 35.3 mmol) was dissolved in 100 mL of freshly degassed methanol. The mixture was cooled to 0ºC and Raney Ni (12g, 141 mmol) was added. To the suspension was added in small batches a solution of $NaBH_4$ (13.4g, 350 mmol) in 15 mL of 8M NaOH over the course of 1 hour. The mixture was kept at 0ºC for an additional hour and then slowly heated to 40ºC for 72 hours. The mixture was then diluted with 200 mL of water and extracted into diethyl ether (3x 250 mL). The organic extracts were then washed with brine (3x 100 mL) and dried with Na_2SO_4. The solvent was evaporated under reduced pressure to afford a pale-yellow oil (7.3g, 62%). **^{1}H NMR** (500 MHz, Tol) δ 3.19 (s, 2H), 2.49 (t, *J* = 6.7 Hz, 6H), 1.20 (m, 6H), 1.15 – 1.09 (m, 6H), 0.99 (s, 9H), 0.87 (s, 6H). **^{13}C NMR** (126 MHz, Tol) δ 66.81, 43.62, 39.44, 31.49, 27.78, 26.11, 21.42, 18.45, -5.42.

N-[4-[[tert-butyl(dimethyl)silyl]oxymethyl]-7-[(8-phenylmethoxyquinoline-7-carbonyl)amino]-4-[3-[(8-phenylmethoxyquinoline-7-carbonyl)amino]propyl]heptyl]-8-phenylmethoxyquinoline-7-carboxamide (24): In a 100 mL round-bottom flask equipped with a reflux condenser and magnetic stir bar, **14** (4.3g, 15.4 mmol) was dissolved in 50 mL of anhydrous THF. To this was added carbonyl diimidazole (2.8g, 17 mmol) and the mixture heated to reflux for 1 hour. Then **23** (1.6g, 5.0 mmol) was added and the mixture refluxed for an additional 16 hours. The volatiles were then evaporated under reduced pressure and the residue redissolved in DCM, washed with water (3x 100 mL) and brine (3x 100 mL). The organic layer was dried with Na_2SO_4 and evaporated to afford a thick yellow oil. The residue was purified via flash chromatography (SiO_2 1:1 DCM:EtOAc) to afford a yellow foam (2.6g, 47%). **^{1}H NMR** (700 MHz, $CDCl_3$) δ 8.97 – 8.93 (m, 3H), 8.27 (dd, *J* = 8.6, 0.8 Hz, 3H), 8.20 (t, *J* = 5.6 Hz, 3H), 8.14 (dd, *J* = 8.2, 1.7 Hz, 3H), 7.61 (d, *J* = 8.7 Hz, 3H), 7.53 – 7.49 (m, 6H), 7.46 – 7.43 (m, 3H), 7.41 – 7.35 (m, 9H), 5.56 (s, 6H), 3.25 (q, *J* = 6.8 Hz, 6H), 3.12 (s, 2H), 1.19 (m, 6H), 1.07 – 1.02 (m, 6H), 0.83 (s, 9H), -0.00 (s, 6H). **^{13}C NMR** (176 MHz, $CDCl_3$) δ 164.92, 153.85, 149.64, 142.53, 136.63, 136.05, 131.34, 128.83, 128.75, 128.71, 128.69, 127.67, 125.15, 123.23, 122.32, 78.32, 66.03, 53.47, 50.57, 40.59, 39.17, 30.99, 25.81, 25.79, 25.76, 22.86, 18.03, -5.58, -5.60.

N-[4-(hydroxymethyl)-7-[(8-phenylmethoxyquinoline-7-carbonyl)amino]-4-[3-[(8-phenylmethoxyquinoline-7-carbonyl)amino]propyl]heptyl]-8-phenylmethoxyquinoline-7-carboxamide (25): In a 100 mL round-bottom flask fitted with magnetic stir bar and reflux condenser was dissolved **24** (1.2 g, 1.1 mmol) in 40 mL of anhydrous THF. The mixture was cooled to 0ºC and tetra butyl ammonium fluoride (2.1 mL of a 1M solution in THF, 2.1 mmol) was added slowly via syringe. The mixture was then heated to reflux for two hours, the volatiles evaporated and the residue redissolved in 50 mL of DCM. The organic layer was washed with

water (3x 75 mL), brine (3x 75 mL) and dried with anhydrous Na_2SO_4. Evaporation of solvent afforded a crude white solid which was purified via flash chromatography (SiO_2 95:5 DCM:MeOH). Evaporation of the solvent under reduced pressure afforded a white foam (867 mg, 82%). **^{1}H NMR** (700 MHz, $CDCl_3$) δ 8.92 (dt, *J* = 3.8, 1.8 Hz, 3H), 8.23 – 8.16 (m, 6H), 8.09 (dt, *J* = 8.4, 1.7 Hz, 3H), 7.56 (dd, *J* = 8.7, 1.4 Hz, 3H), 7.51 – 7.46 (m, 6H), 7.42 – 7.31 (m, 12H), 5.52 (s, 6H), 3.20 (q, *J* = 6.8 Hz, 6H), 3.13 (s, 2H), 1.17 (q, *J* = 8.0 Hz, 6H), 1.05 – 1.00 (m, 6H). **^{13}C NMR** (176 MHz, $CDCl_3$) δ 165.02, 153.88, 149.63, 142.52, 136.68, 136.04, 131.35, 128.75, 128.72, 128.71, 127.63, 125.09, 123.22, 122.32, 78.33, 65.96, 40.53, 39.14, 30.81, 22.78.

N-[4-formyl-7-[(8-phenylmethoxyquinoline-7-carbonyl)amino]-4-[3-[(8-phenylmethoxyquinoline-7-carbonyl)amino]propyl]heptyl]-8-phenylmethoxyquinoline-7-carboxamide (26): In a 25 mL Schlenk flask equipped with a magnetic stir bar was added DCM (3 mL) and cooled to -78ºC. Then dimethyl sulfoxide (90 μL, 1.2 mmol) and oxalyl chloride (54μL, 0.6 mmol) were added and allowed to react for 15 minutes at -78ºC. Then a pre-cooled solution of **25** (564mg, 0.56 mmol) in 2 mL of DCM was added into the flask and the mixture stirred for an additional 10 minutes. Triethylamine (785 μL, 5.6 mmol) was then added and the mixture allowed to warm to room temperature slowly over 2 hours. The mixture was then diluted with 50 mL of DCM and 50 mL of water. The organic layer was then washed with additional water (3x 30 mL), brine (3x 30 mL) and dried with anhydrous Na_2SO_4. The solvent was removed under reduced pressure to afford a white foam (540 mg, 96%). **^{1}H NMR** (500 MHz, $CDCl_3$) δ 9.19 (s, 1H), 8.95 – 8.88 (m, 3H), 8.21 (d, *J* = 8.7 Hz, 3H), 8.16 (t, *J* = 5.6 Hz, 3H), 8.09 (dd, *J* = 8.3, 1.7 Hz, 3H), 7.56 (d, *J* = 8.7 Hz, 3H), 7.47 – 7.43 (m, 6H), 7.42 – 7.30 (m, 14H), 5.53 (s, 6H), 3.18 (q, *J* = 6.8 Hz, 6H), 1.32 – 1.21 (m, 6H), 1.13 – 1.01 (m, 6H). **^{13}C NMR** (126 MHz,

$CDCl_3$) δ 205.50, 165.00, 154.03, 149.67, 142.53, 136.68, 136.07, 131.45, 128.84, 128.80, 128.77, 127.64, 124.85, 123.24, 122.40, 78.50, 51.02, 40.03, 29.09, 23.25.

5-[(8-phenylmethoxyquinoline-7-carbonyl)amino]-2,2-bis[3-[(8-phenylmethoxyquinoline-7-carbonyl)amino]propyl]pentanoic acid (27): In a 50 mL round-bottom flask equipped with a magnetic stir bar was dissolved **26** (195 mg, 0.2 mmol) in 3 mL of THF and 3 mL of water. To this was added sulfamic acid (25 mg, 0.25 mmol) and the mixture stirred for 10 minutes. Then sodium chlorite (20 mg, 0.22 mmol) was added, and the mixture stirred at room temperature for an additional two hours. The mixture was diluted with 50 mL of DCM and 50 mL of water. The organic layer was washed with additional water (3x 30 mL), brine (3x 30 mL) and dried with anhydrous Na_2SO_4. The solvent was evaporated under reduced pressure and the residue purified via flash chromatography (SiO_2 DCM:MeOH 95:5). The solvent was evaporated to afford a white foam (190 mg, 96%). **^{1}H NMR** (500 MHz, $CDCl_3$) δ 8.92 (dd, *J* = 4.2, 1.8 Hz, 3H), 8.18 (d, *J* = 8.7 Hz, 3H), 8.12 (t, *J* = 5.6 Hz, 3H), 8.07 (dd, *J* = 8.3, 1.8 Hz, 3H), 7.53 (d, *J* = 8.7 Hz, 3H), 7.45 – 7.36 (m, 9H), 7.35 – 7.23 (m, 9H), 5.44 (s, 6H), 3.19 (q, *J* = 6.7 Hz, 6H), 1.44 – 1.29 (m, 6H), 1.24 – 1.12 (m, 6H). **^{13}C NMR** (126 MHz, $CDCl_3$) δ 178.83, 165.00, 153.78, 149.65, 142.33, 136.52, 136.16, 131.32, 128.73, 128.70, 128.66, 127.66, 125.19, 123.21, 122.35, 78.36, 47.83, 40.18, 31.69, 23.74.

Fmoc-Dap(DNS)-OH (28): In a 250 mL round-bottom flask equipped with a magnetic stir bar, Fmoc-diaminopropionic acid (1.50 g, 4.6 mmol) and DIPEA (2.40 mL, 9.20 mmol) were suspended in 50 mL of dry DCM. A solution of dansyl chloride (1.36 g, 5.06 mmol) in 50 mL of dry DCM was added dropwise over 30 min. The reaction was stirred at room temperature under N_2 for an additional 2 hours after dansyl chloride addition. The reaction mixture was then washed with 1M HCl (3x 100 mL) and brine (3x 100 mL). The solvent was evaporated under

reduced pressure and the residue purified via column chromatography (SiO_2 DCM:MeOH 9:1). Fractions containing the desired product were pooled and concentrated in vacuo to obtain a yellow-green solid (1.26 g, 49%) for use in peptide synthesis. **^{1}H NMR** (DMSO-d6, TMS): δ 2.75 (s, 6H), 3.09 (m, 2H), 4.04 (m, 1H), 4.17 (m, 3H), 7.18 (d, *J = 8.00 Hz*, 1H), 7.28 (dd, *J = 8.0, 8.0 Hz*, 2H), 7.37 (dd, *J = 8.0 Hz*, 2H), 7.41 (d,*J = 8.0 Hz*, 1H), 7.51 (dd, *J = 8.0, 8.0 Hz*, 1H), 7.58 (dd, *J = 8.0 Hz*, 1H), 7.65 (d,*J = 7.2 Hz*, 2H), 7.85 (d, *J = 7.2 Hz*, 2H), 8.01 (dd, *J = 6.4 Hz*, 1H), 8.05 (d,*J = 7.2*, 1H), 8.22 (d, *J = 8.8 Hz*, 1H), 8.42 (d, J = 8.8 Hz, 1H). **^{13}C NMR** (DMSO-d6, TMS): δ 172.67, 156.13, 151.73, 144.28, 141.15, 136.24, 129.88, 129.53, 128.66, 128.32, 128.09, 127.57, 125.76, 124.01, 120.55, 119.54, 115.53, 66.15, 55.38, 47.05, 45.47, 44.65.

Peptide Synthesis

Peptides were synthesized manually using standard Fmoc- solid phase peptide synthesis techniques in a fritted glass tube. Phenoxy or ChemMatrix Rink amide linker resin was swollen in DMF for 30 min before the initial Fmoc deprotection was accomplished with 20% (v/v) piperidine in DMF (2 x 10min). Initial resin loading was accomplished with 3 equivalents relative to resin loading of the symmetric anhydride of the C-terminal amino acid. All subsequent couplings were accomplished with 3 equivalents relative to resin loading of amino acid, ethyl (hydroxyamino)cyanoacetate and DIC. Acylation was monitored with the Kaiser test.[90] Each Fmoc deprotection was accomplished with 20% v/v piperidine in DMF (2 x 10min). In the case of [Lis]SS-20 (**P-8**), the first residue installed was Fmoc-Dap(ivDde)-OH. Removal of the ivDDE protecting group was done with 2% v/v hydrazine hydrate in DMF (6 x 10 min). For peptides **P-2**, **P-3**, **P-5** and **P-6** a Fmoc-Lys(Mmt) residue was installed as the Lys residue. On-resin removal of the Mmt protecting group was accomplished by treating the resin with

1:2:97 TFA:TIPS:DCM (6x 10 min). Removal of the peptide from the resin was accomplished with treatment of 2% v/v water and 2% v/v TIPS in TFA solution for 3 hours. The resin was then washed with neat TFA (3 x 2.5 mL) and DCM (3 x 2.5 mL). The collected supernatant was then evaporated under a stream of nitrogen to a volume of ~ 1 mL before being precipitated in cold diethyl ether. The precipitate was then centrifuged, and the pellet washed with fresh diethyl ether five times. The pellet was then dissolved in a minimal amount of water and lyophilized.

Sample Method for Symmetric Anhydride

3 equivalents relative to desired resin loading of Fmoc-amino acid was dissolved in 5 mL of DCM and cooled to 0°C. 1.5 equivalents relative to desired resin loading of DCC was then added all at once. A white precipitate was observed to form almost immediately. The mixture was stirred at 0°C for 30 min. The mixture was then filtered, and the filtrate evaporated under reduced pressure. The residue was then dissolved in a minimal amount of DMF and added directly to the resin without further purification.

P-1: ESI MS calculated m/z = 787.3714, found m/z = 787.3701

P-2: Directly after on-resin deprotection of the lysine residue, the resin was treated with a solution of **3** in DMF (3 eq relative to resin substitution) and DIPEA (2 eq relative to resin substitution) for 1 hour. Coupling was monitored with the Kaiser test and incomplete couplings were repeated. ESI MS calculated m/z = 938.4221, found m/z = 937.4143

P-3: The resin was treated in the same procedure as **P-2** with compound **9.** ESI MS calculated m/z = 952.4378, found m/z = 951.4306

P-4: ESI MS calculated m/z = 1263.7750, found m/z = 422.2657 (z = 3)

P-5: Resin treated in the same was as **P-2.** ESI MS calculated m/z = 1434.8071, found m/z = 1433.7997

P-6: Resin treated in the same was as **P-3**. ESI MS calculated m/z = 1448.8227, found m/z = 1447.8137

P-7: ESI MS calculated m/z = 1020.5823, found m/z = 1020.5817

P-8: Directly after on-resin deprotection of the Dap residue, the resin bound peptide was treated with a solution of Lissamine Rhodamine B sulfonyl chloride (6 equivalents relative to resin loading) in DMF for 16 hours. Coupling was monitored with the kaiser test and incomplete couplings were repeated. ESI MS calculated m/z = 1094.4592, found m/z= 1094.4561

P-10: ESI MS calculated m/z = 767.3901, found m/z = 768.3965

HPLC

Reverse-Phase High performance liquid chromatography (HPLC) was conducted using a Waters HPLC system equipped with a diode array UV-Vis detector and Waters XBridge Shield RP18 5 mm column with 4.6 x 250 mm dimensions. Separations were performed using an aqueous mobile phase (MP) (A) of HPLC-grade water with 0.1% trifluoroacetic acid (TFA) and an organic MP (B) of HPLC-grade acetonitrile with 0.1% TFA. A linear gradient of 0% to 60% B over 50 minutes at a flow rate of 1 ml/min was used and elution was monitored at wavelengths between 277 and 563 nm.

Job's Plots

1.0 mM Solutions of **P-2** and **11** were prepared in aqueous 12.5 mM Mops buffer, pH=7.4. **11** was prepared in a 50% DMSO/H_2O (v/v) to ensure solubility. 10 mM $Fe(NO_3)_3$ was prepared in 0.1M HNO_3 to ensure no premature precipitation of $Fe(OH)_3$ would occur. Example test solution is as follows, 200µL of either **P-2** or **11** was combined with 80µL Fe^{3+} solution and 1220µL of the appropriate buffer to achieve a final volume of 1.5 mL. The amounts of the ligand, metal and buffer solutions were varied to measure multiple mol fractions of each analyte while maintaining a constant concentration of total analytes. Each resulting solution was quickly measured to avoid any precipitation of $Fe(OH)_3$ and the A_{595} values were plotted against the mol fraction of ligand. The intersection of the two trendlines indicates a stoichiometric mixture of ligand to metal.

Selectivity Studies

A 1.0 mM solution of **P-2** was prepared in 25 mM Mops buffer pH=7.4. Various metal salt solutions were prepared as 1.0 mM in 0.1M HNO_3 to avoid premature precipitation of hydroxides. **P-2** and metal were mixed in a 3:1 stoichiometry and diluted with 25mM buffer to a final concentration of 18.75µM M(**P-2**)$_x$. Example solution is as follows, 75µL of **P-2** solution was combined with 25µL of the appropriate metal and diluted with 3900µL of buffer. The resulting complexes were incubated at room temperature for 20 minutes before being excited with 330 nm light and fluorescence emission spectra were recorded. This was compared against the metal complex with the addition of 1/3 equivalent of either Fe^{3+} or Fe^{2+}. Example solution is as follows, 75µL of **P-2** solution was combined with 25µL of the appropriate metal and allowed to incubate at room temperature for 20 minutes. Then 25µL of either Fe^{3+} or Fe^{2+} and 3875µL of buffer were added before the sample was incubated at room temperature for 20 minutes. The fluorescence emission spectra were then recorded and normalized against the no-iron sample and the relative intensities plotted adjacent to one another.

2-Deoxyribose Degradation Assay

The assay was conducted as follows, a 1 mL sample containing a final concentration of 2mM ascorbate, 15mM 2-deoxyribose, 400μM Fe^{3+}, 400μM H_2O_2 and 400μM ETDA (1.2 mM **P-2** and **11** were used to ensure stoichiometric binding) was prepared in aqueous 25 mM Mops buffer pH=7.4 containing 50% DMSO (v/v). The sample was incubated at 37ºC for 1 hour at which point the reaction was quenched with 1.0 mL of a 1% thiobarbituric acid solution which was prepared in 50mM NaOH. To this was added 1 mL of glacial acetic acid and the mixture heated to 100ºC for 20 minutes. The UV-Vis spectra of the resulting mixtures were then recorded.

Fluorescence Quenching

Multiple 5mL samples containing 12 μM **P-2** and varying Fe^{3+} concentrations were prepared in 25 mM Mops buffer pH=7.4. Each solution was incubated at room temperature for 20 minutes and the fluorescence emission spectra were recorded. Fe^{3+} stock solutions were prepared in 0.1 M HNO_3 to avoid precipitation of $Fe(OH)_3$. A sample solution is as follows, 120μL of a 0.5mM **P-2** solution in 25mM Mops buffer pH=7.4 was combined with 10μL of a 20mM $Fe(NO_3)_3$ and diluted with 4870μL of buffer. The solution was allowed to incubate for 20 minutes, and the fluorescence emission spectrum recorded.

Formation Constant

A standard curve was generated using 50 mM **11** with [Fe^{3+}] ranging from 50-300 μM. All solutions were prepared in 25 mM Mops buffer pH=7.4 containing 50% DMSO (v/v). This was then used to calculate the equilibrium concentration of Fe(**11**)$_3$ from the Job's plots and the resulting equilibrium concentrations of Fe^{3+} and **11** were also calculated. The formation constant

was calculated using ML_3 stoichiometry and for each point on the Job's plot. The values were then averaged.

References

(1) Acevedo, K.; Masaldan, S.; Opazo, C. M.; Bush, A. I. Redox active metals in neurodegenerative diseases. *JBIC Journal of Biological Inorganic Chemistry* **2019**, *24* (8), 1141-1157. DOI: 10.1007/s00775-019-01731-9.

(2) Ba, L. A.; Doering, M.; Burkholz, T.; Jacob, C. Metal trafficking: from maintaining the metal homeostasis to future drug design. *Metallomics* **2009**, *1* (4), 292-311. DOI: 10.1039/b904533c.

(3) Al Alawi, A. M.; Majoni, S. W.; Falhammar, H. Magnesium and Human Health: Perspectives and Research Directions. *Int J Endocrinol* **2018**, *2018*, 9041694. DOI: 10.1155/2018/9041694 From NLM.

(4) Silver, S. BioMetals: a historical and personal perspective. *BioMetals* **2011**, *24* (3), 379-390. DOI: 10.1007/s10534-011-9417-6.

(5) Wallace, D. F. The Regulation of Iron Absorption and Homeostasis. *Clin Biochem Rev* **2016**, *37* (2), 51-62. PubMed.

(6) Valko, M.; Morris, H.; Cronin, M. T. D. Metals, toxicity and oxidative stress. *Curr. Med. Chem.* **2005**, *12* (10), 1161-1208.

(7) Chandrangsu, P.; Rensing, C.; Helmann, J. D. Metal homeostasis and resistance in bacteria. *Nature Reviews Microbiology* **2017**, *15* (6), 338-350. DOI: 10.1038/nrmicro.2017.15.

(8) Palmer, A. E.; Franz, K. J. Introduction to "Cellular Metal Homeostasis and Trafficking". *Chemical Reviews* **2009**, *109* (10), 4533-4535. DOI: 10.1021/cr900293t.

(9) Collins, J. F.; Prohaska, J. R.; Knutson, M. D. Metabolic crossroads of iron and copper. *Nutr Rev* **2010**, *68* (3), 133-147. DOI: 10.1111/j.1753-4887.2010.00271.x From NLM.

(10) Gaur, K.; Vázquez-Salgado, A. M.; Duran-Camacho, G.; Dominguez-Martinez, I.; Benjamín-Rivera, J. A.; Fernández-Vega, L.; Carmona Sarabia, L.; Cruz García, A.; Pérez-Deliz,

F.; Méndez Román, J. A.; et al. Iron and Copper Intracellular Chelation as an Anticancer Drug Strategy. In *Inorganics*, 2018; Vol. 6.

(11) Mao, L.; Huang, C.-H.; Shao, J.; Qin, L.; Xu, D.; Shao, B.; Zhu, B.-Z. An unexpected antioxidant and redox activity for the classic copper-chelating drug penicillamine. *Free Radical Biology and Medicine* **2020**, *147*, 150-158. DOI: https://doi.org/10.1016/j.freeradbiomed.2019.12.013.

(12) Wood, M. J.; Skoien, R.; Powell, L. W. The global burden of iron overload. *Hepatol Int* **2009**, *3* (3), 434-444. DOI: 10.1007/s12072-009-9144-z From NLM.

(13) Butterfield, D. A.; Halliwell, B. Oxidative stress, dysfunctional glucose metabolism and Alzheimer disease. *Nature Reviews Neuroscience* **2019**, *20* (3), 148-160. DOI: 10.1038/s41583-019-0132-6.

(14) Nie, J.; Lin, B.; Zhou, M.; Wu, L.; Zheng, T. Role of ferroptosis in hepatocellular carcinoma. *J Cancer Res Clin Oncol* **2018**, *144* (12), 2329-2337. DOI: 10.1007/s00432-018-2740-3 From NLM.

(15) Kruszewski, M. Labile iron pool: the main determinant of cellular response to oxidative stress. *Mutation Research/Fundamental and Molecular Mechanisms of Mutagenesis* **2003**, *531* (1), 81-92. DOI: https://doi.org/10.1016/j.mrfmmm.2003.08.004.

(16) Outten, F. W.; Munson, G. P. Lability and liability of endogenous copper pools. *J Bacteriol* **2013**, *195* (20), 4553-4555. DOI: 10.1128/jb.00891-13 From NLM.

(17) Hirayama, T.; Tsuboi, H.; Niwa, M.; Miki, A.; Kadota, S.; Ikeshita, Y.; Okuda, K.; Nagasawa, H. A universal fluorogenic switch for Fe(ii) ion based on N-oxide chemistry permits the visualization of intracellular redox equilibrium shift towards labile iron in hypoxic tumor cells. *Chem. Sci.* **2017**, *8* (7), 4858-4866, 10.1039/C6SC05457A. DOI: 10.1039/C6SC05457A.

(18) Abbate, V.; Reelfs, O.; Kong, X.; Pourzand, C.; Hider, R. C. Dual selective iron chelating probes with a potential to monitor mitochondrial labile iron pools. *Chem Commun (Camb)* **2016**, *52* (4), 784-787. DOI: 10.1039/c5cc06170a.

(19) Hider, R. C.; Kong, X. L. Glutathione: a key component of the cytoplasmic labile iron pool. *Biometals* **2011**, *24* (6), 1179-1187, Article. DOI: 10.1007/s10534-011-9476-8.

(20) Cabantchik, Z. I.; Glickstein, H.; Milgram, P.; Breuer, W. A Fluorescence Assay for Assessing Chelation of Intracellular Iron in a Membrane Model System and in Mammalian Cells. *Analytical Biochemistry* **1996**, *233* (2), 221-227. DOI: https://doi.org/10.1006/abio.1996.0032.

(21) Levi, S.; Rovida, E. The role of iron in mitochondrial function. *Biochimica et Biophysica Acta (BBA) - General Subjects* **2009**, *1790* (7), 629-636. DOI: https://doi.org/10.1016/j.bbagen.2008.09.008.

(22) Dixon, Scott J.; Lemberg, Kathryn M.; Lamprecht, Michael R.; Skouta, R.; Zaitsev, Eleina M.; Gleason, Caroline E.; Patel, Darpan N.; Bauer, Andras J.; Cantley, Alexandra M.; Yang, Wan S.; et al. Ferroptosis: An Iron-Dependent Form of Nonapoptotic Cell Death. *Cell* **2012**, *149* (5), 1060-1072. DOI: https://doi.org/10.1016/j.cell.2012.03.042.

(23) Abbate, V.; Reelfs, O.; Hider, Robert C.; Pourzand, C. Design of novel fluorescent mitochondria-targeted peptides with iron-selective sensing activity. *Biochemical Journal* **2015**, *469* (3), 357-366. DOI: 10.1042/BJ20150149 (acccessed 3/23/2020).

(24) Stockwell, B. R.; Friedmann Angeli, J. P.; Bayir, H.; Bush, A. I.; Conrad, M.; Dixon, S. J.; Fulda, S.; Gascón, S.; Hatzios, S. K.; Kagan, V. E.; et al. Ferroptosis: A Regulated Cell Death Nexus Linking Metabolism, Redox Biology, and Disease. *Cell* **2017**, *171* (2), 273-285. DOI: https://doi.org/10.1016/j.cell.2017.09.021.

(25) Aron, A. T.; Reeves, A. G.; Chang, C. J. Activity-based sensing fluorescent probes for iron in biological systems. *Current opinion in chemical biology* **2018**, *43*, 113-118. DOI: 10.1016/j.cbpa.2017.12.010 PubMed.

(26) Hirayama, T. Development of Chemical Tools for Imaging of Fe(II) Ions in Living Cells: A Review. *ACTA HISTOCHEMICA ET CYTOCHEMICA* **2018**, *51* (5), 137-143. DOI: 10.1267/ahc.18015.

(27) Ma, Y.; Abbate, V.; Hider, R. C. Iron-sensitive fluorescent probes: monitoring intracellular iron pools. *Metallomics* **2015**, *7* (2), 212-222. DOI: 10.1039/c4mt00214h.

(28) Domaille, D. W.; Que, E. L.; Chang, C. J. Synthetic fluorescent sensors for studying the cell biology of metals. *Nature Chemical Biology* **2008**, *4* (3), 168-175. DOI: 10.1038/nchembio.69.

(29) Aron, A. T.; Loehr, M. O.; Bogena, J.; Chang, C. J. An Endoperoxide Reactivity-Based FRET Probe for Ratiometric Fluorescence Imaging of Labile Iron Pools in Living Cells. *Journal of the American Chemical Society* **2016**, *138* (43), 14338-14346. DOI: 10.1021/jacs.6b08016.

(30) Au-Yeung, H. Y.; Chan, J.; Chantarojsiri, T.; Chang, C. J. Molecular Imaging of Labile Iron(II) Pools in Living Cells with a Turn-On Fluorescent Probe. *Journal of the American Chemical Society* **2013**, *135* (40), 15165-15173, Article. DOI: 10.1021/ja4072964.

(31) Wu, L.; Ding, Q.; Wang, X.; Li, P.; Fan, N.; Zhou, Y.; Tong, L.; Zhang, W.; Zhang, W.; Tang, B. Visualization of Dynamic Changes in Labile Iron(II) Pools in Endoplasmic Reticulum Stress-Mediated Drug-Induced Liver Injury. *Analytical Chemistry* **2020**, *92* (1), 1245-1251. DOI: 10.1021/acs.analchem.9b04411.

(32) Zhang, X.; Chen, Y.; Cai, X.; Liu, C.; Jia, P.; Li, Z.; Zhu, H.; Yu, Y.; Wang, K.; Li, X.; et al. A highly sensitive rapid-response fluorescent probe for specifically tracking endogenous

labile Fe2+ in living cells and zebrafish. *Dyes and Pigments* **2020**, *174*, 108065. DOI: https://doi.org/10.1016/j.dyepig.2019.108065.

(33) Kan, C.; Song, F.; Shao, X.; Wu, L.; Zhang, X.; Zhang, Y.; Zhu, J. Imaging of living organisms and determination of real water samples using a rhodamine-based Fe(III)-induced fluorescent probe. *Microchemical Journal* **2020**, *154*, 104587. DOI: https://doi.org/10.1016/j.microc.2019.104587.

(34) Kan, C.; Song, F.; Shao, X.; Wu, L.; Zhu, J. Fe(III) induced fluorescent probe based on triamine and rhodamine derivatives and its applications in biological imaging. *Journal of Photochemistry and Photobiology A: Chemistry* **2020**, *390*, 112306. DOI: https://doi.org/10.1016/j.jphotochem.2019.112306.

(35) Yan, L.; Xie, Y.; Li, J. A Colorimetric and Fluorescent Probe Based on Rhodamine B for Detection of Fe3+ and Cu2+ Ions. *J. Fluoresc.* **2019**, *29* (5), 1221-1226. DOI: 10.1007/s10895-019-02438-5.

(36) Burdette, S. C. Key Considerations for Sensing FeII and FeIII in Aqueous Media. *Eur. J. Inorg. Chem.* **2015**, *2015* (35), 5728-5729. DOI: 10.1002/ejic.201500566.

(37) Hirayama, T.; Nagasawa, H. Chemical tools for detecting Fe ions. *J Clin Biochem Nutr* **2017**, *60* (1), 39-48. DOI: 10.3164/jcbn.16-70 PubMed.

(38) Serratrice, G.; Boukhalfa, H.; Béguin, C.; Baret, P.; Caris, C.; Pierre, J.-L. O-TRENSOX, a New Tripodal Iron Chelator Based on 8-Hydroxyquinoline Subunits: Thermodynamic and Kinetic Studies. *Inorganic Chemistry* **1997**, *36* (18), 3898-3910. DOI: 10.1021/ic9608096.

(39) Moulinet d'Hardemare, A. d.; Gellon, G.; Philouze, C.; Serratrice, G. Oxinobactin and Sulfoxinobactin, Abiotic Siderophore Analogues to Enterobactin Involving 8-Hydroxyquinoline

Subunits: Thermodynamic and Structural Studies. *Inorganic Chemistry* **2012**, *51* (22), 12142-12151. DOI: 10.1021/ic301081a.

(40) Reelfs, O.; Abbate, V.; Cilibrizzi, A.; Pook, M. A.; Hider, R. C.; Pourzand, C. The role of mitochondrial labile iron in Friedreich's ataxia skin fibroblasts sensitivity to ultraviolet A. *Metallomics* **2019**, *11* (3), 656-665, 10.1039/C8MT00257F. DOI: 10.1039/C8MT00257F.

(41) Reelfs, O.; Abbate, V.; Hider, R. C.; Pourzand, C. A Powerful Mitochondria-Targeted Iron Chelator Affords High Photoprotection against Solar Ultraviolet A Radiation. *Journal of Investigative Dermatology* **2016**, *136* (8), 1692-1700. DOI: 10.1016/j.jid.2016.03.041.

(42) Okano, K.; Okuyama, K.-i.; Fukuyama, T.; Tokuyama, H. Mild Debenzylation of Aryl Benzyl Ether with BCl3 in the Presence of Pentamethylbenzene as a Non-Lewis-Basic Cation Scavenger. *Synlett* **2008**, *2008* (13), 1977-1980. DOI: 10.1055/s-2008-1077980.

(43) Imbert, D.; Baret, P.; Gaude, D.; Gautier-Luneau, I.; Gellon, G.; Thomas, F.; Serratrice, G.; Pierre, J.-L. Hydrophilic and lipophilic iron chelators with the same complexing abilities. *Chemistry--A European Journal* **2002**, *8* (5), 1091-1100.

(44) Baret, P.; Beaujolais, V.; Beguin, C.; Gaude, D.; Pierre, J. L.; Serratrice, G. Towards new iron(III) chelators. Synthesis and complexing ability of a water-soluble tripodal ligand based on 2,2'-dihydroxybiphenyl subunits. *European Journal of Inorganic Chemistry* **1998**, (5), 613-619.

(45) Prachayasittikul, V.; Prachayasittikul, S.; Ruchirawat, S. 8-Hydroxyquinolines: a review of their metal chelating properties and medicinal applications. *Drug Des Devel Ther* **2013**, *7*, 1157-1178. DOI: 10.2147/dddt.s49763 From NLM.

(46) Imbert, D.; Thomas, F.; Baret, P.; Serratrice, G.; Gaude, D.; Pierre, J.-L.; Laulhère, J.-P. Synthesis and iron(III) complexing ability of CacCAM, a new analog of enterobactin possessing

a free carboxylic anchor arm. Comparative studies with TRENCAM. *New Journal of Chemistry* **2000**, *24* (5), 281-288. DOI: 10.1039/b000229l.

(47) Duff, M. R., Jr.; Grubbs, J.; Howell, E. E. Isothermal titration calorimetry for measuring macromolecule-ligand affinity. *J Vis Exp* **2011**, (55). DOI: 10.3791/2796 From NLM.

(48) Turan, B.; Tuncay, E. Impact of Labile Zinc on Heart Function: From Physiology to Pathophysiology. In *International Journal of Molecular Sciences*, 2017; Vol. 18.

(49) Halliwell, B.; Gutteridge, J. M.; Aruoma, O. I. The deoxyribose method: a simple "test-tube" assay for determination of rate constants for reactions of hydroxyl radicals. *Anal Biochem* **1987**, *165* (1), 215-219. DOI: 10.1016/0003-2697(87)90222-3 From NLM.

(50) Gehlen, M. H. The centenary of the Stern-Volmer equation of fluorescence quenching: From the single line plot to the SV quenching map. *Journal of Photochemistry and Photobiology C: Photochemistry Reviews* **2020**, *42*, 100338. DOI: https://doi.org/10.1016/j.jphotochemrev.2019.100338.

(51) Osellame, L. D.; Blacker, T. S.; Duchen, M. R. Cellular and molecular mechanisms of mitochondrial function. *Best Pract Res Clin Endocrinol Metab* **2012**, *26* (6), 711-723. DOI: 10.1016/j.beem.2012.05.003 PubMed.

(52) Giacomello, M.; Pyakurel, A.; Glytsou, C.; Scorrano, L. The cell biology of mitochondrial membrane dynamics. *Nature Reviews Molecular Cell Biology* **2020**, *21* (4), 204-224. DOI: 10.1038/s41580-020-0210-7.

(53) Giorgi, C.; Marchi, S.; Pinton, P. The machineries, regulation and cellular functions of mitochondrial calcium. *Nature Reviews Molecular Cell Biology* **2018**, *19* (11), 713-730. DOI: 10.1038/s41580-018-0052-8.

(54) Porporato, P. E.; Filigheddu, N.; Pedro, J. M. B.-S.; Kroemer, G.; Galluzzi, L. Mitochondrial metabolism and cancer. *Cell Research* **2018**, *28* (3), 265-280. DOI: 10.1038/cr.2017.155.

(55) Tirichen, H.; Yaigoub, H.; Xu, W.; Wu, C.; Li, R.; Li, Y. Mitochondrial Reactive Oxygen Species and Their Contribution in Chronic Kidney Disease Progression Through Oxidative Stress. *Front Physiol* **2021**, *12*, 627837. DOI: 10.3389/fphys.2021.627837 From NLM.

(56) Wang, H.; Fang, B.; Peng, B.; Wang, L.; Xue, Y.; Bai, H.; Lu, S.; Voelcker, N. H.; Li, L.; Fu, L.; et al. Recent Advances in Chemical Biology of Mitochondria Targeting. *Frontiers in Chemistry* **2021**, *9*, Review.

(57) Fernie, A. R.; Carrari, F.; Sweetlove, L. J. Respiratory metabolism: glycolysis, the TCA cycle and mitochondrial electron transport. *Curr Opin Plant Biol* **2004**, *7* (3), 254-261. DOI: 10.1016/j.pbi.2004.03.007 From NLM.

(58) Gorman, G. S.; Chinnery, P. F.; DiMauro, S.; Hirano, M.; Koga, Y.; McFarland, R.; Suomalainen, A.; Thorburn, D. R.; Zeviani, M.; Turnbull, D. M. Mitochondrial diseases. *Nature Reviews Disease Primers* **2016**, *2* (1), 16080. DOI: 10.1038/nrdp.2016.80.

(59) Nissanka, N.; Moraes, C. T. Mitochondrial DNA damage and reactive oxygen species in neurodegenerative disease. *FEBS Lett* **2018**, *592* (5), 728-742. DOI: 10.1002/1873-3468.12956 PubMed.

(60) Battogtokh, G.; Cho, Y.-Y.; Lee, J. Y.; Lee, H. S.; Kang, H. C. Mitochondrial-Targeting Anticancer Agent Conjugates and Nanocarrier Systems for Cancer Treatment. *Frontiers in Pharmacology* **2018**, *9*, Review. DOI: 10.3389/fphar.2018.00922.

(61) Hoye, A. T.; Davoren, J. E.; Wipf, P.; Fink, M. P.; Kagan, V. E. Targeting Mitochondria. *Accounts of Chemical Research* **2008**, *41* (1), 87-97. DOI: 10.1021/ar700135m.

(62) Lyamzaev, K. G.; Tokarchuk, A. V.; Panteleeva, A. A.; Mulkidjanian, A. Y.; Skulachev, V. P.; Chernyak, B. V. Induction of autophagy by depolarization of mitochondria. In *Autophagy*, Vol. 14; 2018; pp 921-924.

(63) Johnson, L. V.; Walsh, M. L.; Chen, L. B. Localization of mitochondria in living cells with rhodamine 123. *Proceedings of the National Academy of Sciences* **1980**, *77* (2), 990-994. DOI: 10.1073/pnas.77.2.990 (acccessed 2023/01/22).

(64) Cerrato, C. P.; Kunnapuu, K.; Langel, U. Cell-penetrating peptides with intracellular organelle targeting. *Expert Opinion on Drug Delivery* **2017**, *14* (2), 245-255. DOI: 10.1080/17425247.2016.1213237.

(65) Szeto, H. H. Cell-permeable, mitochondrial-targeted, peptide antioxidants. *AAPS J* **2006**, *8* (2), E277-E283. DOI: 10.1007/bf02854898 PubMed.

(66) Mitchell, W.; Ng, E. A.; Tamucci, J. D.; Boyd, K. J.; Sathappa, M.; Coscia, A.; Pan, M.; Han, X.; Eddy, N. A.; May, E. R.; et al. The mitochondria-targeted peptide SS-31 binds lipid bilayers and modulates surface electrostatics as a key component of its mechanism of action. *Journal of Biological Chemistry* **2020**, *295* (21), 7452-7469. DOI: https://doi.org/10.1074/jbc.RA119.012094.

(67) Szeto, H. H.; Schiller, P. W. Novel Therapies Targeting Inner Mitochondrial Membrane—From Discovery to Clinical Development. *Pharmaceutical Research* **2011**, *28* (11), 2669-2679. DOI: 10.1007/s11095-011-0476-8.

(68) Carmine, P. C.; Marco, P.; Efstathios, N. V.; Ülo, L. Novel cell-penetrating peptide targeting mitochondria. *The FASEB Journal* **2015**, *29* (11), 4589-4599. DOI: 10.1096/fj.14-269225.

(69) Zhao, K.; Luo, G.; Zhao, G.-M.; Schiller, P. W.; Szeto, H. H. Transcellular Transport of a Highly Polar 3+ Net Charge Opioid Tetrapeptide. *Journal of Pharmacology and Experimental Therapeutics* **2003**, *304* (1), 425. DOI: 10.1124/jpet.102.040147.

(70) Zhao, K.; Zhao, G. M.; Wu, D.; Soong, Y.; Birk, A. V.; Schiller, P. W.; Szeto, H. H. Cell-permeable peptide antioxidants targeted to inner mitochondrial membrane inhibit mitochondrial swelling, oxidative cell death, and reperfusion injury. *J Biol Chem* **2004**, *279* (33), 34682-34690. DOI: 10.1074/jbc.M402999200 From NLM.

(71) Schaefer, P. M.; Kalinina, S.; Rueck, A.; von Arnim, C. A. F.; von Einem, B. NADH Autofluorescence—A Marker on its Way to Boost Bioenergetic Research. *Cytometry Part A* **2019**, *95* (1), 34-46, https://doi.org/10.1002/cyto.a.23597. DOI: https://doi.org/10.1002/cyto.a.23597 (acccessed 2022/05/03).

(72) Hirayama, T.; Kadota, S.; Niwa, M.; Nagasawa, H. A mitochondria-targeted fluorescent probe for selective detection of mitochondrial labile Fe(II). *Metallomics* **2018**, *10* (6), 794-801, Article. DOI: 10.1039/c8mt00049b.

(73) Falabella, M.; Vernon, H. J.; Hanna, M. G.; Claypool, S. M.; Pitceathly, R. D. S. Cardiolipin, Mitochondria, and Neurological Disease. *Trends in Endocrinology & Metabolism* **2021**, *32* (4), 224-237. DOI: 10.1016/j.tem.2021.01.006 (acccessed 2022/04/28).

(74) Shashkova, S.; Leake, Mark C. Single-molecule fluorescence microscopy review: shedding new light on old problems. *Bioscience Reports* **2017**, *37* (4). DOI: 10.1042/bsr20170031 (acccessed 4/26/2022).

(75) *Molinspiration Cheminformatics free web services*. https://www.molinspiration.com (accessed.

(76) Soliman, K.; Grimm, F.; Wurm, C. A.; Egner, A. Predicting the membrane permeability of organic fluorescent probes by the deep neural network based lipophilicity descriptor DeepFl-LogP. *Scientific Reports* **2021**, *11* (1), 6991. DOI: 10.1038/s41598-021-86460-3.

(77) Horton, K. L.; Stewart, K. M.; Fonseca, S. B.; Guo, Q.; Kelley, S. O. Mitochondria-Penetrating Peptides. *Chemistry & Biology* **2008**, *15* (4), 375-382. DOI: https://doi.org/10.1016/j.chembiol.2008.03.015.

(78) Bessalle, R.; Kapitkovsky, A.; Gorea, A.; Shalit, I.; Fridkin, M. All-D-magainin: chirality, antimicrobial activity and proteolytic resistance. *FEBS Lett* **1990**, *274* (1), 151-155. DOI: https://doi.org/10.1016/0014-5793(90)81351-N.

(79) Dennison, S. R.; Harris, F.; Bhatt, T.; Singh, J.; Phoenix, D. A. The effect of C-terminal amidation on the efficacy and selectivity of antimicrobial and anticancer peptides. *Molecular and Cellular Biochemistry* **2009**, *332* (1), 43. DOI: 10.1007/s11010-009-0172-8.

(80) García-Martín, F.; White, P.; Steinauer, R.; Côté, S.; Tulla-Puche, J.; Albericio, F. The synergy of ChemMatrix resin® and pseudoproline building blocks renders Rantes, a complex aggregated chemokine. *Peptide Science* **2006**, *84* (6), 566-575, https://doi.org/10.1002/bip.20564. DOI: https://doi.org/10.1002/bip.20564 (acccessed 2023/02/22).

(81) Fattori, D.; Urbani, A.; Brunetti, M.; Ingenito, R.; Pessi, A.; Prendergast, K.; Narjes, F.; Matassa, V. G.; De Francesco, R.; Steinkühler, C. Probing the Active Site of the Hepatitis C Virus Serine Protease by Fluorescence Resonance Energy Transfer. *Journal of Biological Chemistry* **2000**, *275* (20), 15106-15113. DOI: 10.1074/jbc.275.20.15106.

(82) Kholmukhamedov, A.; Schwartz, J. M.; Lemasters, J. J. Mitotracker probes and mitochondrial membrane potential. *Shock* **2013**, *39* (6).

(83) Rodríguez, V.; Román, J. T.; Fierro, R.; Rivera, Z. J.; García, J. E. Hydrazine hydrate: A new reagent for Fmoc group removal in solid phase peptide synthesis. *Tetrahedron Letters* **2019**, *60* (1), 48-51. DOI: https://doi.org/10.1016/j.tetlet.2018.11.054.

(84) Berezowska, I.; Chung, N. N.; Lemieux, C.; Zelent, B.; Szeto, H. H.; Schiller, P. W. Highly potent fluorescent analogues of the opioid peptide [Dmt1]DALDA. *Peptides* **2003**, *24* (8), 1195-1200. DOI: https://doi.org/10.1016/j.peptides.2003.07.004.

(85) Cerrato, C. P.; Pirisinu, M.; Vlachos, E. N.; Langel, Ü. Novel cell-penetrating peptide targeting mitochondria. *The FASEB Journal* **2015**, *29* (11), 4589-4599. DOI: 10.1096/fj.14-269225 (acccessed 2020/03/23).

(86) Sikora, K.; Jaśkiewicz, M.; Neubauer, D.; Bauer, M.; Bartoszewska, S.; Barańska-Rybak, W.; Kamysz, W. Counter-ion effect on antistaphylococcal activity and cytotoxicity of selected antimicrobial peptides. *Amino Acids* **2018**, *50* (5), 609-619. DOI: 10.1007/s00726-017-2536-9 From NLM.

(87) Cornish, J.; Callon, K. E.; Lin, C. Q.; Xiao, C. L.; Mulvey, T. B.; Cooper, G. J.; Reid, I. R. Trifluoroacetate, a contaminant in purified proteins, inhibits proliferation of osteoblasts and chondrocytes. *Am J Physiol* **1999**, *277* (5), E779-783. DOI: 10.1152/ajpendo.1999.277.5.E779 From NLM.

(88) Naylor, M. R.; Ly, A. M.; Handford, M. J.; Ramos, D. P.; Pye, C. R.; Furukawa, A.; Klein, V. G.; Noland, R. P.; Edmondson, Q.; Turmon, A. C.; et al. Lipophilic Permeability Efficiency Reconciles the Opposing Roles of Lipophilicity in Membrane Permeability and Aqueous Solubility. *Journal of Medicinal Chemistry* **2018**, *61* (24), 11169-11182. DOI: 10.1021/acs.jmedchem.8b01259.

(89) Battogtokh, G.; Choi, Y. S.; Kang, D. S.; Park, S. J.; Shim, M. S.; Huh, K. M.; Cho, Y.-Y.; Lee, J. Y.; Lee, H. S.; Kang, H. C. Mitochondria-targeting drug conjugates for cytotoxic, anti-oxidizing and sensing purposes: current strategies and future perspectives. *Acta Pharmaceutica Sinica B* **2018**, *8* (6), 862-880. DOI: https://doi.org/10.1016/j.apsb.2018.05.006.

(90) Kaiser, E.; Colescott, R. L.; Bossinger, C. D.; Cook, P. I. Color test for detection of free terminal amino groups in the solid-phase synthesis of peptides. *Anal Biochem* **1970**, *34* (2), 595-598. DOI: 10.1016/0003-2697(70)90146-6 From NLM.

Appendix

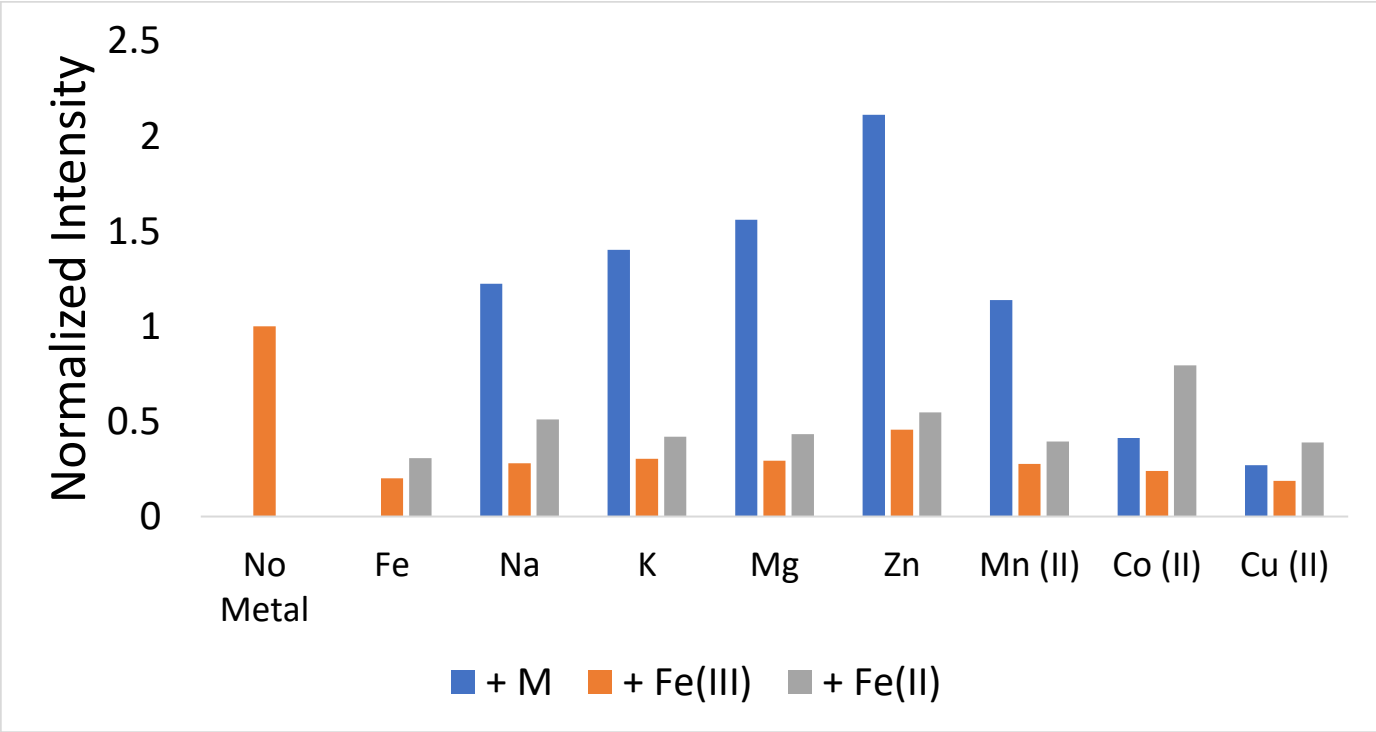

Figure A1: **P-2** Metal ion selectivity with fluorescence intensity normalized to a no-metal peptide emission.

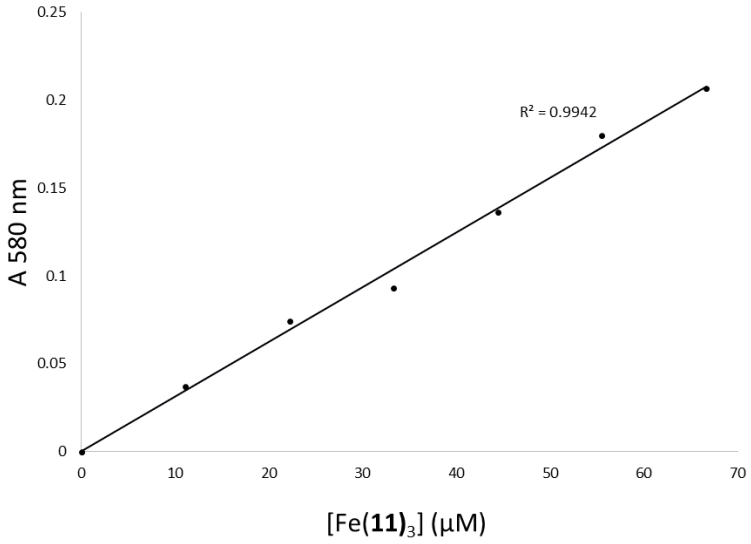

Figure A2: Standard curve used to determine equilibrium concentrations of Fe(**11**)$_3$ complex.

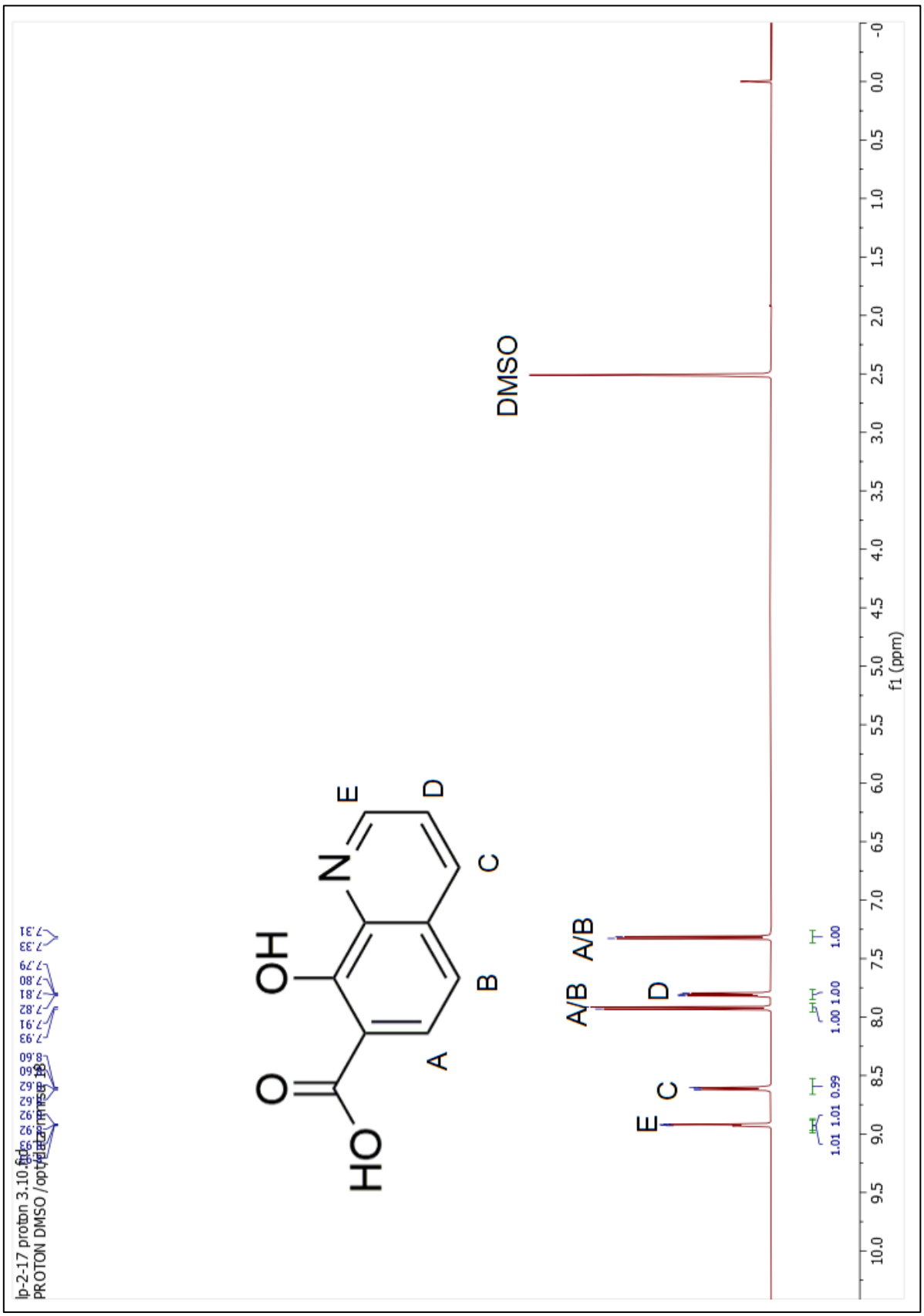

^{1}H NMR Compound **1**

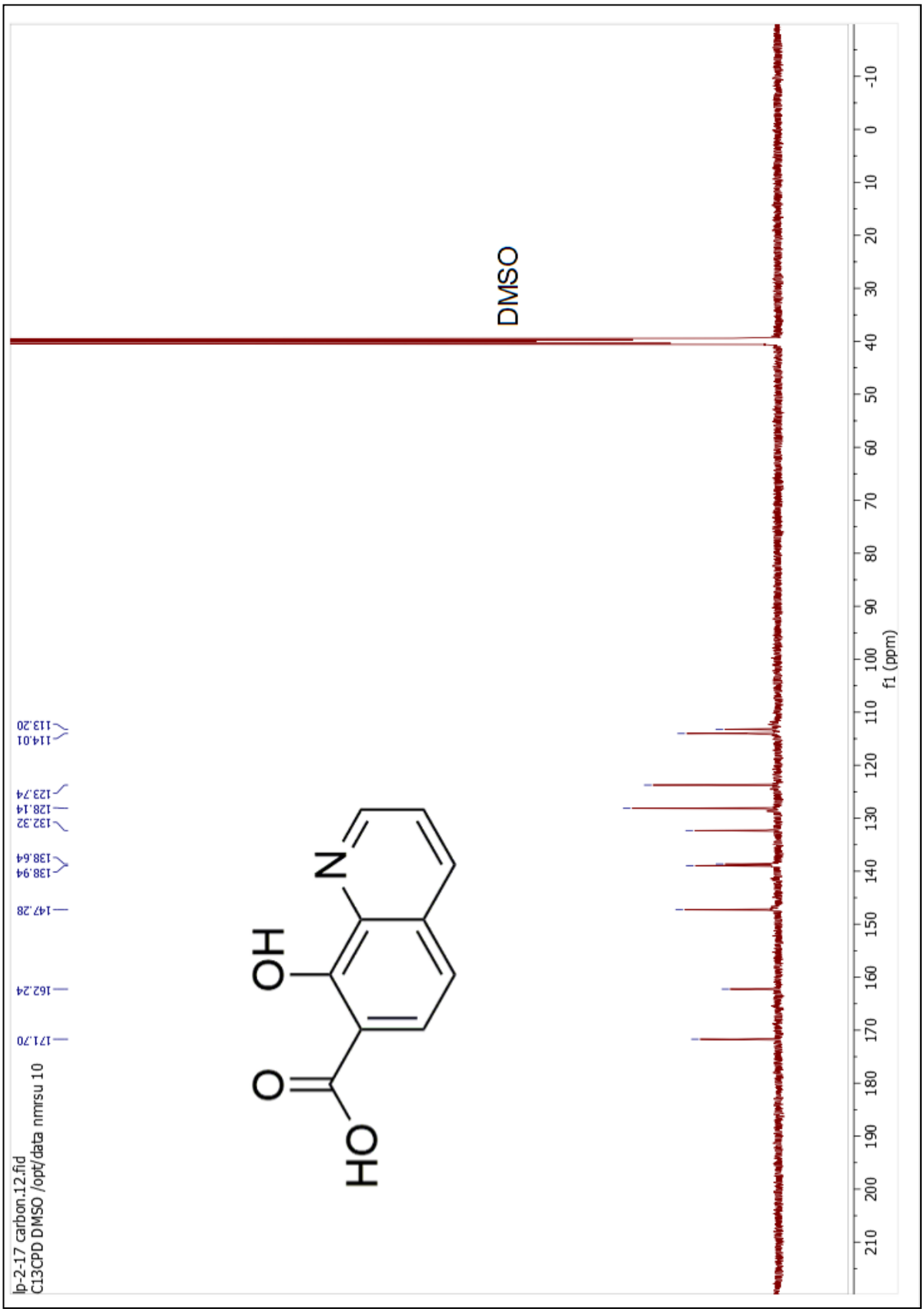

^{13}C NMR Compound **1**

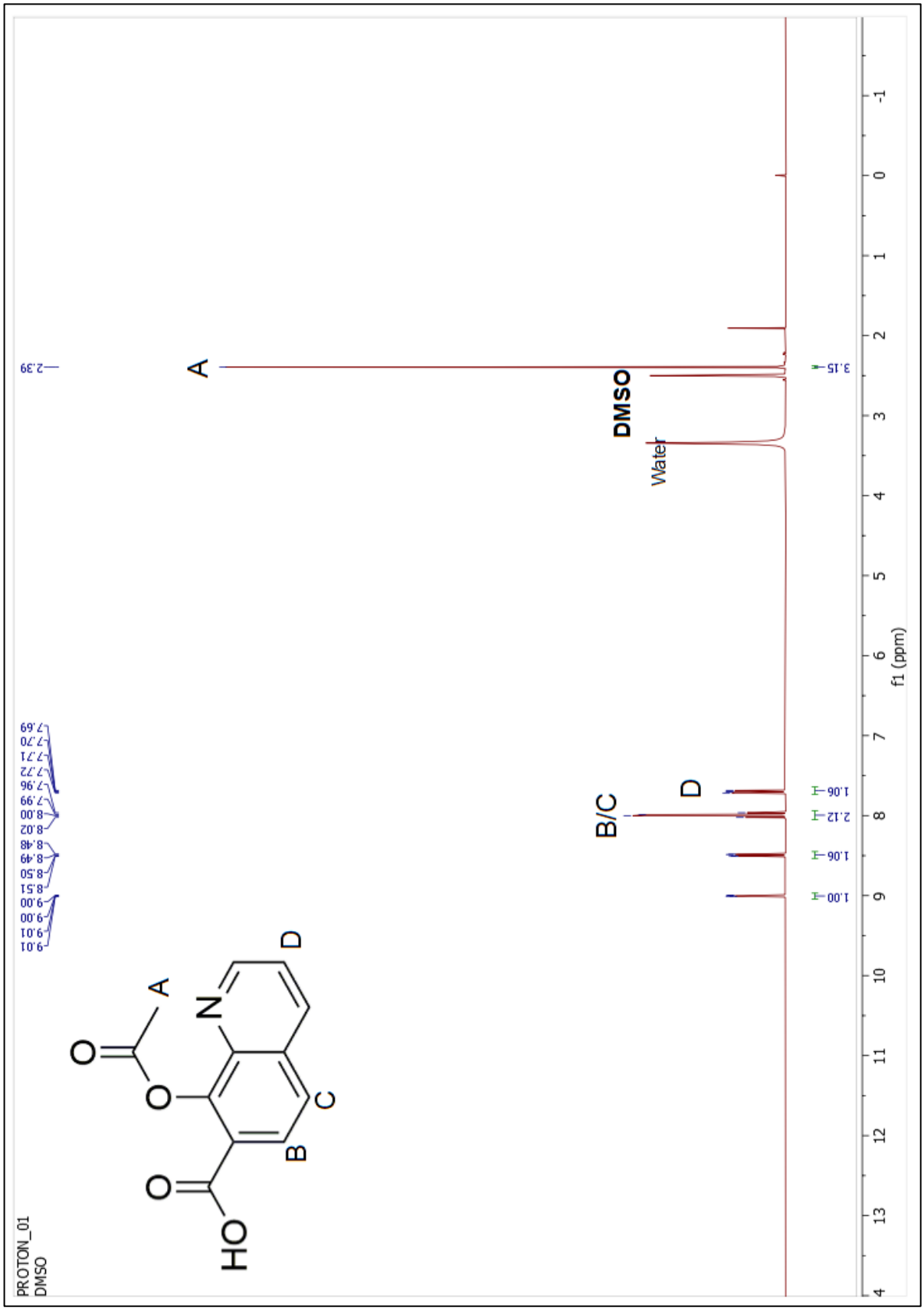

^{1}H NMR Compound **2**
v

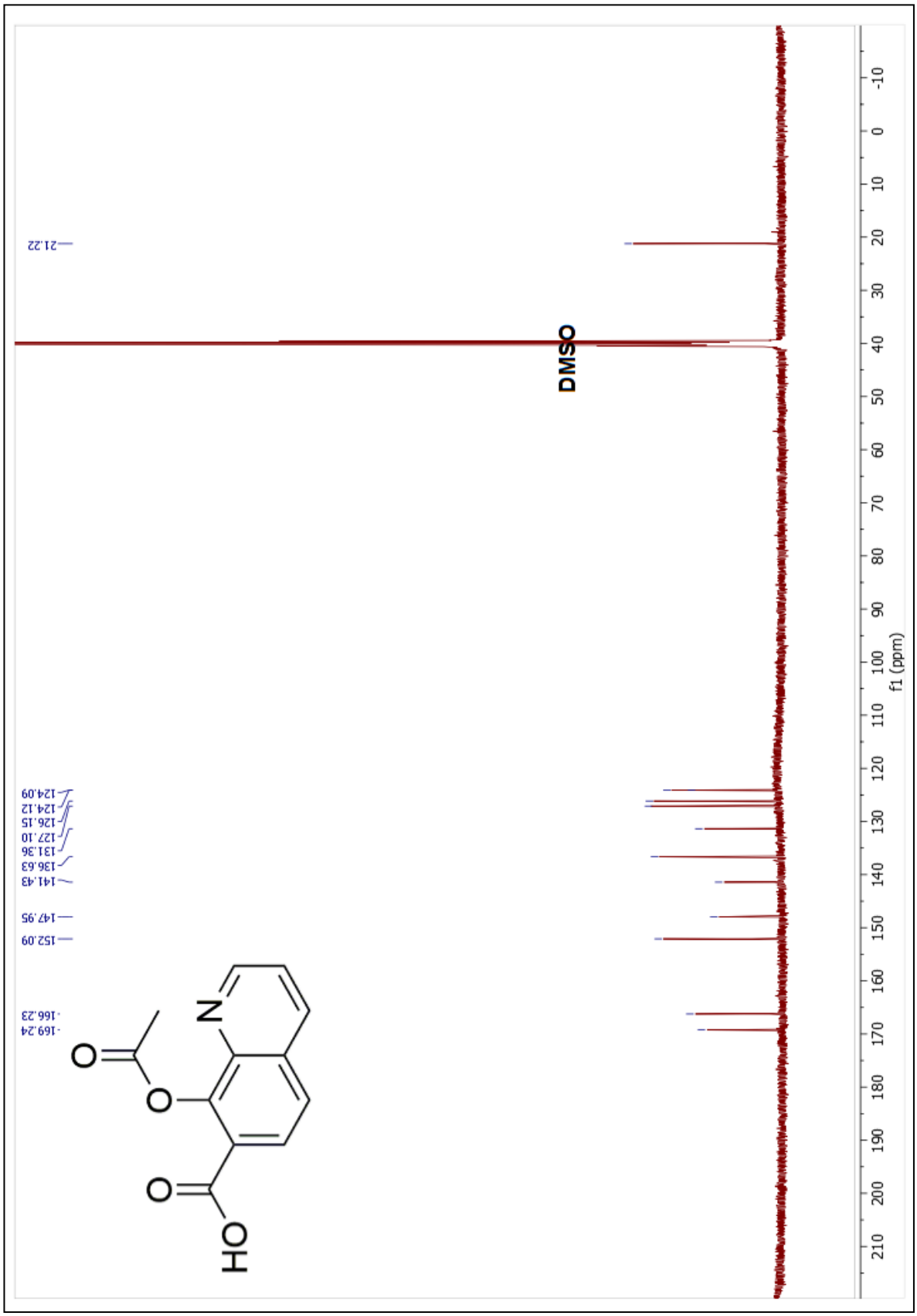

^{13}C NMR Compound **2**

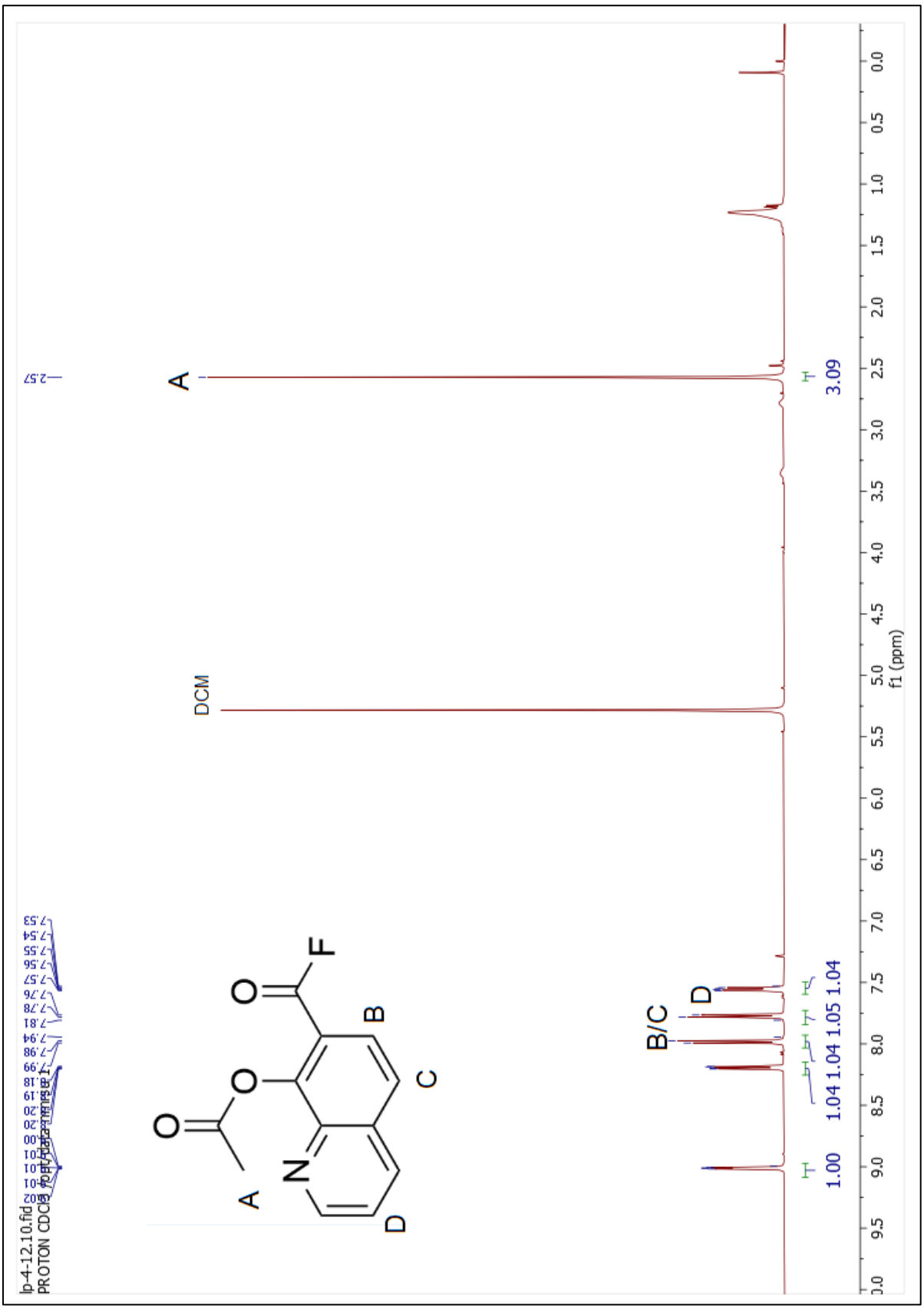

^{1}H NMR Compound **3**

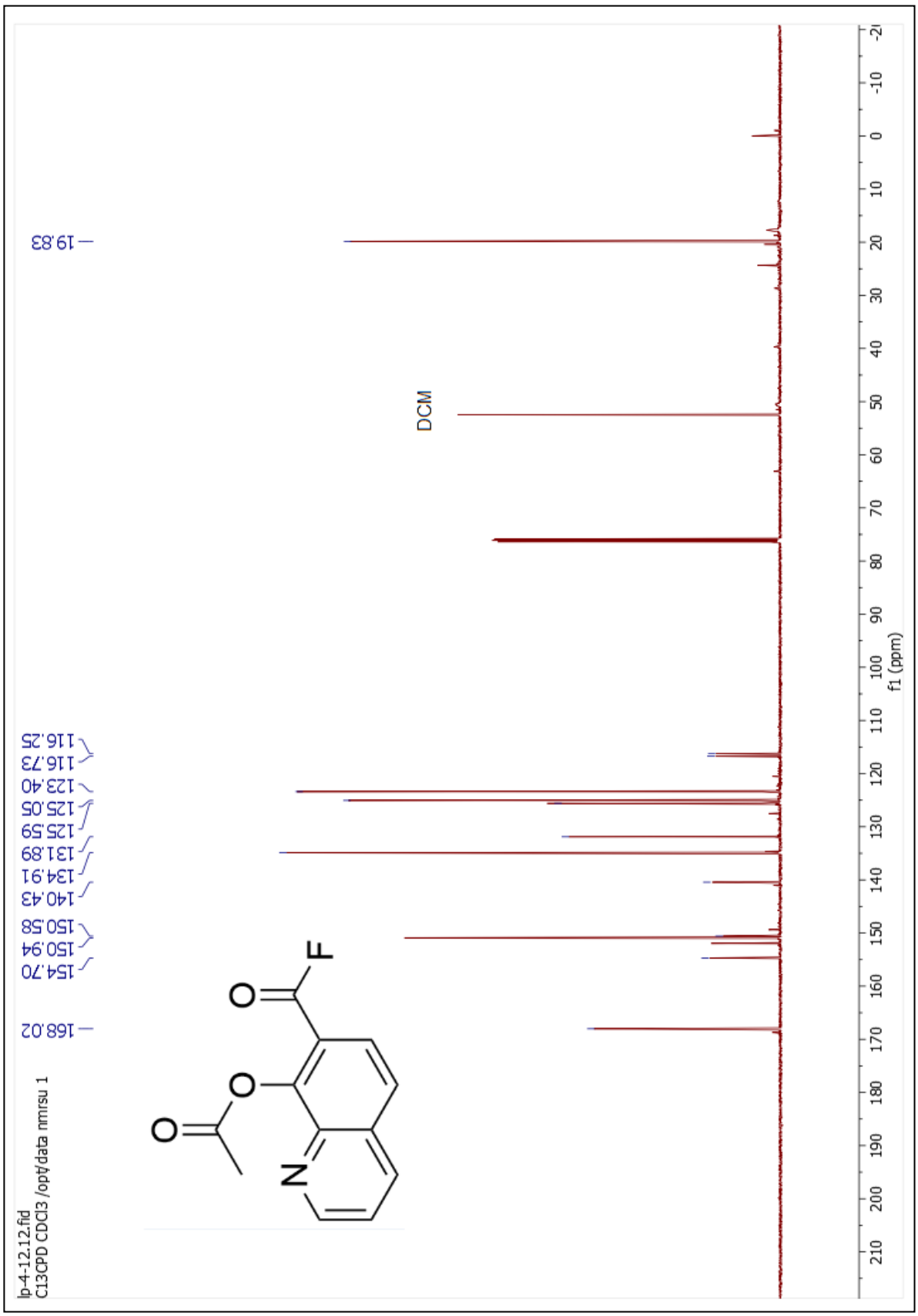

^{13}C NMR Compound **3**

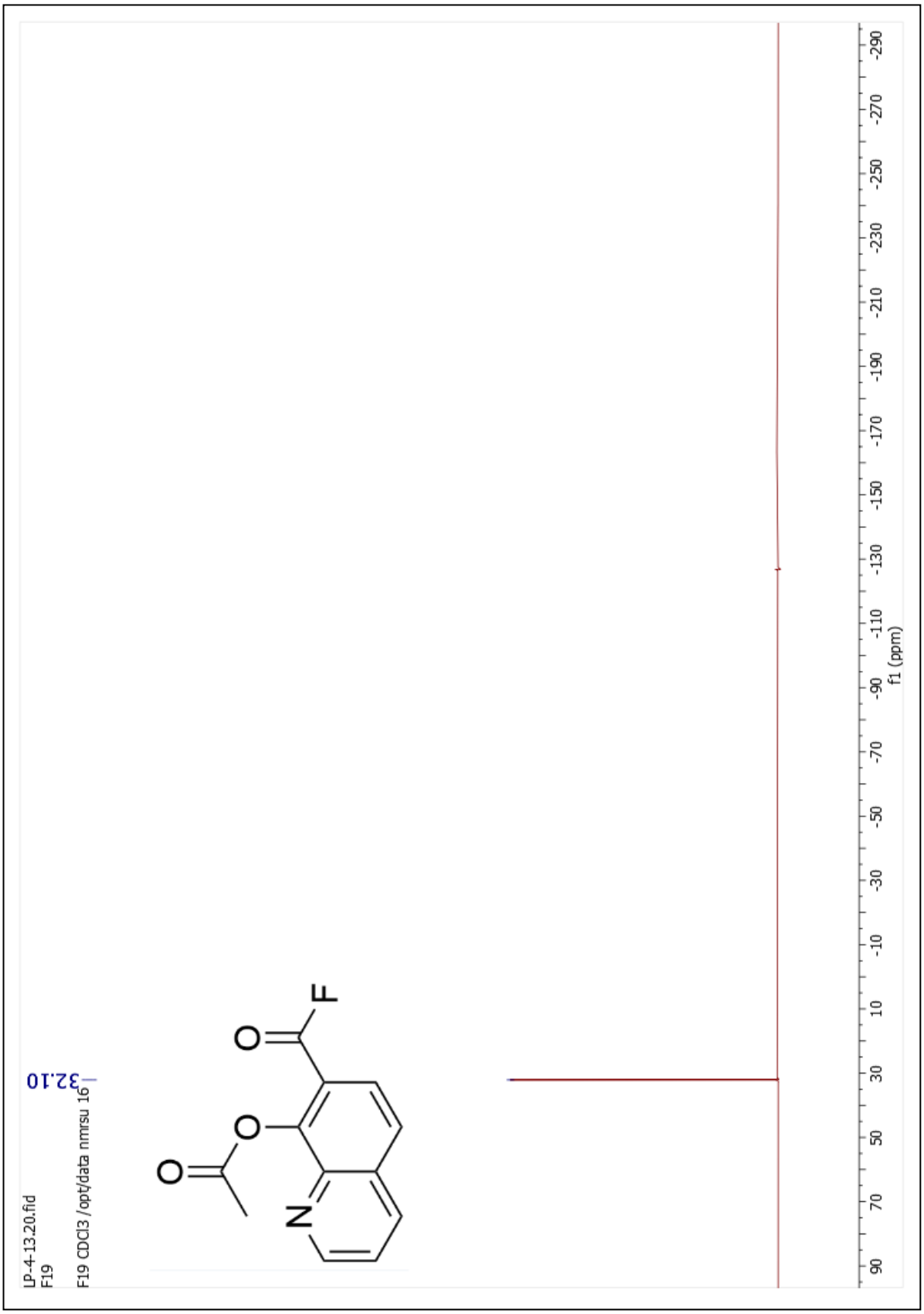

^{19}F NMR Compound **3**

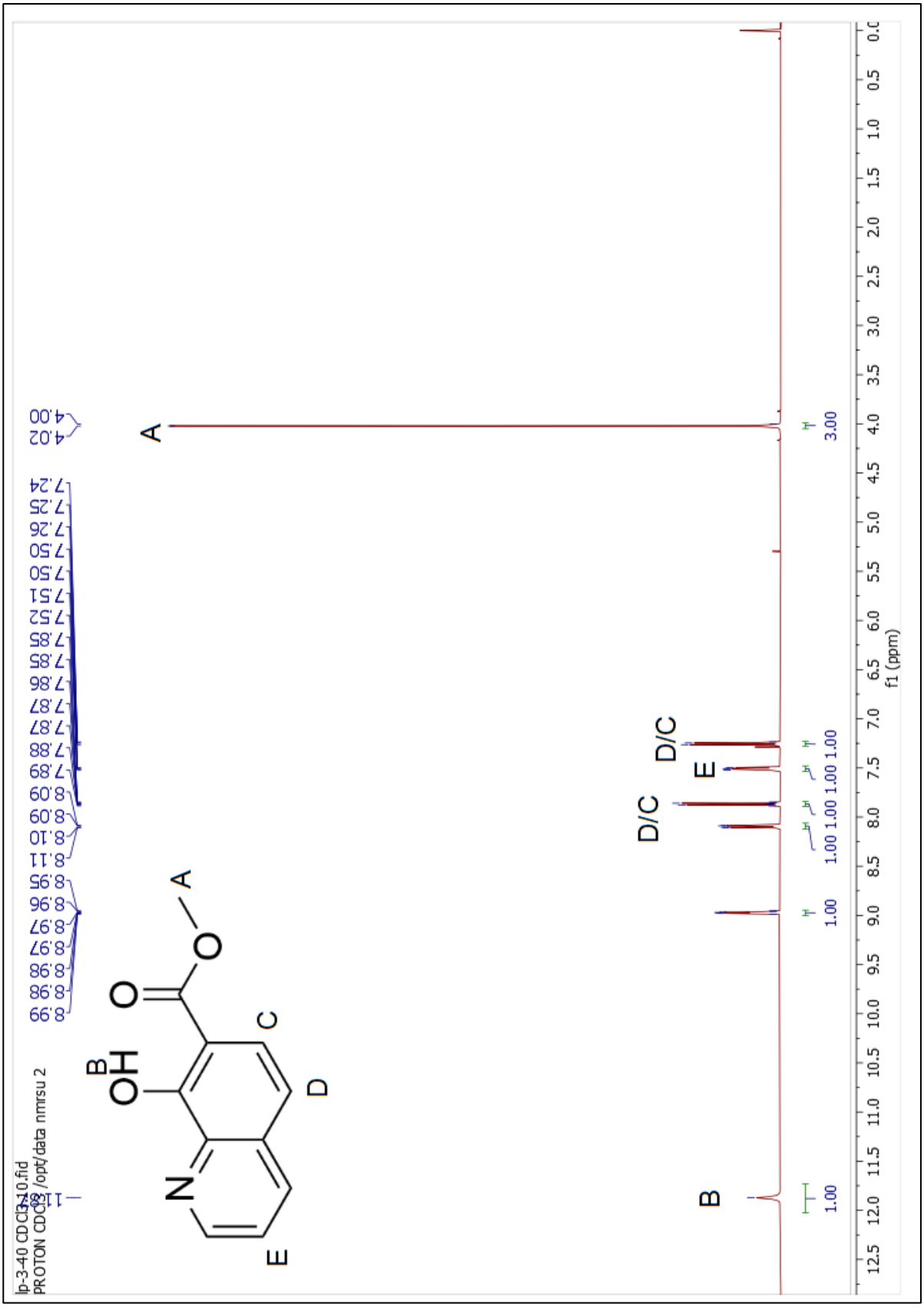

^{1}H NMR Compound **4**

x

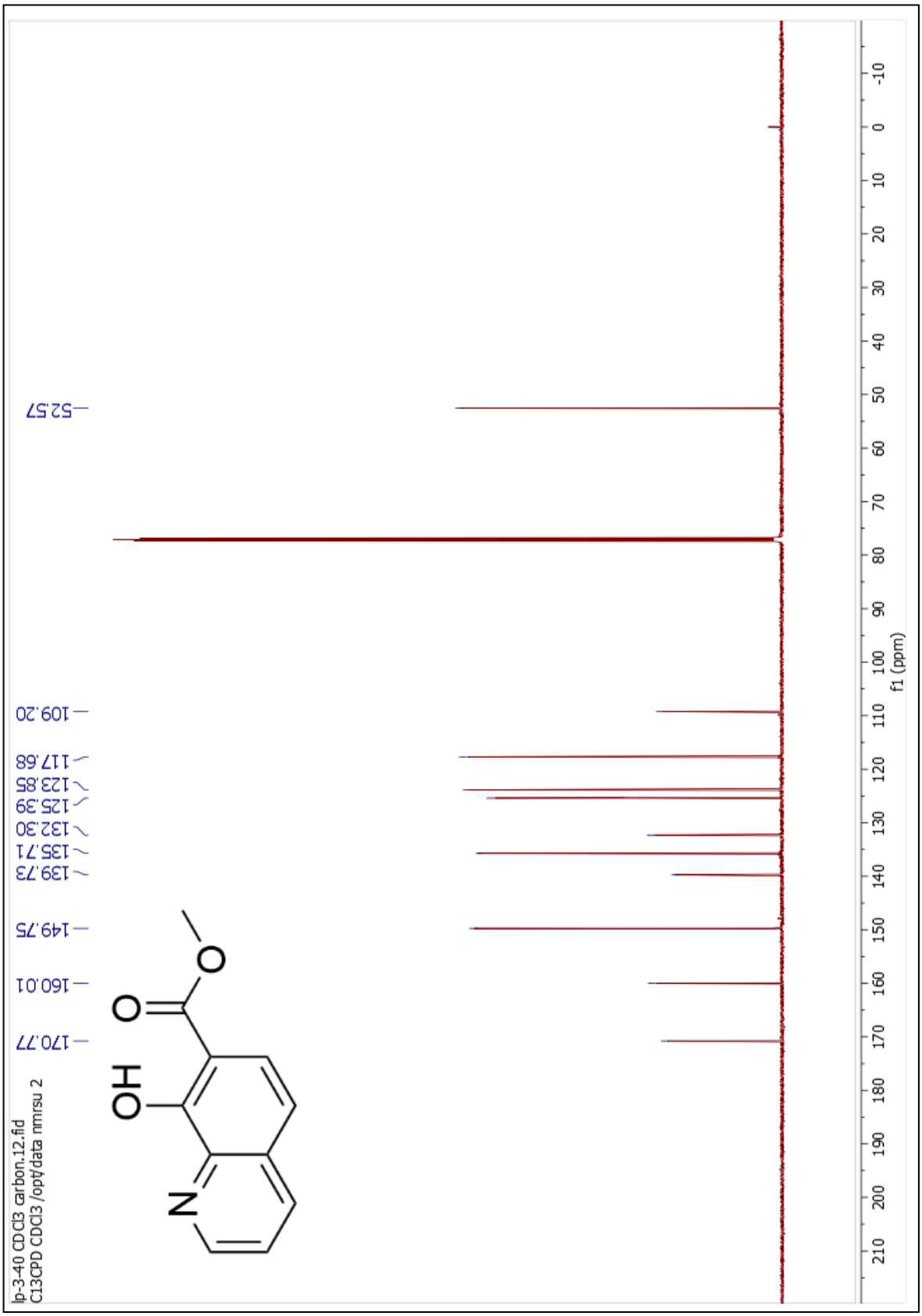

^{13}C NMR Compound **4**

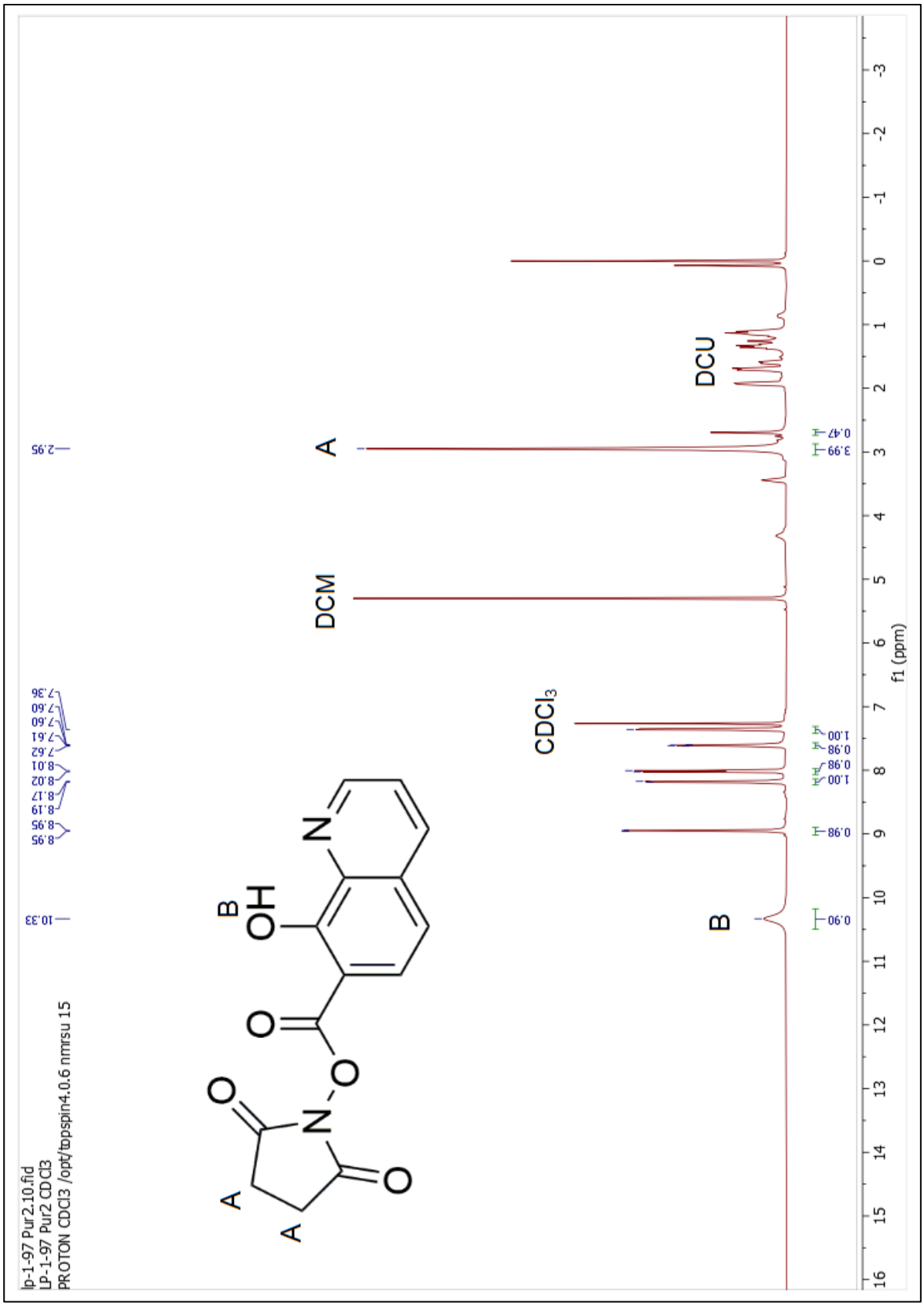

^{1}H NMR Compound **5**

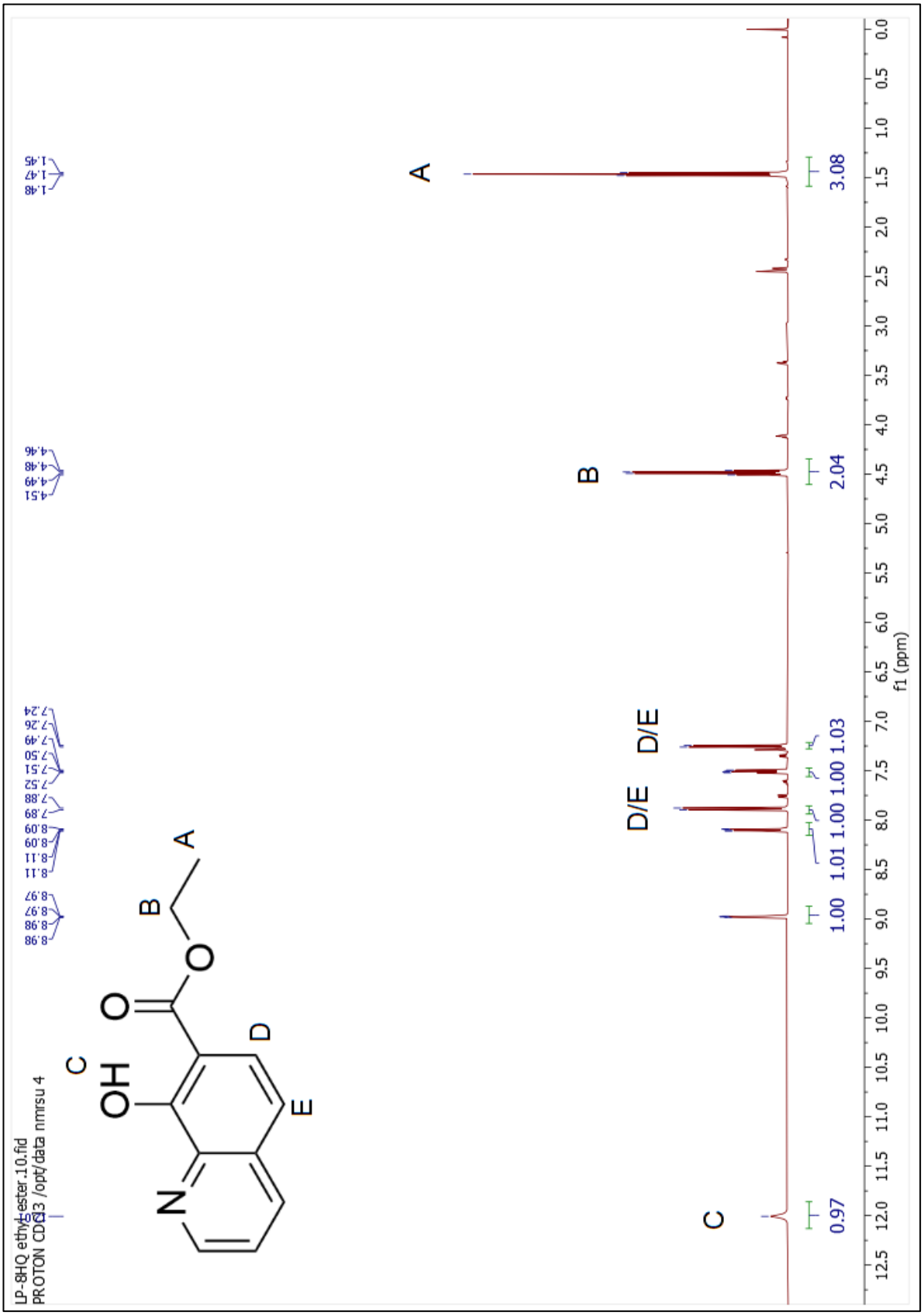

^{1}H NMR Compound **6**

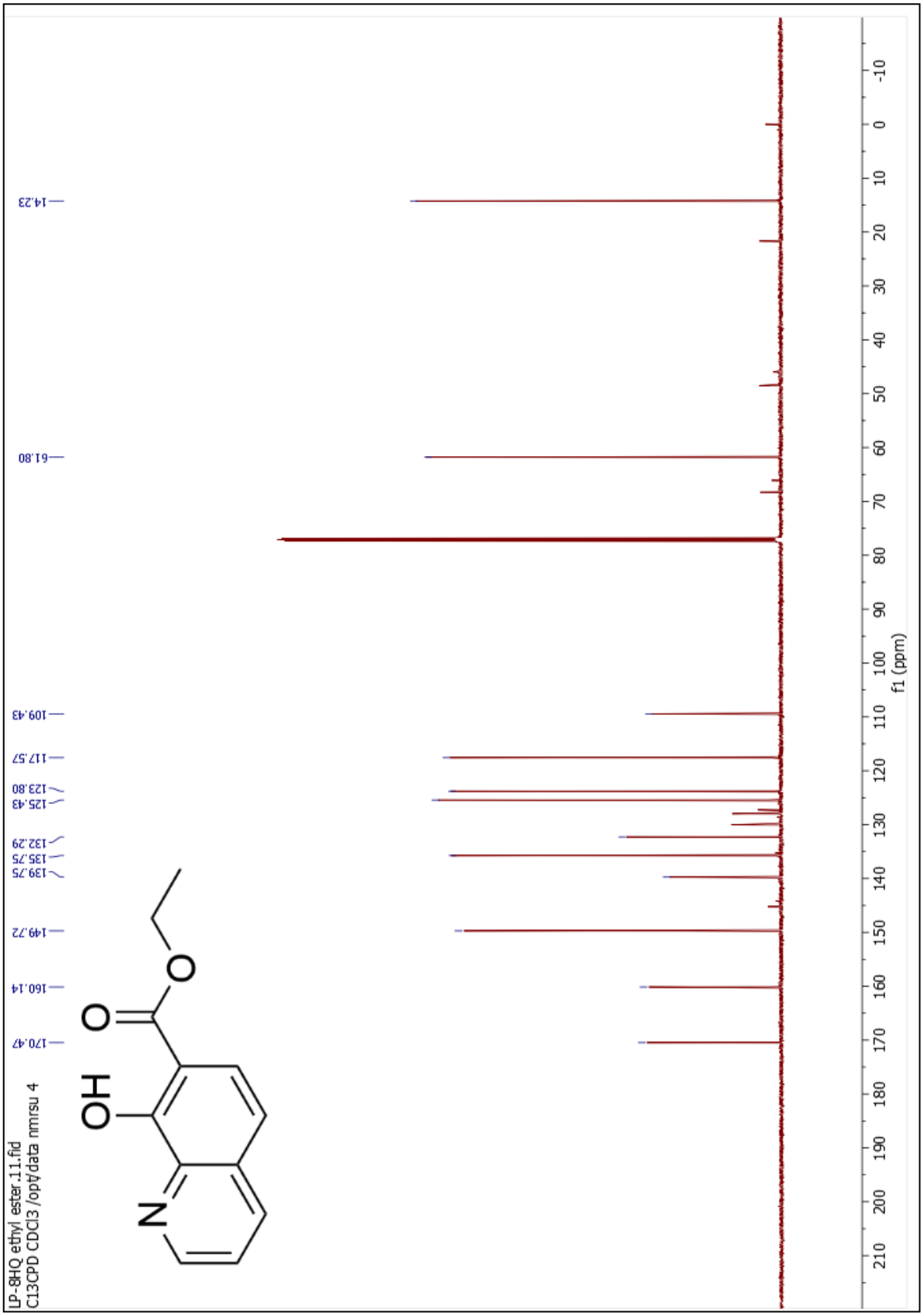

^{13}C NMR Compound **6**

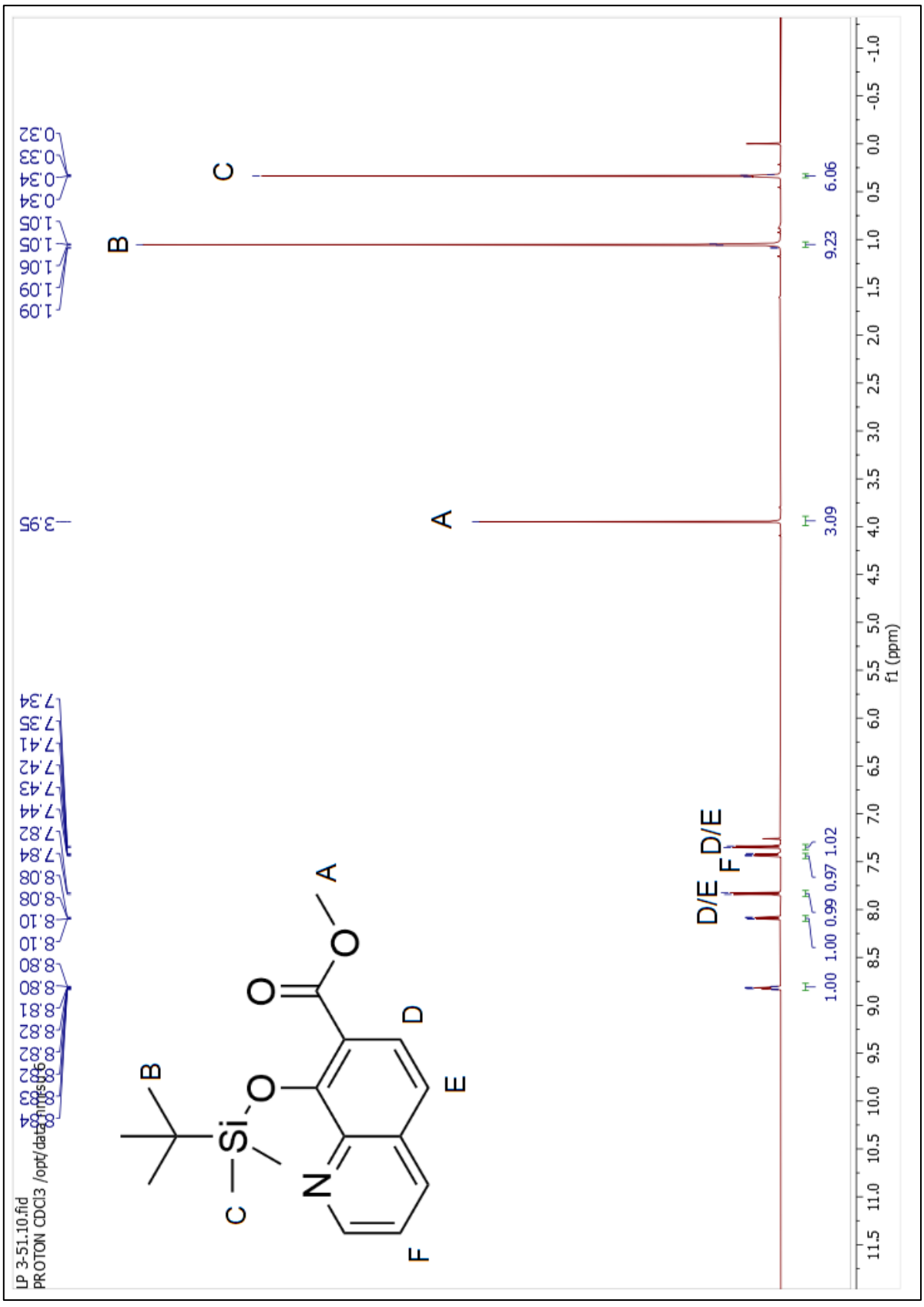

^{1}H NMR Compound **7**

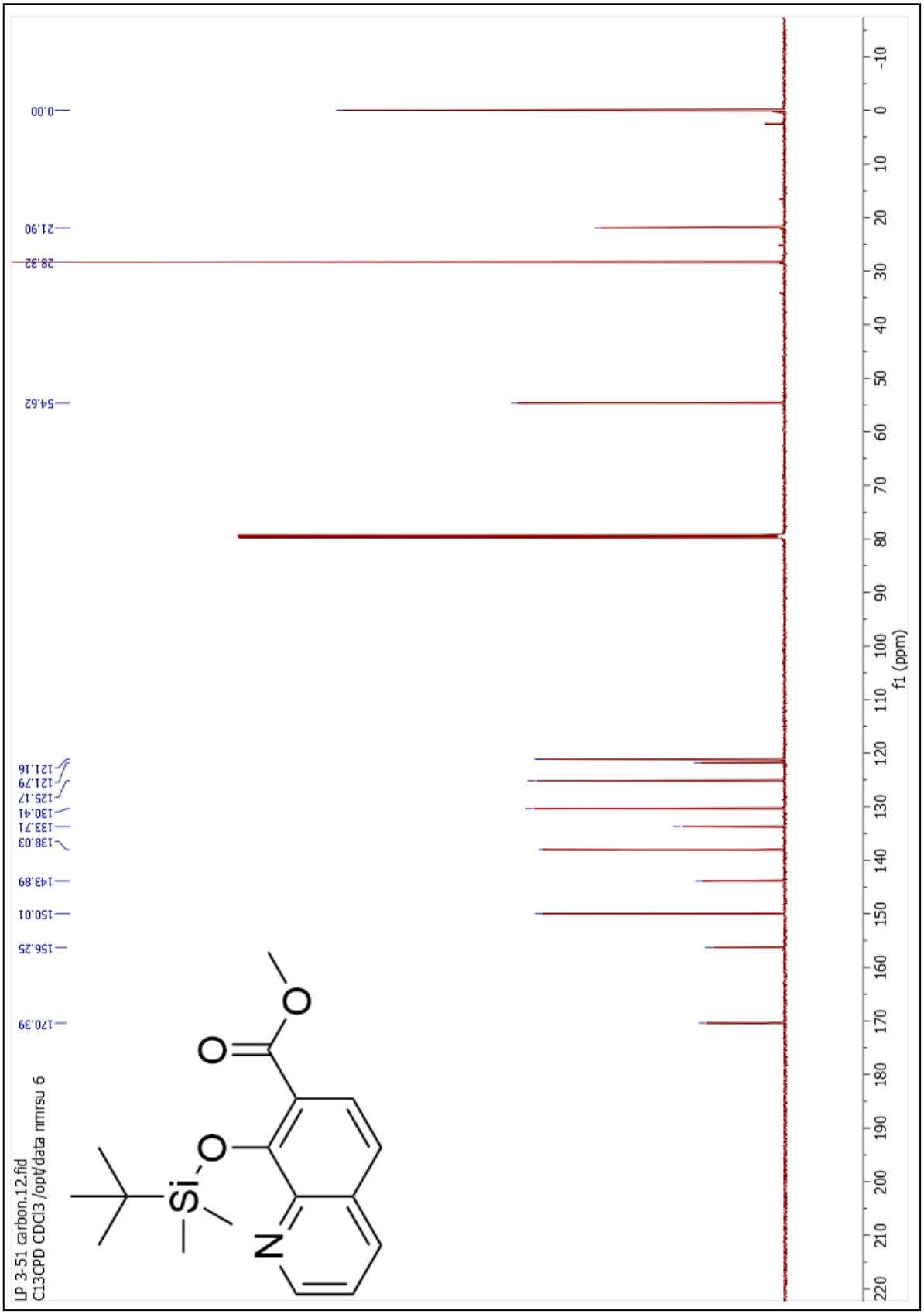

^{13}C NMR Compound **7**

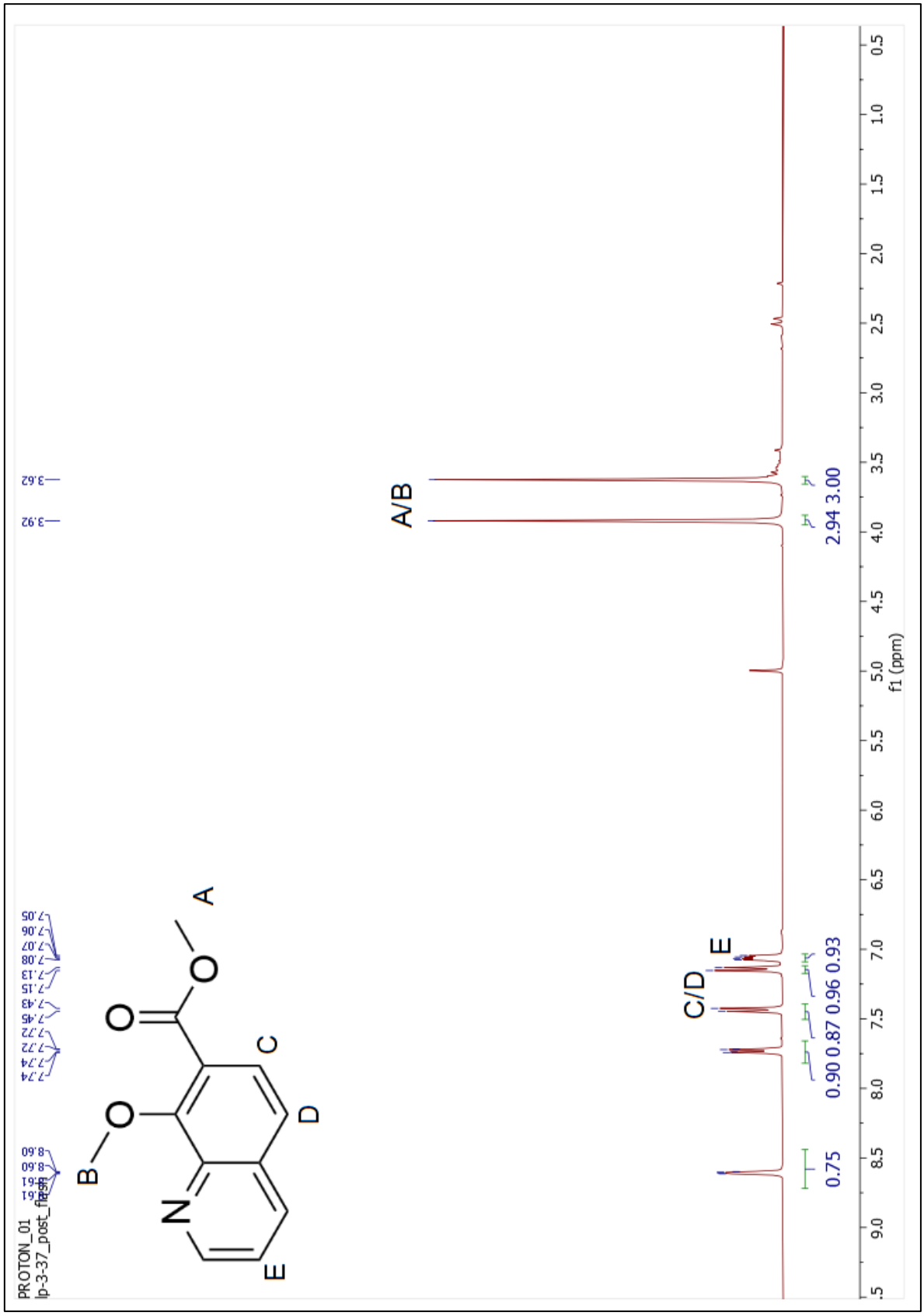

^{1}H NMR Compound **8**

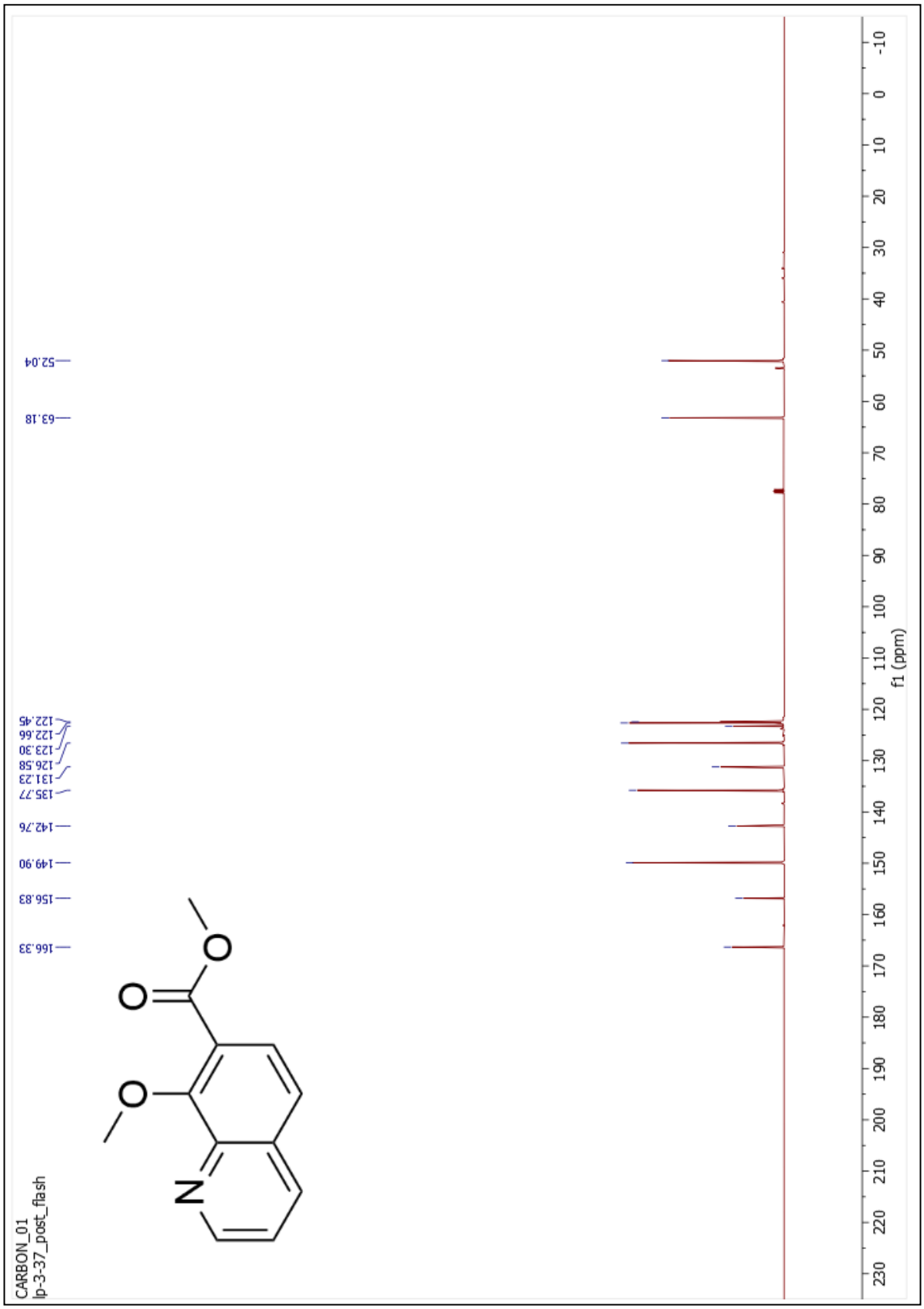

^{13}C NMR Compound **8**

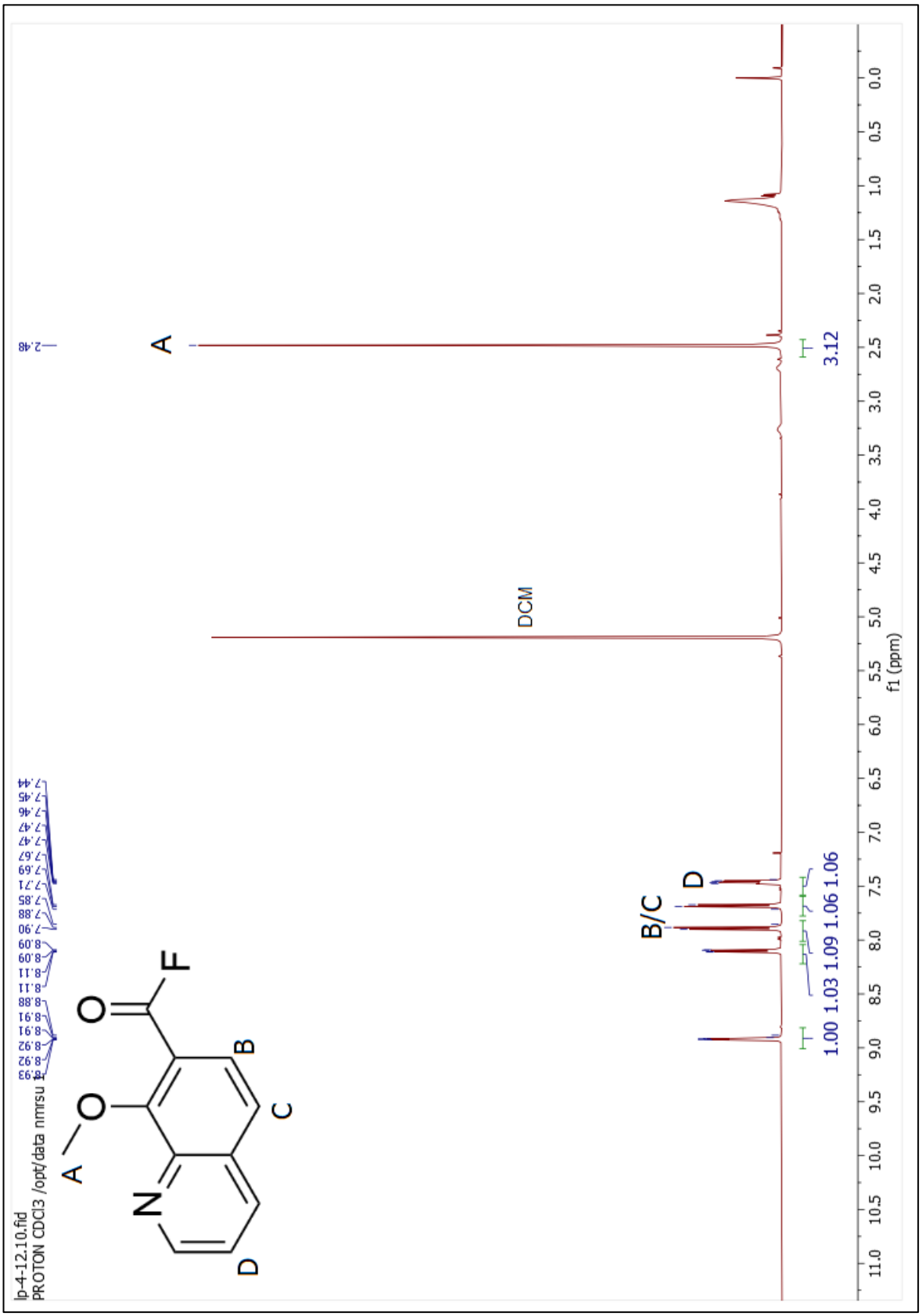

^{1}H NMR Compound **9**

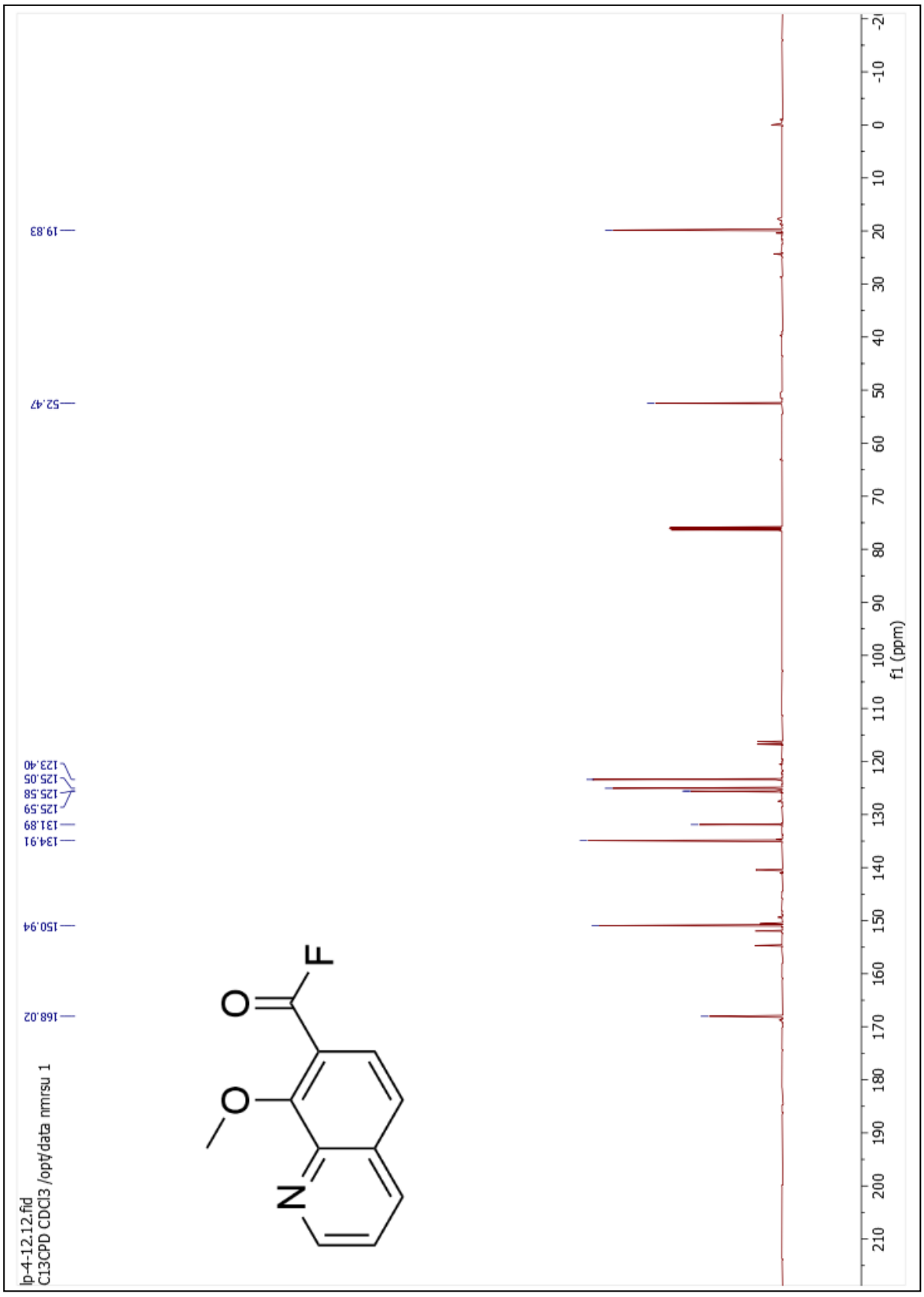

^{13}C NMR Compound **9**

xx

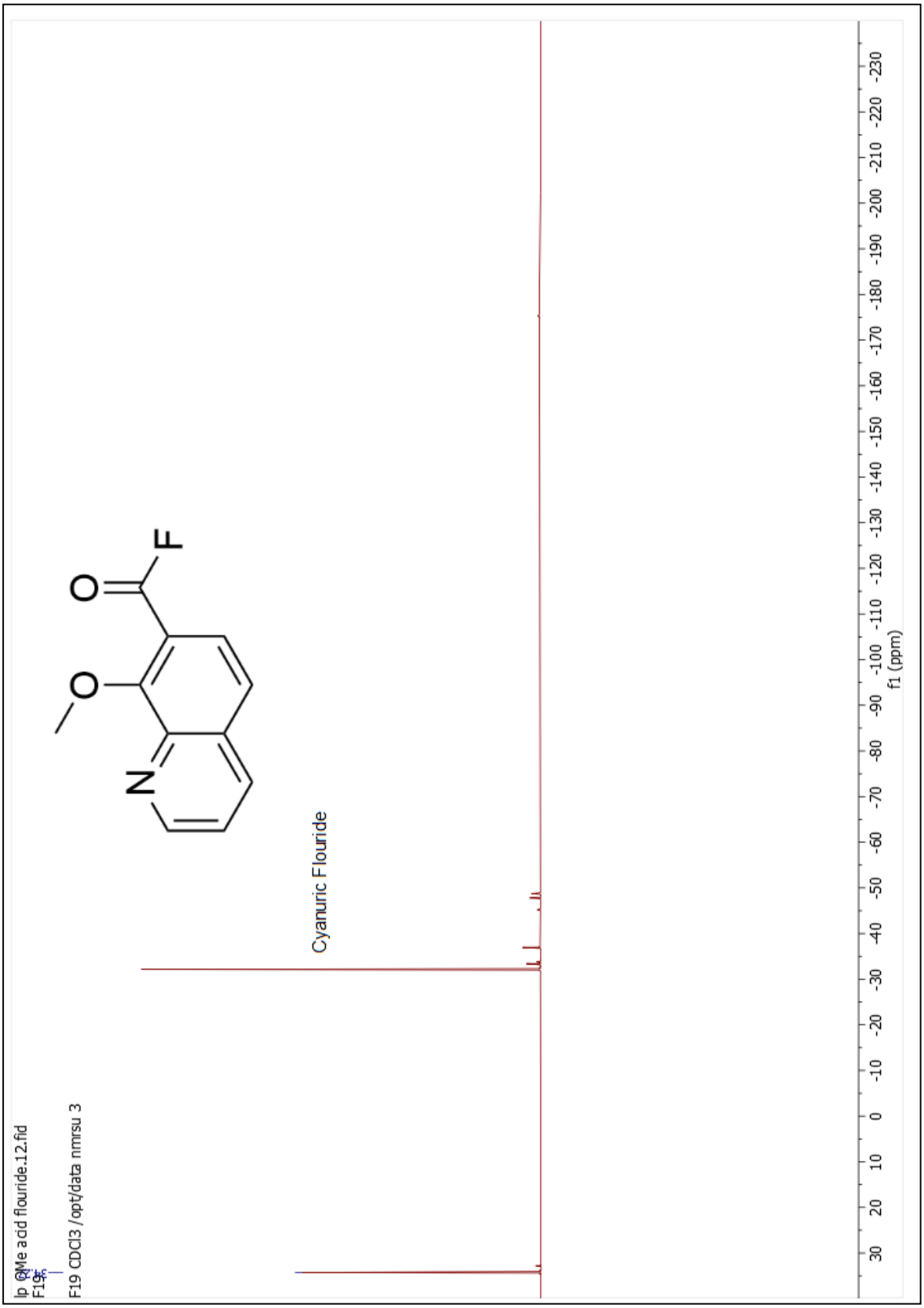

^{19}F NMR Compound **9**

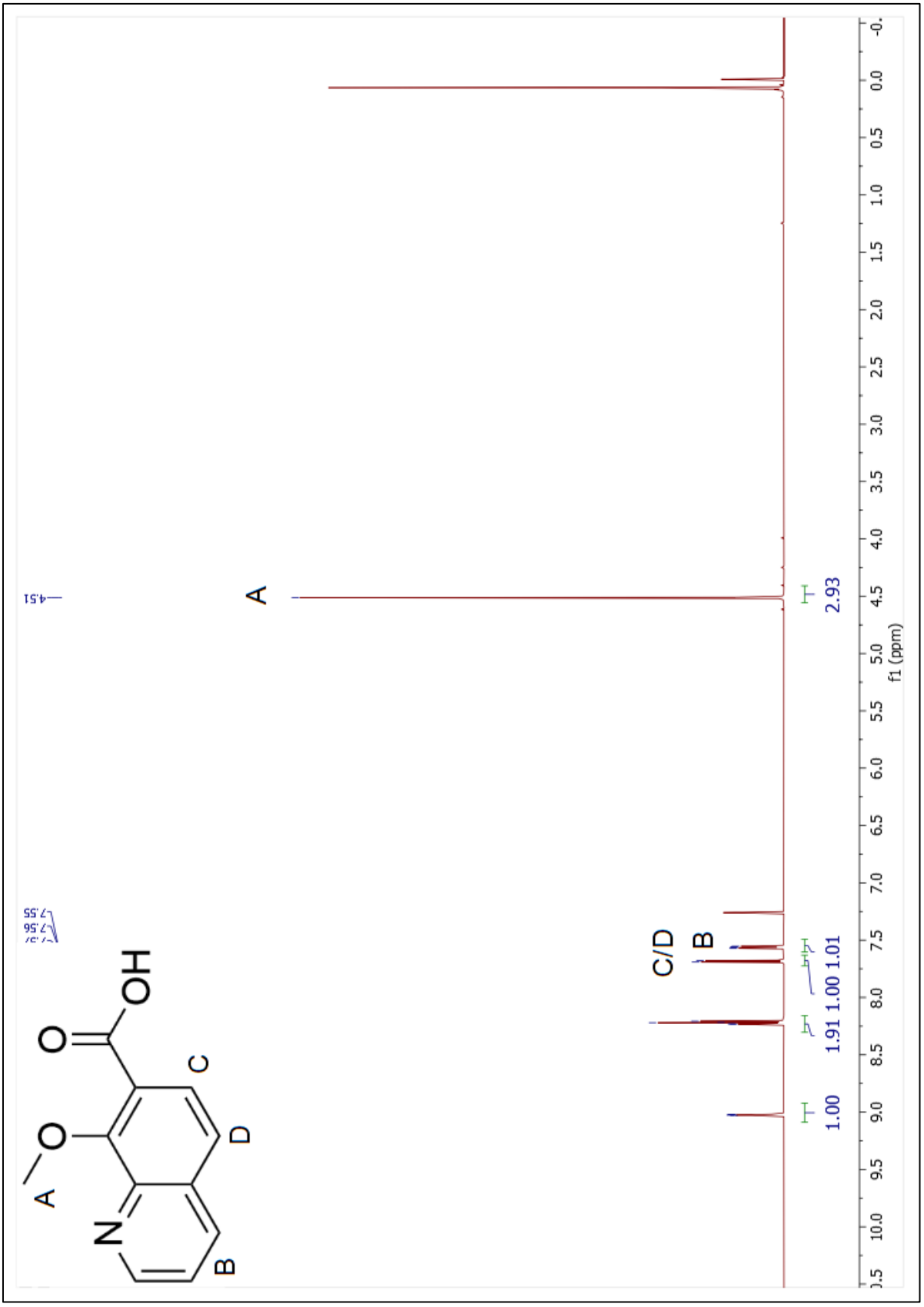

^{1}H NMR Compound **10**

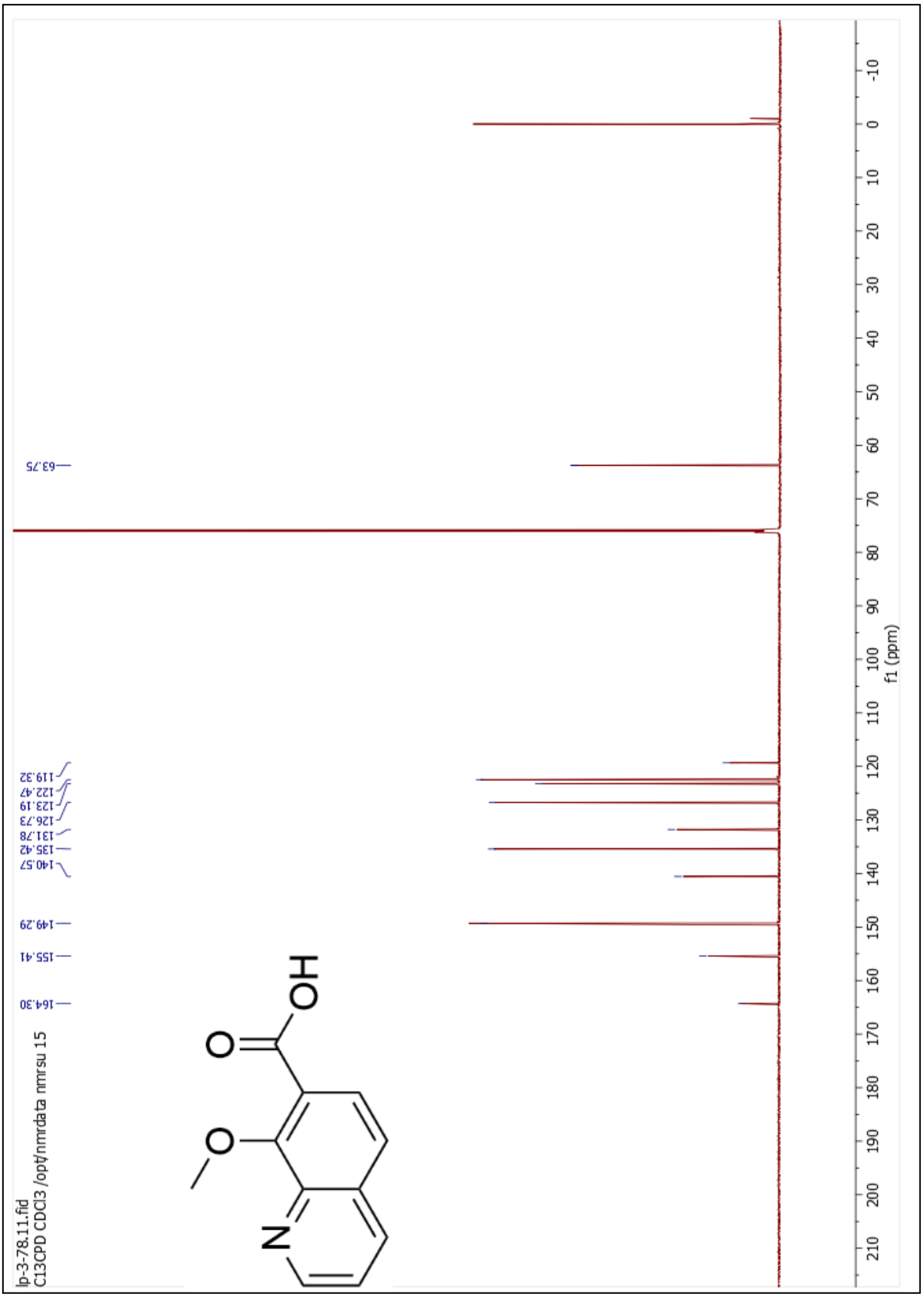

^{13}C NMR Compound **10**

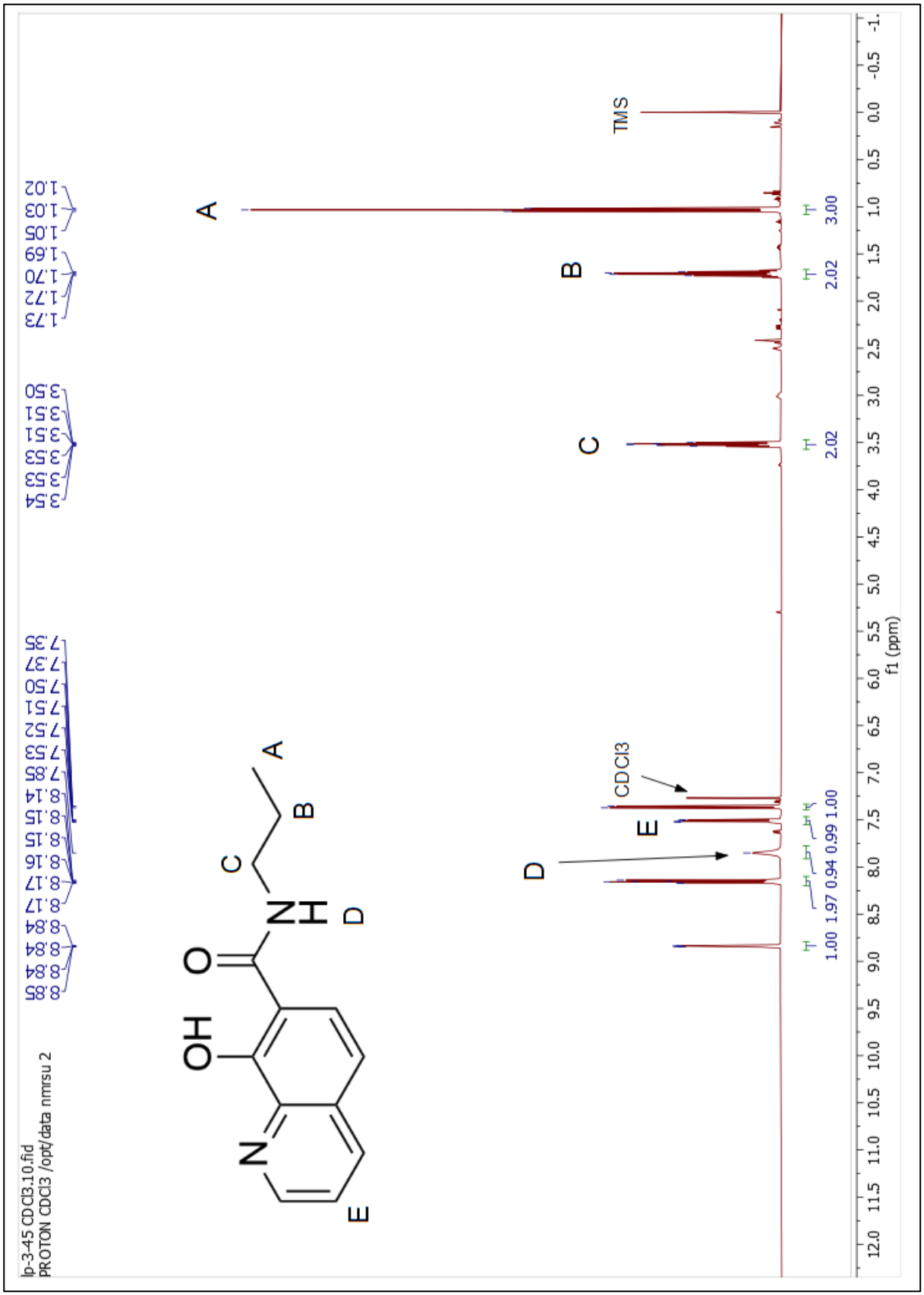

^{1}H NMR Compound **11**

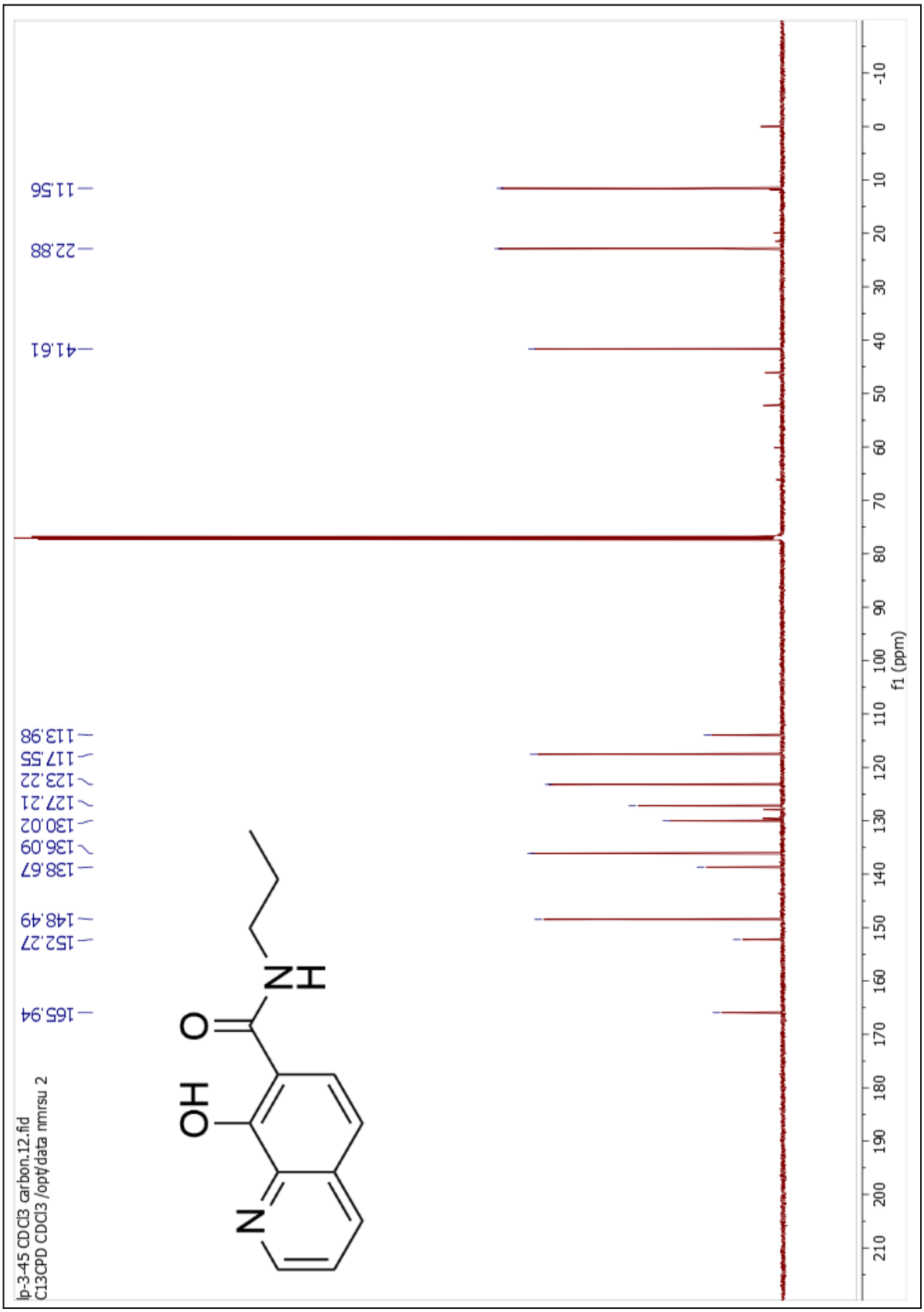

^{13}C NMR Compound **11**

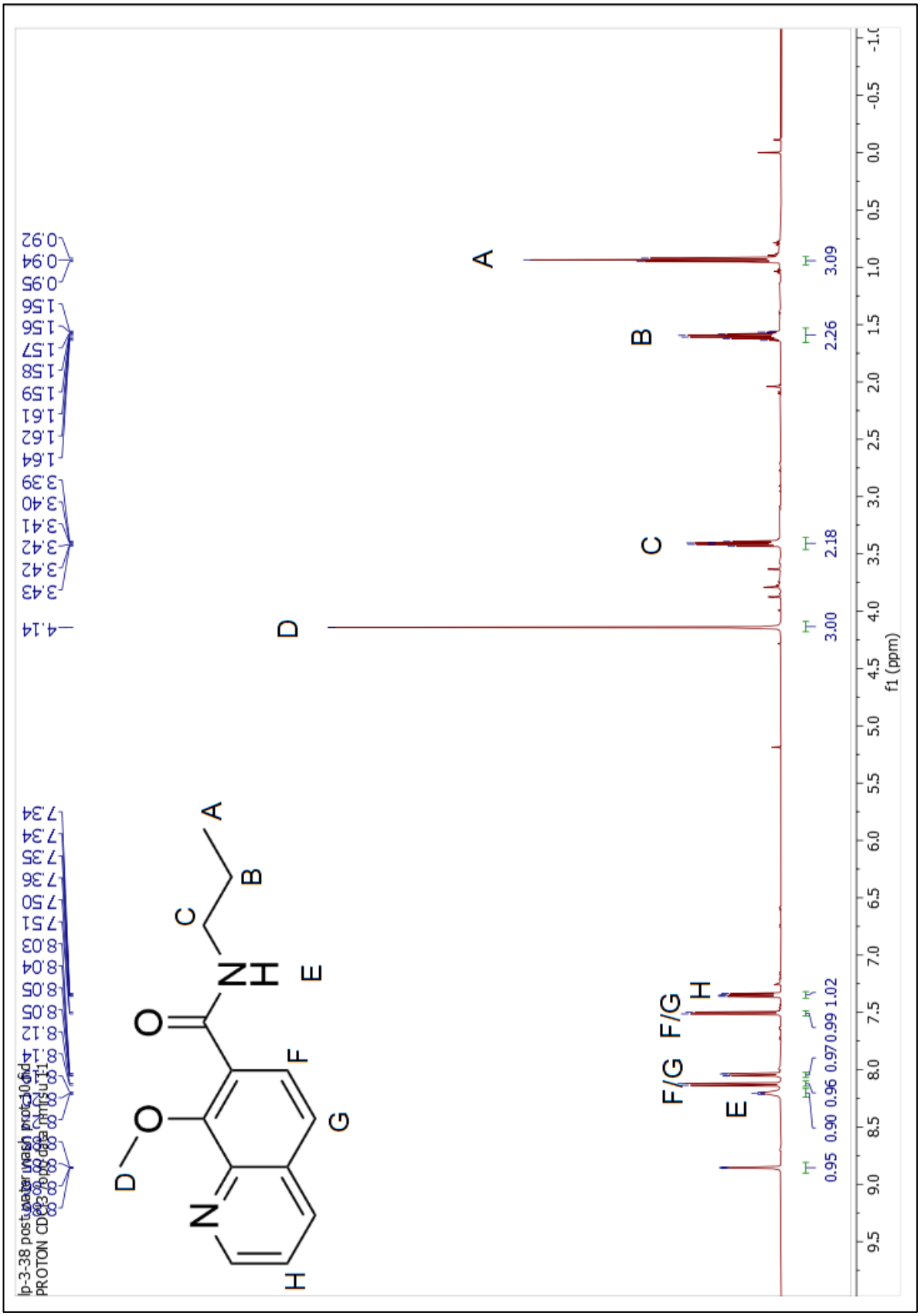

^{1}H NMR Compound **12**

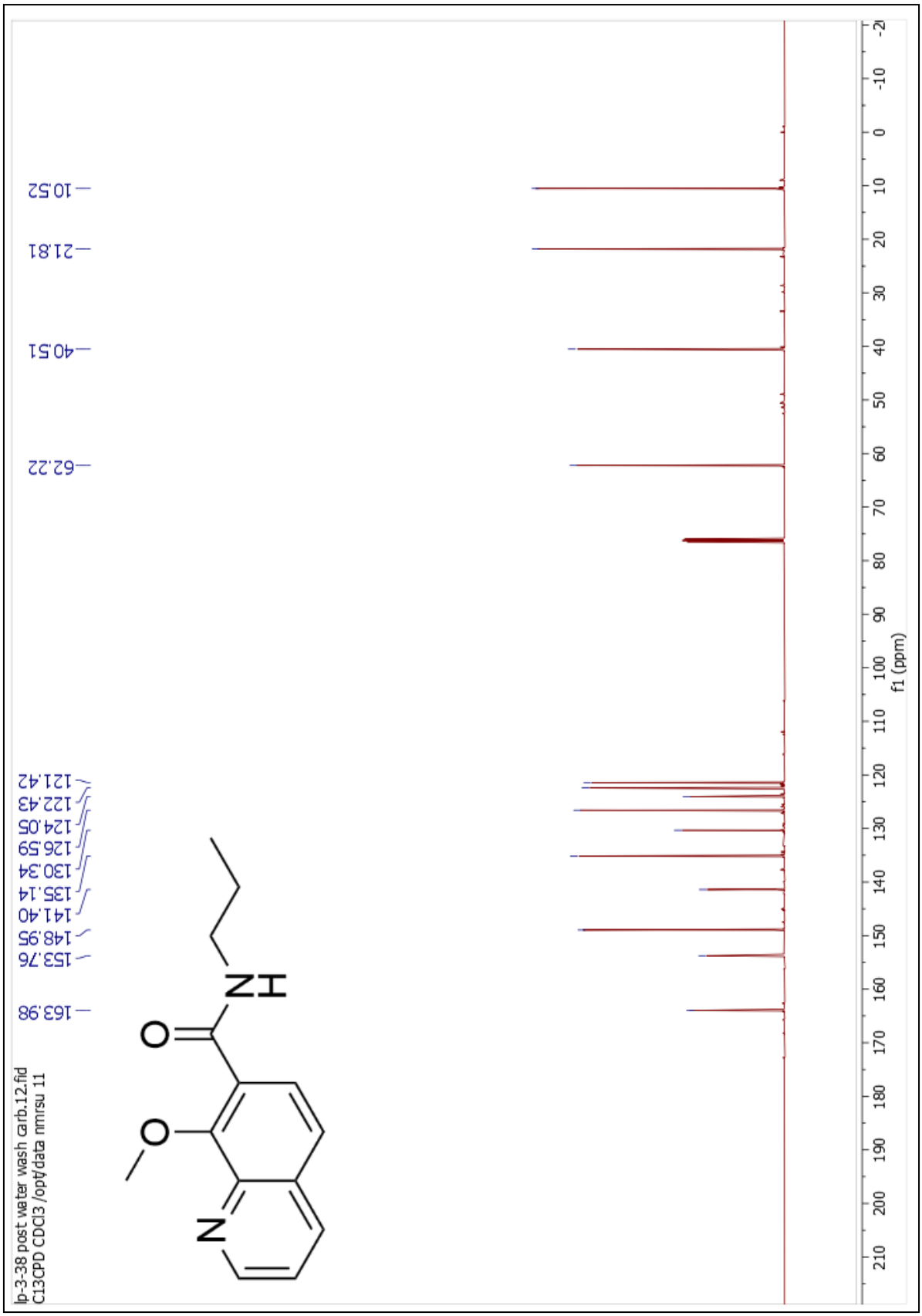

^{13}C NMR Compound **12**

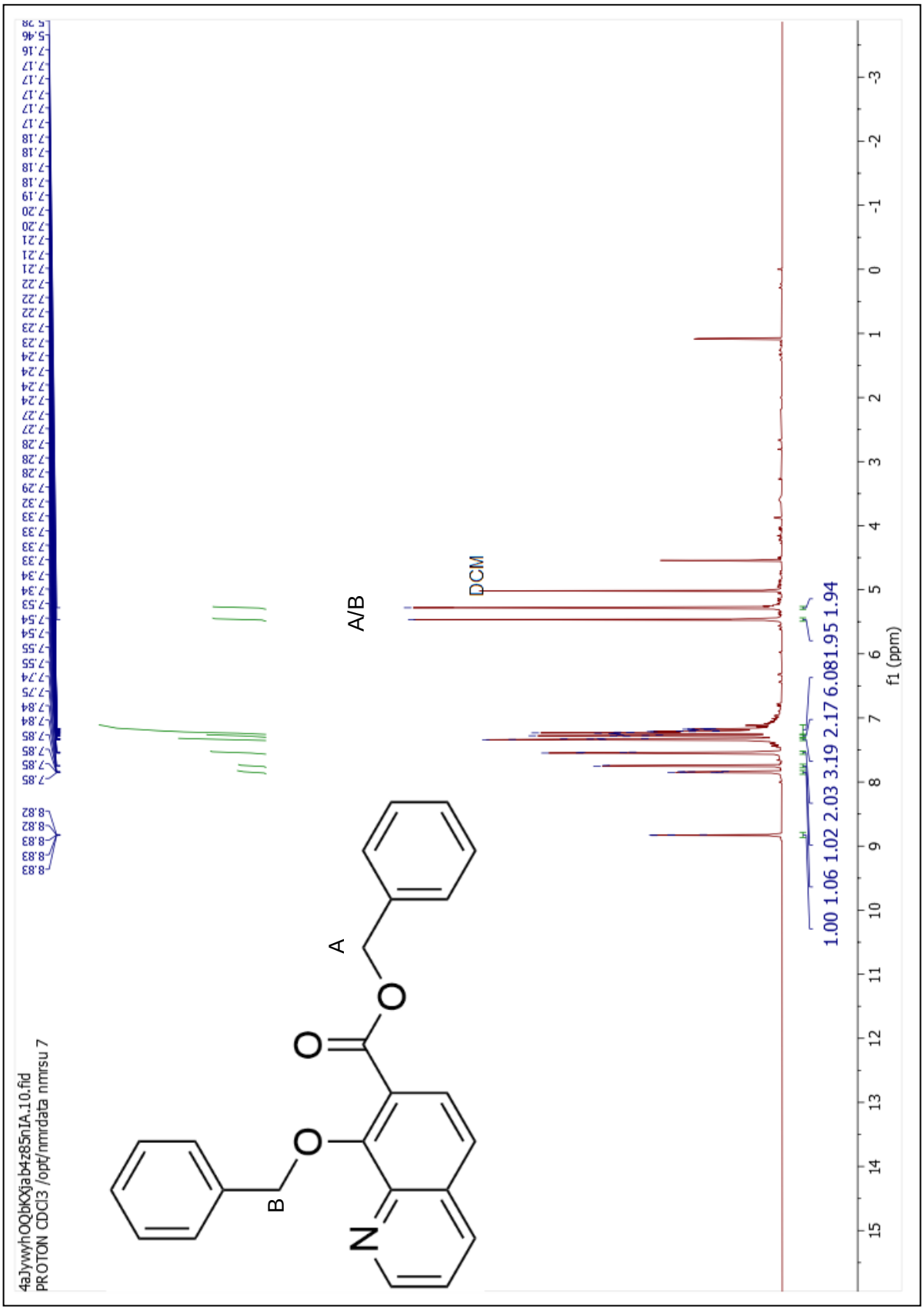

^{1}H NMR Compound **13**

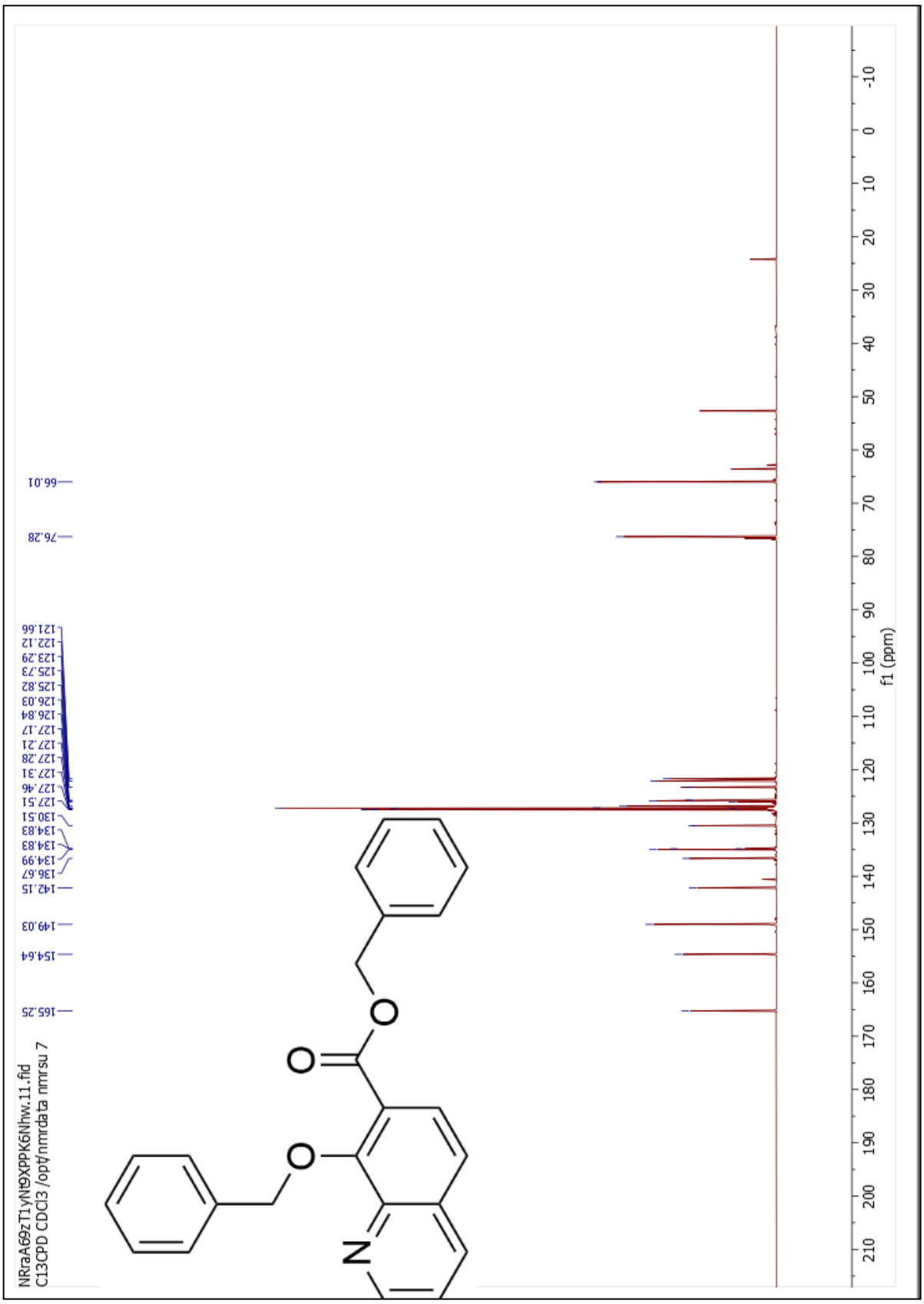

^{13}C NMR Compound **13**

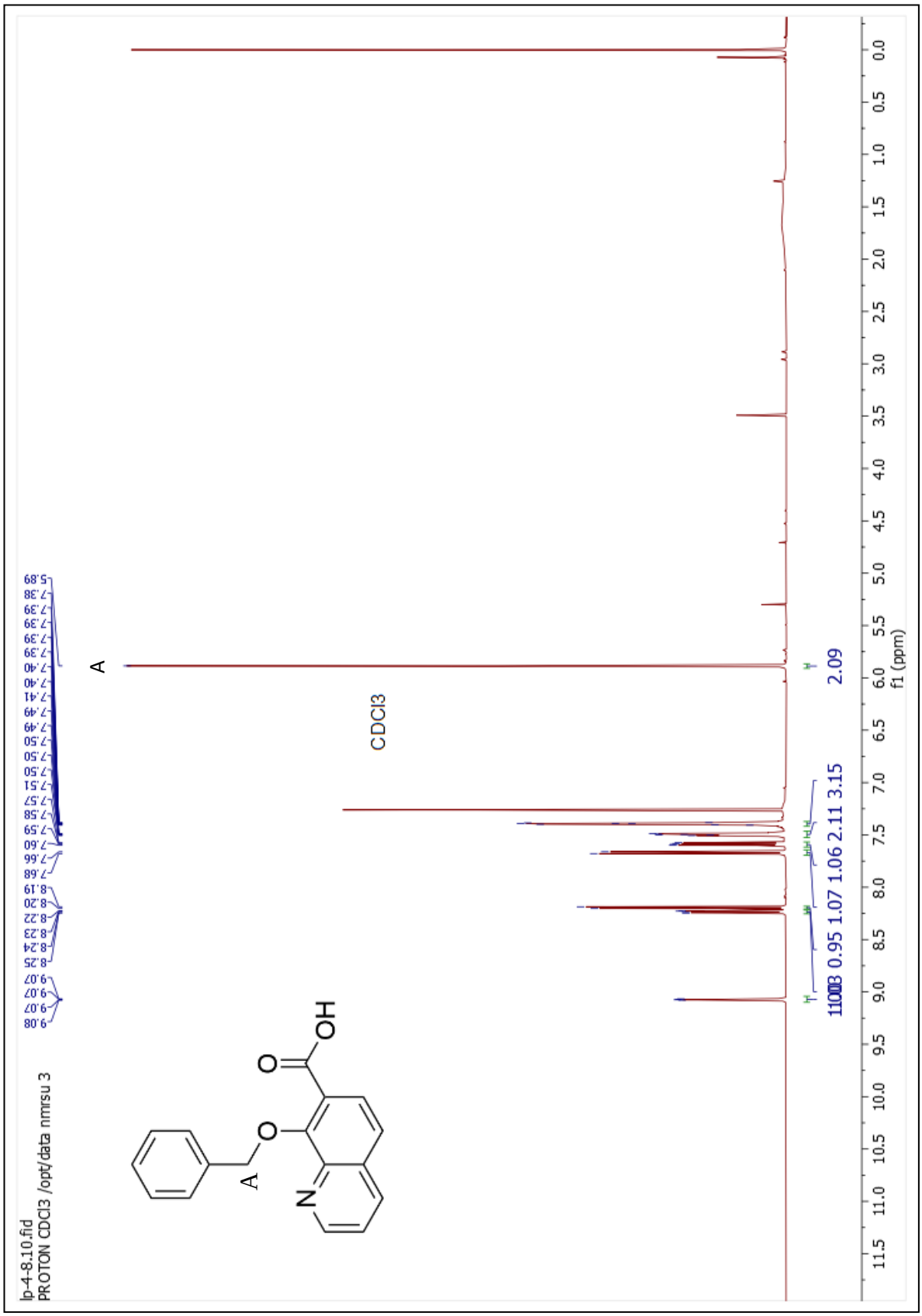

^{1}H NMR Compound **14**
xxx

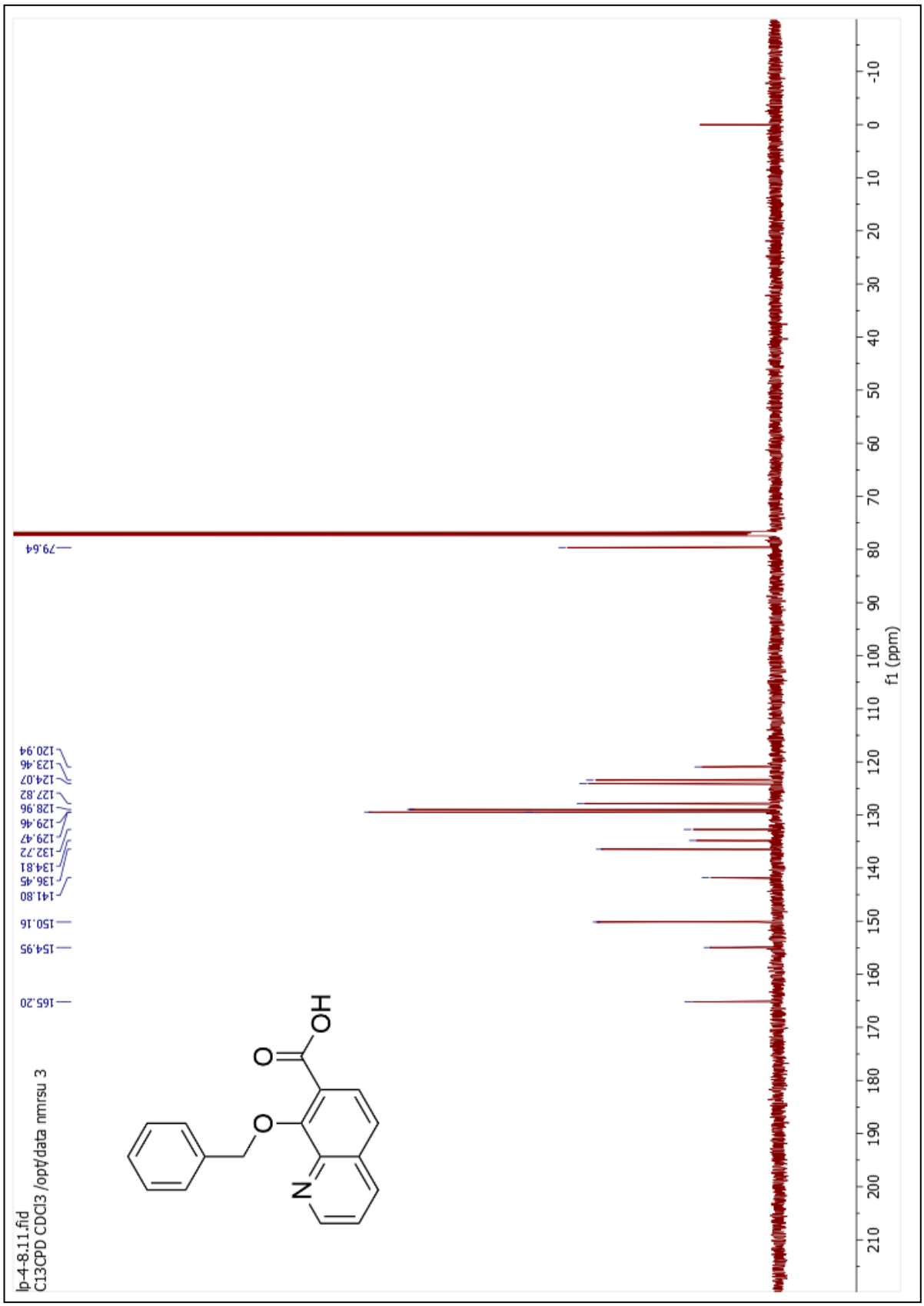

^{13}C NMR Compound **14**

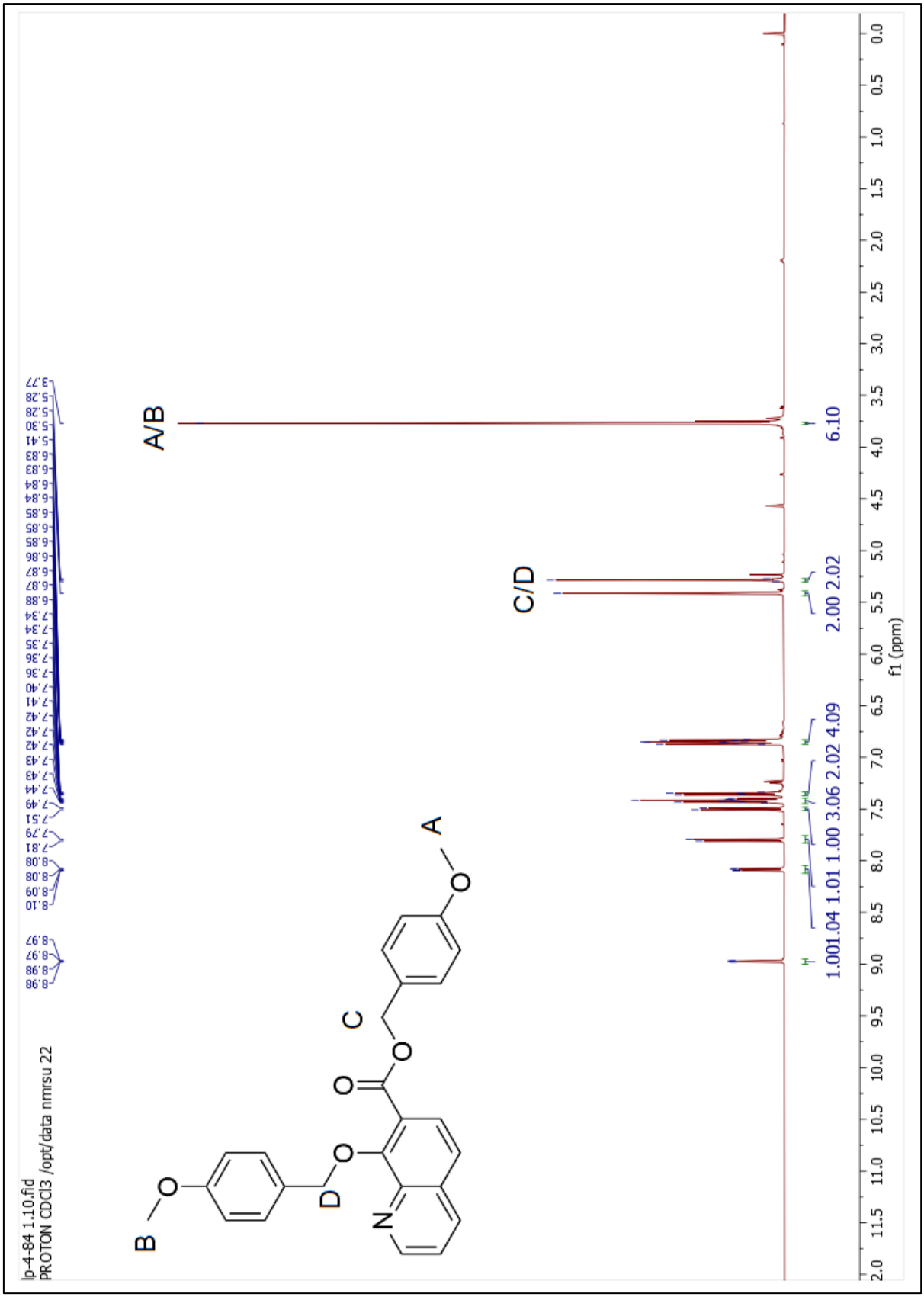

^{1}H NMR Compound **15**

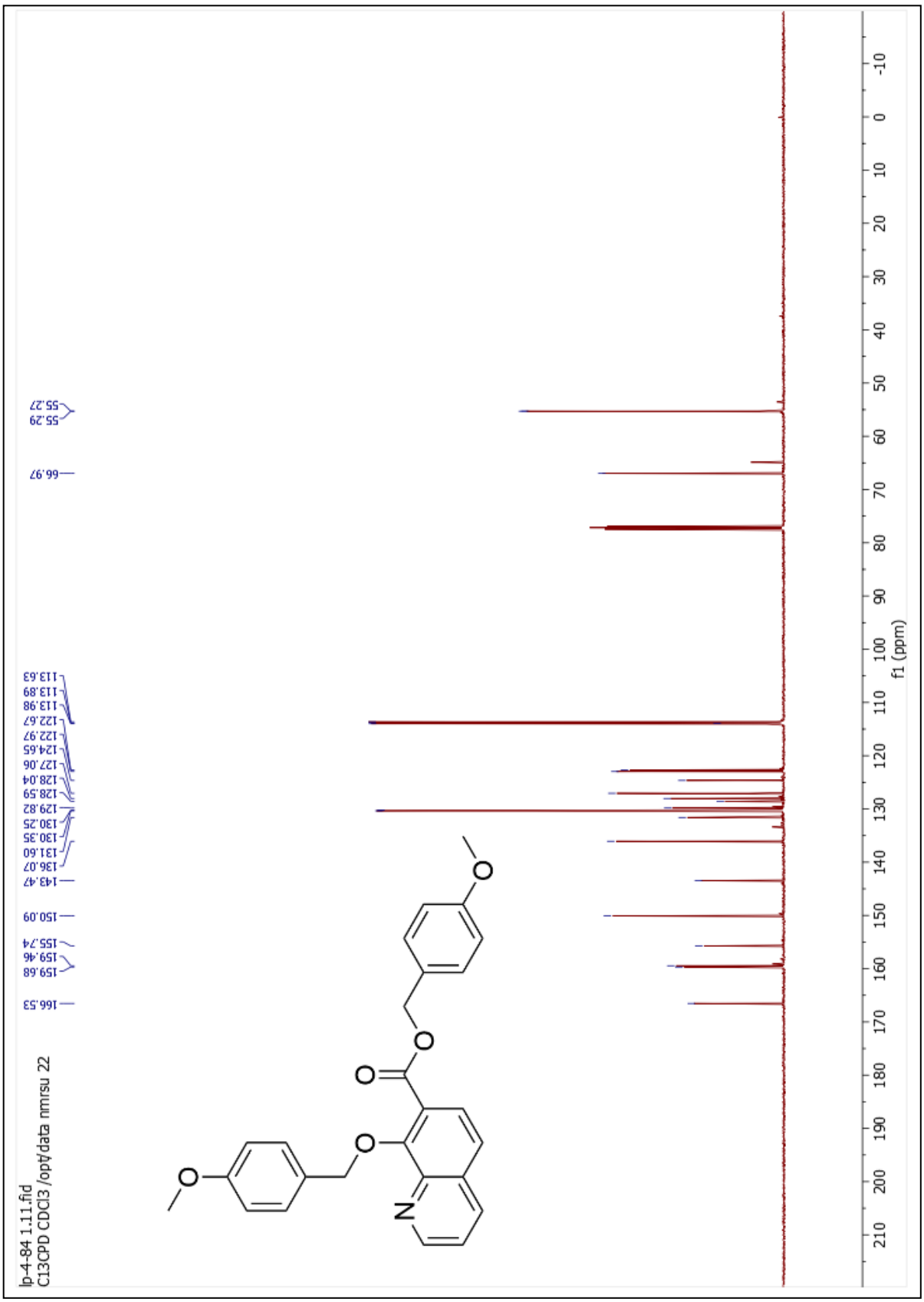

^{13}C NMR Compound **15**

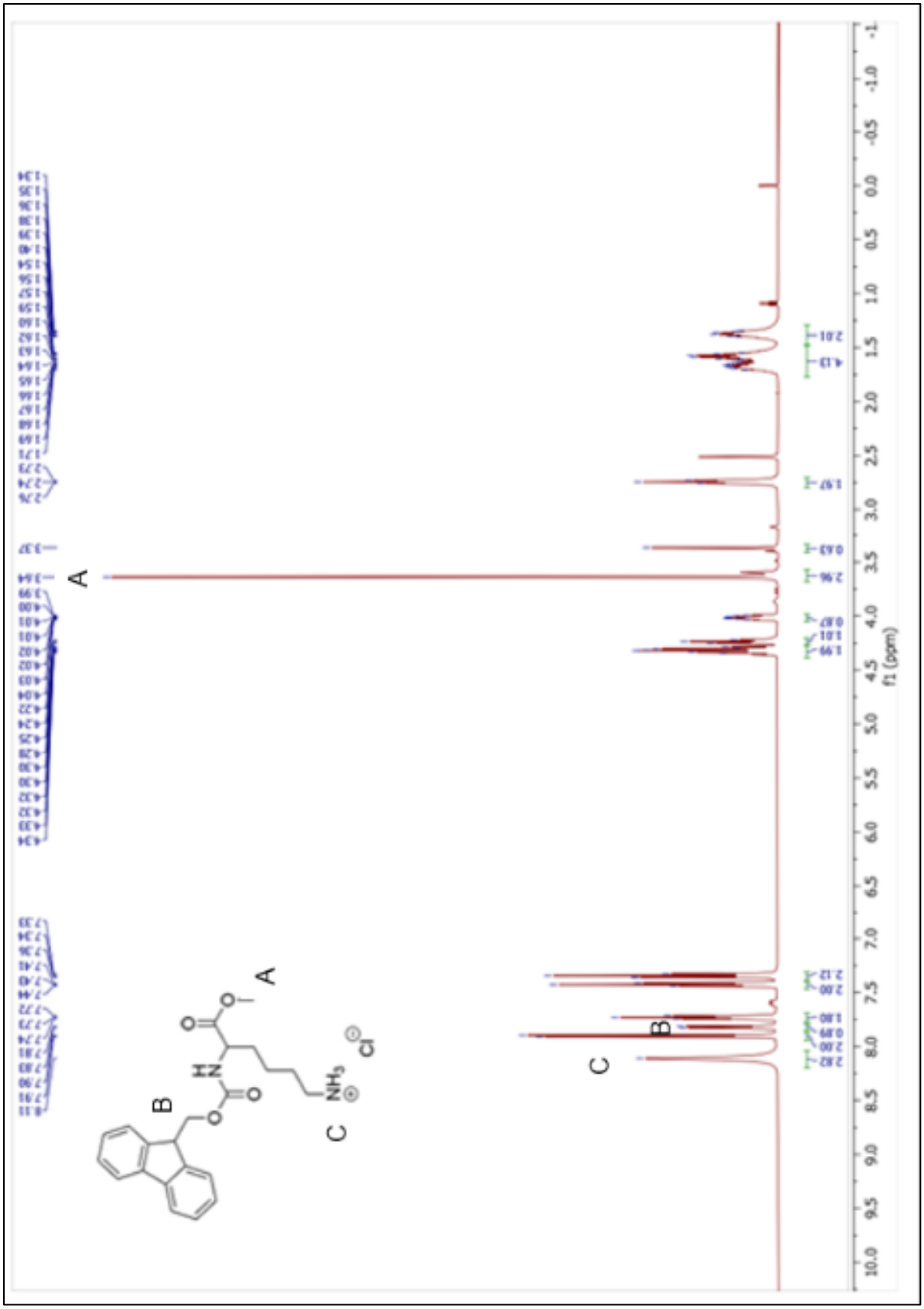

^{1}H NMR Compound **16**

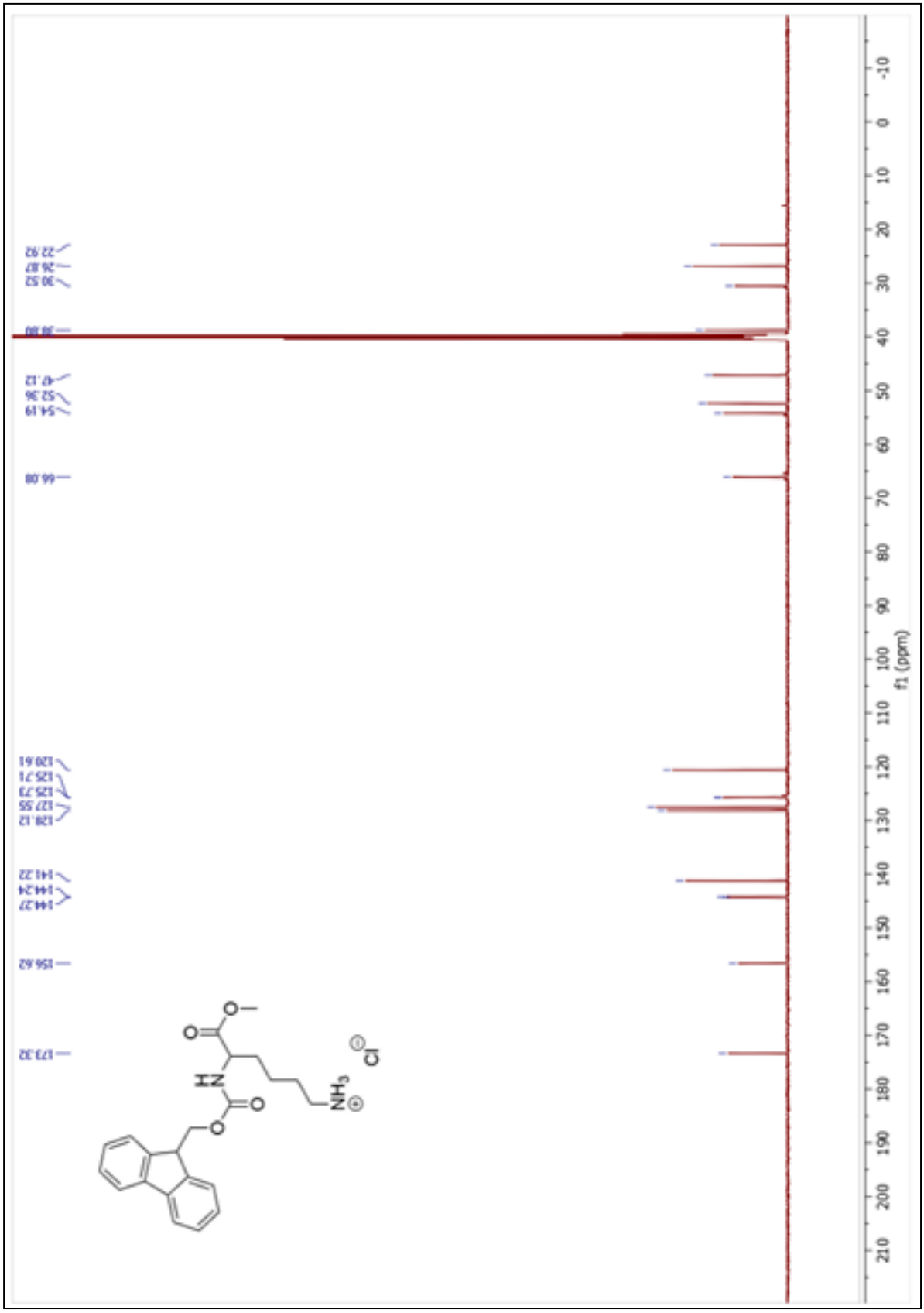

^{13}C NMR Compound **16**

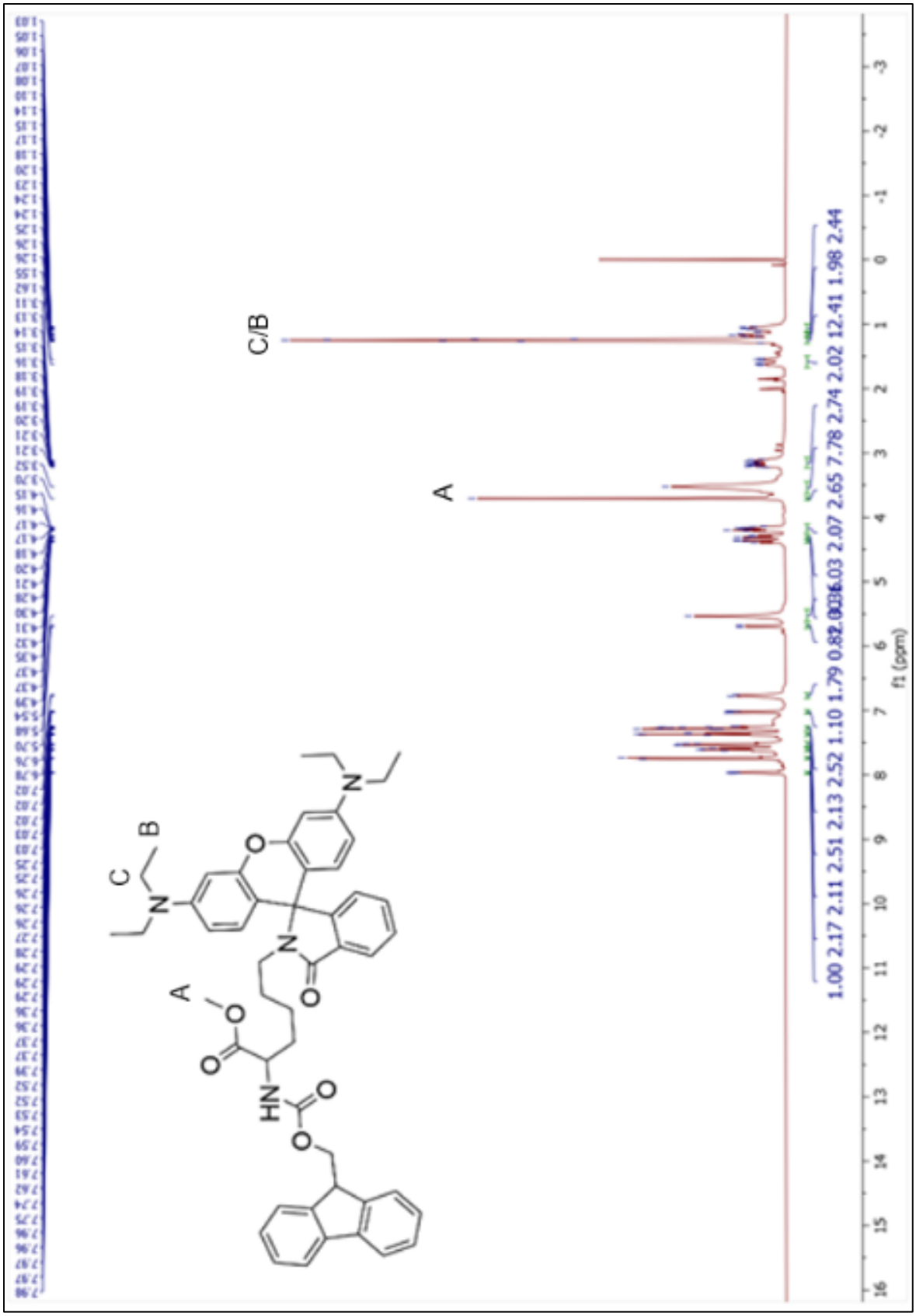

^{1}H NMR Compound **17**

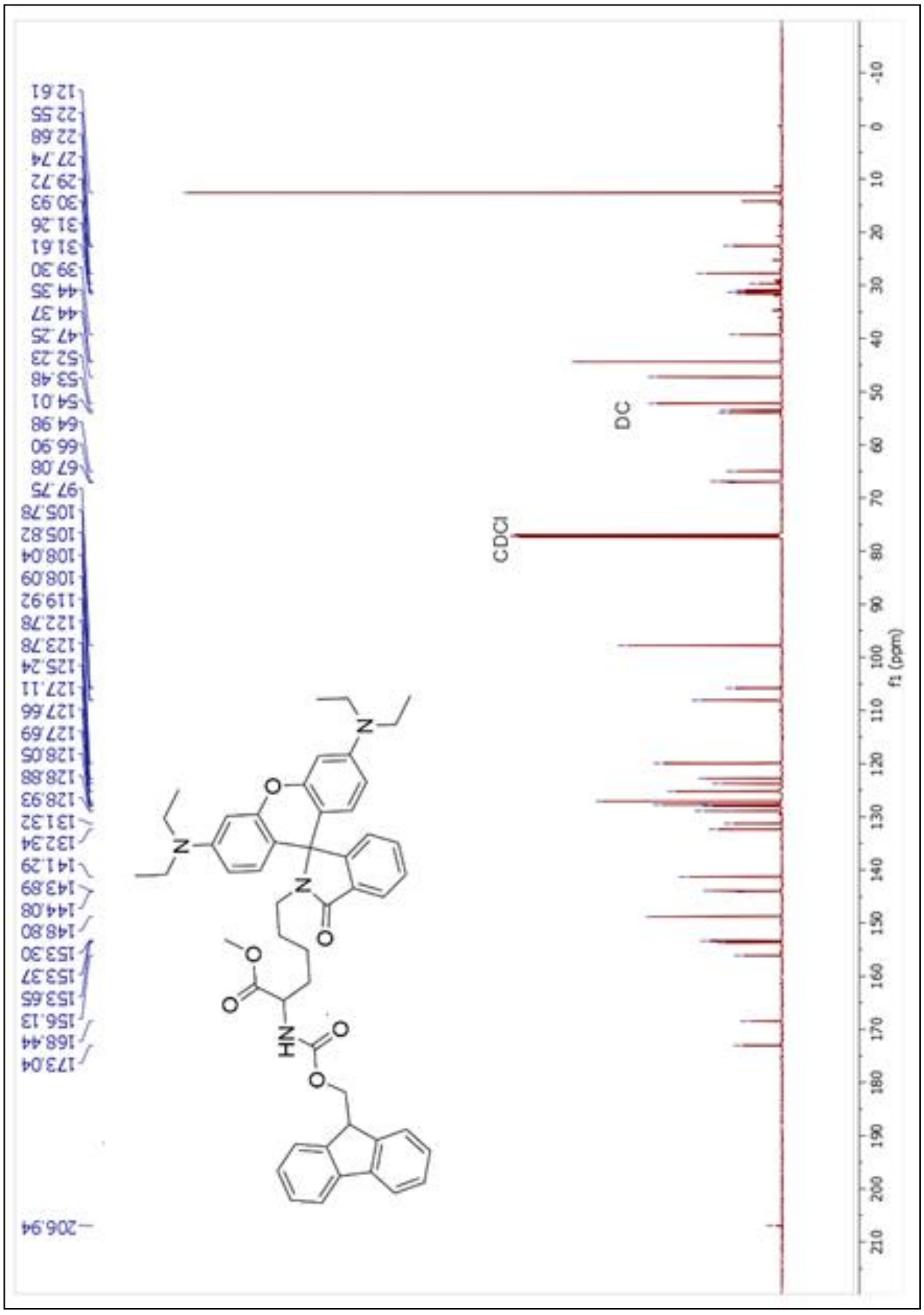

^{13}C NMR Compound **17**

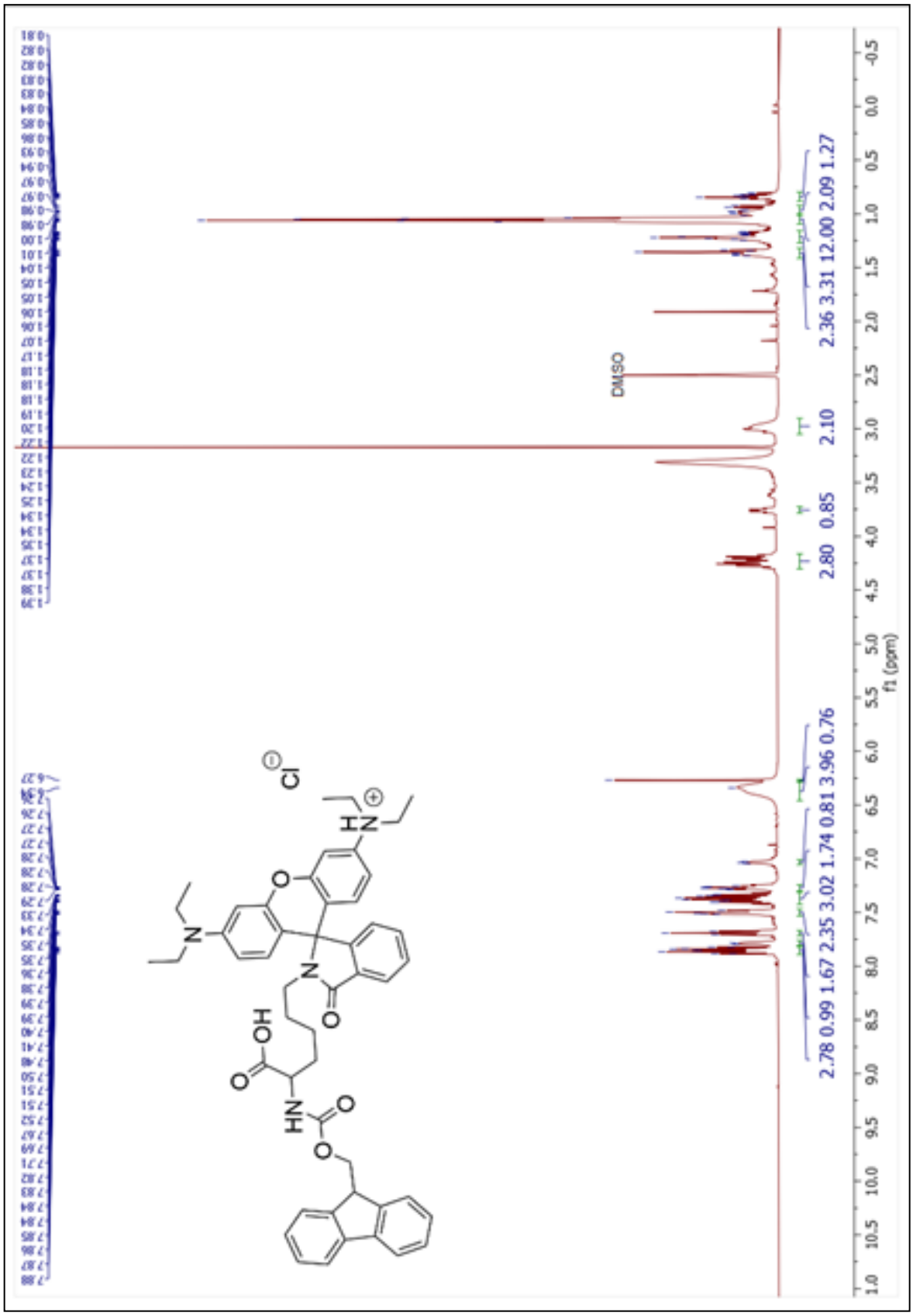

^{1}H NMR Compound **18**

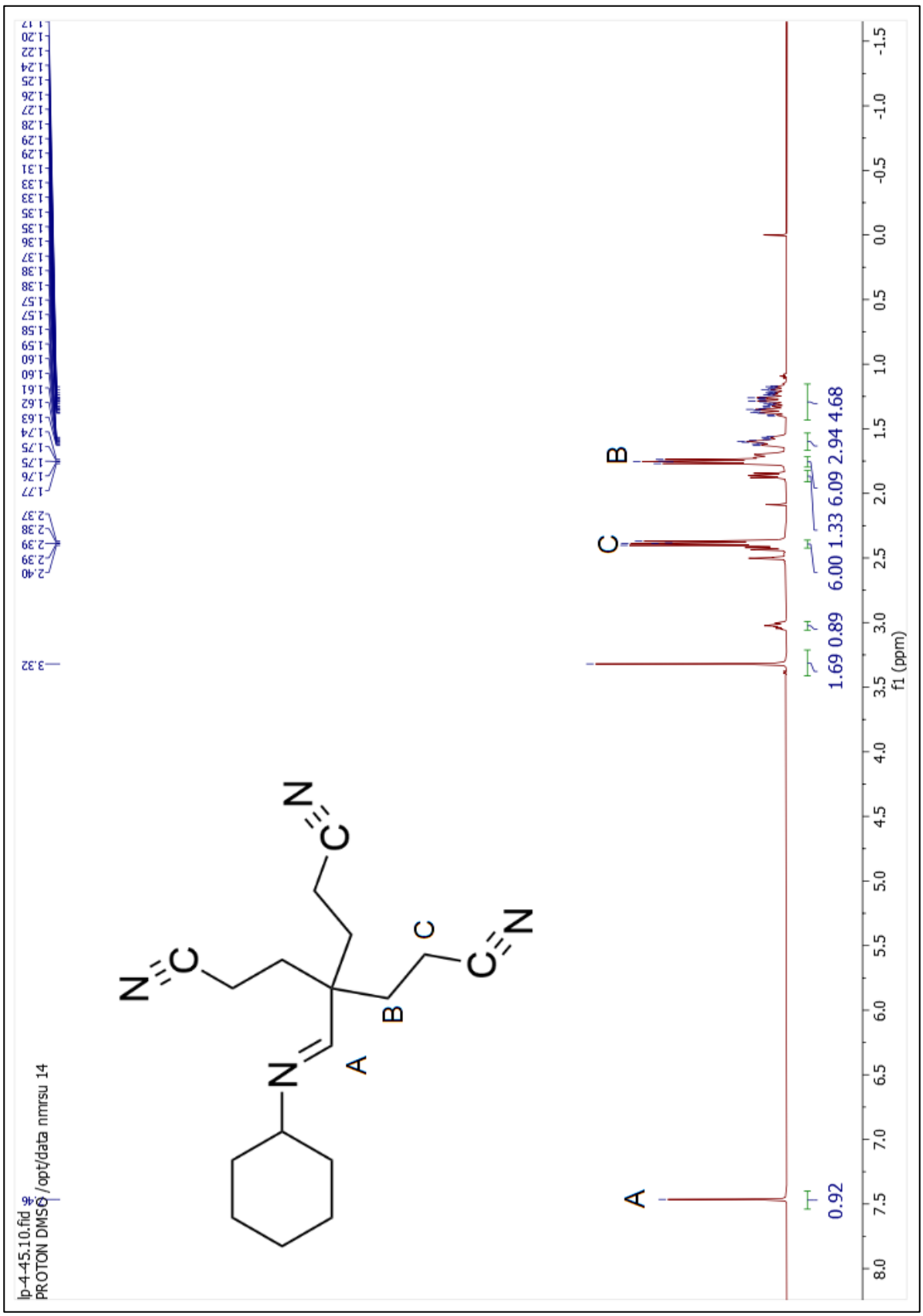

^{1}H NMR Compound **19**

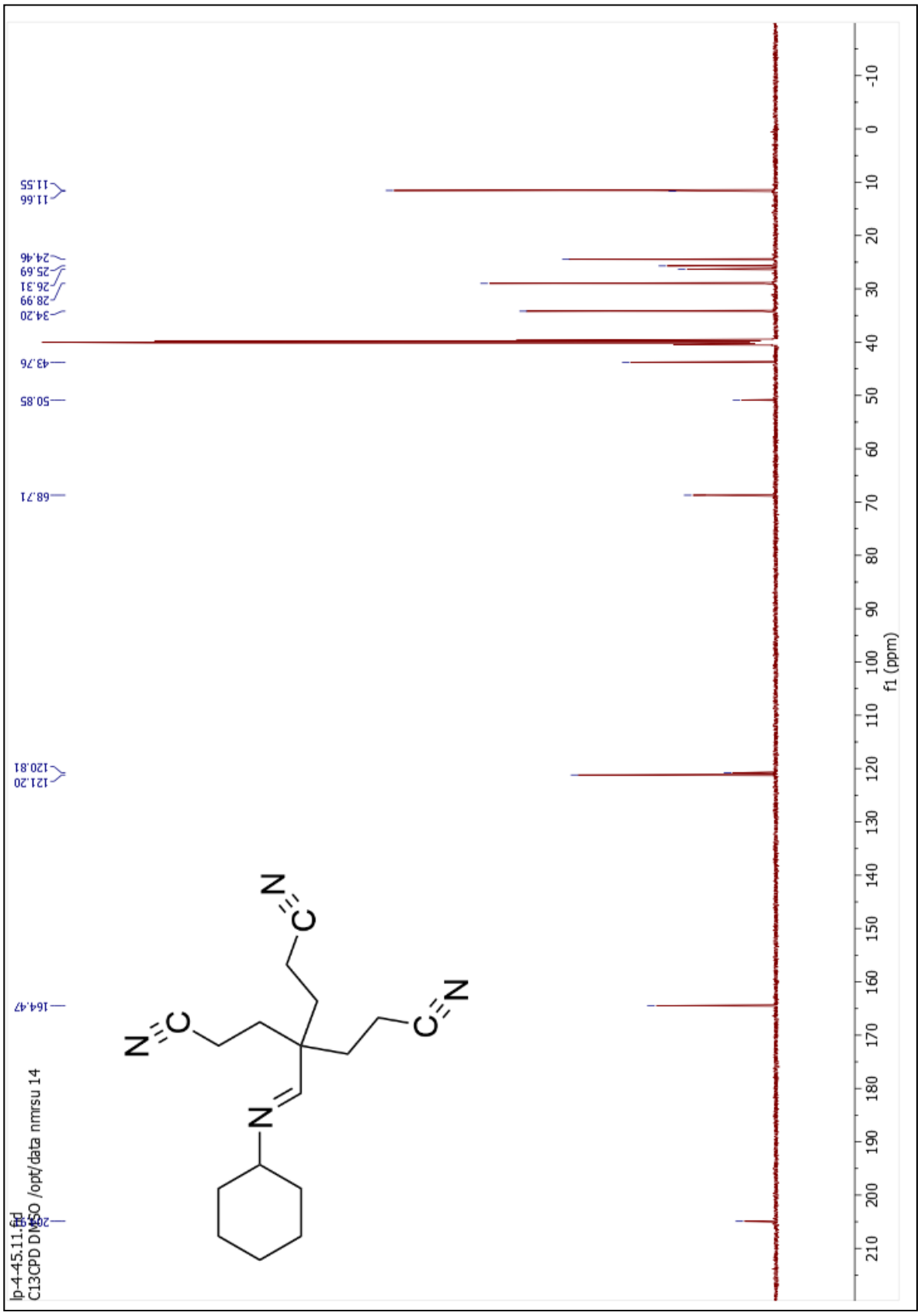

^{13}C NMR Compound **19**

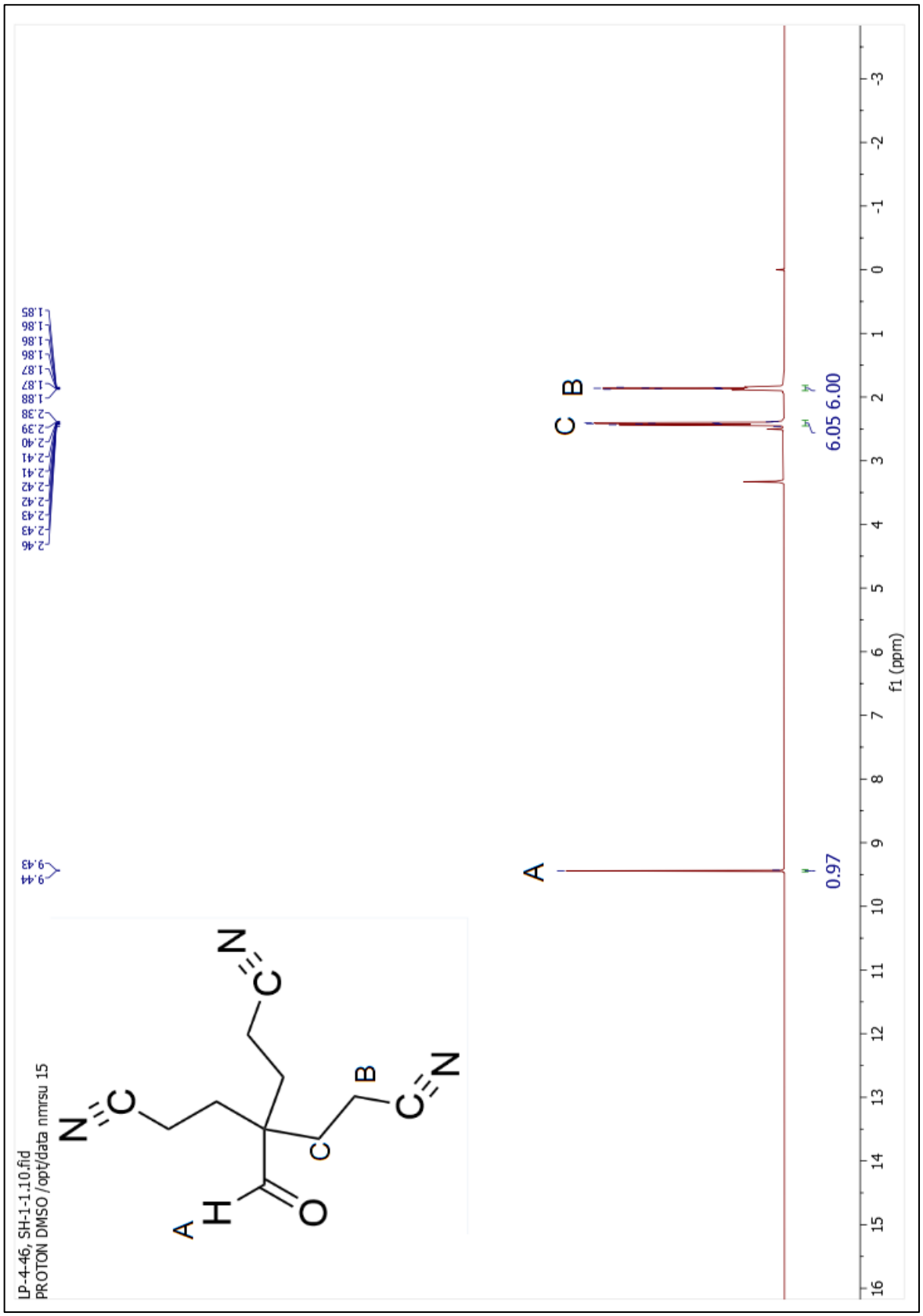

^{1}H NMR Compound **20**

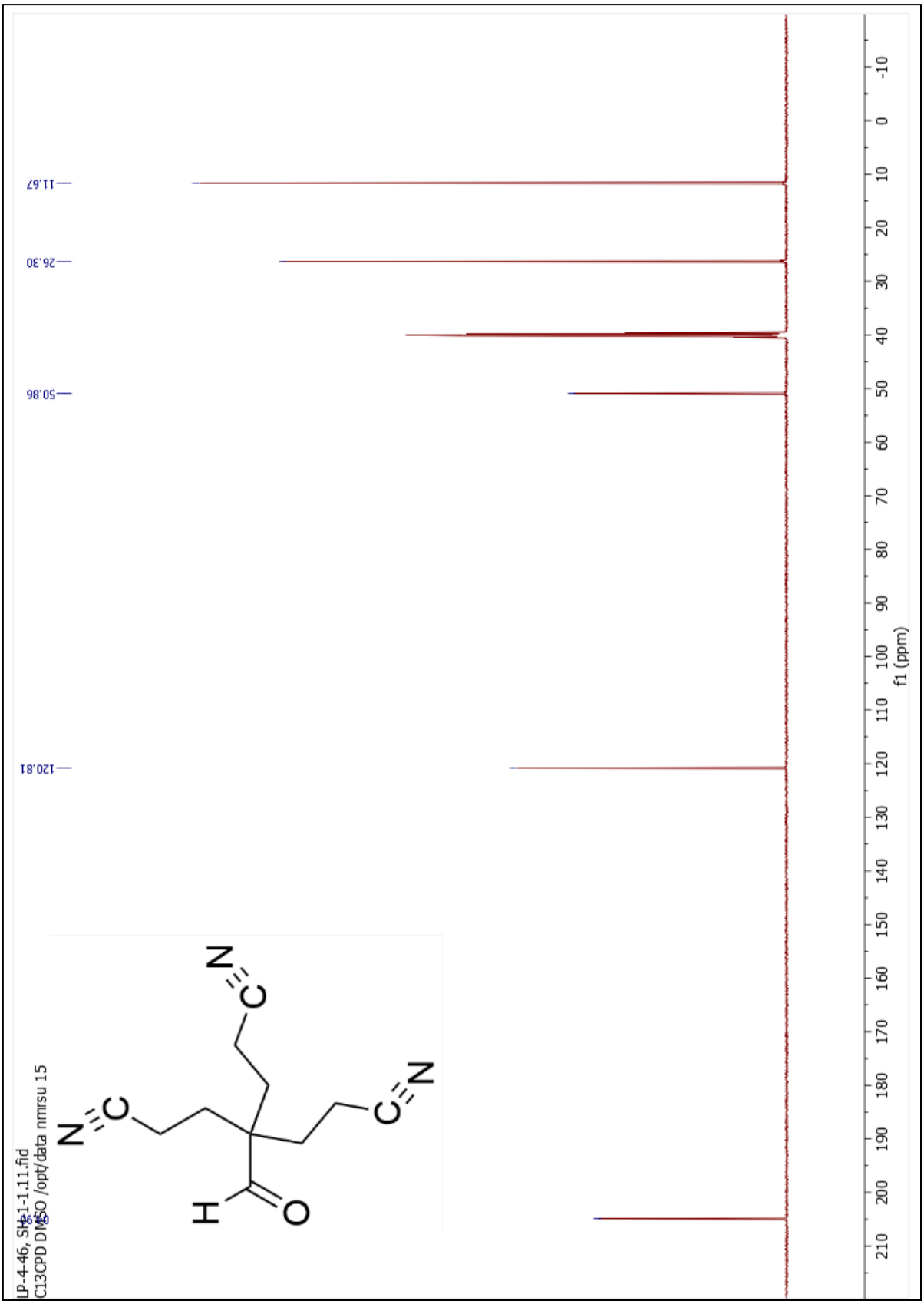

^{13}C NMR Compound **20**

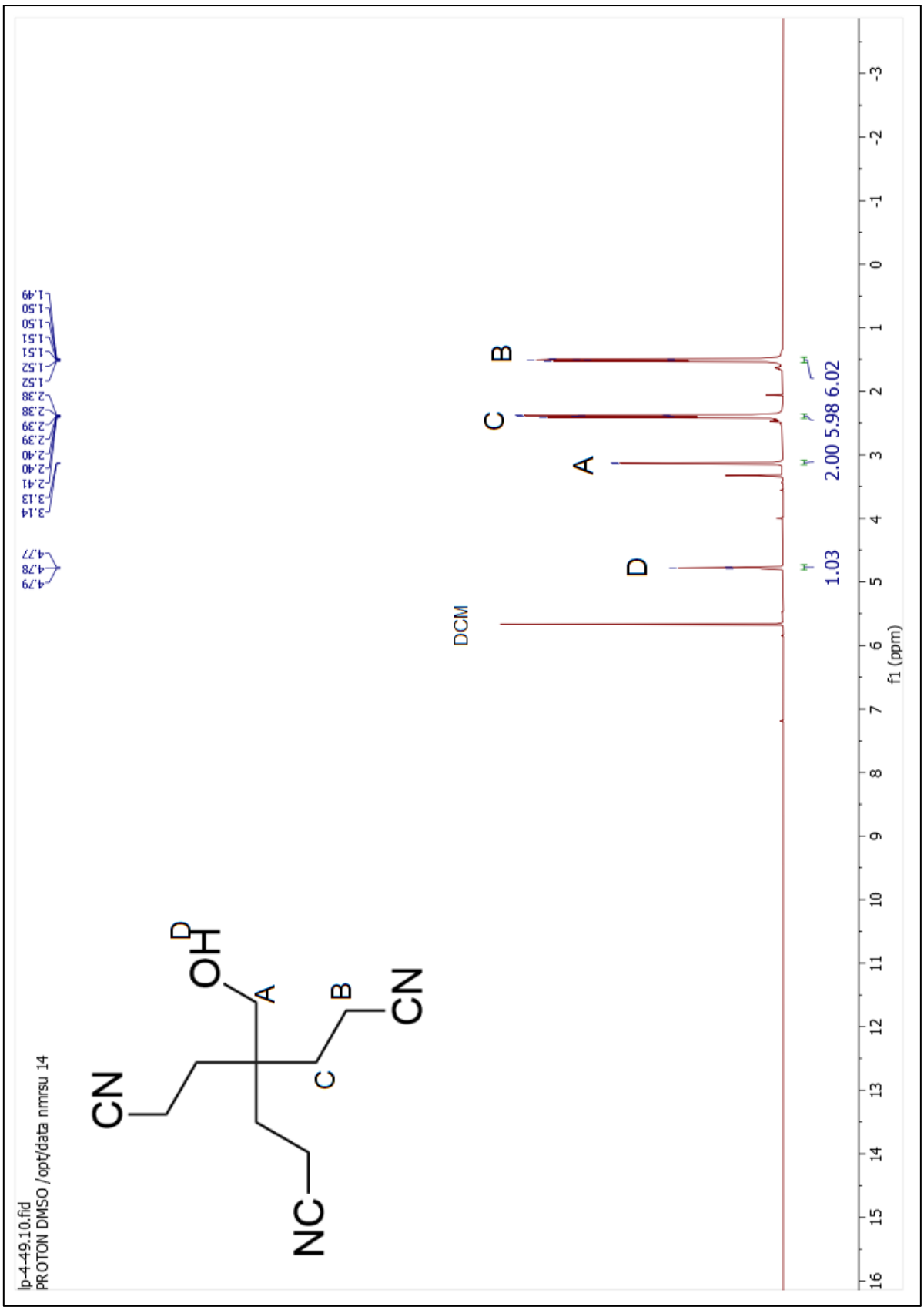

^{1}H NMR Compound **21**

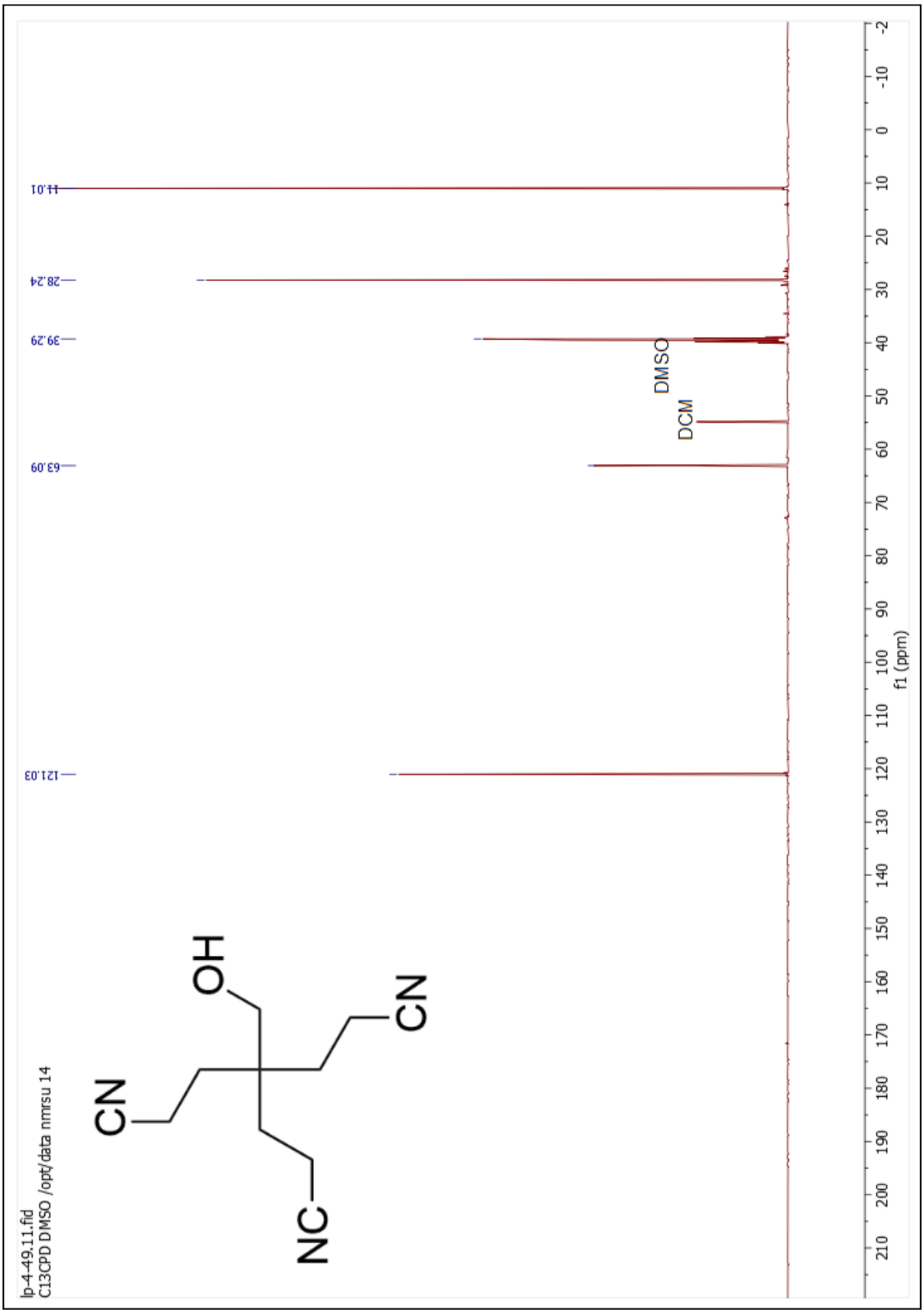

^{13}C NMR Compound **21**

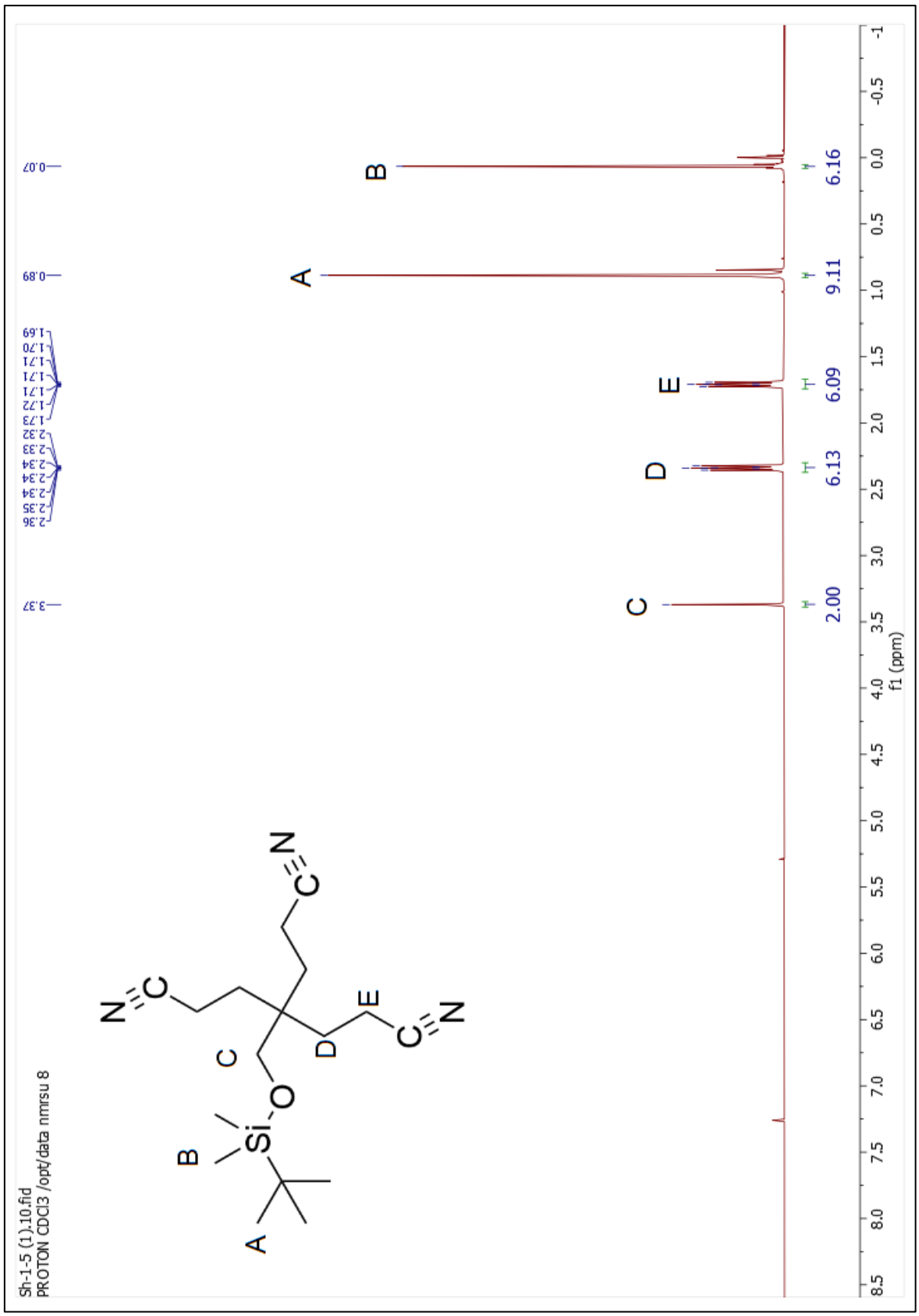

^{1}H NMR Compound **22**

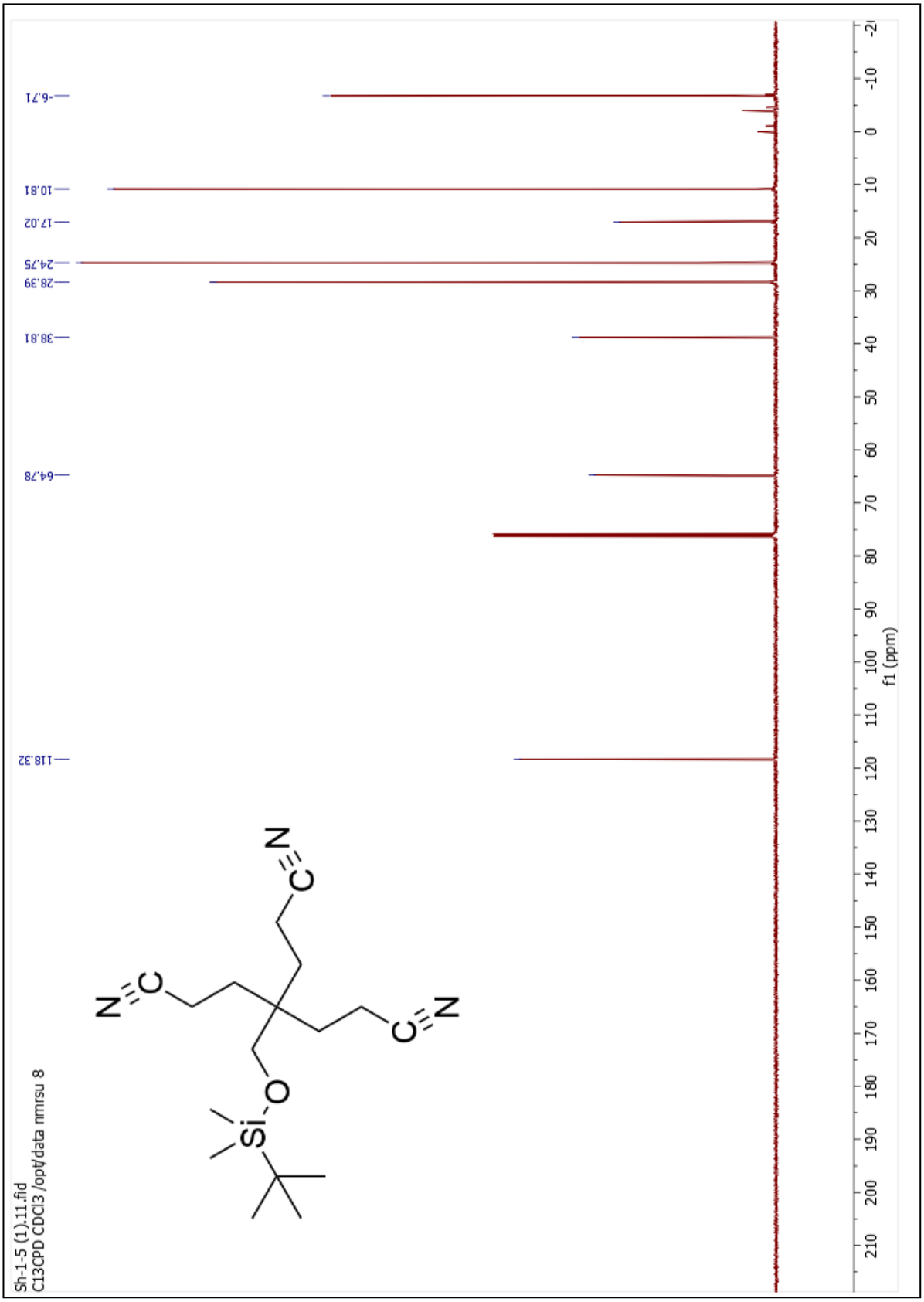

^{13}C NMR Compound **22**

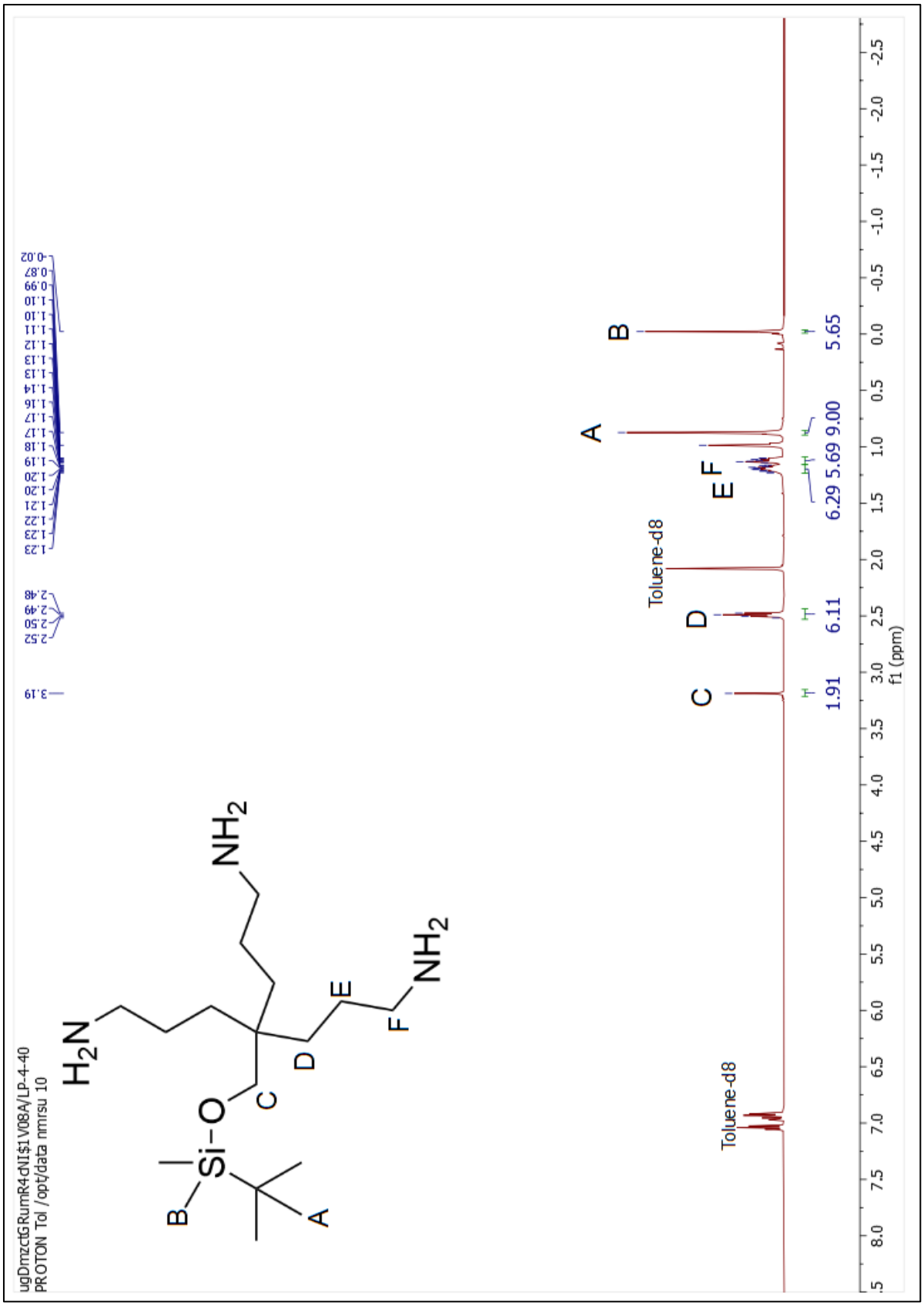

^{1}H NMR Compound **23**

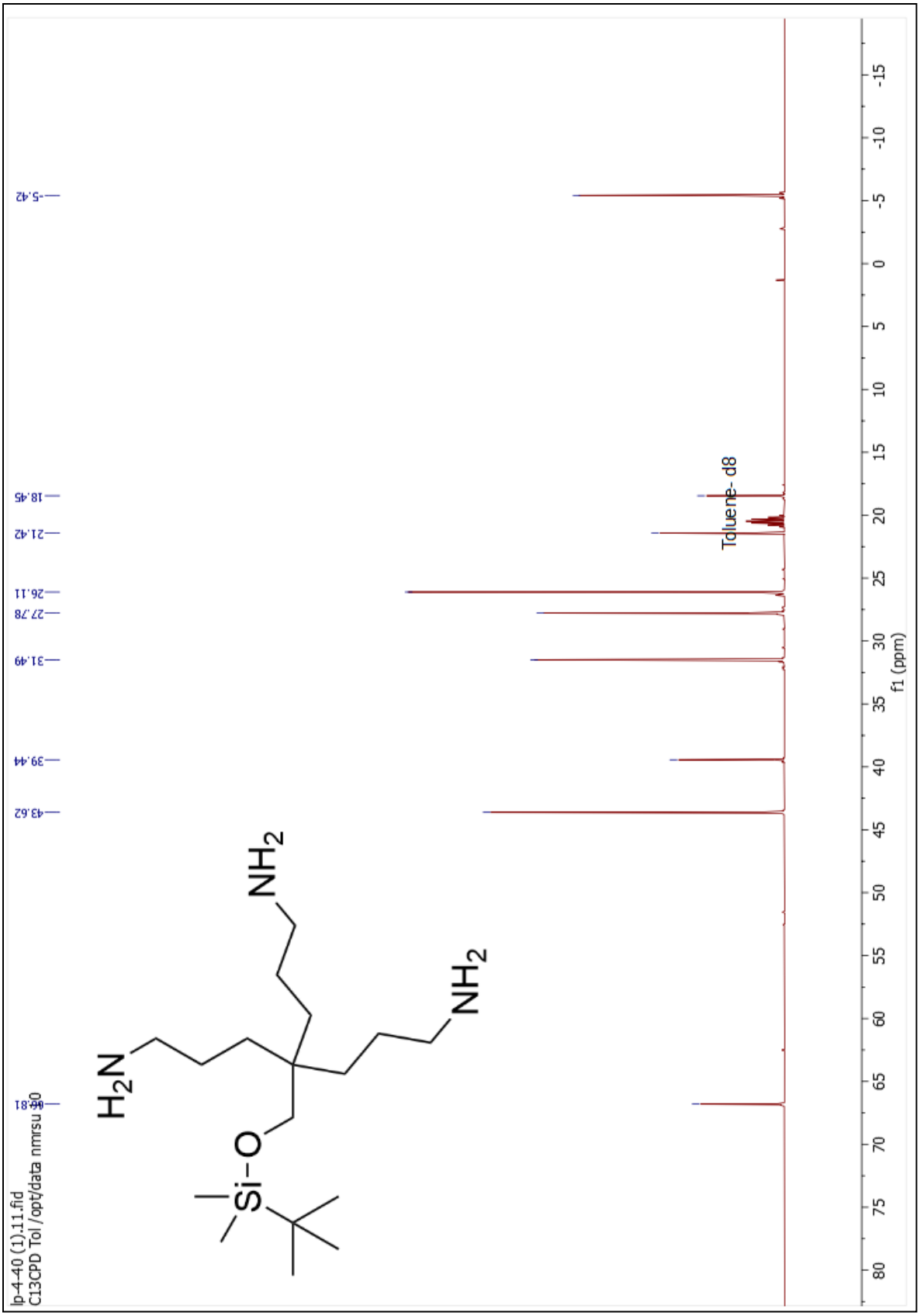

^{13}C NMR Compound **23**

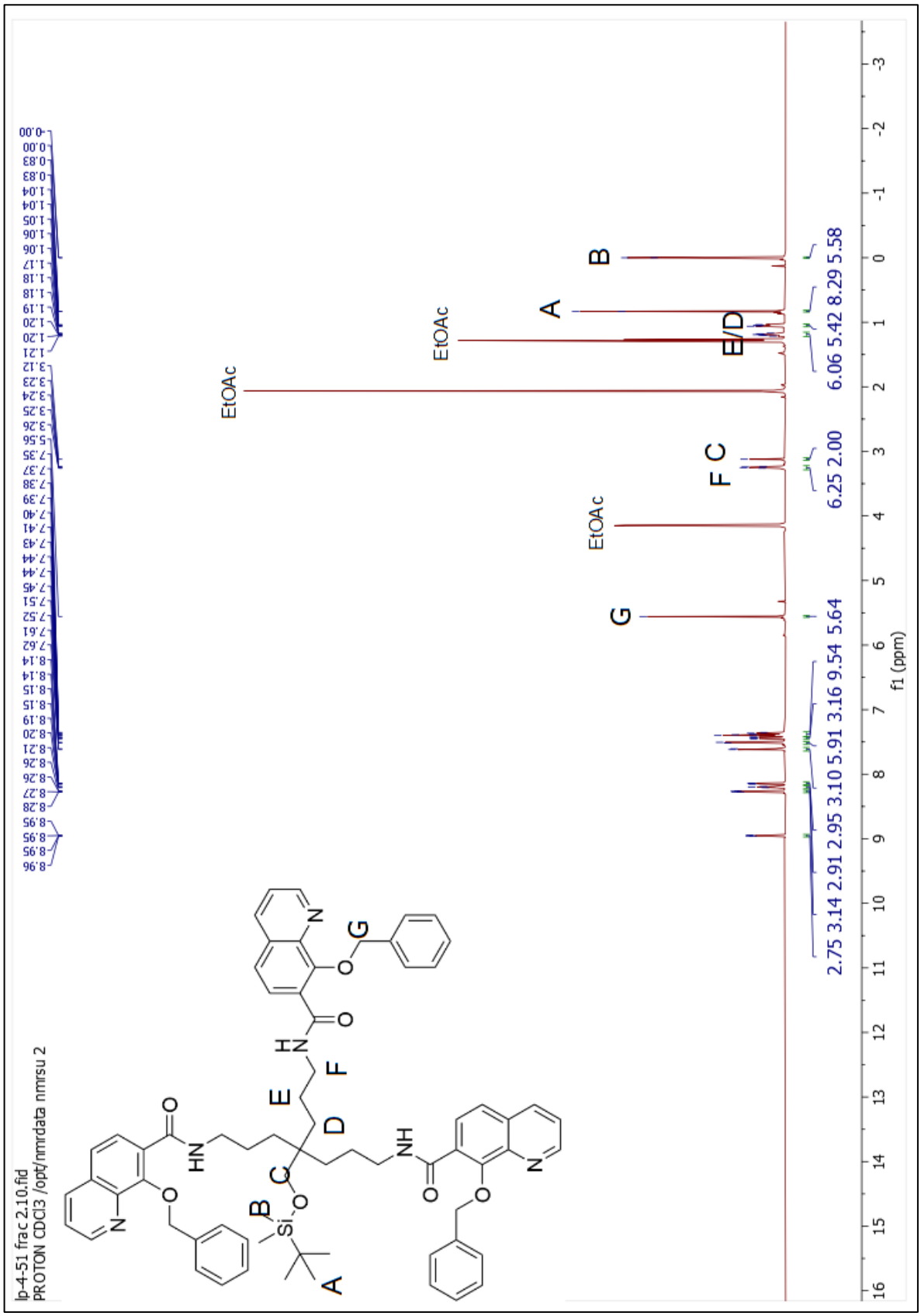

^{1}H NMR Compound **24**

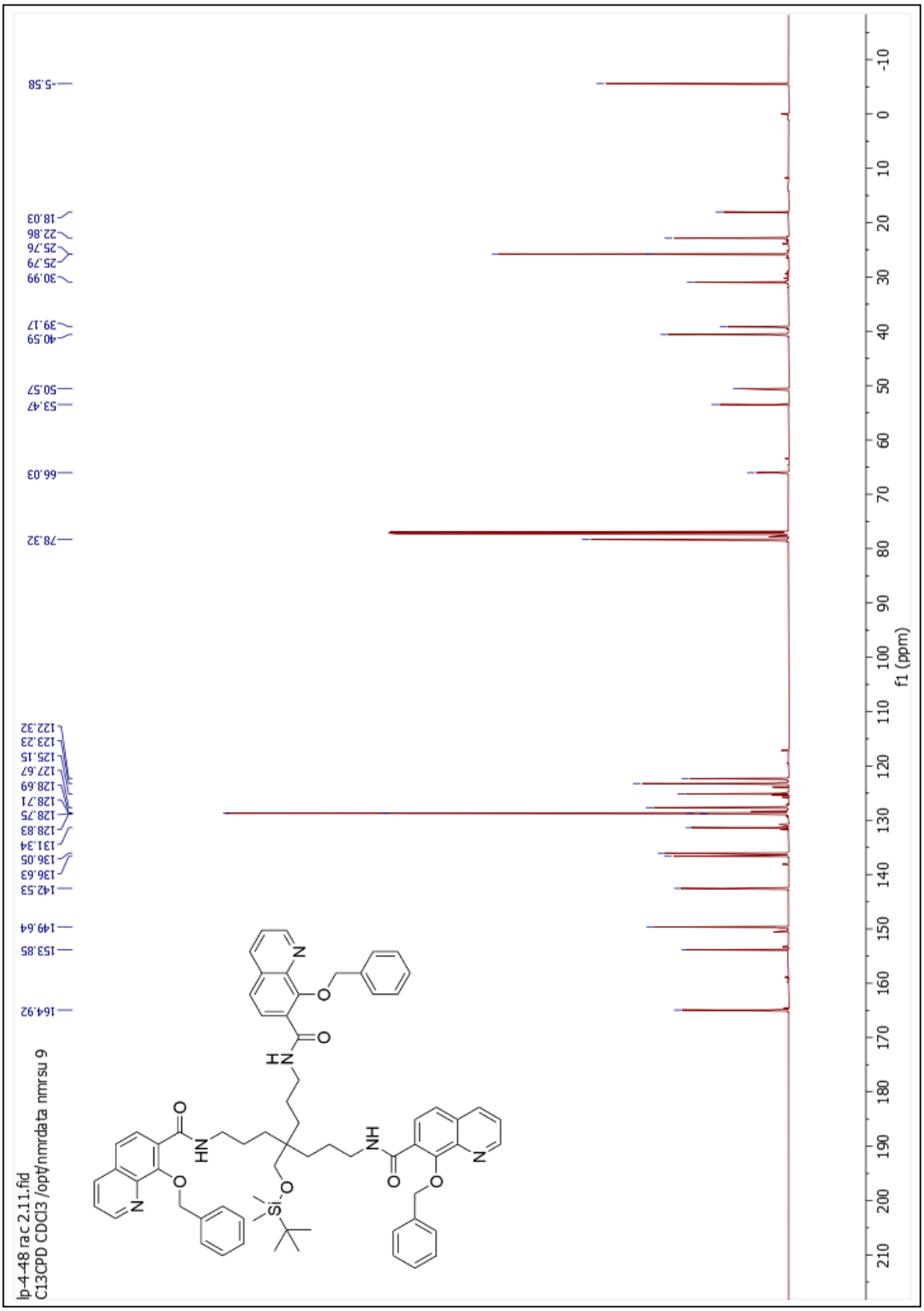

^{13}C NMR Compound **24**

I

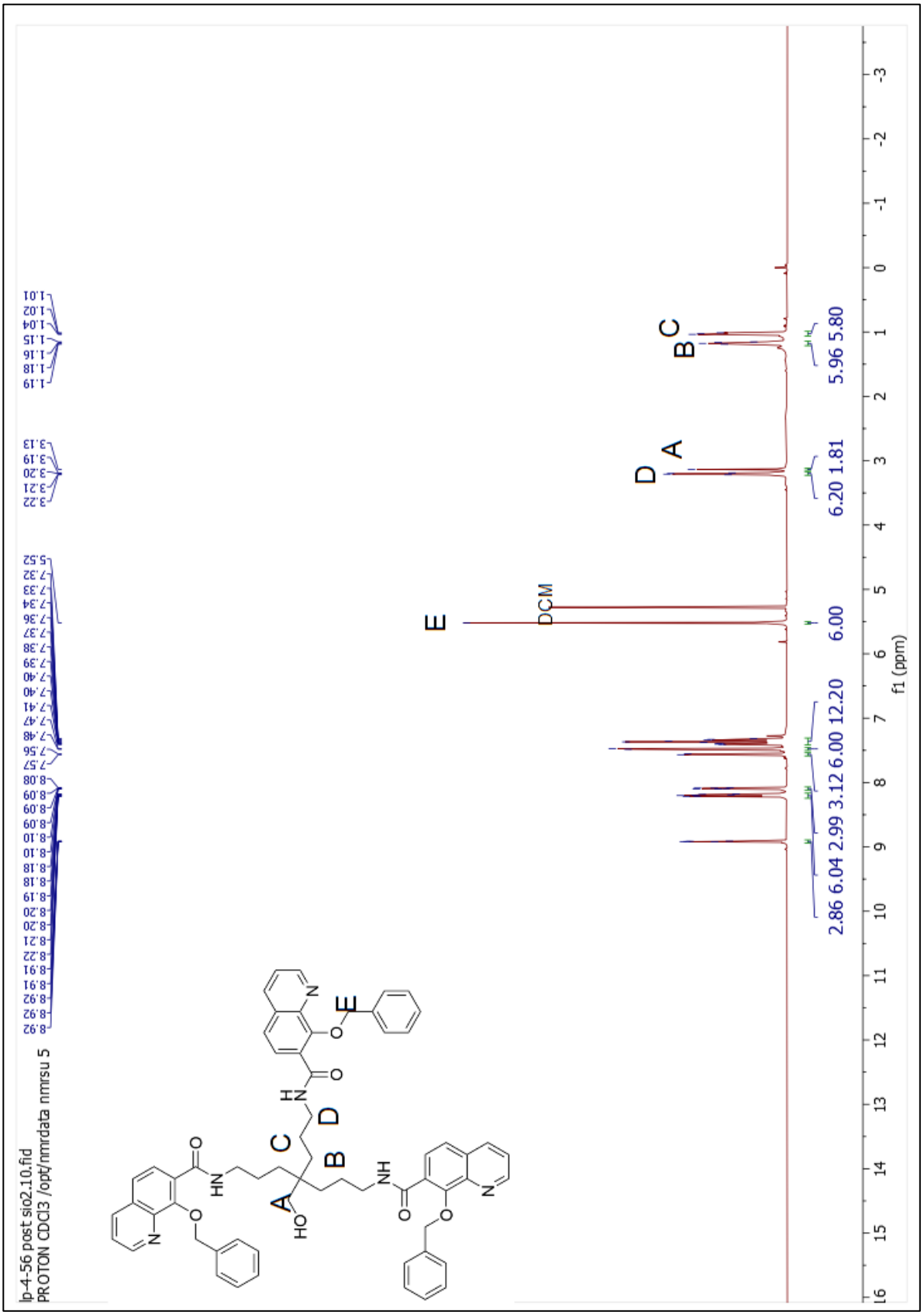

^{1}H NMR Compound **25**

li

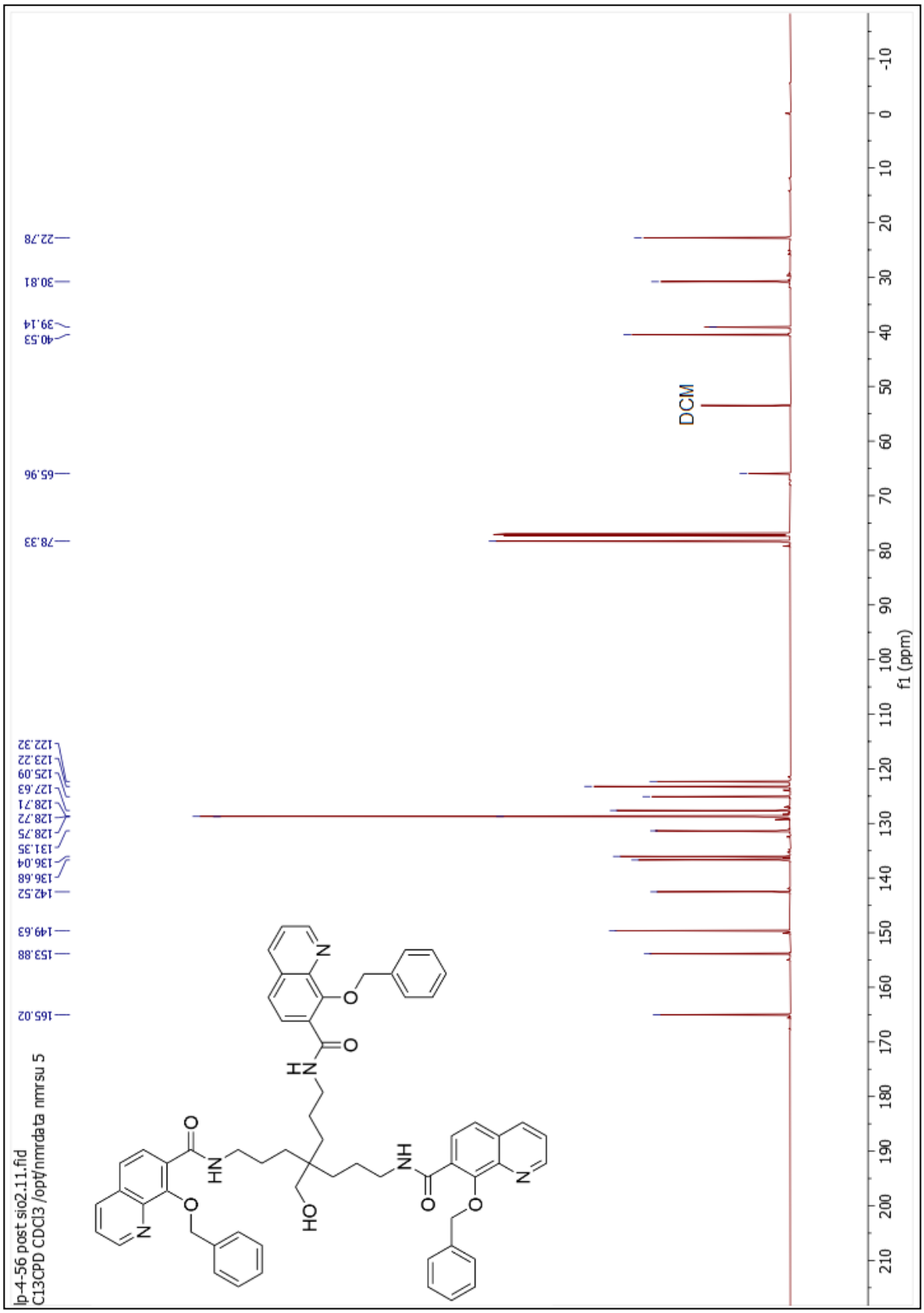

^{13}C NMR Compound **25**

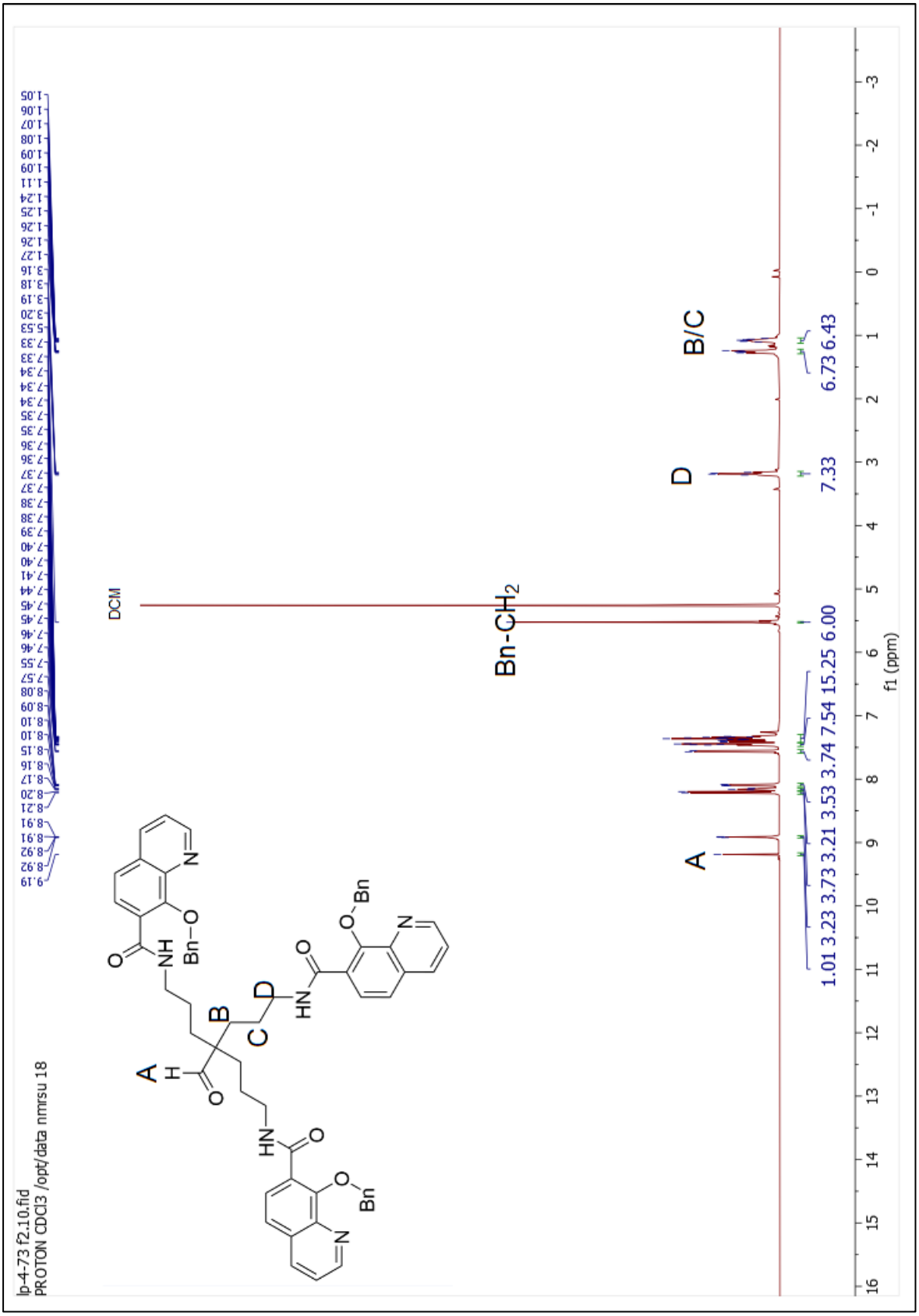

^{1}H NMR Compound **26**

liii

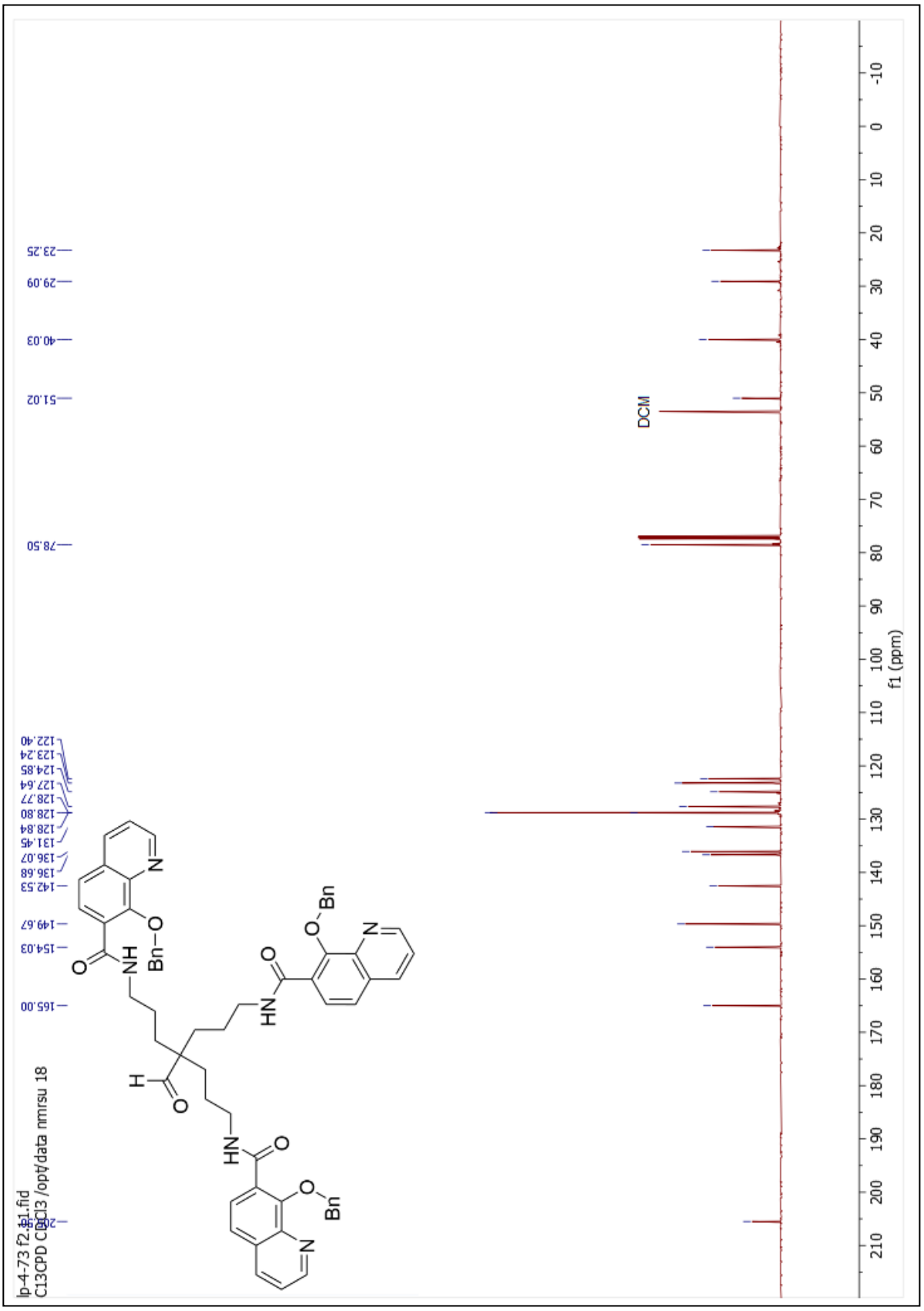

^{13}C NMR Compound **26**

liv

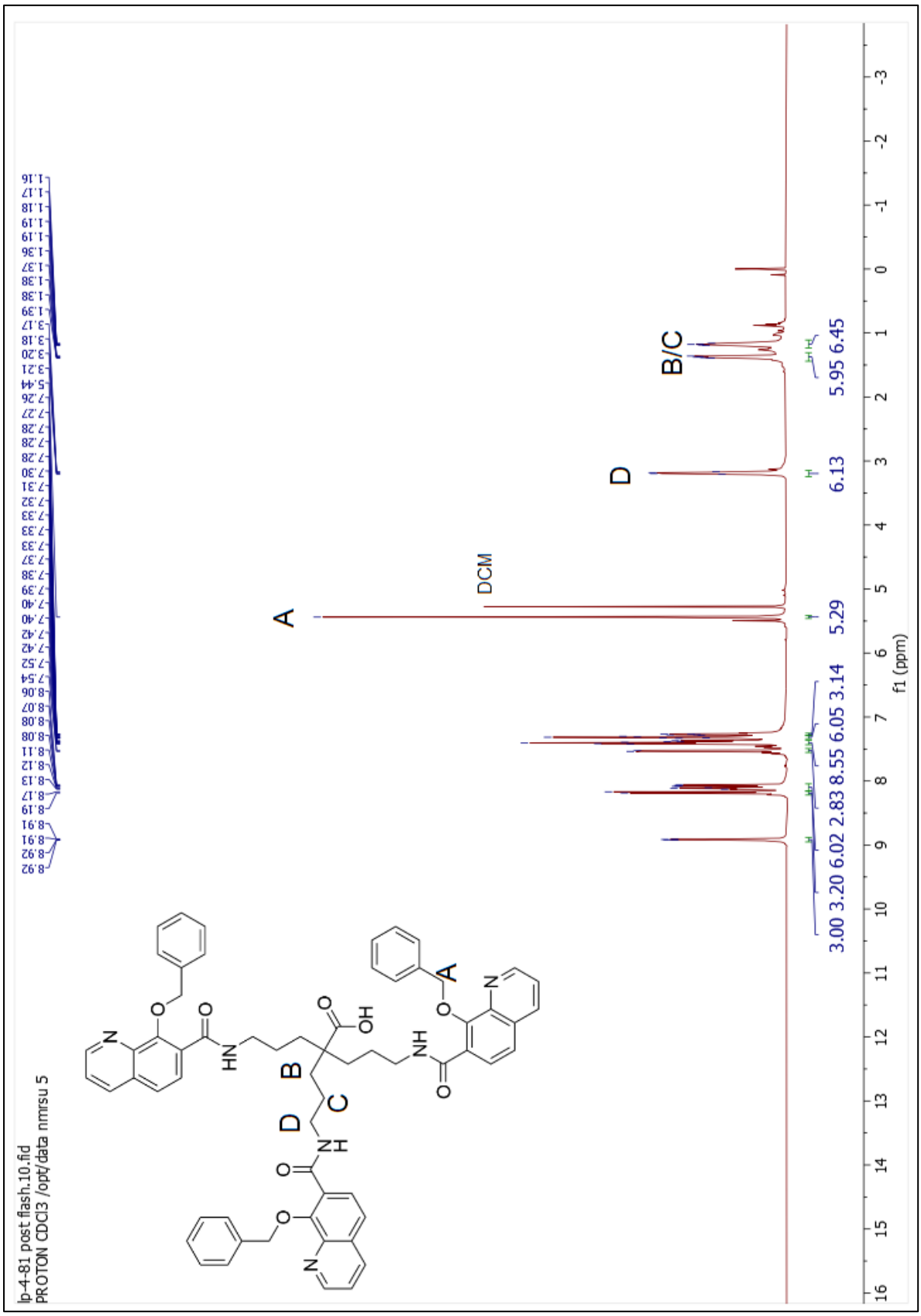

^{1}H NMR Compound **27**

lv

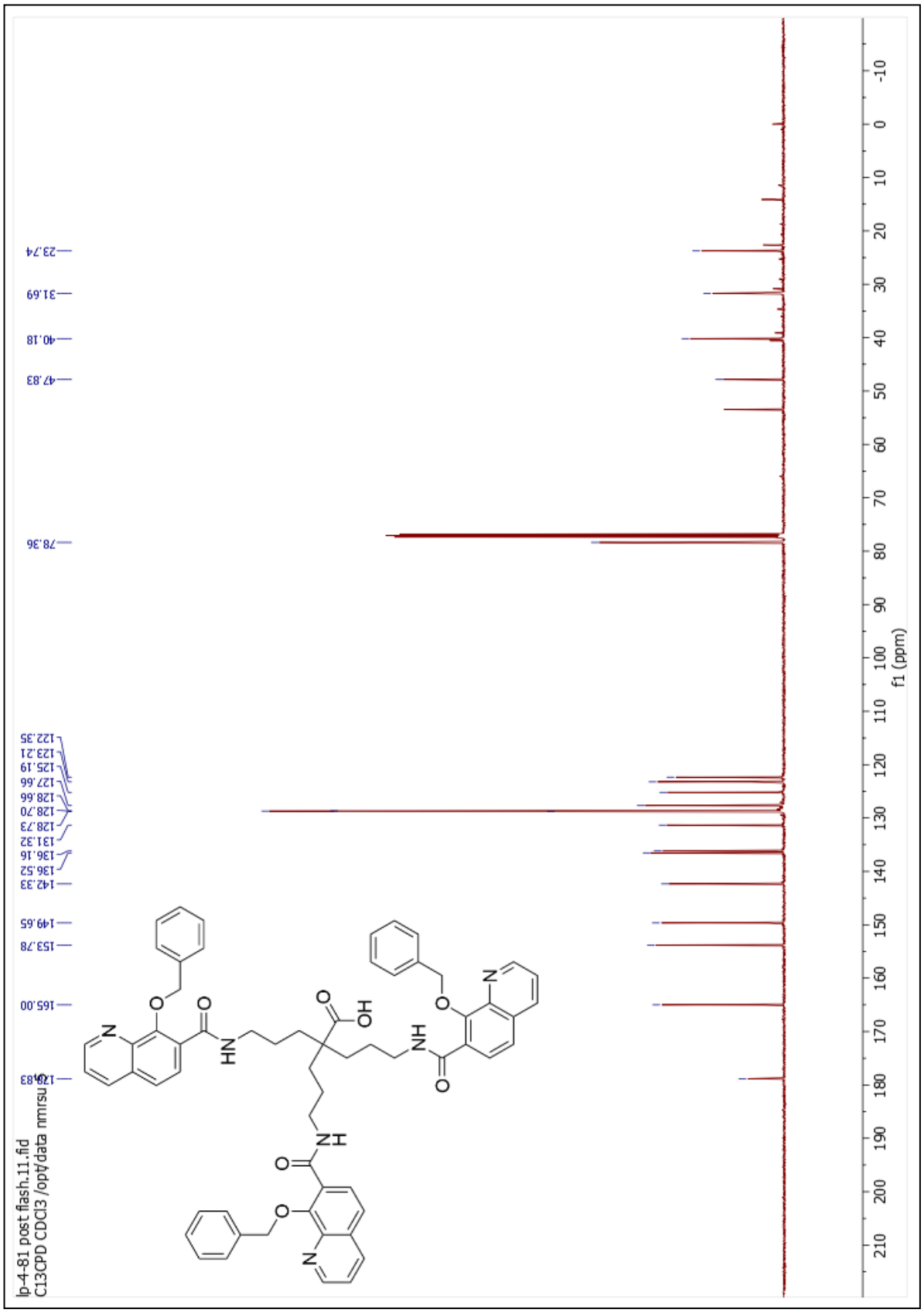

^{13}C NMR Compound **27**

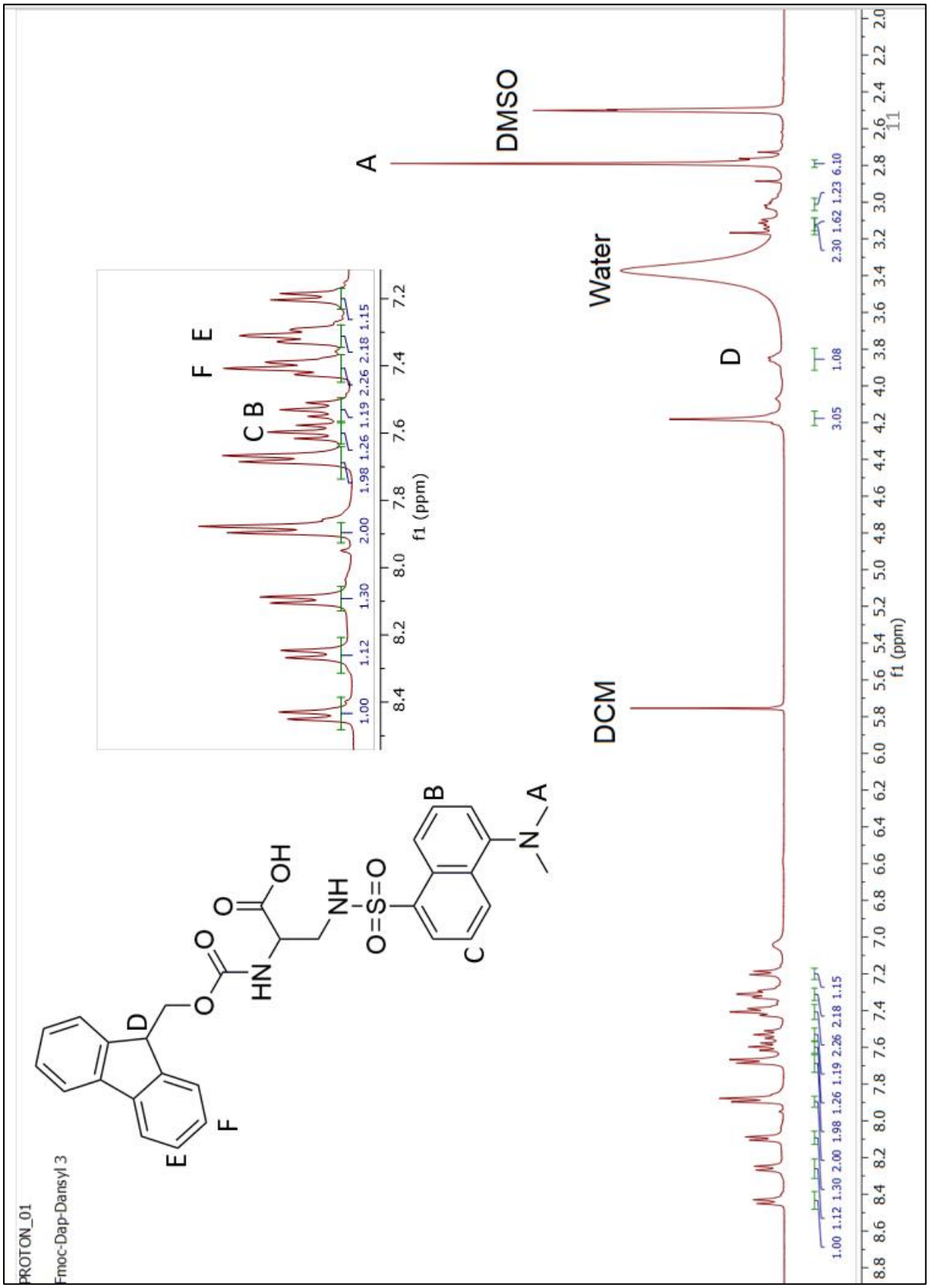

^{1}H NMR Compound **28**

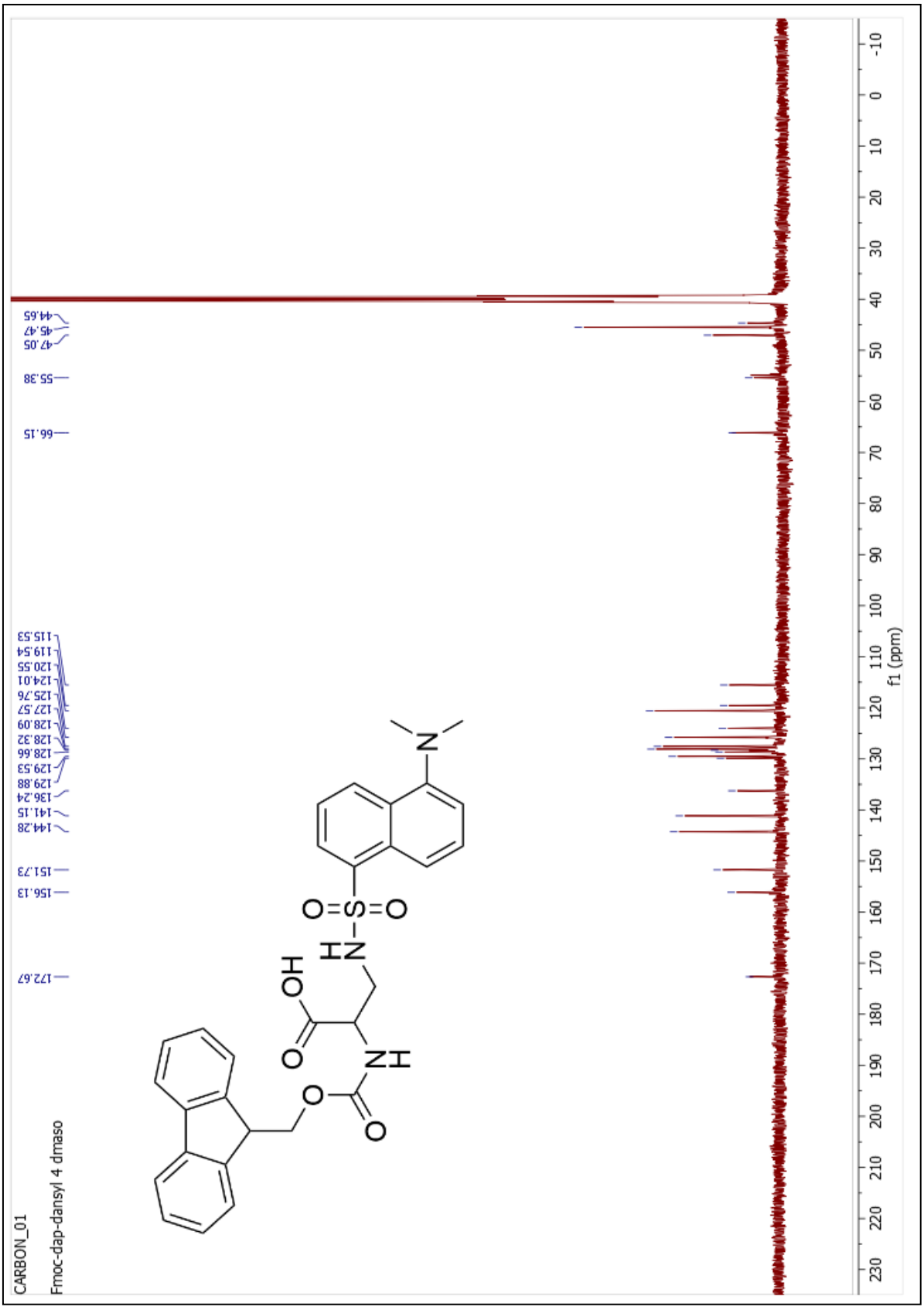

^{13}C NMR Compound **28**

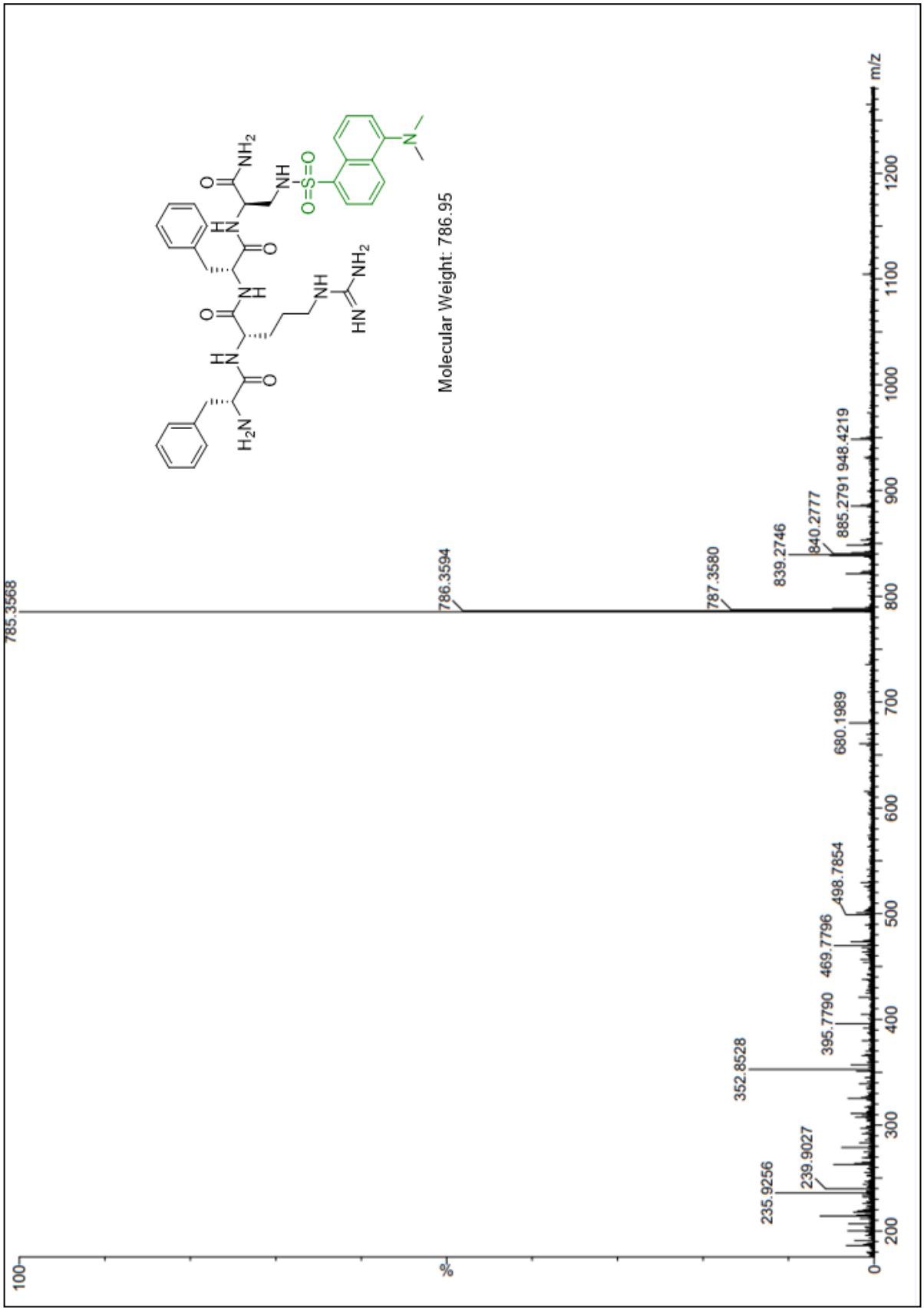
Molecular Weight: 786.95
m/z
%
100
0
200
300
400
500
600
700
800
900
1000
1100
1200
785.3568
786.3594
787.3580
839.2746
840.2777
885.2791
948.4219
680.1989
498.7854
469.7796
395.7790
352.8528
239.9027
235.9256

ESI HRMS **P-1**

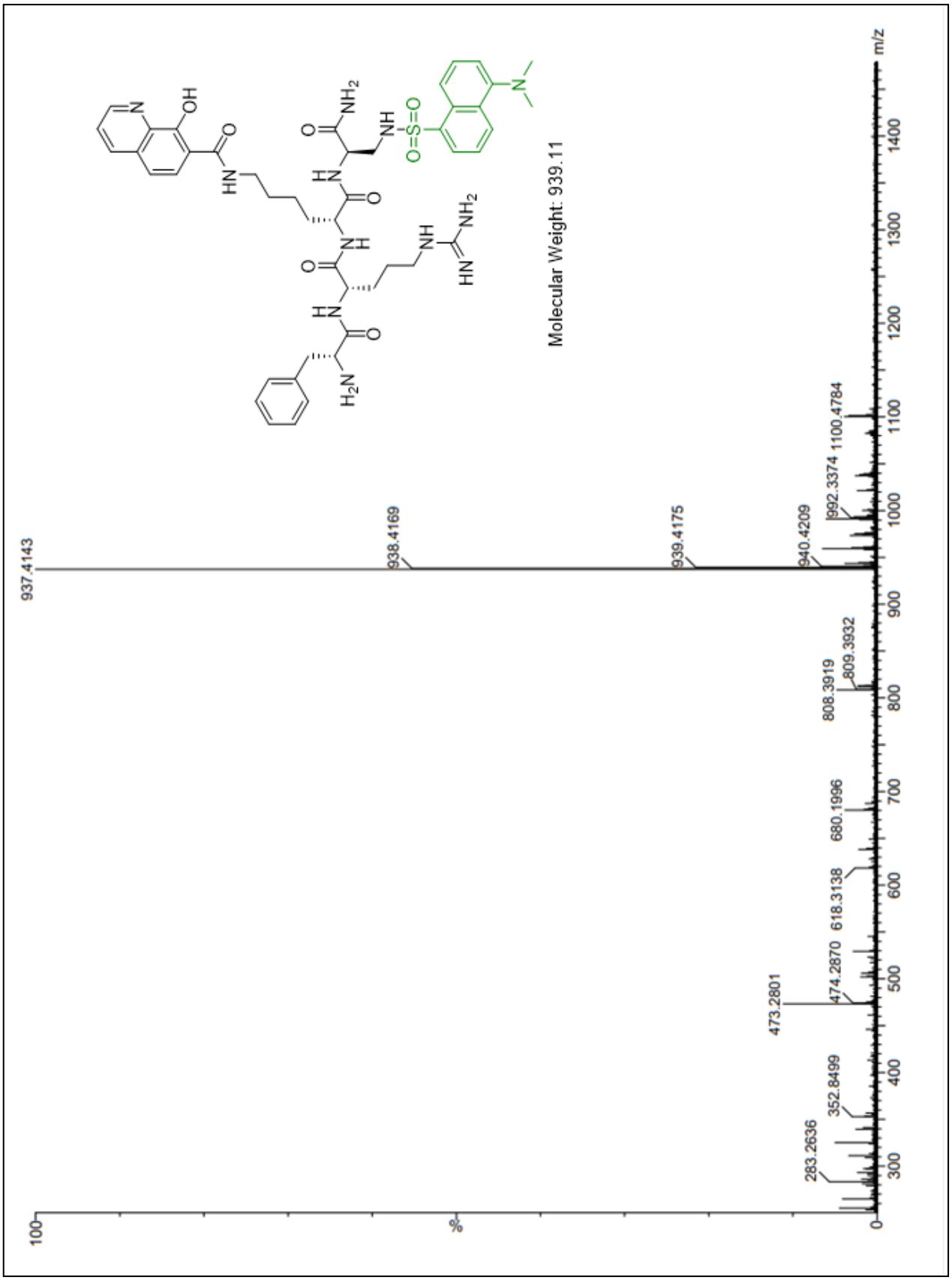
Molecular Weight: 939.11
m/z
%
100
0
937.4143
938.4169
939.4175
940.4209
992.3374
1100.4784
808.3919
809.3932
680.1996
618.3138
474.2870
473.2801
352.8499
283.2636

ESI HRMS **P-2**

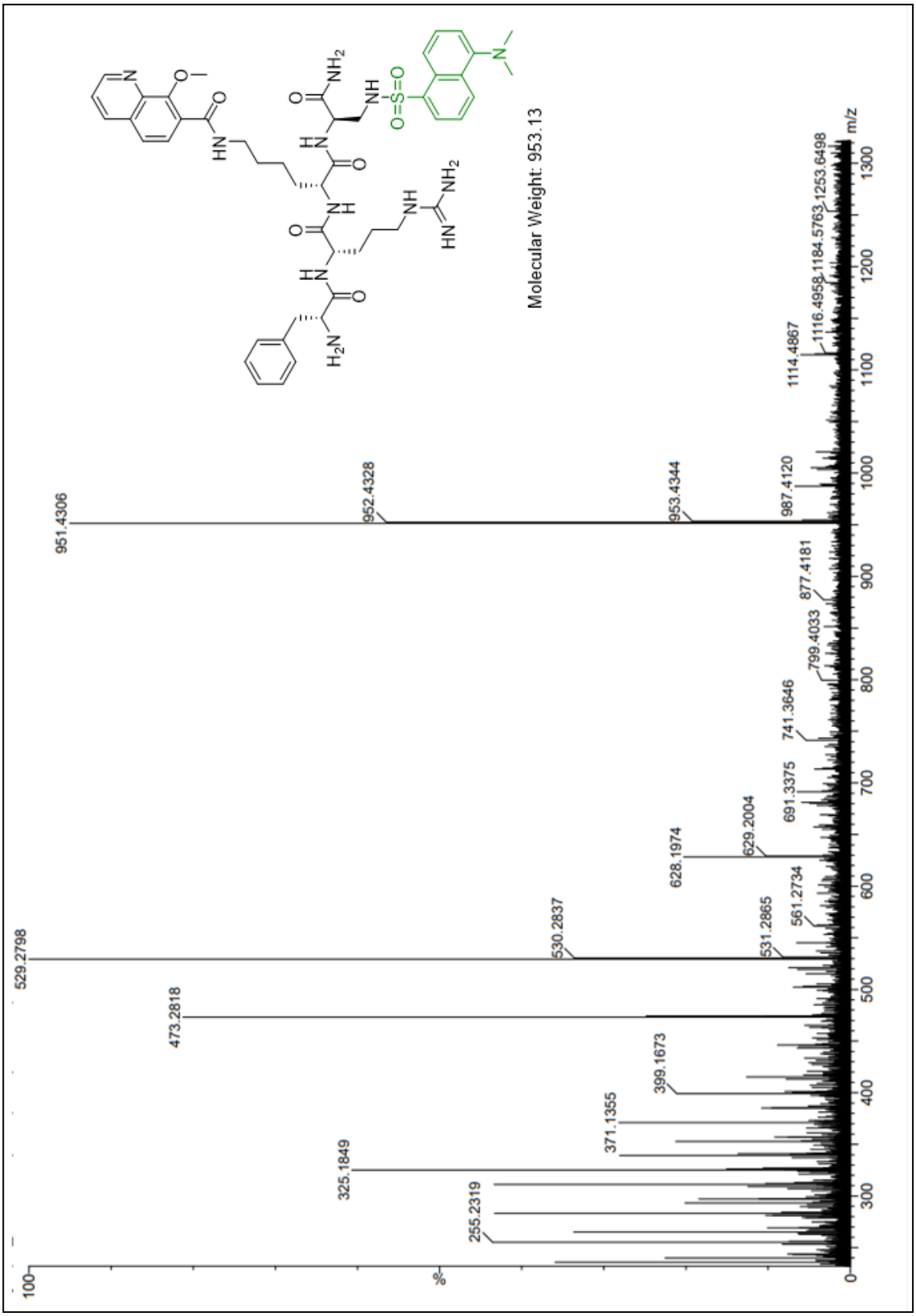
Molecular Weight: 953.13
m/z
%
100
0
300
400
500
600
700
800
900
1000
1100
1200
1300
529.2798
473.2818
325.1849
255.2319
371.1355
399.1673
628.1974
629.2004
691.3375
741.3646
799.4033
877.4181
951.4306
952.4328
953.4344
987.4120
1114.4867
1116.4958
1184.5763
1253.6498

ESI HRMS **P-3**

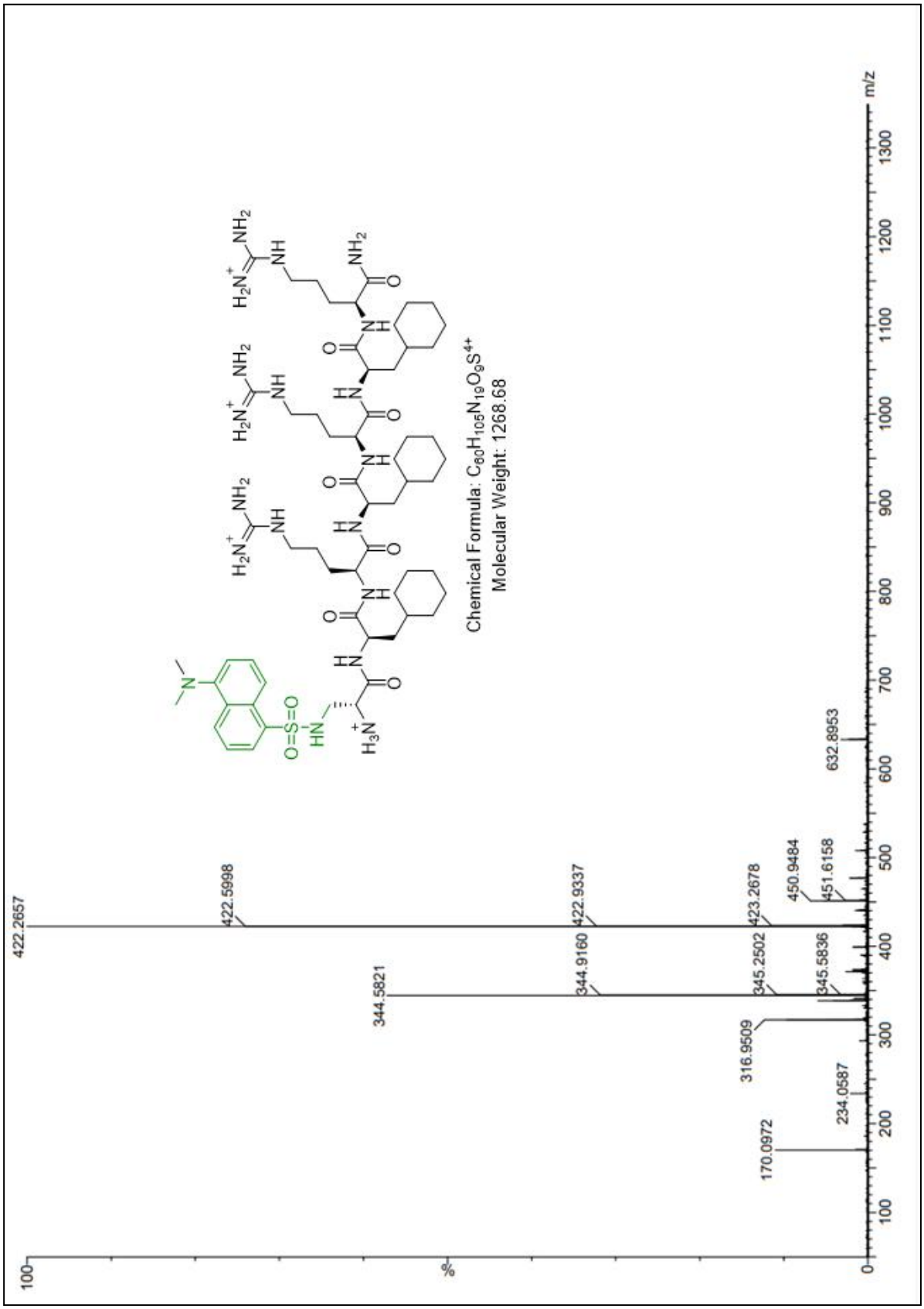
Chemical Formula: $C_{60}H_{105}N_{19}O_9S^{4+}$
Molecular Weight: 1268.68
422.2657
422.5998
422.9337
423.2678
450.9484
451.6158
632.8953
344.5821
344.9160
345.2502
345.5836
316.9509
234.0587
170.0972
100
%
0
m/z

ESI HRMS **P-4**

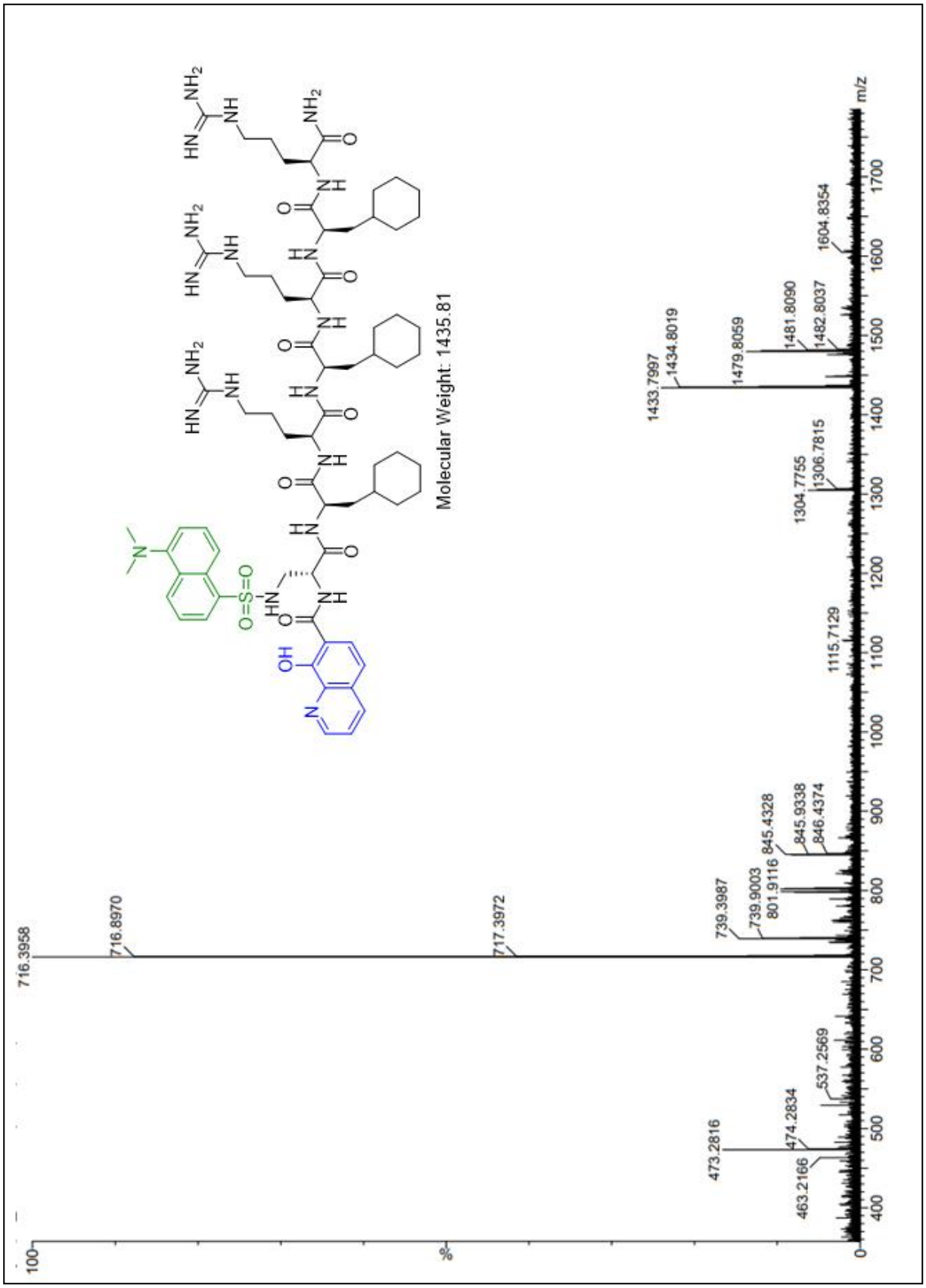
Molecular Weight: 1435.81
100
%
0
m/z
400
500
600
700
800
900
1000
1100
1200
1300
1400
1500
1600
1700
716.3958
716.8970
717.3972
739.3987
739.9003
801.9116
845.4328
845.9338
846.4374
1115.7129
1304.7755
1306.7815
1433.7997
1434.8019
1479.8059
1481.8090
1482.8037
1604.8354
473.2816
474.2834
463.2166
537.2569

ESI HRMS **P-5**

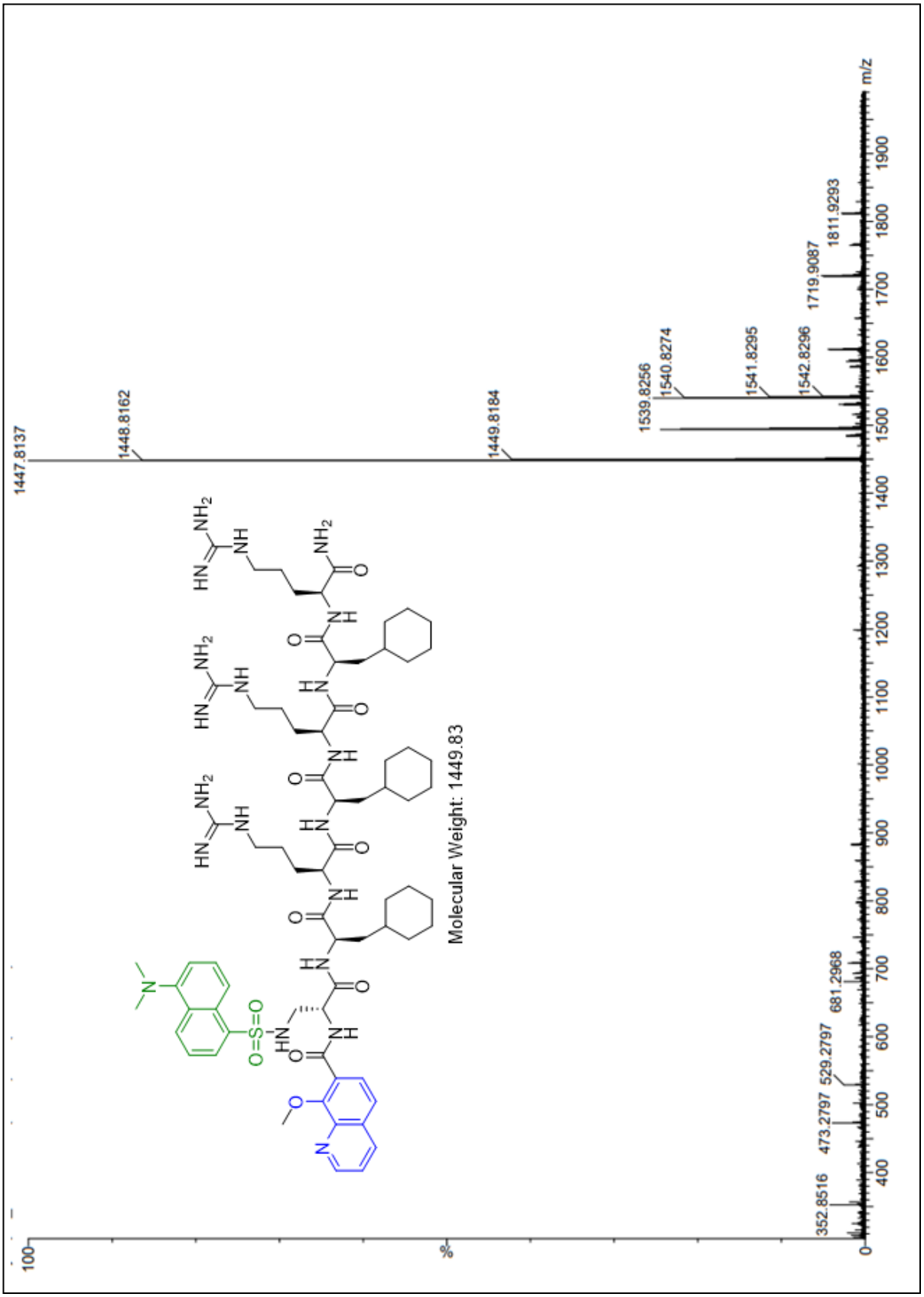
1447.8137
1448.8162
1449.8184
1539.8256
1540.8274
1541.8295
1542.8296
1719.9087
1811.9293
352.8516
473.2797
529.2797
681.2968
Molecular Weight: 1449.83
100
%
0
m/z
400
500
600
700
800
900
1000
1100
1200
1300
1400
1500
1600
1700
1800
1900

ESI HRMS **P-6**

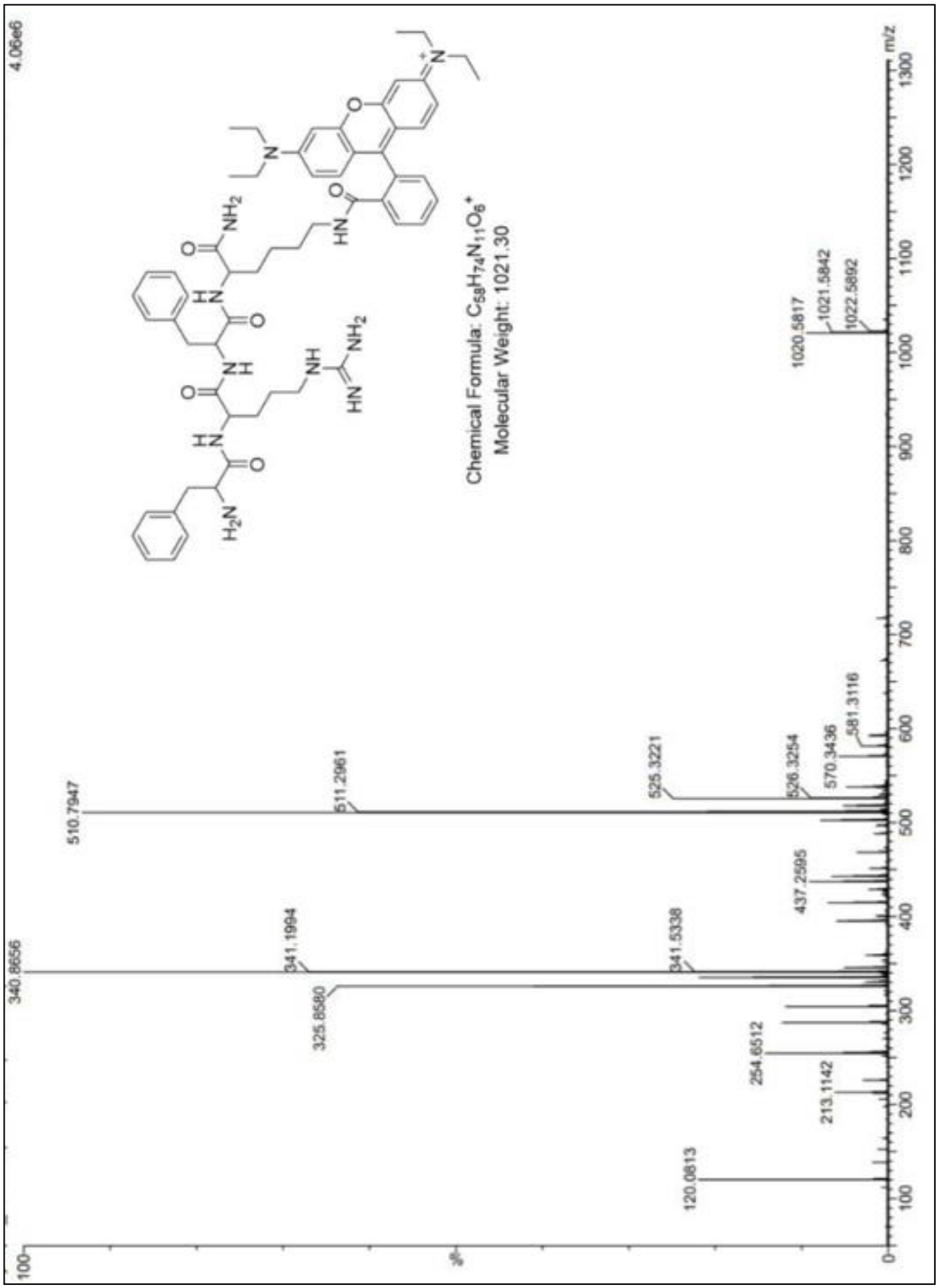
4.06e6
Chemical Formula: $C_{58}H_{74}N_{11}O_6^+$
Molecular Weight: 1021.30
m/z
%
100
0
120.0813
213.1142
254.6512
325.8580
340.8656
341.1994
341.5338
437.2595
510.7947
511.2961
525.3221
526.3254
570.3436
581.3116
1020.5817
1021.5842
1022.5892

ESI HRMS **P-7**

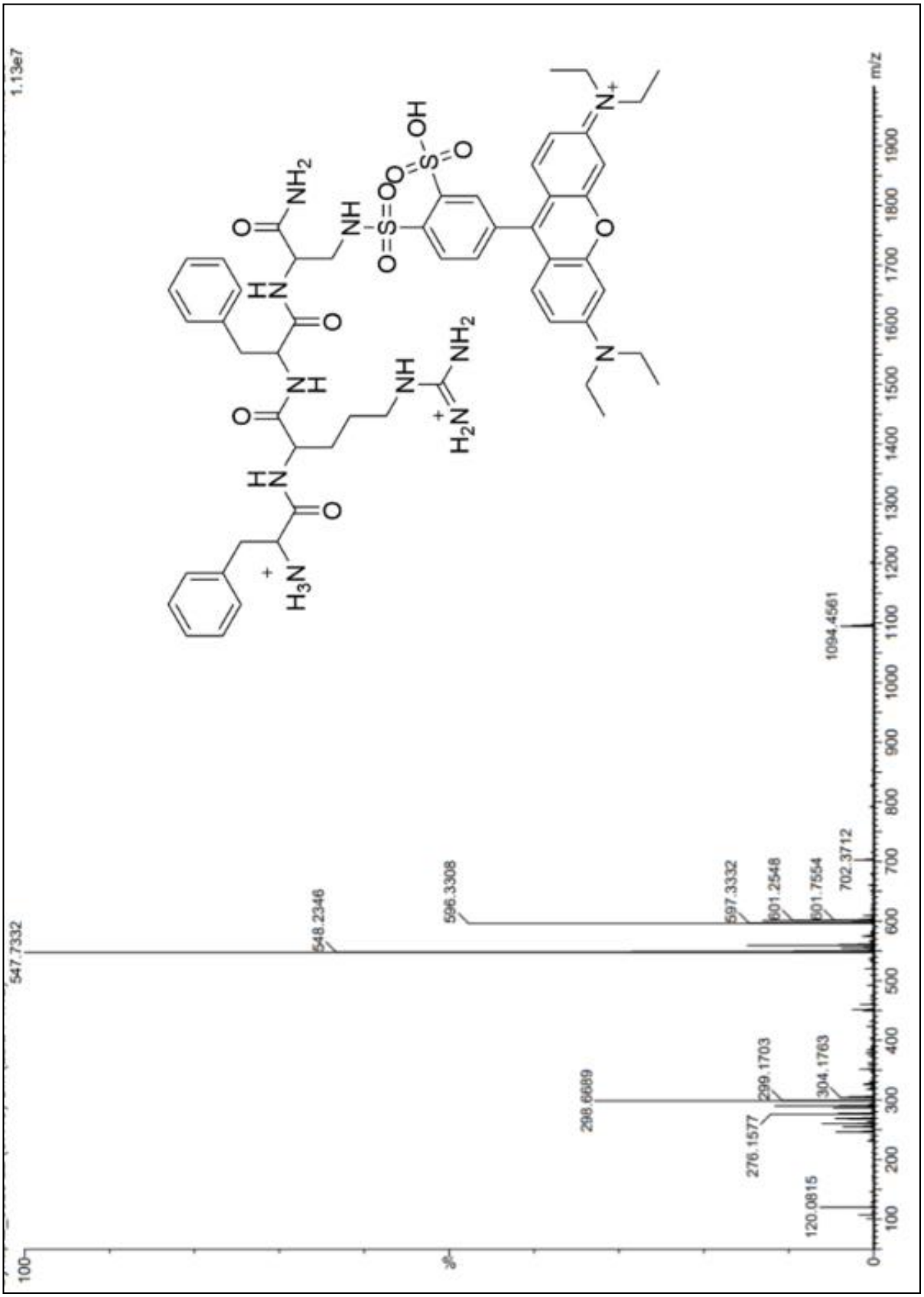
1.13e7
100
%
0
m/z
547.7332
548.2346
596.3308
597.3332
601.2548
601.7554
702.3712
1094.4561
298.6689
299.1703
304.1763
276.1577
120.0815
100
200
300
400
500
600
700
800
900
1000
1100
1200
1300
1400
1500
1600
1700
1800
1900

ESI HRMS **P-8**

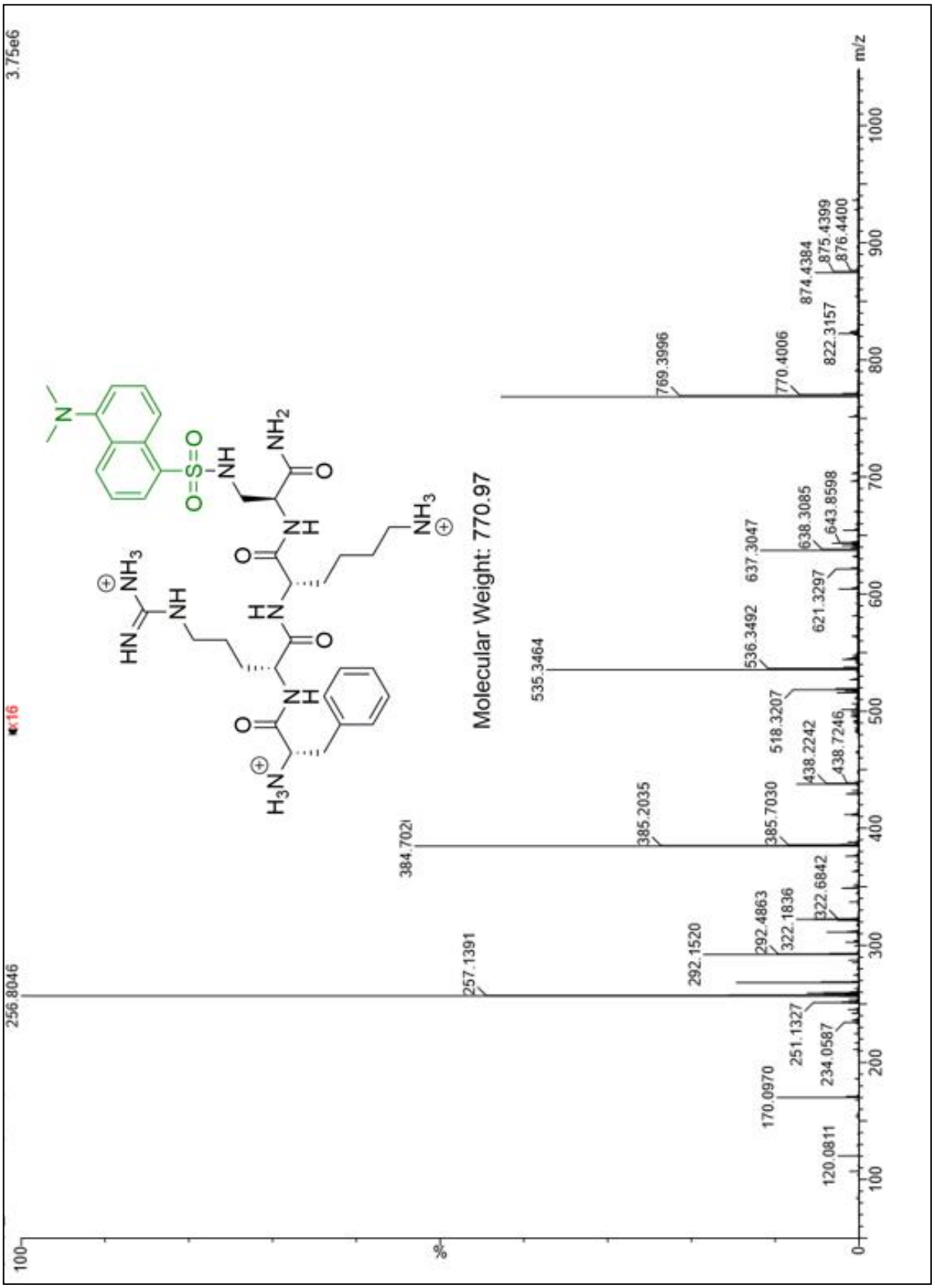
3.75e6
x16
100
%
0
m/z
Molecular Weight: 770.97
256.8046
257.1391
292.1520
292.4863
322.1836
322.6842
384.7021
385.2035
385.7030
438.2242
438.7246
518.3207
535.3464
536.3492
621.3297
637.3047
638.3085
643.8598
769.3996
770.4006
822.3157
874.4384
875.4399
876.4400
170.0970
251.1327
234.0587
120.0811
100
200
300
400
500
600
700
800
900
1000

ESI HRMS **P-10**

RP HPLC **P-1**

lxviii

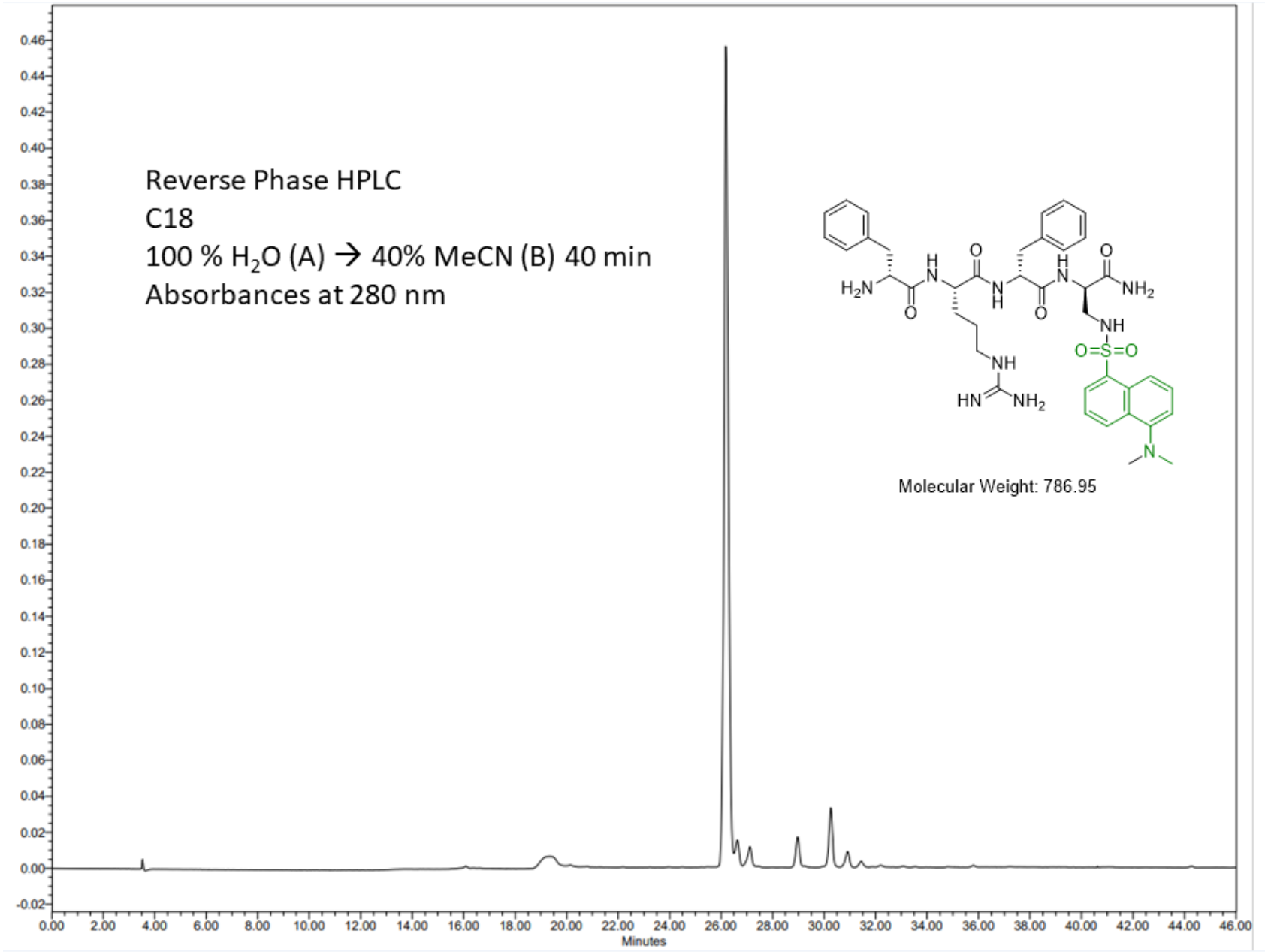

RP HPLC **P-2**

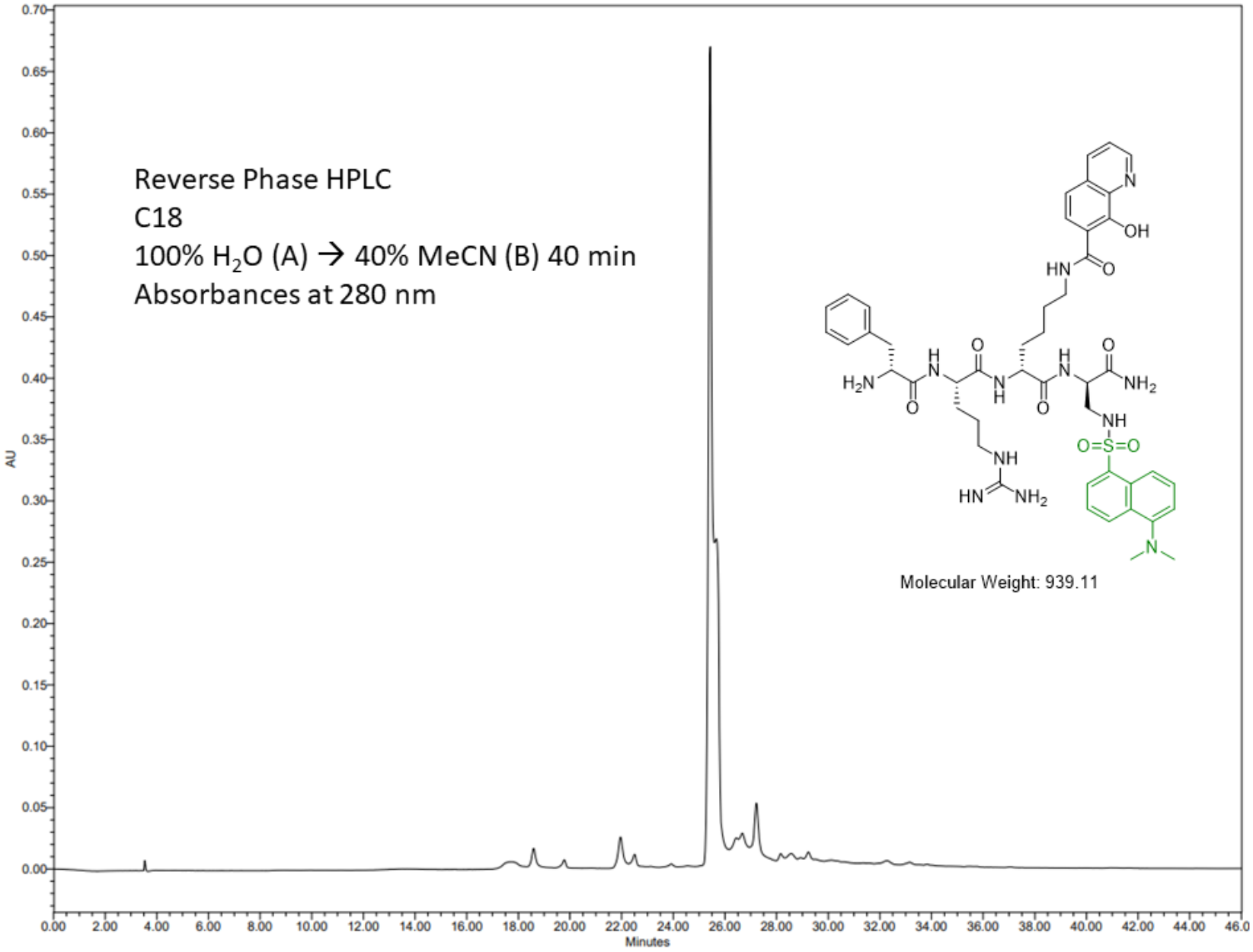
Reverse Phase HPLC
C18
100% H_2O (A) → 40% MeCN (B) 40 min
Absorbances at 280 nm
AU
Minutes
Molecular Weight: 939.11

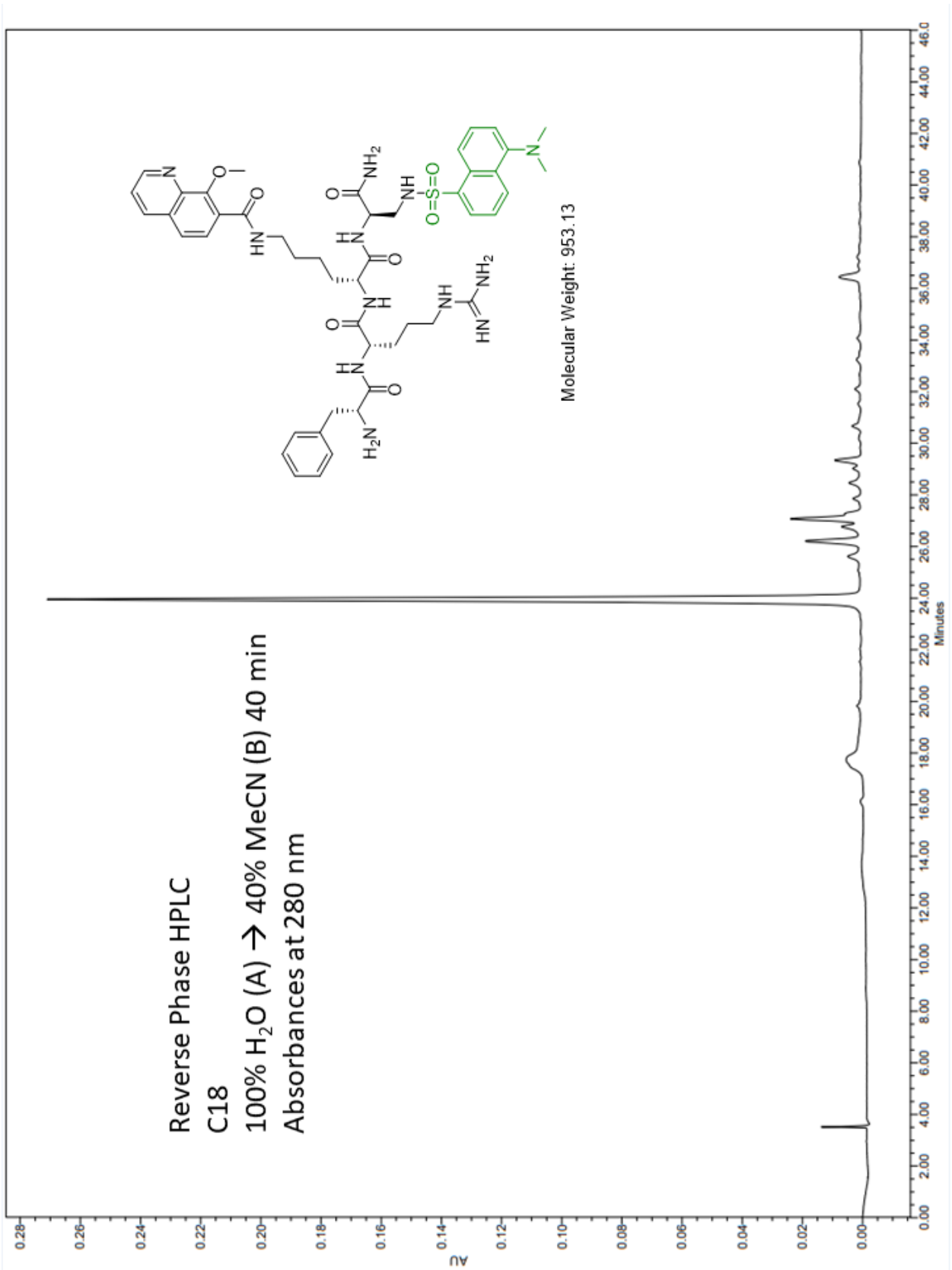
Reverse Phase HPLC
C18
100% H_2O (A) → 40% MeCN (B) 40 min
Absorbances at 280 nm
Molecular Weight: 953.13
AU
Minutes

RP HPLC **P-3**

RP HPLC **P-4**

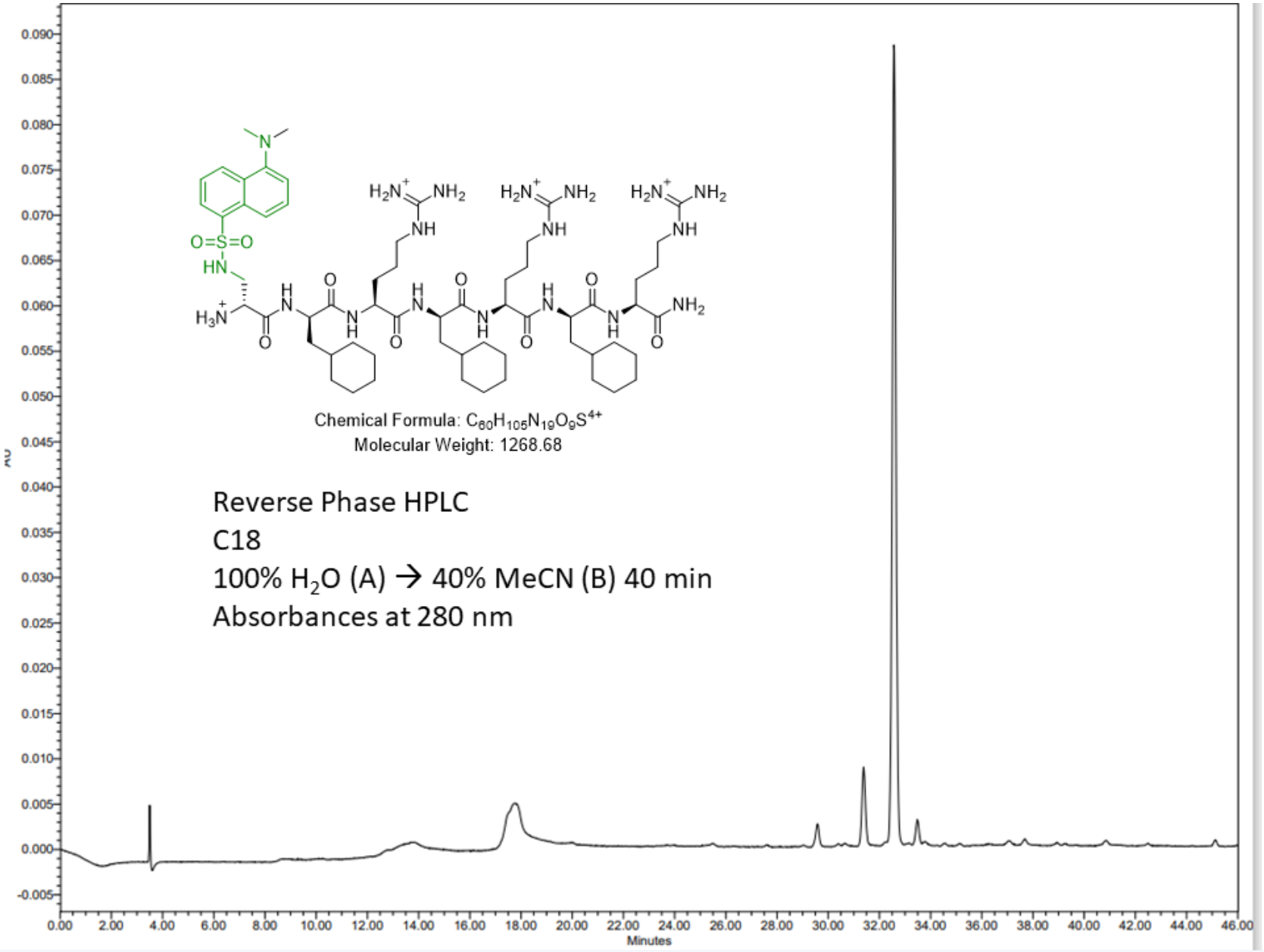
Chemical Formula: $C_{60}H_{105}N_{19}O_9S^{4+}$
Molecular Weight: 1268.68
Reverse Phase HPLC
C18
100% H_2O (A) → 40% MeCN (B) 40 min
Absorbances at 280 nm
AU
Minutes

RP HPLC **P-5**

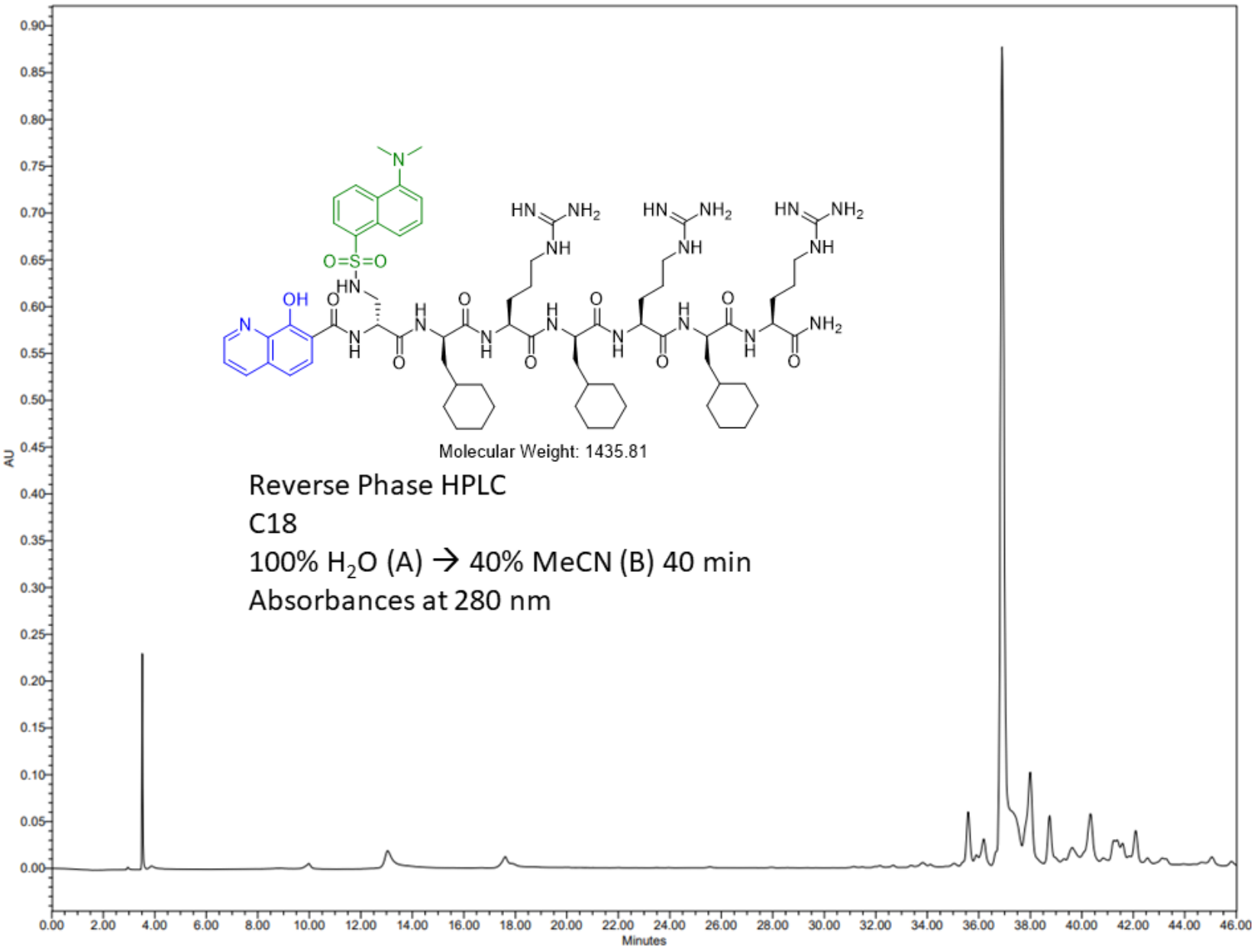
Molecular Weight: 1435.81
Reverse Phase HPLC
C18
100% H_2O (A) → 40% MeCN (B) 40 min
Absorbances at 280 nm
AU
Minutes

RP HPLC **P-6**

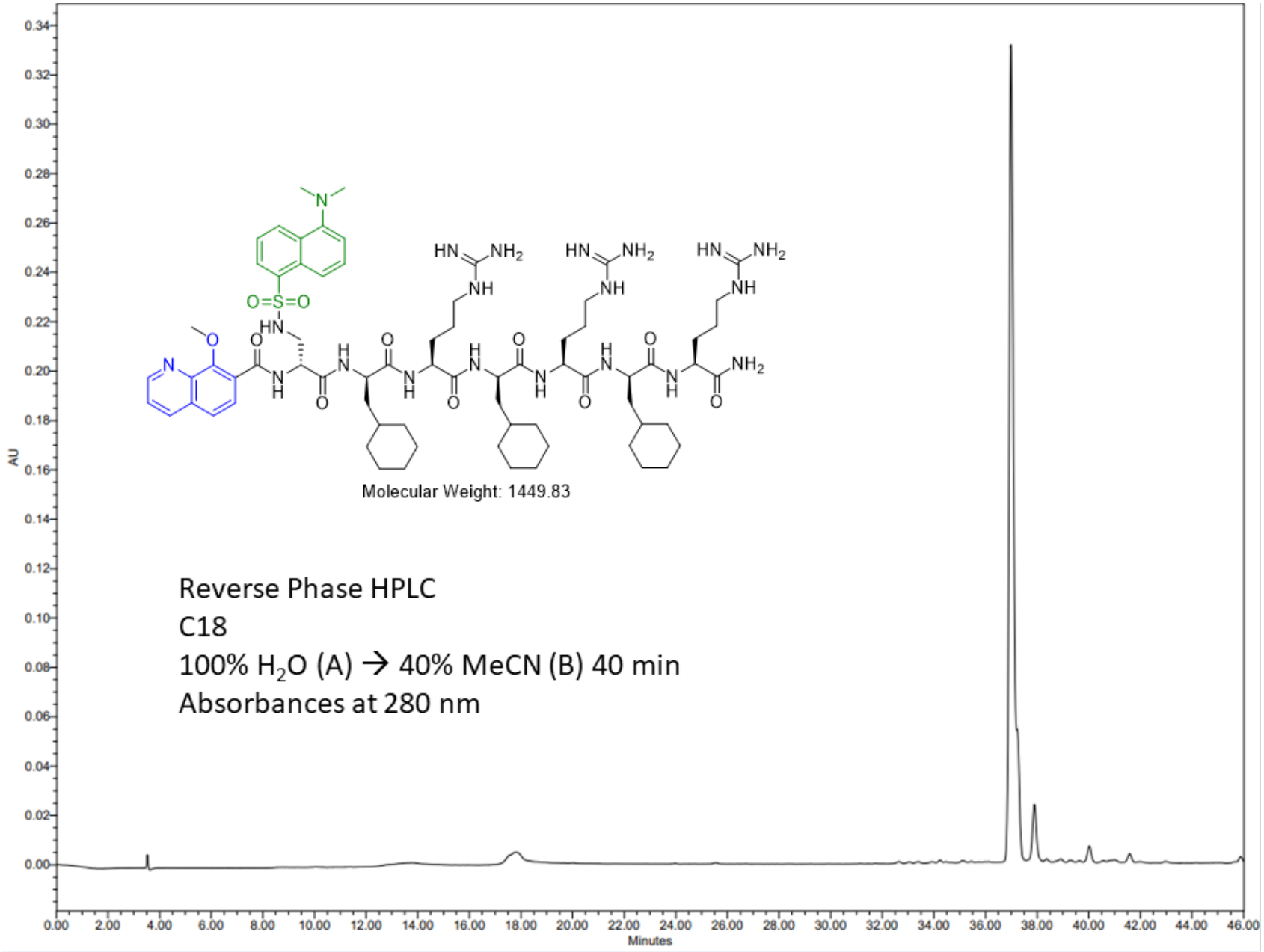
Molecular Weight: 1449.83
Reverse Phase HPLC
C18
100% H2O (A) → 40% MeCN (B) 40 min
Absorbances at 280 nm
AU
Minutes

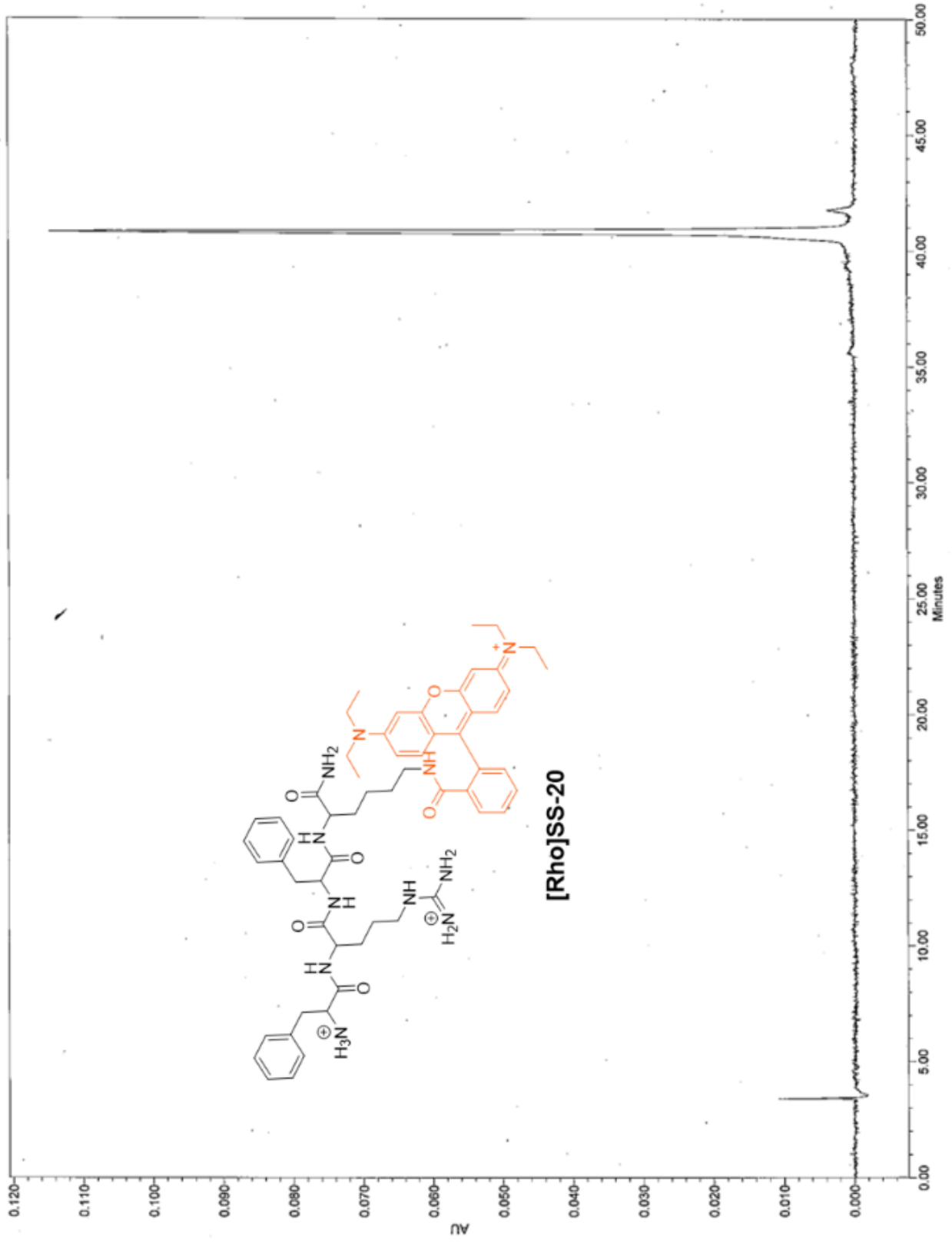

RP HPLC **P-7**

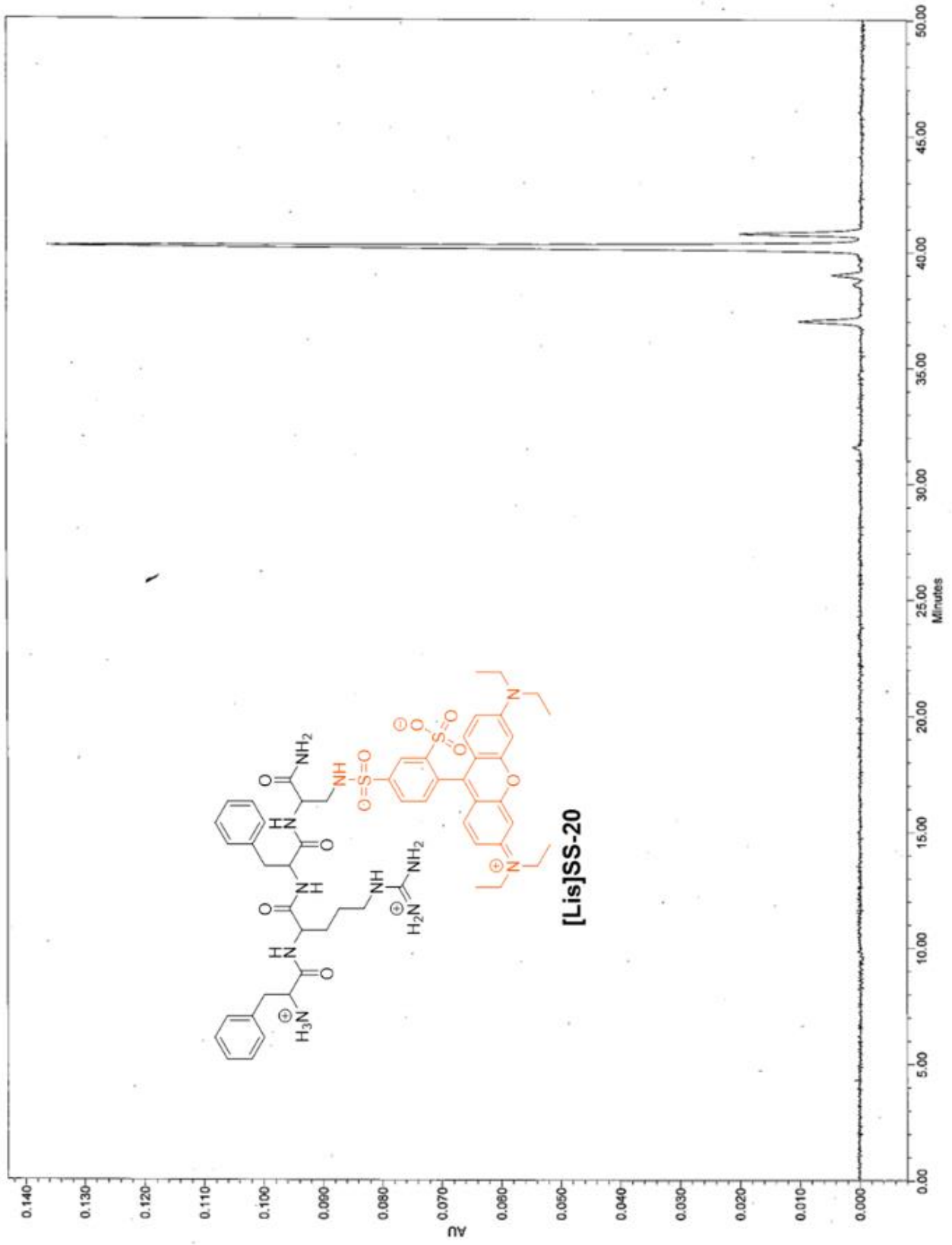

RP HPLC **P-8**